

Design and Synthesis of Inhibitors of 1-Deoxy-D-xylulose-5-phosphate reductoisomerase (DXR) and *Mycobacterium tuberculosis* Uracil DNA Glycosylase (MtUng) as Potential Antimicrobial Agents

THESIS

Submitted in partial fulfillment of the requirements for the degree of
DOCTOR OF PHILOSOPHY

by

Sharyu Kesharwani

2019PHXF0051P

Under the Supervision of

Dr. Sandeep Sundriyal



BIRLA INSTITUTE OF TECHNOLOGY AND SCIENCE PILANI

Pilani campus

Pilani 333 031, Rajasthan, India

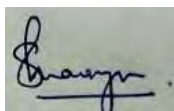
2023

Declaration

I hereby declare that the work carried out in this thesis titled “Design and Synthesis of Inhibitors of 1-Deoxy-D-xylulose-5-phosphate reductoisomerase (DXR) and *Mycobacterium tuberculosis* Uracil DNA Glycosylase (*MtUng*) as Potential Antimicrobial Agents” is an original piece of research work carried out under the guidance of Dr. Sandeep Sundriyal at BITS-Pilani, Pilani Campus, Pilani, India. This thesis has not been submitted by me for the award of any other degree of any other University/Institute.

Name: SHARYU KESHARWANI

Signature:

A handwritten signature in black ink, appearing to read 'Sharyu', with a horizontal line underneath.

Date: 22/11/2023

BIRLA INSTITUTE OF TECHNOLOGY AND SCIENCE, PILANI

CERTIFICATE

This is to certify that the thesis entitled “**Design and Synthesis of Inhibitors of 1-Deoxy-D-xylulose-5-phosphate reductoisomerase (DXR) and *Mycobacterium tuberculosis* Uracil DNA Glycosylase (*MtUng*) as Potential Antimicrobial Agents**” submitted by **Ms. Sharyu Kesharwani**, ID No. **2019PHXF0051P** for the award of Ph.D. Degree of the Institute, embodies the original work done by her under my supervision.

Signature of the Supervisor:

Name in capital letters: DR. SANDEEP SUNDRIYAL

Designation: Associate Professor

Date:

TABLE OF CONTENTS

Section	Title	Page no.
	<i>Certificate</i>	
	<i>Acknowledgements</i>	iv
	<i>Abstract</i>	vii
	<i>List of Figures</i>	ix
	<i>List of Tables</i>	xii
	<i>List of Schemes</i>	xii
	<i>Abbreviations</i>	xiii
CHAPTER I	Introduction and background	2
	1.1 Introduction and background	2
	1.1.1 FDA-approved antimicrobial agents	5
	1.1.2 Malaria	8
	1.1.3 Tuberculosis (TB)	10
	1.2 Drug discovery process	13
	1.2.1 Structure-based drug design	15
	1.2.2 Fragment-based Drug Design	16
	1.2.2.1 Fragment growing	18
	1.2.2.2 Fragment linking	18
1.2.2.3 Scaffold hopping/fragment merging	19	
CHAPTER II	Design and synthesis of non-hydroxamate lipophilic 1-deoxy-D-xylulose 5-phosphate reductoisomerase (DXR/<i>Ispc</i>) inhibitors	25
	2.1 Introduction and background	26
	2.1.1 Isoprenoids	26
	2.1.1.1 MEP Pathway	27
	2.1.1.2 MVA Pathway vs MEP Pathway	29
	2.1.2 1-Deoxy-D-Xylulose 5-Phosphate Reductoisomerase	30
	2.1.2.1 Discovery of DXR	30
	2.1.2.2 Mechanism of action for the conversion of DXP into MEP	31
	2.1.2.3 Structure of DXR	32
	2.1.2.4 The structure of <i>Pf</i> DXR	34
	2.1.3 Fosmidomycin: A natural DXR Inhibitor	35
	2.1.3.1 Discovery and antimicrobial agent	35
	2.1.3.2 Binding mode of FSM and enzyme kinetics	37
	2.2 Literature	39
	2.2.1 Modifications around hydroxamate	39
	2.2.2 Reversal of Hydroxamate	40
	2.2.3 Attempts to design non-hydroxamate DXR inhibitors	42
	2.3 Gaps in the existing research and objectives	49

2.4 Result and discussion	52
2.4.1 Fragment selection and <i>in vitro</i> screening	52
2.4.2 Docking studies on 5JAZ, 2Y1D and 3R0I protein	58
2.4.3 Design of inhibitors with selected MBGs	62
2.4.4 Chemical synthesis of designed inhibitors	65
2.4.4.1 Synthesis of α -aminophosphonates	65
2.4.4.2 Synthesis of molecules based on SA (F12), NA (F7), 8-HQ (F8), DHBA (F2), and CCA (F10) as MBGs	66
2.4.4.3 Synthesis of 2-HNQ (F5) derivatives	69
2.4.5 <i>In-vitro</i> DXR enzyme inhibition and SAR analysis	70
2.5 Methodology	88
2.5.1 Fragment screen	88
2.5.1.1 Protein Preparation	88
2.5.1.2 Ligand Preparation	88
2.5.1.3 Docking	88
2.5.2 Synthetic methodology	89
2.5.2.1 General synthesis procedure of Alpha-amino phosphonates (58a-i)	90
2.5.2.2 General synthesis procedure for non-hydroxamate lipophilic DXR inhibitors using benzyl group protection and deprotection approach	92
2.5.2.2.1 General synthesis procedure for benzyl group protection (59a-c)	92
2.5.2.2.2 General synthesis procedure for deprotection of benzyl carboxylate group (59d-f)	93
2.5.2.2.3 2.5.2.2.3 General synthesis procedure for amide coupling (59g-h)	94
2.5.2.2.4 Synthesis procedure for phenolic benzyl deprotection (59i)	95
2.5.2.3 General synthesis procedure for non-hydroxamate phosphonates (61a-h, 63a-h, 65a-h, 66a-h, 67a-c, 70, 69a, 69c, 69g and 72a)	96
2.5.2.4 Synthesis procedure for hydrolysis of phosphonates to phosphonic acids (62a-h, 64a-h, 68a-h, 71a, 71c, 71g and 73 a)	107
2.5.2.5 General procedure for the synthesis of 2,3-dihydroxybenzaldehyde derived phosphonates	113
2.5.2.6 Synthesis procedure for hydrolysis of 2,3-dihydroxybenzaldehyde derivatives (76a-b)	114
2.5.2.7 Synthesis procedure of 2-HNQ derivatives (79a-b, 80a-b and 81a-b)	115
2.5.3 Biological evaluation	115
2.5.3.1 DXR enzyme inhibition screening	115
2.5.3.2 Screening of compounds against <i>M. tuberculosis</i> and ESKAPE pathogens	116

CHAPTER III	CHAPTER III: Design and synthesis of <i>Mycobacterium tuberculosis</i> Uracil DNA Glycosylase (<i>MtUng</i>) inhibitors	136
	3.1 Introduction and background	137
	3.1.1 Base excision repair pathway (BER)	137
	3.1.2 DNA glycosylase	139
	3.1.3 Uracil DNA Glycosylase (UDG/UNG)	140
	3.1.4 Properties and structure of UNG	140
	3.2 Literature	143
	3.2.1 UNG Inhibitor	143
	3.2.2 <i>Mycobacterium</i> UNG	148
	3.3 Gaps in the research and objectives	149
	3.4 Results and discussion	150
	3.4.1 Selection, molecular docking and <i>in-vitro</i> evaluation of ring fragments	150
	3.4.2 Design, synthesis and <i>in-vitro</i> evaluation of BA derivatives	154
	3.5 Methodology	164
	3.5.1 Fragment selection	164
	3.5.2 Docking	164
	3.5.3 Chemistry	165
	3.5.3.1 General synthesis procedure of compounds (43a-c)	166
	3.5.3.2 General synthesis procedure of compound (44a-f)	166
	3.5.3.3 Synthesis procedure of compound (45 a-f)	168
	3.5.3.4 General Synthesis procedure of compound (47a-c)	170
	3.5.3.5 General Synthesis procedure of compound (48a-f)	170
	3.5.3.6 General Synthesis procedure of compound (49a-f)	172
	3.5.3.7 General Synthesis procedure of compound (50a-b)	173
	3.5.4 <i>In vitro</i> screening for <i>MtUng</i> activity inhibition assay	174
	3.5.4.1 Fluorescence-based assay	174
	3.5.4.2 Radioactivity based assay	175
References	176	
CHAPTER IV	CONCLUSION AND FUTURE PERSPECTIVE	187
	4.1.1 DXR Inhibitors development	
	4.1.1.1 Scope for future work	191
	4.1.2 <i>MtUng</i> Inhibitors	192
	4.1.2.1 Scope for future work	194
Appendix I	List of publication and awards	195
Appendix II	Biographies	196
Appendix III	Representative NMR spectra	198

ACKNOWLEDGEMENTS

There have been so many individuals who have positively contributed throughout my doctoral education and research at Birla Institute of Technology and Sciences (BITS). I want to thank and show my heartfelt gratitude to all those people for their assistance, support, guidance, and motivation.

First, I would like to express my sincere appreciation and gratitude to Dr. Sandeep Sundriyal for his constant support, guidance, motivation, and supervision during my Ph.D. I will be grateful to him for giving me the opportunity to pursue a Ph.D. in his laboratory and learn various techniques during my Ph.D. training. I am thankful to my doctoral advisory committee members, Prof. S. Murugesan, Prof. Atish T. Paul, and Dr. Vaibhav A. Dixit (former member), for their valuable suggestions, continued support, and motivation. I would also like to thank doctoral research committee members Dr. Anil Jindal and Dr. Deepak Chitkara (former DRC convener) for their contributions in managing documentation work.

I am grateful to Prof. V. Ramgopal Rao (Vice- Chancellor, BITS Pilani, Pilani campus), Prof. Sudhirkumar Barai (Director of BITS Pilani, Pilani campus), Col Soumyabrata Chakraborty (Retd) (Registrar BITS Pilani, Pilani campus), Prof. M. B. Srinivas (Dean of AGSRD), Prof. Shamik Chakraborty, (Associate Dean of AGSRD) for academic administration support for this research work. My wholehearted gratitude to Prof. Anil Gaikwad, Professor and Head of the Department of Pharmacy, Prof. Hemant R. Jadhav (former department head), and Prof. Atish T. Paul (former department head) during the tenure of my Ph.D. work for the opportunity to pursue my doctoral education, help and support. I am thankful to other faculty members of the department of Pharmacy, especially Dr. Richa Srivastava, for her guidance related to statistics during my Ph.D. work at the Birla Institute of Technology and Sciences (BITS), Pilani. I will always be grateful to all the faculty members and course instructors who helped me to gain advanced knowledge and skills in the pharmaceutical sciences at BITS Pilani. I am also thankful to the non-teaching staff of the department of pharmacy and lab attendants, Mr. Tarachand Saini, Mr. Laxman Kumar, Mr. Puran Singh, Mr. Ram Suthar, Mr. Vishal for assisting with the smooth research in the laboratory and providing the required materials. In addition, I am also thankful to our collaborators Prof. B. Gopal (IISc Bangalore), Prof. Umesh Varshney (IISc Bangalore), and Prof. Nisheeth Agarwal (THSTI, Faridabad) and their lab members for their contribution and support. I would like to thank the Instrumental Method Analysis Laboratory in BITS Pilani and Laboratory personnel Mr. Naveen Singh Rana, Mr. Abhishek and Mr. Sandeep for assisting the smooth operations of the instruments.

I would like to acknowledge the Department of Science and Technology, Science and Engineering Research Board (DST-SERB), The office of Principle Scientific Advisor (PSA) Government of India, and BITS Pilani for providing the opportunity to work on different projects as JRF and SRF and providing me the fellowship during my Ph.D. tenure. DST-SERB has also provided the International Travel Support (ITS) grant to present my work at the American Chemical Society (ACS) Fall Annual Meeting, August 2022, held in Chicago, IL, USA.

Further, I am thankful to past and current fellow graduate students, all my previous and current lab members, including Ms. Nancy Tripathi, Ms. Surbhi Saini, Mr. Mukul Kore, Ms. Harsha Valluri, and Mr. Animesh Majumdar, Mr. Atharva Bhide and Ms. Manisha Chowdhari for their help and support. I especially thank and acknowledge Mr. Shailesh Mani Tripathi for his help, support, guidance, and training on computational techniques during my Ph.D. work.

Finally, I am expressing my sincere gratitude and utmost respect to my parents, Mr. Shailesh Kesharwani, Mrs. Mahima S. Kesharwani, Mr. Shivkumar D. Kesharwani, Mrs. Sushma Kesharwani, my sister Dr. Kartiki Kesharwani, Dr. Pooja Kesharwani and brother Dr. Kuldeep Kesharwani for their continuous motivation, support, encouragement, advice, affection, love and well wishes to pursue my higher education. My special thanks to Mr. Siddharth Kesharwani for his patience, advice, faith and making everything possible. I am thankful to Mrs. Ritu Kesharwani for inspiring me to pursue higher education in the early days of my education. I am always fortunate to have great friends (Shreya, Harsha, Shivam, Ashok, Rudra, Shikha, Shobha, Priyanka, Rutuja, Sneha, Gurpreet, and Punita) around me who supported me through thick and thin of my life and during the journey in BITS. I especially thank Ms. Shreya Das and Ms. Harsha Valluri for their constant mental support, motivation, help and accompanied me in the journey.

I will always remain grateful to the Department of Pharmacy for providing me assistantship and research facility to support my graduate education and research.

Last but not the least, I am thankful to almighty god for blessed me to identify the right path to finish this work.

**THIS WORK IS DEDICATED TO MY FAMILY WHO
ALWAYS SUPPORTED ME FOR HIGHER EDUCATION**

ABSTRACT

Design and Synthesis of inhibitors of 1-deoxy-D-xylulose-5-phosphate reductoisomerase (DXR) and *Mycobacterium tuberculosis* Uracil DNA glycosylase (*MtUng*) as potential antimicrobial agents

SHARYU KESHARWANI

2023

Antimicrobial resistance (AMR) is caused by several clinical pathogens posing a serious threat to the healthcare system, including deadly pathogens like *Mycobacterium tuberculosis* (*Mtb*) and *Plasmodium falciparum* are responsible for Tuberculosis and Malaria respectively. The rise of resistant strains in pathogens has rendered the existing antibiotics ineffective, leading to the failure of the current therapies. Rapidly spreading AMR has led researchers to search for unique targets with distinct mechanisms of action. Structure-based drug design (SBDD) is a promising strategy for developing inhibitors for which the target structure is available.

This work demonstrates the SBDD-driven development of potent inhibitors of the two enzyme targets, namely DXR and UNG. Several clinical pathogens utilize DXR from the MEP pathway to synthesize isoprenoid precursors essential for the survival of *Mtb* and *Plasmodium* species. The absence of the MEP pathway in mammals makes this pathway more attractive for inhibitor development. Another enzyme target, Uracil DNA Glycosylase (UDG), removes the uracil from DNA by base excision repair mechanism to maintain the genomic integrity of the pathogens. Inhibiting UNG could leave DNA unrepaired, thus, leading to ultimate cell death. Inhibiting both these enzymes could be an excellent choice for the development of antimicrobial agents.

Chapter II demonstrates the SBDD-driven design and synthesis of lipophilic non-hydroxamate small molecule inhibitors. The current DXR inhibitors are hydroxamate based and are highly hydrophilic in nature. The highly polar nature of the current inhibitors poses several challenges, including the inability to penetrate the lipophilic cell membrane of several pathogens. A fragment-based screening approach was employed initially to identify the effective metal binding group (MBG) with a dioxygen donor motif from a library of fragments collated from the literature. Based on the docking and enzyme inhibition screening of the fragments, we selected five fragments that could be grown further by attaching a phosphonate moiety, an essential pharmacophoric feature of DXR inhibitors. Molecular docking was used to guide the

design of the final molecules, followed by the synthesis of a total 31 non-hydroxamate and lipophilic proposed ligands. Seventeen molecules showed moderate enzyme inhibition and were checked for IC₅₀ determination. Out of the synthesized analogs, compound **68b** showed the submicromolar range (IC₅₀ = 0.294 μM) of enzyme inhibition, comparable to the potent DXR inhibitor Fosmidomycin (IC₅₀ = 0.130 μM). Few other analogs showed low to moderate enzyme inhibition. Thus, non-hydroxamate lipophilic DXR inhibitors were designed and synthesized using a fragment-based approach.

Chapter III demonstrates the design and synthesis of barbituric acid (BA) derived *Mt*UNG inhibitors. The essentiality of the UNG for survival in *Mtb* offers an advantage to inhibiting the enzyme for the development of *Mt*UNG inhibitors. Current UNG inhibitors are weak inhibitors and mostly based on the uracil ring. Guided by the molecular docking studies and similarity to the uracil ring, we selected several non-uracil ring fragments. Based on the docking pose, synthetic tractability, and commercial availability, these twelve ring fragments were screened against *Mt*Ung, *in vitro*. Two orthogonal methods, radioactivity-based assay and fluorescence-based assay, were employed for *Mt*Ung inhibition evaluation. Out of 12 rings, barbituric acid (BA) showed potency better or comparable to the uracil ring (IC₅₀ = 1 mM). The X-ray crystal structure of several of these ring fragments was also solved in complex with the protein by our collaborators, thus further providing the experimental validity. As a case study, we selected BA ring (IC₅₀ = 1 mM) for derivatization and SAR study using a tethering strategy. Thus, a total of 17 BA derivatives were synthesized and tested against *Mt*Ung. Compounds **45a** (IC₅₀ = 0.50 mM) and **49a** (IC₅₀ = 0.1 mM) exhibited the highest potency compared to the other molecules in the series in the radioactive-based assay. The detailed SAR study is reported with the ester-bearing lipophilic aromatic ring, demonstrating the importance of the substituent's position for effective inhibition.

In summary, we have developed novel small-molecule enzyme inhibitors for the DXR and UNG targets as potential antimicrobial agents. We obtained a few lead molecules from each target, which could be explored in the future to develop more potent molecules.

LIST OF FIGURES

Figure no.	Title	Page no.
CHAPTER I		
Fig. 1.1	Bar chart representing the total number of deaths attributed to different pathogens which are associated with antibiotic resistance and susceptible to antibiotics	3
Fig. 1.2	Deaths associated and attributed by antibiotic resistance in respective pathogens	4
Fig. 1.3	Percentage of drugs approved by FDA for the treatment of infectious diseases	5
Fig. 1.4	Current antimalarial drugs used in the treatment	9
Fig. 1.5	The total number of deaths occurred due to various pathogens	11
Fig. 1.6	Total deaths per 100k attributed by <i>Mtb</i> globally	12
Fig. 1.7	Current first line and MDR anti-TB agents	13
Fig. 1.8	New drug discovery and development timeline	14
Fig. 1.9	Different stages involved in the phenotypic and molecular target screening	15
Fig. 1.10	A Flow diagram representing the process of Structure-based drug design	15
Fig. 1.11	Structures of the FDA-approved drugs discovered by SBDD	16
Fig. 1.12	Different approaches used for the fragment based drug discovery	19
Fig. 1.12	Zelboraf (PLX4032), from fragment to therapeutic drug	20
CHAPTER II		
Fig. 2.1	A timeline representing research advances in Isoprenoid biosynthesis	27
Fig. 2.2	Mechanistic difference between two pathways for isoprenoid biosynthesis	29
Fig. 2.3	Mechanism for conversion of DXP into MEP	32
Fig. 2.4	Structure of <i>Mt</i> DXR (PDB code: 2JD1) in complex with NADPH	34
Fig. 2.5	Structure of <i>Pf</i> DXR (PDB code 1Q0Q) with NADPH AND DXP	35
Fig. 2.6	Potent DXR inhibitors discovered in the early 1980s	36
Fig. 2.7	3D structure of the FSM-bound quaternary complex of <i>Mt</i> DXR (PDB Code: 2Y1D)	37
Fig. 2.8	Essential structural features of FSM, a natural DXR inhibitor	40
Fig. 2.9	Various modifications around FSM to develop a potent lipophilic inhibitor	41
Fig. 2.10	SAR analysis of hydroxamate-based DXR inhibitors	42
Fig. 2.11	(A) Binding mode comparison of hydrophobic inhibitors 20 (PDB 3ANM) and 21 (PDB 3ANN) with FSM (1) (PDB 2EGH	43
Fig. 2.12	Non-hydroxamate MBG-based DXR inhibitors from the literature	46
Fig. 2.13	HDAC inhibitors with hydroxamate group	49
Fig. 2.14	Possible resonance of the hydroxamate group contributing to the metal coordination	50
Fig. 2.15	Proposed structure for designed DXR inhibitors	51
Fig. 2.16	Structure of fragments in metal chelator library (MCL)	53
Fig. 2.17	The graphical representation of the calculated properties of the fragments from MCL	56
Fig. 2.18	Interactions of co-crystallized ligand at the binding site of 5JAZ (A), 2Y1D (B), and 3ANM (C)	57

Fig. 2.19	Aromatic rings occupying Pocket B (lined with Pro274 and Met276)	.59
Fig. 2.20	Docking poses of MBGs (cyan balls and sticks) showing bidentate chelation of the Mn ²⁺ ion (purple ball) inside the DXR pocket (PDB 3R0I)	60
Fig. 2.21	Graphical representation of enzyme inhibition activity of fragments at 100 μM concentration	61
Fig. 2.22	Pocket B and Pocket A occupied by designed molecules	63
Fig. 2.23	Docking poses of several MBG containing non-hydroxamate DXR inhibitors (cyan balls and sticks) showing bidentate chelation of the Mn ²⁺ ion (purple ball) inside the DXR pocket (3R0I)	65
Fig. 2.24	Binding mode of 68b and FSM	75
Fig. 2.25	Binding pose comparison of 68a (green), 68b (blue), and 68e (orange)	77
Fig. 2.26	The binding poses of 62e (pink) and 62a (green) shows flipped orientations compared to 68b (cyan)	79
Fig. 2.27	Two different metal chelation modes observed in the DHBA	80
Fig. 2.28	Binding pose comparison for the various derivatives 64a-b , 64d	81
Fig. 2.29	Binding pose comparison for 71a (blue), 68a (pink), and 68b	83
Fig. 2.30	Restricted rotation in 68a vs. 68b and 76a vs. 76b	84
Fig. 2.31	Determination of MIC against Mtb (>80% inhibition by Alamar Blue Assay)	86

CHAPTER III

Fig. 3.1	General representation of Base Excision Repair Mechanism	138
Fig. 3.2	The stepwise BER process	138
Fig. 3.3	Species showing the presence of UDG	140
Fig. 3.4	Five stretches of conserved motifs in UNG	141
Fig. 3.5	(A) Crystal structure of UNG:DNA complex from <i>E. coli</i> showing the seven α-helices and four parallel β-strands (B) Image showing the interacting residues of UNG (pink ribbons) and DNA (cyan ladder) interface (green-balls and sticks)	142
Fig. 3.6	Ugi:UNG complex	144
Fig. 3.7	Various 4 and 5 position substituted uracil derivatives and their reported IC ₅₀ values in mM	144
Fig. 3.8	Molecular interactions shown by ring fragments in docking studies	151
Fig. 3.9	<i>MtUng</i> co-crystals with the uracil-mimicking ring fragments	152
Fig. 3.10	3D view of <i>MtUDG</i> bound to uracil (1) (yellow ball and sticks) in the uracil binding pocket (UBP) (PDB ID 4WLP)	154
Fig. 3.11	Predicted binding pose of analogs 43a-c	156
Fig. 3.12	Docked poses of BA derivatives 45a , 45b and 45c with <i>MtUDG</i>	158
Fig. 3.13	Docked poses of BA derivatives 45d , 45e , 45f , and 45a with <i>MtUng</i>	161
Fig. 3.14	Docked poses of BA derivatives 49a and 49b	162

CHAPTER IV

Fig. 4.1	Structure and IC ₅₀ values of non-hydroxamate DXR inhibitors	189
Fig. 4.2	From fragment to potent inhibitor	191
Fig. 4.3	Structures and IC ₅₀ values of <i>MtUng</i> inhibitors	193

LIST OF TABLES

Table no.	Title	Page no.
CHAPTER I		
Table 1.1	List of antimicrobial agents approved during 2015-2023	5
CHAPTER II		
Table 2.1	Metal chelators and their properties	54
Table 2.2	Interactions shown by cocrystallized ligand at the binding site	57
Table 2.3	Percentage inhibition of DXR enzyme by fragments in DXR inhibition assay	.61
Table 2.4	Structures of <i>O</i> -alkylated and <i>C</i> -alkylated derivatives of 2-Hydroxy-1,4-naphthoquinone	70
Table 2.5	IC ₅₀ and enzyme inhibition data for non-hydroxamate synthesis derivatives	71
Table 2.6	Physicochemical Properties of the synthesized derivatives	74
CHAPTER III		
Table 3.1	Summary of uracil-derived compounds reported as UNG inhibitor	146
Table 3.2	IC ₅₀ values and predicted binding energies of uracil and similar ring fragments	152
Table 3.3	IC ₅₀ values and predicted binding energies for the BA-based molecules	158

LIST OF SYNTHESIS SCHEMES

Scheme 2.1	Synthesis of different primary α -aminophosphonates	66
Scheme 2.2	Synthesis of the derivatives of F2, F7 and F8 MBGs using benzylation chemistry	67
Scheme 2.3	General synthesis scheme for the derivatives of F12, salicylic acid (SA) MBG	67
Scheme 2.4	General synthesis scheme for the derivatives of F2, 2,3-Dihydroxy benzoic acid (DHBA) MBG	68
Scheme 2.5	General synthesis scheme for the derivatives of F7, 1-Hydroxy-2-naphthoic acid (NA) MBG	68
Scheme 2.6	General synthesis scheme for the derivatives of F8, 8-Hydroxyquinoline-7-carboxylic acid (8-HQ) MBG	68
Scheme 2.7	General synthesis scheme for the derivatives of F10, Chromone-3-carboxylic acid (CCA) MBG	68
Scheme 2.8	General synthesis scheme for the derivatives of 2,3-Dihydroxy benzaldehyde (F9) MBG	69
Scheme 2.9	Attempts to obtain the <i>O</i> -alkylated and <i>C</i> -alkylated derivatives of 2-HNQ (F5)	70
Scheme 3.1	Synthesis of barbituric acid derivatives	155
Scheme 3.1	Synthesis of barbituric acid derivatives	155

LIST OF ABBREVIATIONS

μM	Micromolar
5-FAM	5-Carboxyfluorescein
AMR	Antimicrobial resistance
AP site	Apurinic/apyrimidinic site
AR	Antibiotic Resistance
BA	Barbituric acid
BER	Base excision repair pathway
BHQ-1	Black Hole Quencher-1
BSA	Bovine serum albumin
CAs	Carbonic anhydrase
CDC	Centres for Disease Control and Prevention
CDCl_3	Chloroform
CDP-ME	4-diphosphocytidyl-2C-methyl-D-erythritol
clogP	Partition coefficient
CMP	Cytidine monophosphate
Cyt	Cytosine
DCM	Dichloromethane
DXS	Deoxy-D-xylulose-5-phosphate synthase
D-GAP	D-glyceraldehyde-3-phosphate
DHBA	2,3-dihydroxy benzoic acid
DMAPP	Dimethylallyl pyrophosphate
DMAP	4-Dimethylaminopyridine
DMSO	Dimethyl sulfoxide
DMF	Dimethyl formamide
DXP	1-deoxy-D-xylulose-5-phosphate
DXR/ IspC	1-deoxy-D-xylulose-5-phosphate reductoisomerase
DXS	1-deoxy-D-xylulose-5-phosphate synthase
<i>E. coli</i>	<i>Escherichia coli</i>
<i>EcUng</i>	<i>Escherichia coli</i> -DNA glycosylase
EtOH	Ethanol
ECDC	European Centre for Disease Prevention and Control
EDCI.HCl	(3-Dimethylamino-propyl)-ethyl-carbodiimide Hydrochloride
EtOH	Ethanol
FBDD	Fragment-based drug design
FDA	Food and Drug Administration
FPLC	Fast protein liquid chromatography
FSM	Fosmidomycin
glpT	Glycerol-3-phosphate transporter
GRAM	Global Research on Antimicrobial Resistance
H_2O	Water
HBA	H bond acceptors
HBD	H bond donors
HDACs	Histone deacetylases
HMG-CoA	(S)-3-hydroxy-3-methylglutaryl-CoA
HNQ	8-hydroxyquinoline-7-carboxylic acid
HOBt	Hydroxybenzotriazole
HRMS	High-resolution mass spectrometry
HTS	High-throughput screening

hUNG	Human UNG
IC ₅₀	Half Inhibitory concentration
IPP	Isopentenyl pyrophosphate
K ₂ CO ₃	Potassium carbonate
KI	Potassium iodide
LB	Luria-Bertani medium
MBG	Metal-binding group
MCL	Metal chelator library
MD	Molecular dynamics
MDR	Multidrug-resistance
MEcPP	2C-methyl-D-erythritol-2,4-cyclodiphosphate
MeOH	Methanol
MEP	2-C-methyl-D erythritol 4-phosphate
MgSO ₄	Magnesium sulphate
MIC ₉₀	Maximum inhibitory concentration of an compound inhibiting 90% isolates
MIDA	N-methyl iminodiacetic acid
mM	Millimolar
MMGBSA	Molecular mechanics with generalised Born and surface area solvation
MMPs	Matrix metalloproteinases
MMR	Mismatch repair
Mtb	<i>Mycobacterium tuberculosis</i>
MtUng	<i>Mycobacterium tuberculosis</i> UNG
MVA	(3R)-3,5-dihydroxy-3-methylpentanoic acid mevalonic acid
MW	Molecular weight
NA	1-Hydroxy-2-naphthoic acid
Na ₂ EDTA	Disodium salt of ethylenediaminetetraacetic acid
NaCl	Sodium chloride
NADPH	Nicotinamide adenine dinucleotide phosphate
NaOH	Sodium Hydroxide
NCEs	New chemical entities
NER	Nucleotide excision repair
NHP	N-hydroxy pyridone
nM	Nanomolar
NMR	Nuclear magnetic resonance
PDB	Protein Data Bank
PDR	Pandrug-resistance
PBS-I/II	Bacillus subtilis phage I and II
PMSF	Phenylmethylsulfonyl fluoride
ppm	Parts per million
RMSD	Root mean square deviation
RNI	Reactive nitrogen intermediates
RO3	Rule of Three
RO5	Rule of Five
ROS	Reactive oxygen species
RPM	Rate per minute
RT	Room temperature
SA	Salicylic acid
SAR	Structure activity relationship
SBDD	Structure-based drug design

SEC	Size exclusion chromatography
SP	Standard precision
TB	Tuberculosis
TDR-TB	Total drug-resistance
TLC	Thin layer chromatography
TMSBr	Bromotrimethylsilane
UBP	Uracil-binding pocket
UDG/UNG	Uracil DNA glycosylase
UTIs	Urinary tract infections
WHO	World Health Organisation
XDR	Extensive drug-resistance
XP	Extra precision

CHAPTER 1
Introduction and Background

1.1 INTRODUCTION AND BACKGROUND

Antimicrobial resistance (AMR) is a top threat to global health management systems.¹ AMR occurs when clinical pathogens evolve in a way that leads to ineffective antimicrobial treatments. It is a resistance developed by bacteria, viruses, fungi, and parasites to the current antimicrobial agents by various mechanisms such as genetic modulation, efflux mechanisms, spontaneous evolution, and horizontal gene transfer. AMR has already shown its devastating effect in cases of various infectious diseases such as malaria, tuberculosis (TB), blood poisoning, diarrhea, pneumonia, HIV/AIDS, and gonorrhea. AMR is responsible for treatment failures, extended treatment periods, hiked healthcare costs, serious ailments, and prolonged hospitalization. The ineffectiveness of the current therapy due to AMR is pushing the healthcare system into a vulnerable future where seemingly harmless pathogens could result in lethal infections. Many healthcare advancements depend on antimicrobial agents to treat the infections, such as organ transplants, joint replacements, cancer therapy, and chronic disease treatments.

According to the Centers for Disease Control and Prevention (CDC), more than 2.8 million people in the United States are infected with antibiotic-resistant diseases annually, leading to more than 35,000 deaths. Antibiotic Resistance (AR) Threats Report published in 2019 estimated 4.95 million deaths were attributed to bacterial antibiotic resistance, including 1.27 million deaths directly associated with drug-resistant infections worldwide, with the highest number of deaths reported from sub-Saharan Africa and South Asia.^{2,3} This death toll is estimated to rise to 10 million by 2050 if the issue of AMR is not effectively addressed.

European Centre for Disease Prevention and Control (ECDC) and CDC collectively standardized the terminologies to define the AMR into a different pattern to distinguish the level of resistance such as multidrug-resistance (MDR), which is non-susceptibility to at least one agent in three or more antimicrobial categories. Similarly, extensive drug resistance (XDR) is defined as non-susceptibility to at least one agent in all but two or fewer antimicrobial categories, and pandrug-resistance (PDR) is non-susceptibility to all agents in all antimicrobial categories.⁴

According to Global Research on Antimicrobial Resistance (GRAM) Project report, out of the 23 pathogens included in the study, drug resistance was observed in six pathogens alone by *E. coli*, *K. pneumoniae*, *S. aureus*, *P. aeruginosa*, *A. baumannii*,

and *S. pneumoniae* as shown in Fig 1.1. In 2017, World Health Organization (WHO) mentioned a list of pathogens ESKAPE (*Enterococcus faecium*, *Staphylococcus aureus*, *Klebsiella pneumoniae*, *Acinetobacter baumannii*, *Pseudomonas aeruginosa*, and *Enterobacter* species) against which new antibiotic development is crucially demanded.⁵ These ESKAPE pathogens caused nearly 929,000 deaths among 3.57 million associated cases.^{3,6} Across all pathogens included in the study, most resistance was observed to two classes of antibiotics, fluoroquinolones, and beta-lactam antibiotics, often used in severe infections as the first line of defense. More than 70% of deaths were accounted for by resistance to fluoroquinolones and beta-lactam antibiotics only, by clinical pathogens.

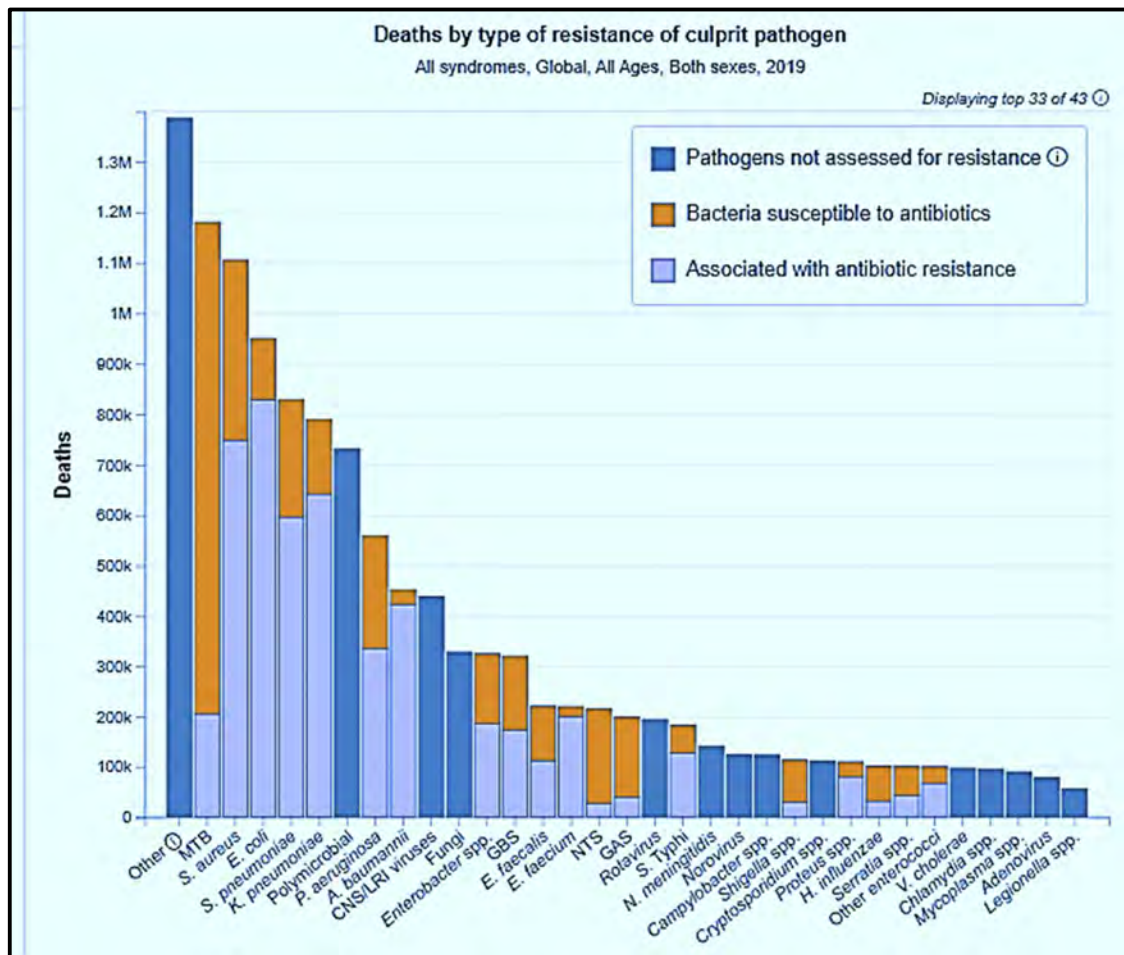


Fig. 1.1 Bar chart representing the total number of deaths attributed to different pathogens associated with antibiotic resistance and susceptibility to antibiotics (Data generated using antimicrobial resistance visualization tool, GRAM).⁷

One of the significant reasons for the development of AMR is misuse, lack of patient adherence to complete the course, and overuse of antibiotics. In a decade, from 2000-2010, the consumption rate of antibiotics in humans was dramatically hiked by 36%.⁸ Apart from human medicine consumption, routine addition of antibiotics has been increased in veterinary medicine, disease prevention in agriculture and horticulture, and growth promotion in animals.^{9,10} In the long term, AMR compromises the functional capacity of the immunity system in humans to battle infectious diseases, especially increasing complications for patients with immune-compromised conditions such as dialysis, chemotherapy, and surgery. It may significantly impact patients with chronic clinical conditions such as diabetes, rheumatoid arthritis, and asthma.⁹ Fig. 1.2 represents the deaths that occurred due to AMR by different clinical pathogens.

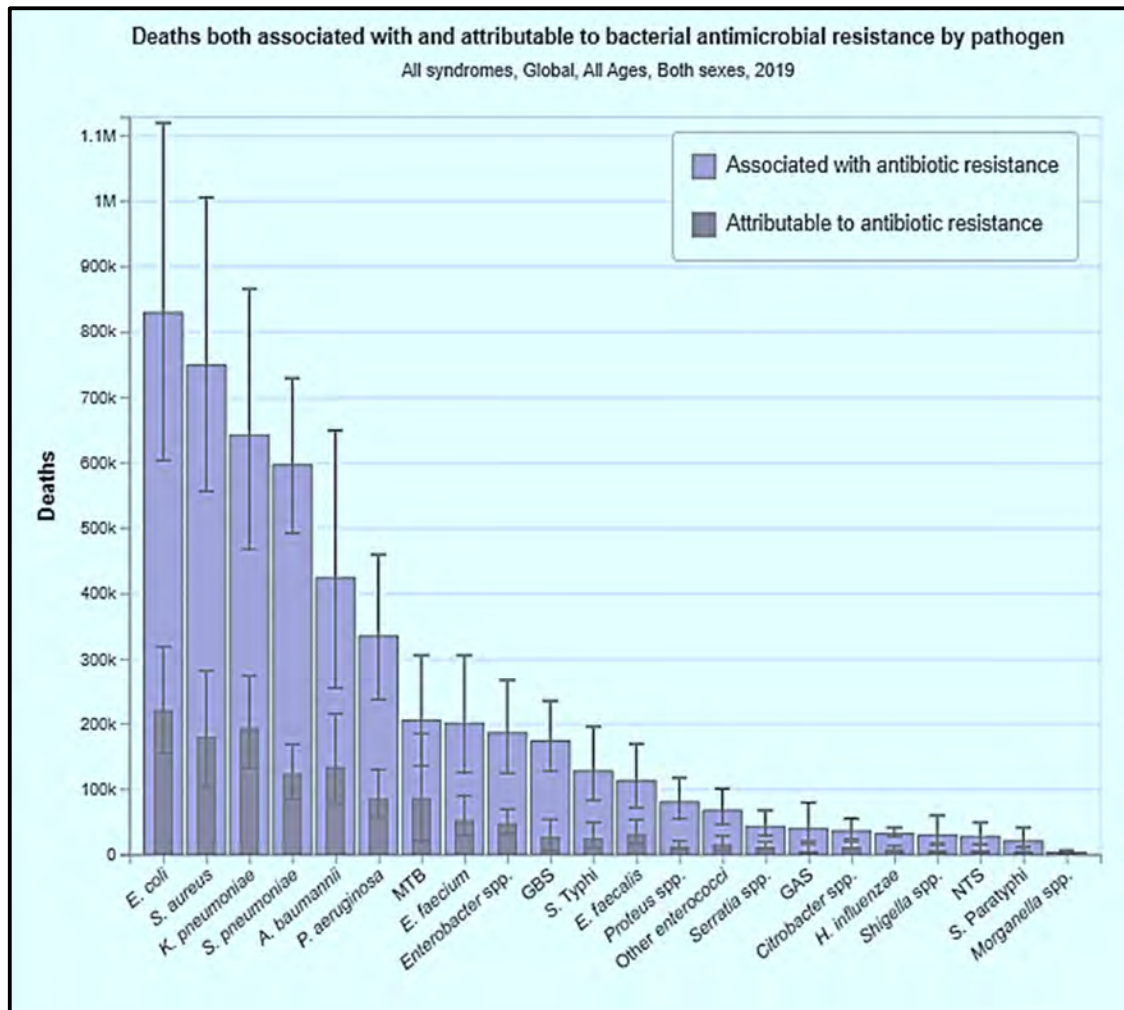


Fig. 1.2 Deaths associated and attributed by antibiotic resistance in respective pathogens⁷

1.1.1 FDA-approved antimicrobial agents:

Major pharmaceutical companies are continuously working towards developing newer antimicrobial agents, and very few of them receive Food and Drug Administration (FDA) approval every year. Between 2015 and 2023, nearly 389 new drugs received FDA approval for the treatment of various clinical conditions, in which only 52 drugs (~13%) were approved for treating various infectious diseases, as shown in Fig. 1.3. Table 1.1 represents the antimicrobial agents approved during 2015-2023.¹¹

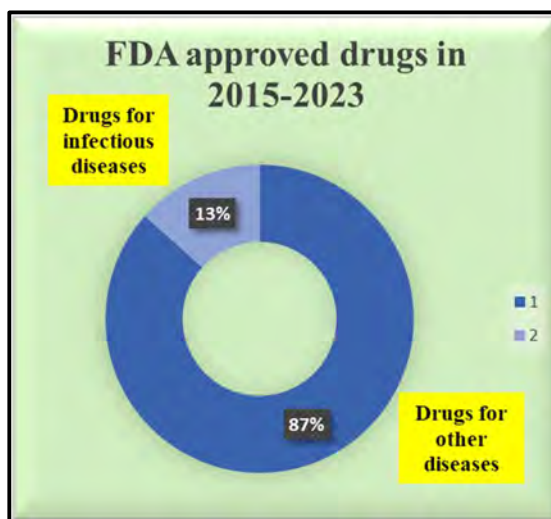


Fig. 1.3 Percentage of drugs approved by FDA for the treatment of infectious diseases¹¹

Table 1.1: List of antimicrobial agents approved during 2015-2023. Data obtained from the USFDA website New Drugs at FDA: CDER’s New Molecular Entities and New Therapeutic Biological Products¹¹

Drug	Indication	Year Approved	Company
Rezzayo (rezafungin)	Candidemia and invasive candidiasis	2023	Cidara
Sunlenca (lenacapavir)	HIV infections (which are non-curable by available treatments due to resistance, intolerance, or safety considerations)	2022	Gilead Sciences
Rolvedon (eflapegrastim)	To decrease the incidence of infection in patients with non-myeloid malignancies receiving myelosuppressive anti-cancer drugs associated with clinically significant incidence of febrile neutropenia	2022	Spectrum Pharmaceuticals
Voquezna	<i>Helicobacter pylori</i> infection	2022	Phantom Pharma

Vivjoa	To treat recurrent vulvovaginal candidiasis (RVVC) in females with a history of RVVC who are not of reproductive potential	2022	Mycovia pharma
Brexafemme	Vulvovaginal candidiasis	2021	Scynexis
Cabenuva	HIV-1	2021	ViiV Healthcare
Fexinidazole	Human African trypanosomiasis	2021	Sanofi
Livtency	Cytomegalovirus infection	2021	Takeda
Artesunate	Malaria	2020	Amivas
Ebanga	Ebola	2020	Ridgeback Biotherapeutics
Inmazeb	Ebola	2020	Regeneron
Lampit	Chagas disease	2020	Bayer
Rukobia	HIV-1	2020	ViiV Healthcare
Veklury	COVID-19	2020	Gilead
Egaten	Fascioliasis	2019	Novartis
Fetroja	Urinary tract infection	2019	Shionogi
Pretomanid	Lung tuberculosis	2019	Mylan
Recarbrio	Urinary tract infection	2019	Merck
Xenleta	Bacterial pneumonia	2019	NABRIVA Therapeutics
Aemcolo	Travelers diarrhea	2018	Conventus BioMedical Solutions
Biktarvy	HIV-1	2018	Gilead
Krintafel	Malaria	2018	GlaxoSmithKline
Moxidectin	Onchocerciasis	2018	Medicines Development for Global Health
Nuzyra-1	Acute bacterial skin and skin structure infections	2018	Paratek Pharmaceuticals
Nuzyra-2	Community-acquired bacterial pneumonia	2018	Paratek Pharmaceuticals
Pifeltro	HIV-1	2018	Merck
Tpoxx	Smallpox disease	2018	SIGA Technologies
Trogarzo	HIV-1	2018	Thera
Xerava	Intra-abdominal infections	2018	Tetraphase Pharmaceuticals
Xofluza	Influenza	2018	Genentech
Zemdri	Urinary tract infection	2018	Achaogen

Baxdela	Acute bacterial skin and skin structure infections	2017	Melinta Therapeutics
Benznidazole	Chagas disease	2017	Exeltis
Giapreza	To increase blood pressure in septic shock	2017	La Jolla Pharmaceutical Company
Mavyret	Chronic Hepatitis-C	2017	AbbVie
Prevymis	Prevention of cytomegalovirus infection	2017	Merck
Solosec	Bacterial vaginosis	2017	Symbiomix Therapeutics
Vabomere	Urinary tract infection	2017	The Medicines Company
Vosevi	Chronic Hepatitis-C	2017	Gilead
Xepi	Impetigo	2017	Medimetriks Pharmaceuticals
Anthim	Inhalational anthrax	2016	Elusys Therapeutics
Epclusa	Chronic Hepatitis-C	2016	Gilead
Zepatier	Chronic Hepatitis-C	2016	Merck
Zinplava	Clostridium difficile infection	2016	Merck
Avycaz-1	Complicated intra-abdominal infection	2015	Forest Pharmaceuticals
Avycaz-2	Urinary tract infection	2015	Forest Pharmaceuticals
Cresemba-1	Invasive aspergillosis	2015	Astellas Pharma
Cresemba-2	Invasive mucormycosis	2015	Astellas Pharma
Daklinza	Chronic Hepatitis-C	2015	Bristol-Myers-Squibb
Genvoya-1	HIV-1	2015	Gilead
Genvoya-2	HIV-1	2015	Gilead

Resistant strains of *Plasmodium* and *Mycobacterium* causing malaria and TB, respectively, are spreading rapidly. These diseases are most prevalent in low-income countries where the healthcare system is already stressed. Thus, there is an escalated demand for discovering new antimicrobial agents with a novel mode of action and a novel target. In the last eight years (2015-2023), only two and one new chemical entities (NCEs) have received FDA approval for Malaria and TB, respectively. Thus, while AMR poses a severe challenge, it also presents opportunities to fill the gap in the antimicrobial drug discovery pipeline.

1.1.2 Malaria:

Malaria is a mosquito-borne disease caused by the *Plasmodium* parasite and remains a significant public health challenge in many parts of the world. Nearly 50% of the world's population was at risk of malaria in 2020. Among various species, *P. falciparum* and *P. vivax* are responsible for a greater number of infections. According to the WHO, malaria remains a major infectious disease, with an estimated 247 million cases and 619,000 deaths reported in 2021, out of which 94% of cases occur in the African region. Malaria is endemic to nearly 84 countries in the world. Most of the malaria cases (95%) and deaths (96%) occurred in sub-Saharan Africa, with the majority of deaths occurring in sub-Saharan Africa. Malaria is endemic in many countries in sub-Saharan Africa and parts of South Asia, Southeast Asia, and Latin America. Sub-Saharan Africa continues to bear the highest burden of malaria, accounting for over 95% of global malaria cases and deaths. In 2019, 29 countries accounted for 95% of global malaria cases, with Nigeria having the highest burden (27%), followed by the Democratic Republic of the Congo (12%), Uganda (5%), and Mozambique (4%). Children under five years of age and pregnant women are particularly vulnerable to malaria. According to WHO estimation, children under five years of age accounted for 80% of total deaths in 2019. India accounted for 79% of cases in the South Asia region. Current antimalarial treatment consists of drugs mentioned in Fig. 1.4.¹²

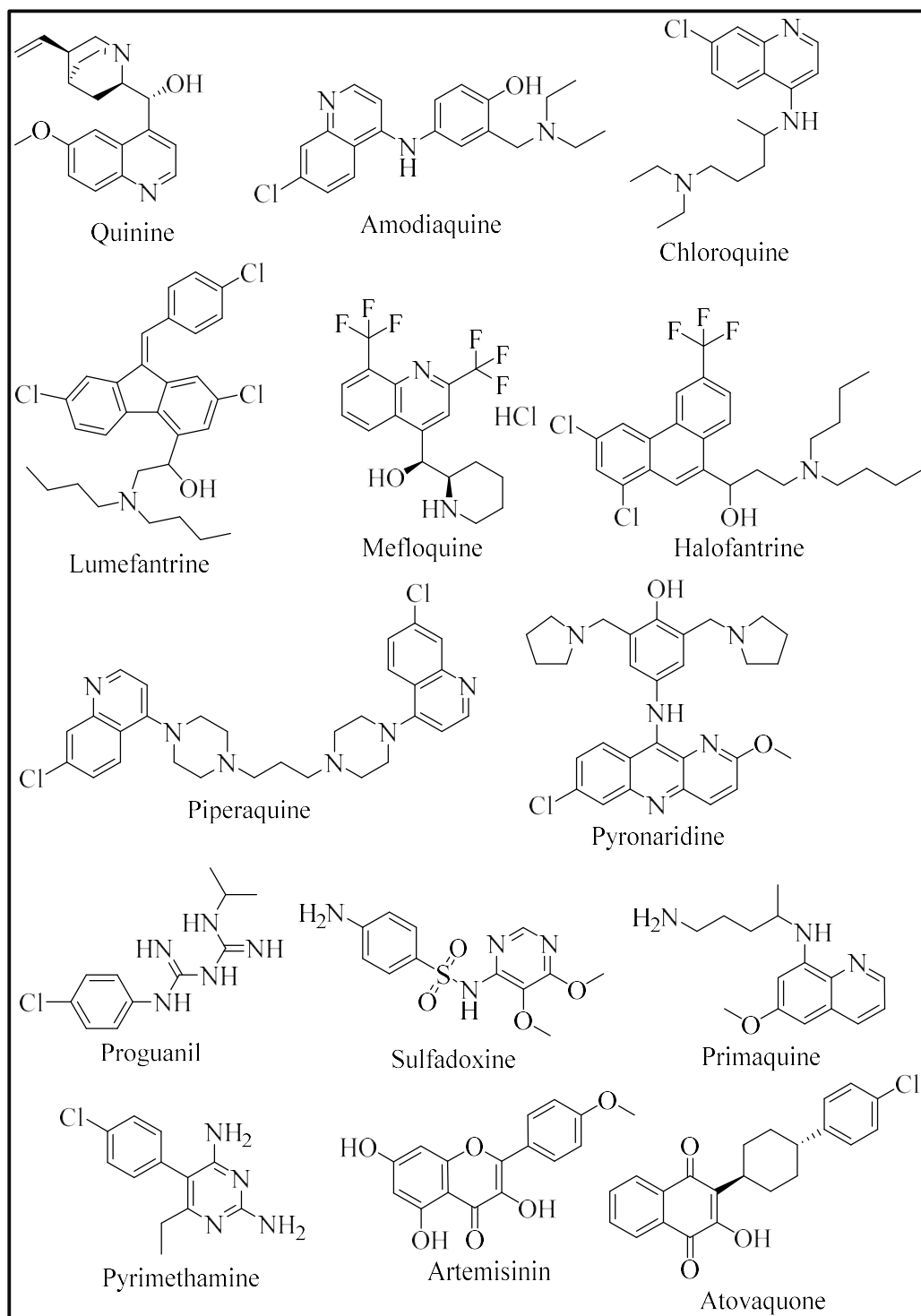


Fig. 1.4 Current antimalarial drugs used in the treatment¹³

Malaria prevention and control efforts have significantly progressed over the years to combat these infectious diseases. The battle is worldwide, with several countries in Asia, Latin America, and the Middle East having made progress toward malaria

elimination, with some achieving or approaching malaria-free status. Many countries are working towards malaria elimination, intending to achieve zero malaria transmission in defined geographic areas. As of 2021, 40 countries and territories have been declared malaria-free by the WHO, and several others are progressing toward elimination. Between 2000 and 2020, the global malaria incidence rate decreased by 36%, and the mortality rate declined by 60%. Many global malaria eradication strategies have been planned to eradicate the disease. In collaboration with partner organizations, the WHO has set global targets for malaria control and elimination. The "Global Technical Strategy for Malaria 2016-2030" aims to reduce malaria cases and deaths by at least 90% by 2030 and eliminate malaria in at least 35 countries by 2030. However, sustaining elimination efforts and preventing reoccurrences of the disease remains a challenge. There are ongoing efforts to develop new tools and strategies to combat malaria, including the development of new drugs, vaccines, and insecticides. Research into new tools, such as gene editing techniques to create genetically modified mosquitoes resistant to the *Plasmodium* parasite, shows promise but raises ethical concerns. Despite these efforts, malaria remains a significant public health challenge, and efforts to prevent, diagnose, and treat malaria remain a global priority.

1.1.3 Tuberculosis (TB)

TB is a contagious disease that spreads by inhaling the infectious mucus and saliva droplets expelled by active TB patients and primarily affects the respiratory. *Mycobacterium* resides in the lungs and acts on macrophages. In active TB patients, the infection can spread to the lungs and other organs of the body. In passive TB patients, the healthy immune system fights the pathogen, encapsulating it inside the macrophage's endocytic vacuole, leading to latent TB. In immunocompromised conditions, latent TB becomes active TB. The causative agent for TB is *Mycobacterium tuberculosis* which is transmitted via the respiratory route. *Mtb* is gram-positive bacteria with high G+C genomic content (60-71%) and acid-fast due to mycolic acid, a unique structural component of the cell wall. *Mtb* is divided into three categories, *Mtb* complex is the causative agent for TB, *M. leprae* is the causative agent for Leprosy and non-tuberculous bacteria. The *Mtb* complex comprises *M. tuberculosis*, *M. bovis*, *M. africanum*, *M. microti*, *M. canetti*, and *M. pinnipedii*.

TB is one of the most frequent infectious diseases, as seen in Fig 1.5, other than Malaria and HIV/AIDS, spreading worldwide. Globally, 10 million people are diagnosed with

active TB cases yearly, with ~10% deaths. According to WHO, an estimated 10.6 million people suffered from TB infection, and 1.6 million people died in 2021. Among these, 46% of cases were reported from the Southeast Asian region, and India accounted for ~26% of the global TB burden, as shown in Fig 1.6. The treatment of TB has been impacted dramatically due to resistance developed in almost all the antibiotics used to treat TB. TB is the second most deadly infection, and conditions like MDR-TB, XDR-TB, TDR-TB, and comorbidity with HIV have worsened the scenario. WHO aims to end TB endemic by 2030 by reducing TB cases and death count. The targets for 2030 are a 90% reduction in the number of TB deaths and an 80% reduction in the TB incidence rate (new cases per 100 000 population per year) compared with levels in 2015.^{14,15}

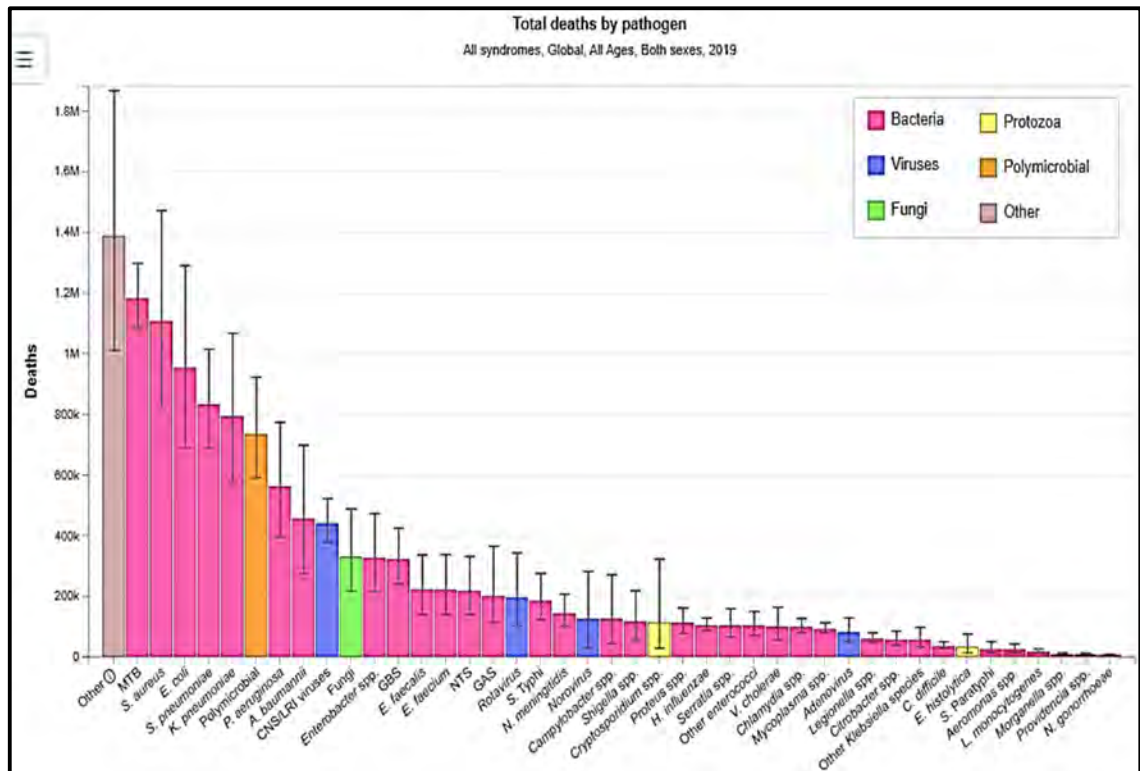


Fig 1.5. The total number of deaths occurred due to various pathogens. *Mtb* is responsible for the highest number of deaths among all the pathogens.

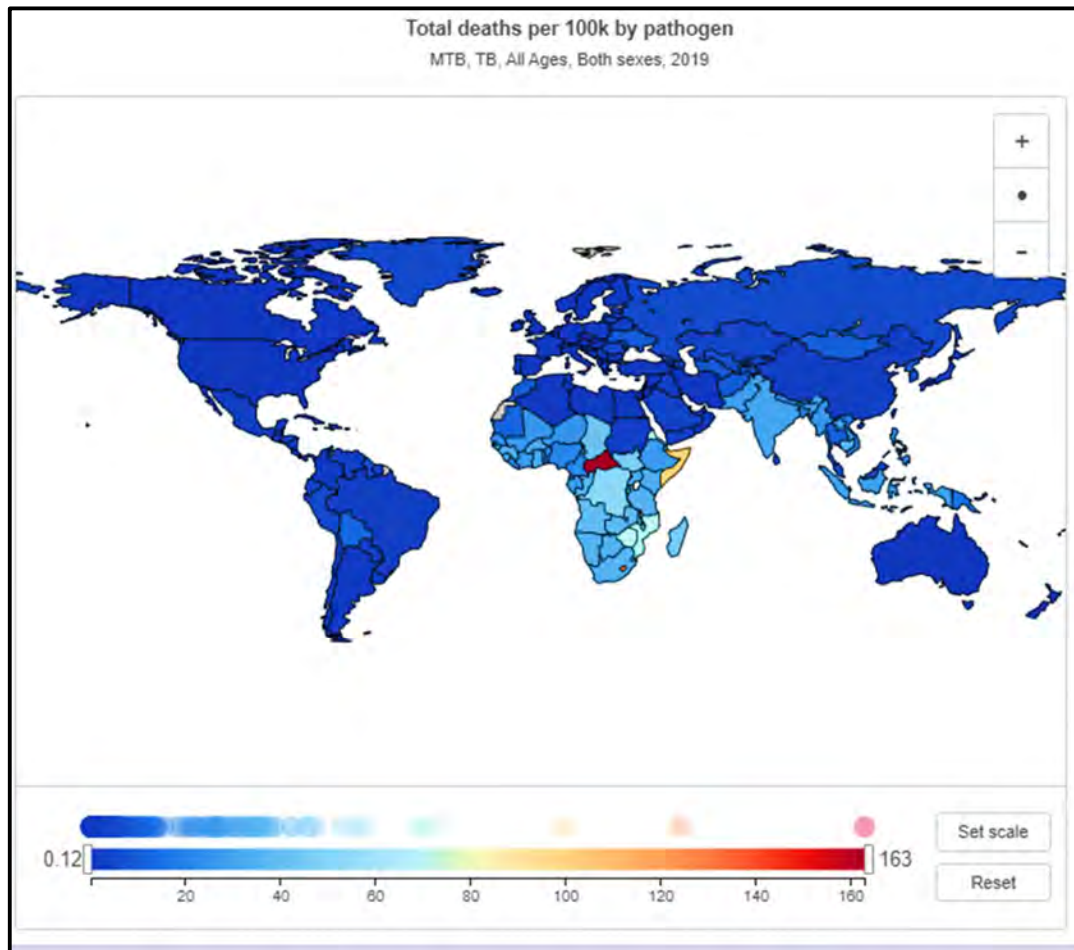


Fig. 1.6 Total deaths per 100k attributed by *Mtb* globally

The current treatment regimen of TB includes isoniazid, rifampicin, ethambutol, and pyrazinamide, and first-line antibiotics and second-line antibiotics available are cycloserine, ethionamide, para-aminosalicylic acid, injectables such as streptomycin, amikacin/kanamycin, capreomycin, and fluoroquinolones.¹⁶ These are old drug regimen for the treatment and has several shortcomings, such as serious adverse effects, very long treatment period, patient non-compliance, and ineffective in resistant strains. In MDR and XDR TB, these antibiotics become useless. These antibiotics are being overused and misused due to a lack of general awareness.

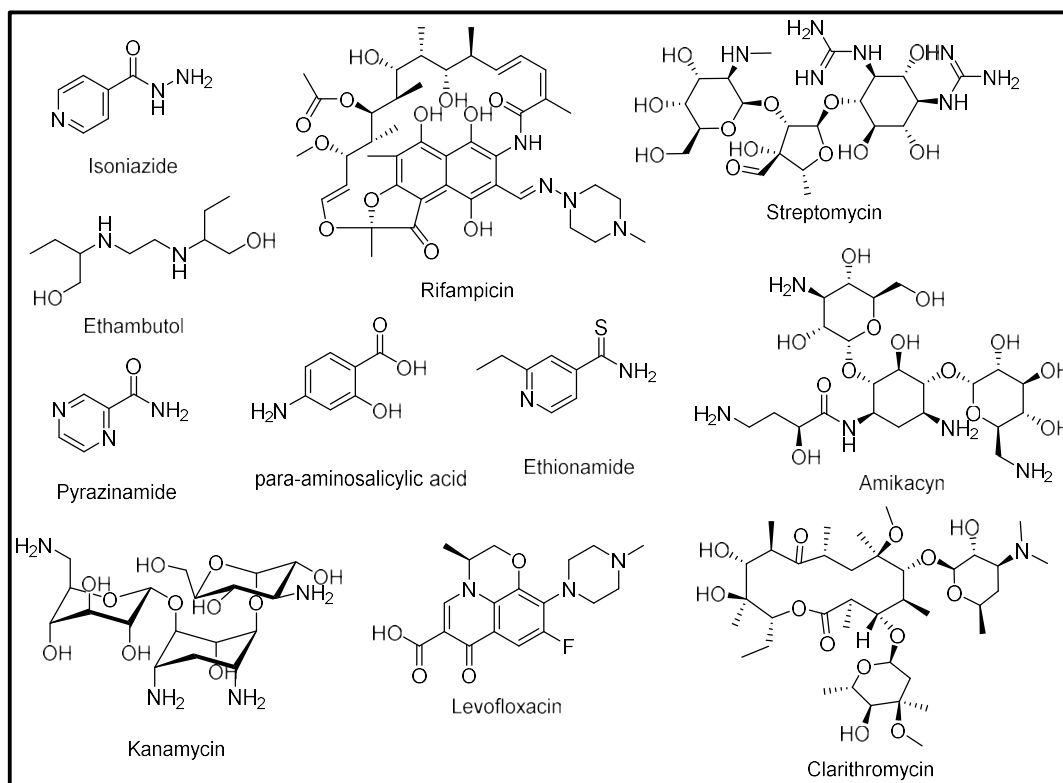


Fig. 1.7 Current first line and MDR anti-TB agents

Continuous advancements in drug discovery and development targeting *Mycobacterium* are ongoing, and still, very few molecules have the potential to become clinical candidates. Many recently discovered antibiotics belong to a previously known class or repurposed drugs. The discovery and development of new antibiotics against TB are challenging due to the unique structural architecture of the cell wall of *Mycobacterium*. Major failure to obtain a potent anti-tubercular agent is due to the lipid-rich waxy nature of the cell wall. Currently, ~50% of clinical candidates target cell wall biosynthesis.¹⁷ To overcome this greatest challenge to the healthcare sector, there is an urgent need to find newer antibiotics inhibiting different promising targets with minimal toxicity and promising therapeutic value.

1.2 DRUG DISCOVERY PROCESS

New drug discovery and development, from start to launch a final product, is a complex and time-consuming journey that takes 10-15 years and costs hundreds of millions to billions of dollars, as shown in Fig.1.8. It involves various stages, with several years, typically a decade or more. The timeline for drug discovery can vary widely depending on many factors, including the complexity of the disease, the availability of existing

research and knowledge, the success of each stage, and regulatory requirements. It can take more or less time than estimated, and the entire process is associated with high costs and risks.



Fig. 1.8 New drug discovery and development timeline

Drug discovery for infectious diseases usually proceeds through rational drug design using a target-based or phenotypic screening of compound libraries, as mentioned in Fig.1.9. The molecular target-based approach is called reverse pharmacology, as it initiates by first identifying the promising target proteins used to screen small molecules.¹⁸ It is frequently preferred when biochemical pathways and the principal cause of the condition are well-known and understood in advance. On the contrary, phenotypic screening is used when prior knowledge of targets and the mechanical approach is lacking or unclear. In this approach, leads are identified without knowing the molecular mechanism or targets.¹⁹ In the last three decades, target-based drug design is becoming popular and the leading drug discovery prototype employed by industry and academia for new drug development. During the beginning of the 20th century (1999-2008), phenotypic screening contributed incredibly to discovering first-in-class drug molecules and received massive success with the approval of 28 clinical candidates overtaking the target-based design, which delivered 17 drugs during this period.²⁰ However, the popularity of phenotypic screening declined over the past 20 years due to cost and a lot of effort to target identification and finding the mechanism of action. Also, it weakens the molecular properties for optimization of the molecule. Both strategies hold several advantages and shortcomings. Target-based methods facilitate the hit optimization easily and are compatible with small molecule design and biologically driven strategies.

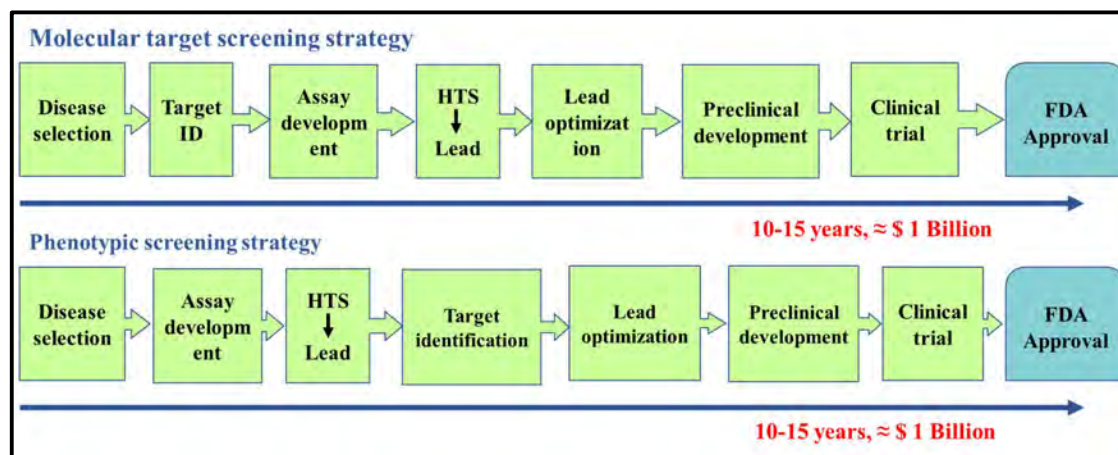


Fig. 1.9 Different stages involved in the phenotypic and molecular target screening

1.2.1 Structure-based drug design

Structure-based drug design (SBDD) refers to using the 3D structure of the therapeutic targets (usually receptors or enzymes) to identify their modulators. Thus, the knowledge of a binding site is exploited to design new ligands using computational or experimental approaches.²¹ *In silico* methods such as molecular docking and molecular dynamics (MD) can be used to estimate the protein-ligand complex binding strength and stability. These methods analyze the ligand-protein interactions and binding energetics and monitor the conformational changes in structures during the docking process.²²

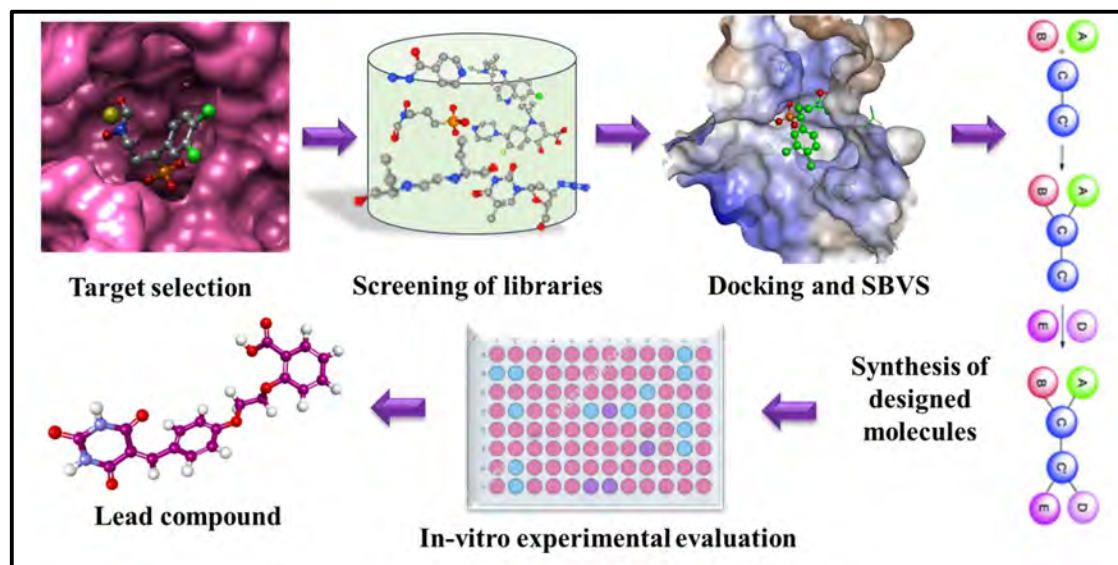


Fig. 1.10 A Flow diagram representing the process of Structure-based drug design

SBDD is an efficient, more specific, and rapid process for lead optimization.²³ The next step is synthesizing promising hit compounds obtained in the virtual screening, followed by *in-vitro* biochemical assays and evaluating biological properties, including affinity, potency, and efficacy, as shown in Fig 1.10.²⁴ These leads act by interfering with important cellular pathways, producing desired pharmacological and therapeutic effects.²⁵ Once the active compounds are identified, the 3D structure of the ligand-receptor complex is obtained and valuable to observe the various intermolecular features and interactions. The analysis of critical intermolecular interactions, binding conformations, identification and exploration of unknown binding sites, explication of ligand-induced conformational alterations, and mechanistic studies can be thoroughly studied with the 3D structure of the complex.²⁴ This complex is used further to correlate the structural analysis with biological activity data. If successful, the most potent candidate enters preclinical and clinical trials and is distributed for clinical uses post-approval. The new molecular modifications can be performed to design the molecules with an improved affinity for the active site based on SBDD-guided information.²⁶ Several FDA-approved drugs were developed using SBDD. The discovery of HIV-1 protease inhibitors, such as amprenavir, represents the success story of SBDD mentioned in Fig. 1.11.²⁷ Other drugs discovered by SBDD and MD and protein modeling,^{27,28} includes antibiotic norfloxacin,²⁹ and raltitrexed (thymidylate synthase inhibitor).³⁰

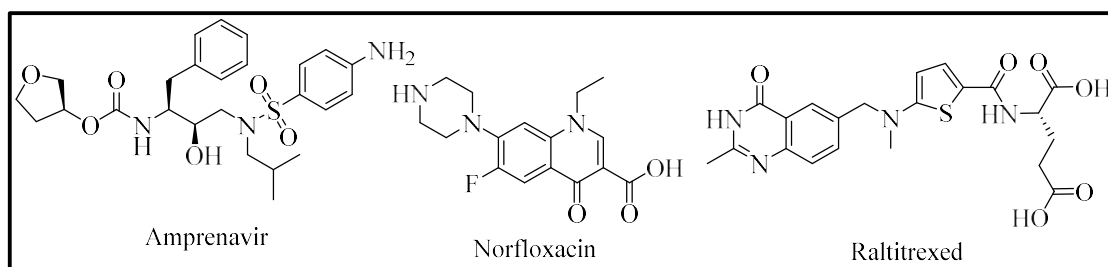


Fig. 1.11 Structures of the FDA-approved drugs discovered by SBDD

1.2.2 Fragment-based Drug Design:

Fragment-based drug design (FBDD) is an approach in drug discovery that involves screening the library of low molecular weight (MW) compounds, known as fragments, against the active site of the desired target. Thus, the fragment libraries are screened using high-throughput screening (HTS) biochemical or binding assays to identify ligands with high ligand efficiency (LE). The NMR-based binding assays are also frequently used for FBDD. Two or more fragments binding in different regions or sub-

pockets of the active site are then linked to generate more potent inhibitors. This rational drug design method is very efficient, rapid, and specific for lead discovery and optimization, yielding high-quality inhibitors.²³ Screening of fragments by SBDD provides detailed insights into the interaction of fragments with the 3D structure of the target protein at the molecular level, increasing the specificity of the fragment.²¹

Usually, smaller fragments are expected to enter and hit an active site and enable few primary interactions at the active site of the target protein while retaining their sufficient small size to limit the unfavorable steric clashes interactions. It shows a better probability of fitting into a cleft of the active site in the protein.³¹ Smaller fragments possess a free range of motion, allowing binding to occur in an energetically favorable mode giving constraint-free binding as functional groups in fragments are not constrained, unlike drug-like bigger drug-like compounds in HTS. It is easier to find a small molecule that complements a particular subsite within a binding site than a larger molecule that is complementary to the entire site. Thus, FBDD usually yields higher hit rates than the traditional approach of screening drug-like molecules. The key trade-off inherent in fragment screening is that, due to the small size of the compounds, even a fragment that is optimally complementary will interact with the target protein over a limited contact area. Thus, fragment hits are generally weak, with binding affinities of 1 mM.

FBDD possesses greater chemical diversity yet yields high hit rates even while employing small libraries with a fraction of size (100–1000 fragments) compared to those employed for conventional HTS campaigns (100000-1000000 compounds). The rational design of a relatively small library of fragments can cover a broader chemical space than an HTS library.³² FBDD seems an effective strategy to establish the binding potential of the target and to identify initial hits. The weaker binding affinity of hit fragments, despite the optimal complementary structure of the fragments, could be explained due to the limited contact area of small fragments over a target protein.³³

Generally, rule of Three (Ro3) is used as the selection criteria for fragments.³⁴ According to Ro3, the MW should be ≤ 300 Da; the number of hydrogen-bond acceptors (HBA) ≤ 3 ; the number of hydrogen-bond donors (HBD) ≤ 3 ; the calculated partition coefficient (clog P) ≤ 3 . Furthermore, polar surface area ≤ 60 and the number of rotatable bonds ≤ 3 can be considered. Typically fragments have low molecular

complexity and lower than 20 heavy atoms. A ZINC database report reveals that more than 70% of conventional fragments have a planar shape.³⁵

FBDD process typically involves four steps: designing and selecting fragments, screening fragments with the target protein, validation of hits, and development into more potent inhibitors.³⁶ Small molecule fragments or libraries can be selected by visual inspection based on the specific pharmacophoric requirement of the inhibitor development. These fragment libraries possess high chemical diversity. The shortlisted hit fragments can then undergo computational studies, such as molecular docking against the specific target, later in combination with *in-vitro* studies to validate and obtain the final best fragment hits. Although these selected fragments are called hits, they show weaker binding affinity towards the target and possess less inhibitory activity. Further chemical alterations and modifications are required to develop these fragment hits into larger, high-affinity ligands to obtain high-quality interactions at the binding site.³⁷⁻³⁹

Different strategies are used to convert fragment hits into lead-like potent inhibitors. These strategies include growing, linking, and/or merging the fragments using different linkers with varying lengths, as mentioned in Fig 1.12. One or a combination of strategies can be used for fragment development.

1.2.2.1 Fragment growing: This is the most popular strategy for growing fragment hits into potent compounds. This approach is used when a single fragment is known, and the conventional SAR strategy is adapted to grow the small fragment to occupy the active site of the target further. It is a more straightforward and easy method as only one starting point is utilized.³⁶ The binding site can be explored by chemically modifying the original binding fragment to capture more ligand-protein interactions, as shown in Fig. 1.12A. Molecular docking methods often aid this method. The elaborated fragments are rescreened to identify the potent ligands. This method has been successfully used to develop inhibitors of numerous targets with four approved drug candidates.⁴⁰ However, the synthetic tractability and binding mode of some fragments may limit the application of this approach

1.2.2.2 Fragment linking: Fragment linking is the most powerful approach in which two different fragments are linked to obtain a potential inhibitor. This approach is used when the binding pocket contains two or more sub-pockets within the target binding

site, as shown in Fig.1.12B. Detailed structural information is necessary as identifying two different fragments in close proximity is challenging, and a linker for connecting two fragments should not negatively affect molecular interactions. A synthetic linker can link the two fragments to yield a large molecule with multiple functional groups, enhancing the ligand interactions and binding affinity at the active site.⁴⁰

1.2.2.3 Scaffold hopping/fragment merging: This strategy is adopted when two different fragments occupy the same or overlapped space in a binding site. In this case, the generated potent compound is obtained by merging/combining potent functional groups to achieve the constructive effect from two fragments (or more), as shown in Fig. 1.12C. This method holds the advantage of replacing non-drug-like structural features in merged molecules to obtain more potent and patentable chemical space. It requires detailed structural information to retain essential structural features of the original fragment, unlike the fragment growing strategy.

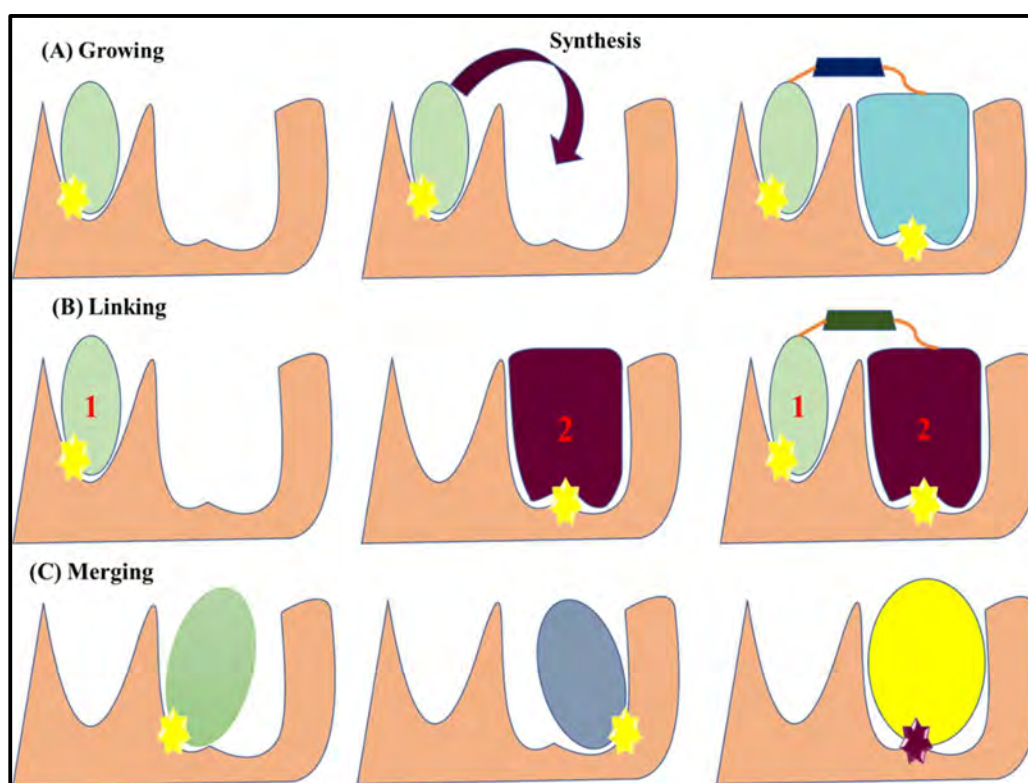


Fig. 1.12 Different approaches used for the fragment-based drug discovery

Recently, several therapeutics discovered by FBDD have gained FDA approval, thereby validating the FBDD approach for new drug discovery. Zelboraf (PLX4032), used to treat metastatic melanoma, was the first drug developed in 2011 using fragment

growing strategy shown in Fig 1.13. Initially, fragment **1** was identified to be active against kinase Pim-1. Further, the fragment growing strategy resulted in B-Raf kinase selective molecule PLX4720, optimized to PLX4032 with good selectivity towards B-raf.⁴¹

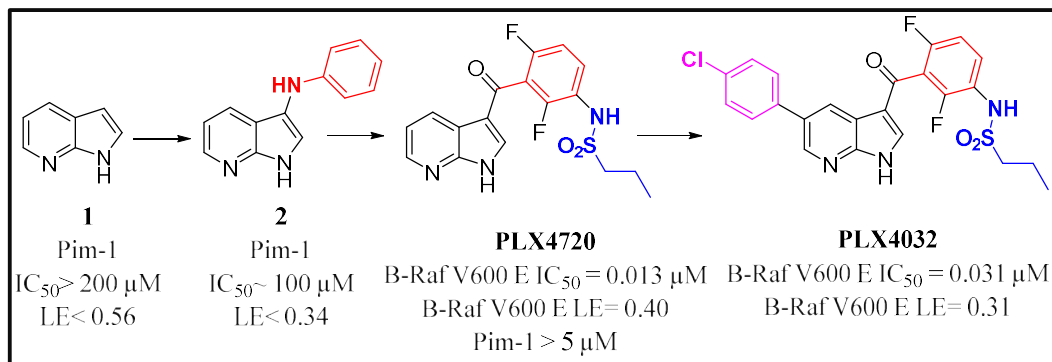


Fig. 1. 13 Zelboraf (PLX4032), from fragment to therapeutic drug

The work presented in this thesis represents the utilization of molecular target-based drug design principles. We identified and picked well-known enzyme targets, DXR and UNG, to design and develop potent inhibitors of these enzymes. These enzymes are essential for survival in many clinical pathogens. Many clinical pathogens utilize DXR for isoprenoid biosynthesis. UNG is responsible for the base excision repair mechanism in pathogens to maintain genetic integrity and survival of pathogens. The following chapters will describe the FBDD inhibitor design strategy against the two enzymes.

REFERENCES

- (1) *Global Antimicrobial Resistance and Use Surveillance System (GLASS) Report 2022 1*; 2022.
- (2) CDC. Antibiotic Resistance Threats in The United States 2019. *Cdc* **2019**, *10* (1). <https://doi.org/10.1186/s13756-020-00872-w>.
- (3) Collaborators, A. R. Global Burden of Bacterial Antimicrobial Resistance in 2019 : A Systematic Analysis. **2022**, *399*. [https://doi.org/10.1016/S01406736\(21\)02724-0](https://doi.org/10.1016/S01406736(21)02724-0).
- (4) Magiorakos, A. P.; Srinivasan, A.; Carey, R. B.; Carmeli, Y.; Falagas, M. E.; Giske, C. G.; Harbarth, S.; Hindler, J. F.; Kahlmeter, G.; Olsson-Liljequist, B.; Paterson, D. L.; Rice, L. B.; Stelling, J.; Struelens, M. J.; Vatopoulos, A.; Weber, J. T.; Monnet, D. L. Multidrug-Resistant, Extensively Drug-Resistant and Pandrug-Resistant Bacteria: An International Expert Proposal for Interim Standard Definitions for Acquired Resistance. *Clin. Microbiol. Infect.* **2012**, *18* (3), 268–281. <https://doi.org/10.1111/j.1469-0691.2011.03570.x>.
- (5) Oliveira, D. M. P. De; Forde, B. M.; Kidd, T. J.; Harris, P. N. A.; Beatson, S. A.; Paterson, D. L.; Walker, J. Antimicrobial Resistance in ESKAPE Pathogens. *Clin. Microbiol. Rev.* **2020**, *33* (3), 1–49.
DOI: <https://doi.org/10.1128/CMR.00181-19>
- (6) Bill, F.; Foundation, M. G.; Trust, W.; Care, S. Global Mortality Associated with 33 Bacterial Pathogens in 2019 : A Systematic Analysis for the Global Burden of Disease Study 2019. **2022**, *400*, 2221–2248. [https://doi.org/10.1016/S0140-6736\(22\)02185-7](https://doi.org/10.1016/S0140-6736(22)02185-7).
- (7) *antimicrobial-resistance-visualization-tool*.
<https://www.tropicalmedicine.ox.ac.uk/gram/research/antimicrobial-resistance-visualization-tool> (accessed 2023-03-22).
- (8) Boeckel, T. P. Van; Gandra, S.; Ashok, A.; Caudron, Q.; Grenfell, B. T.; Levin, S. A.; Laxminarayan, R. Global Antibiotic Consumption 2000 to 2010 : An Analysis of National Pharmaceutical Sales Data. *Lancet Infect. Dis.* **2014**, *3099* (14), 1–9. [https://doi.org/10.1016/S1473-3099\(14\)70780-7](https://doi.org/10.1016/S1473-3099(14)70780-7).
- (9) Dadgostar, P. Antimicrobial Resistance : Implications and Costs Antimicrobial Resistance : Implications and Costs. *Infect. Drug Resist.* **2019**, 3903–3910. <https://doi.org/10.2147/IDR.S234610>.

- (10) Patel, J.; Harant, A.; Fernandes, G.; Mwamelo, A. J.; Hein, W.; Dekker, D.; Sridhar, D. Measuring the Global Response to Antimicrobial Resistance, 2020–21: A Systematic Governance Analysis of 114 Countries. *Lancet Infect. Dis.* **2023**, *3099* (22). [https://doi.org/10.1016/S1473-3099\(22\)00796-4](https://doi.org/10.1016/S1473-3099(22)00796-4).
- (11) *FDA approved drugs*. <https://www.fda.gov/drugs/development-approval-process-drugs/new-drugs-fda-cders-new-molecular-entities-and-new-therapeutic-biological-products>.
- (12) *World Malaria Report 2022*; Geneva: World Health Organization; 2022. License: CC BY-NC-SA 3.0 IGO.
- (13) Hodoamede, P.; Duah-Quashie, N. O.; Quashie, N. Ben. Assessing the Roles of Molecular Markers of Antimalarial Drug Resistance and the Host Pharmacogenetics in Drug-Resistant Malaria. *J. Trop. Med.* **2022**, *2022*. <https://doi.org/10.1155/2022/3492696>.
- (14) *Global tuberculosis report 2022*. Geneva: World Health Organization; 2022. License: CC BY-NC-SA 3.0 IGO.
- (15) Los, U. M. D. E. C. D. E. *Global Tuberculosis Report 2022*; geneva, 2022.
- (16) Tiberi, S.; Scardigli, A.; Centis, R.; D'Ambrosio, L.; Muñoz-Torrico, M.; Salazar-Lezama, M. Á.; Spanevello, A.; Visca, D.; Zumla, A.; Migliori, G. B.; Caminero Luna, J. A. Classifying New Anti-Tuberculosis Drugs: Rationale and Future Perspectives. *Int. J. Infect. Dis.* **2017**, *56*, 181–184. <https://doi.org/10.1016/j.ijid.2016.10.026>.
- (17) Tetali, S. R.; Kunapaeddi, E.; Mailavaram, R. P.; Singh, V.; Borah, P.; Deb, P. K.; Venugopala, K. N.; Hourani, W.; Tekade, R. K. Current Advances in the Clinical Development of Anti-Tubercular Agents. *Tuberculosis* **2020**, *125*, 101989. <https://doi.org/10.1016/j.tube.2020.101989>.
- (18) Swinney, D. C.; Anthony, J. How Were New Medicines Discovered? *Nat. Rev. Drug Discov.* **2011**, *10* (7), 507–519. <https://doi.org/10.1038/nrd3480>.
- (19) Zheng, W.; Thorne, N.; McKew, J. C. Phenotypic Screens as a Renewed Approach for Drug Discovery. *Drug Discov. Today* **2013**, *18* (21–22), 1067–1073. <https://doi.org/10.1016/j.drudis.2013.07.001>.
- (20) Swinney, D. C. Phenotypic vs. Target-Based Drug Discovery for First-in-Class Medicines. *Clin. Pharmacol. Ther.* **2013**, *93* (4), 299–301. <https://doi.org/10.1038/clpt.2012.236>.

- (21) Lionta, E.; Spyrou, G.; Vassilatis, D.; Cournia, Z. Structure-Based Virtual Screening for Drug Discovery: Principles, Applications and Recent Advances. *Curr. Top. Med. Chem.* **2014**, *14* (16), 1923–1938. <https://doi.org/10.2174/1568026614666140929124445>.
- (22) Kalyaanamoorthy, S.; Chen, Y. P. P. Structure-Based Drug Design to Augment Hit Discovery. *Drug Discov. Today* **2011**, *16* (17–18), 831–839. <https://doi.org/10.1016/j.drudis.2011.07.006>.
- (23) Batool, M.; Ahmad, B.; Choi, S. A Structure-Based Drug Discovery Paradigm. *Int. J. Mol. Sci.* **2019**, *20* (11), 2783–2801. <https://doi.org/10.3390/ijms20112783>.
- (24) Fang, Y. Ligand-Receptor Interaction Platforms and Their Applications for Drug Discovery. *Expert Opin. Drug Discov.* **2012**, *7* (10), 969–988. <https://doi.org/10.1517/17460441.2012.715631>.
- (25) Urwyler, S. Allosteric Modulation of Family C G-Protein-Coupled Receptors: From Molecular Insights to Therapeutic Perspectives. *Pharmacol. Rev.* **2011**, *63* (1), 59–126. <https://doi.org/10.1124/pr.109.002501>.
- (26) Ferreira, L. G.; Santos, R. N. Dos; Oliva, G.; Andricopulo, A. D. Molecular Docking and Structure-Based Drug Design Strategies. *Molecules* **2015**, *20* (7), 13384–13421. <https://doi.org/10.3390/MOLECULES200713384>.
- (27) Wlodawer, A.; Vondrasek, J. Inhibitors of HIV-1 Protease: A Major Success of Structure-Assisted Drug Design. *Annu. Rev. Biophys. Biomol. Struct.* **1998**, *27*, 249–284. <https://doi.org/10.1146/annurev.biophys.27.1.249>.
- (28) Clark, D. E. What Has Computer-Aided Molecular Design Ever Done for Drug Discovery? *Expert Opin. Drug Discov.* **2006**, *1* (2), 103–110. <https://doi.org/10.1517/17460441.1.2.103>.
- (29) Rutenber, E. E.; Stroud, R. M. Binding of the Anti-cancer Drug ZD1694 to E. Coli Thymidylate Synthase: Assessing Specificity and Affinity. *Structure* **1996**, *4* (11), 1317–1324. [https://doi.org/10.1016/S0969-2126\(96\)00139-6](https://doi.org/10.1016/S0969-2126(96)00139-6).
- (30) Depeursinge, A.; Racoceanu, D.; Iavindrasana, J.; Cohen, G.; Platon, A.; Poletti, P.-A.; Muller, H. The Process of Structure-Based Drug Design. *Chem. Biol.* **2003**, *10*, 787–897. <https://doi.org/10.1016/j>.
- (31) Philine Kirsch, A. M. H.; Anna K. H. Hirsch and Martin Empting. Concepts and Core Principles of Fragment-Based Drug Design. *Molecules* **2019**, *24*, 4309.

<https://doi.org/10.1017/cbo9780511730412.002>.

- (32) Morrison, C. N.; Prosser, K. E.; Stokes, R. W.; Cordes, A.; Metzler-Nolte, N.; Cohen, S. M. Expanding Medicinal Chemistry into 3D Space: Metallofragments as 3D Scaffolds for Fragment-Based Drug Discovery. *Chem. Sci.* **2020**, *11* (5), 1216–1225. <https://doi.org/10.1039/c9sc05586j>.
- (33) Hall, D. R.; Kozakov, D.; Whitty, A.; Vajda, S. Lessons from Hot Spot Analysis for Fragment-Based Drug Discovery. *Trends Pharmacol. Sci.* **2015**, *36* (11), 724–736. <https://doi.org/10.1016/j.tips.2015.08.003>.
- (34) Bian, Y.; Xie, X. Q. (Sean). Computational Fragment-Based Drug Design: Current Trends, Strategies, and Applications. *AAPS Journal*. Springer New York LLC May 2018, p 59. <https://doi.org/10.1208/s12248-018-0216-7>.
- (35) Hung, A. W.; Ramek, A.; Wang, Y.; Kaya, T.; Wilson, J. A.; Clemons, P. A.; Young, D. W. Route to Three-Dimensional Fragments Using Diversity-Oriented Synthesis. *Proc. Natl. Acad. Sci. U. S. A.* **2011**, *108* (17), 6799–6804. <https://doi.org/10.1073/pnas.1015271108>.
- (36) Ciulli, A.; Abell, C. Fragment-Based Approaches to Enzyme Inhibition. *Curr. Opin. Biotechnol.* **2007**, *18* (6), 489–496. <https://doi.org/10.1016/j.copbio.2007.09.003>.
- (37) Daniel A. Erlanson, Robert S. McDowell, and T. O. Fragment-Based Drug Discovery. *J. Med. Chem.* **2004**, *67* (14), 3463–3482. <https://doi.org/10.1021/jm040031v>
- (38) Ress, D. C.; Congreve, M.; Murray, C. W.; Carr, R. Fragment-Based Lead Discovery. *Nat. Rev. Drug Discov.* **2004**, *3* (8), 660–672. <https://doi.org/10.1038/nrd1467>.
- (39) Lamoree, B.; Hubbard, R. E. Current Perspectives in Fragment-Based Lead Discovery (FBLD). *Essays Biochem.* **2017**, *61* (5), 453–464. <https://doi.org/10.1042/EBC20170028>.
- (40) Li, Q. Application of Fragment-Based Drug Discovery to Versatile Targets. *Front. Mol. Biosci.* **2020**, *7*, 1–13. <https://doi.org/10.3389/fmolb.2020.00180>.
- (41) Velvadapu, V.; Farmer, B. T.; Reitz, A. B. Fragment-Based Drug Discovery. *Pract. Med. Chem. Fourth Ed.* **2015**, 161–180. <https://doi.org/10.1016/B978-0-12-417205-0.00007-9>.

CHAPTER 2

Design and Synthesis of Non-hydroxamate Lipophilic 1-Deoxy-D-Xylulose 5-Phosphate Reductoisomerase (DXR/*IspC*) Inhibitors

2.1 INTRODUCTION AND BACKGROUND

2.1.1 Isoprenoids

Isoprenoids represent the largest class of natural products with more than 55000 molecules that provide essential nutrients for all living organisms. They deliver magnificent diversity in bio-molecules that play a significant role in the framework of cellular components such as cell membranes and cell walls. Isoprenoids help in carrying out vital functions in all living organisms.¹ These are essential components of various ubiquitous cellular mechanisms, such as transcription, protein degradation, apoptosis, and post-translational alterations. They serve as carriers for electron transport ubiquinone and menaquinone, intracellular signaling (prenylation of proteins), photosynthesis (carotenoids, side chain of chlorophyll), protein degradation, growth regulators and hormones (steroid and reproductive hormones, cytokinins, bile acids), secreted defense mechanisms, and mating pheromones. They have been reported as effective herbicides or herbivore repellents.² These are an integral part of all kingdoms of life, producing an enormous subset of secondary metabolites produced by microorganisms, plants, and fungi.³ Despite having colossal diversity in structures, all isoprenoids are made up of repetitive five-carbon isoprene units, which are known as building blocks of isoprenoid molecules and derivatives of isopentenyl pyrophosphate (IPP) and dimethylallyl pyrophosphate (DMAPP). The basic isoprene units are linked by regular (head-to-tail) or irregular (head-to-head) condensation reactions following the isoprene rule. Modification by introducing several functional groups such as alcohols, aldehydes, ketones, ethers, peroxides, carboxylic esters, and peroxides via a vast range of unique combinations of rearrangement yields various natural products. These arrangements include elongation, oxidation, and cyclization reactions, providing vast diversity in linear to cyclic and specific chirality to these bioorganic natural products.⁴ Physical properties of Isoprenoids, like low molecular weights and high vapor pressures, furnish them to act as important messenger molecules in the cellular environment and function as hormones in many higher eukaryotes. They also act as growth regulators such as steroids, hormones, cytokinins,⁵ and effective herbicides or herbivore repellents.^{3,6} Thus, elucidations of biosynthetic pathways which produce isoprenoids have been a fascinating and popular area of active research.

The mevalonic acid (MVA) pathway was thought to operate in all organisms, including mammals, for the biosynthesis of isoprenoids, as mentioned in Fig. 2.2. This pathway

utilizes two molecules of acetyl-CoA as its starting point, followed by the synthesis of different important intermediates, including (S)-3-hydroxy-3-methylglutaryl-CoA (HMG-CoA) and (3R)-3,5-dihydroxy-3-methylpentanoic acid (MVA). MVA is a key intermediate of this pathway; thus, it is named after the MVA intermediate, which is further utilized to synthesize IPP and DMAPP.

However, after 1990 a distinct route for the synthesis of isoprenoids, operating via completely different starting materials, was found to function in several bacteria, algae, plants, and apicomplexan protozoans. This other pathway is named the non-mevalonate pathway and later became popular as the 2-C-methyl-D erythritol 4-phosphate (MEP) pathway due to MEP being the first committed precursor in this pathway.^{4,7} The pathway begins with the utilization of pyruvate and D-glyceraldehyde 3-phosphate as a starting material, unlike the mevalonate pathway, which begins with the Claisen condensation of two acetyl-CoA molecules.^{8,9} The timeline representing advanced isoprenoid biosynthesis has been elucidated in Fig. 2.1.

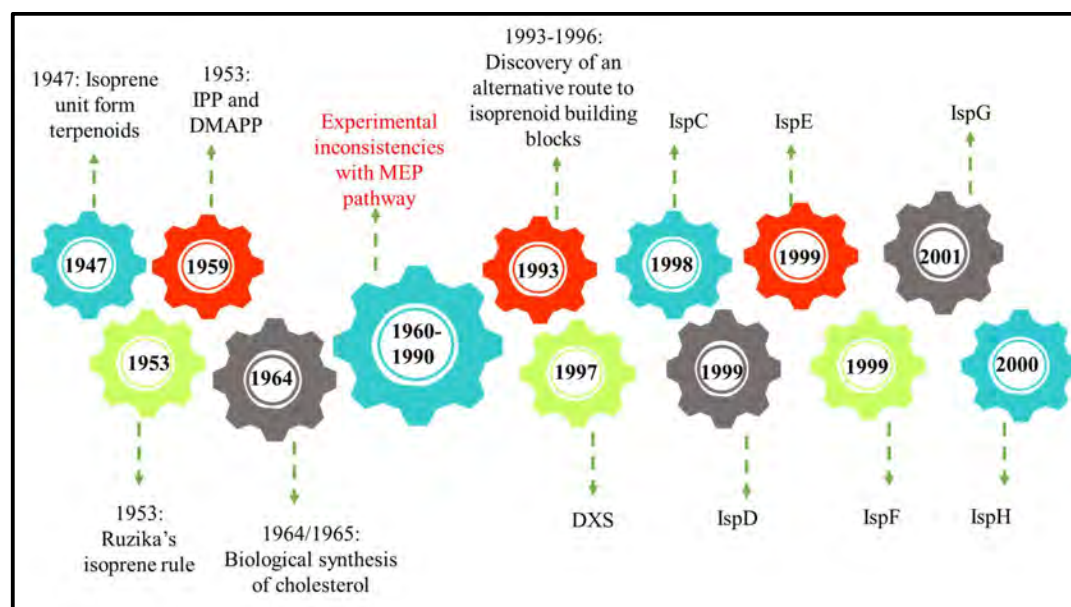


Fig. 2.1 A timeline representing research advances in Isoprenoid biosynthesis⁴

2.1.1.1 MEP PATHWAY

The MEP pathway consists of seven enzymatic steps leading to the synthesis of IPP and DMAPP, the building blocks of isoprenoids.^{4,10} This pathway begins with D-glyceraldehyde-3-phosphate (D-GAP) and three-carbon pyruvate (Pyr) to produce a condensation product, 1-deoxy-D-xylulose-5-phosphate (DXP) utilizing Thiamine diphosphate (ThDP)-dependent, 1-deoxy-D-xylulose-5-phosphate synthase (DXS).

This first step of biosynthesis is catalyzed by DXS releasing carbon dioxide. In the next step, an intramolecular rearrangement of DXP occurs to an aldehyde intermediate which is then reduced to yield MEP. This step is catalyzed by IspC/DXR enzyme utilizing nicotinamide adenine dinucleotide phosphate (reduced) (NADPH) and a divalent metal ion (Mg^{2+} , Mn^{2+}) for conversion of DXP to MEP, which is the most promising step of the MEP pathway.^{11,12} The next step is a conversion of MEP into 4-diphosphocytidyl-2C-methyl-D-erythritol (CDP-ME), which is catalyzed using 4-diphosphocytidyl-2C-methyl-D-erythritol synthase (IspD). In the further step, ATP-dependent phosphorylation of CDP-ME occurs, utilizing 4-Di-phosphocytidyl-2C-methyl-D-erythritol kinase (IspE) to yield 4-diphosphocytidyl-2C-methyl-D-erythritol 2-phosphate (CDP-MEP). CDP-MEP converts into a cyclic product 2C-methyl-D-erythritol-2,4-cyclodiphosphate (MEcPP) in the fifth step. This step utilizes 2C-methyl-D-erythritol 2,4-cyclodiphosphate synthase (IspF), releasing cytidine monophosphate (CMP). The next step is a generation of 1-hydroxy-2-methyl-2- (E)-butenyl 4-diphosphate (HMBPP) by the reductive deoxygenation of MEcPP using 1-hydroxy-2-methyl-2(E)-butenyl-4-diphosphate synthase (IspG) enzyme for catalysis. In the last step of the biosynthetic pathway, HMBPP is converted into IPP and DMAPP, catalyzed by enzyme 1- hydroxy-2-methyl-2(E)-butenyl-4-diphosphate reductase (IspH) enzyme. All enzymes utilized by this pathway play a significant role in MEP biosynthesis.¹³ Fig. 2.2 represents the difference between two pathways.

2.1.1.2 MVA pathway vs. MEP pathway

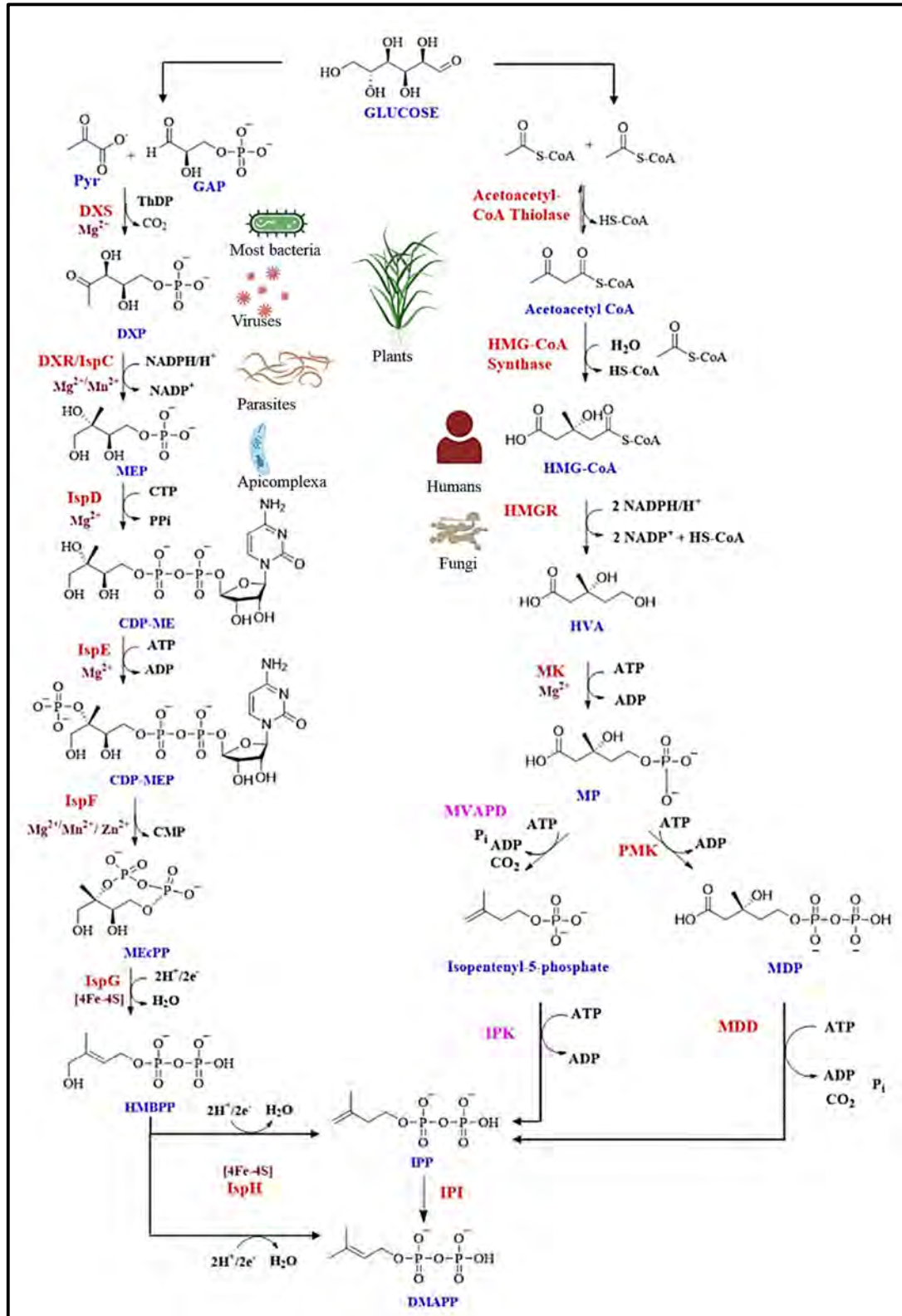


Fig. 2.2 Mechanistic difference between two pathways for isoprenoid biosynthesis¹⁴ (Created with BioRender.com)

2.1.2 1-Deoxy-D-xylulose 5-phosphate reductoisomerase (DXR/IspC):

Many clinical pathogens rely on the MEP pathway, including protozoan *Plasmodium falciparum*, *Escherichia coli*, *Vibrio cholera*, *Mycobacterium tuberculosis (Mtb)*, *Mycobacterium leprae*, *Helicobacter pylori*, and, *Bacillus anthracis*. Some deadly pathogens, such as *P. falciparum* and *Mtb*, are causative agents for Malaria and Tuberculosis, respectively. MEP pathway is essential for survival, and its inhibition leads to antimalarial and anti-tubercular actions. This essentiality for survival presents an excellent opportunity to target this pathway and combat various infectious diseases.^{10,13,15–20} Additionally, due to the nonexistence of the MEP pathway in mammalian cells, selective modulation of MEP enzymes of the pathogen might be possible. Thus, inhibitors of the MEP pathway are likely to be less toxic to the host cells. DXR has been widely studied as an antimicrobial drug target among various MEP enzymes, particularly against the malarial parasite *P. falciparum* and *Mtb*, which causes malaria tuberculosis in humans.^{16,21} These infections remain primarily neglected even though they affect millions of people, particularly in low and middle-income countries.²² In addition to the antimicrobial actions of DXR, the inhibitors are being explored as herbicides since the MEP pathway also exists in plants.²³

DXR is the second and most studied enzyme in the MEP pathway. It catalyzes the first committed and second rate-determining reaction step that converts DXP to MEP. This step is assisted by NADPH as a source of hydride donor and divalent metal cation (Mn^{2+} , Mg^{2+} , and Co^{2+}) for metal chelation, essential for catalytic activity. This single-step reaction proceeds by intra-molecular isomerization of DXP, followed by the reduction of an aldehyde intermediate. DXR reaction product is found to be unique in bacterial metabolism, thus providing an opportunity for selective blocking of the biosynthesis of isoprenoids.⁴ Since the MEP pathway in pathogens is heterologous to the non-mevalonate pathway in humans, it provides an opportunity for the development of antimicrobial agents, non-toxic to mammalian cells.

2.1.2.1 Discovery of DXR

Seto et al. first reported the gene encoding for DXR and expressed the protein by employing screening of ~20,000 *E. coli* mutants and DXR knockout studies. The finding suggested that the *IspC* gene is responsible for the DXR enzyme expression, which aids the conversion of DXP to MEP in a single step.²⁴ Homologs of the *IspC*

gene were observed in various bacteria and plants responsible for plastidic isoprenoids production.¹² The evidence of utilization of the MEP pathway in *M. tuberculosis* for isoprenoid biosynthesis was established by *Argyrou et al.* in 2004, and soon after, a similar finding was observed in *P. falciparum* by *Jomaa et al.* in 1999.^{25,26} Various other clinical pathogens rely on the MEP pathway for isoprenoid biosynthesis.

2.1.2.2 Mechanism of Action for conversion of DXP into MEP

DXR is a validated enzyme target in the MEP pathway to transform DXP to MEP, assisted with the cofactor NADPH in the first dedicated step shown in Fig 2.3. Since NADPH is consumed in the process, it is a co-substrate. DXR enzyme catalyzes the isomerization of DXP to an intermediate, (2R,3R)-2,3-dihydroxy-3-methyl-4-oxobutyl phosphate, in the presence of a divalent metal cation, which is necessary for the transformation, followed by the reduction to MEP and NADP⁺.⁴ The sequential reaction mechanism allows adequate turnover and substrate binding. Before inducing catalysis, the NADPH co-factor binds to the N-terminal domain, and the metal cation binds to a polar pocket inside the active site. This binding induces conformational changes in the flexible loop and C-terminal domain, forming a protected catalytic pocket by covering the central loop. Later, substrate entry occurs to initiate the isomerization. To understand the mechanical aspects of DXR catalysis, two different mechanisms have been proposed for the initial isomerization of DXR. Both mechanisms utilize the divalent metal cation as a Lewis acid that activates the substrate DXP's carbonyl and coordinates it to the C-3 hydroxyl group. The first hypothesis depicts an α -ketol (sigmatropic) rearrangement, which occurs via migrating the C3-C4 bond of DXP by 1,2-alkyl shift, forming an aldehyde intermediate, as mentioned in Fig 2.3. A partial positive charge on C-2 is provided by the coordination of metal ions with the keto group to initiate the bond formation, where metal ions act as Lewis acids. Proton abstraction from the C-3 hydroxyl group produces carbonyl at C-3 and reduces C-2 carbonyl to tertiary alcohol, an isomerization intermediate of MEsP.^{27,28}

An alternative approach for this isomerization intermediate is the subsequent retroaldolization/aldolization mechanism.^{28,29} Here, the C-4 hydroxyl group from DXP undergoes deprotonation leading to the formation carbonyl group. This retro-aldol cleavage of the C-4 carbonyl group leads to the breaking of the C-3 and C-4 C-C bond resulting in the formation of two intermediates, one of which is hydroxylacetone enolate

and another is glycoaldehyde phosphate.^{30,31} An aldol condensation with C-2, which acts as a nucleophile, forms the same aldehyde intermediate MEP, obtained by concerted α -ketol rearrangement, which is reduced by NADPH to form MEP. The precise mechanism of isomerization is still not clear.³² The kinetic isotope effect studies with selectively deuterated DXP substrate revealed the different hybridization states, from sp^3 to sp^2 of C-3 and C-4 carbon atom back to sp^3 , which is incompatible with the α -ketol rearrangement.^{10,28,30} NMR studies intended to detect hydroxyacetone enolate intermediate were unsuccessful, while exogenously added glycoaldehyde phosphate or hydroxyacetone enolate failed to convert into MEP by the DXR. These data debate against the retroaldolization/aldolization mechanism.²⁷ However, few studies assume the more plausible mechanism is the sequential fragmentation-reassembly by retroaldolization/aldolization process. This is due to the strict hold of putative fragments in the active site; therefore, it is difficult to detect or be replaced by exogenous factors.^{31,33,34} Studies with deuterium-labeled DXP, NADPH, and DXR crystal structures complexed with substrate, cofactor, and inhibitors have provided detailed insights into subsequent reduction.^{35,36} The next reduction step of the DXR-catalyzed reaction, the conversion of an intermediate to MEP, is simple and straightforward.

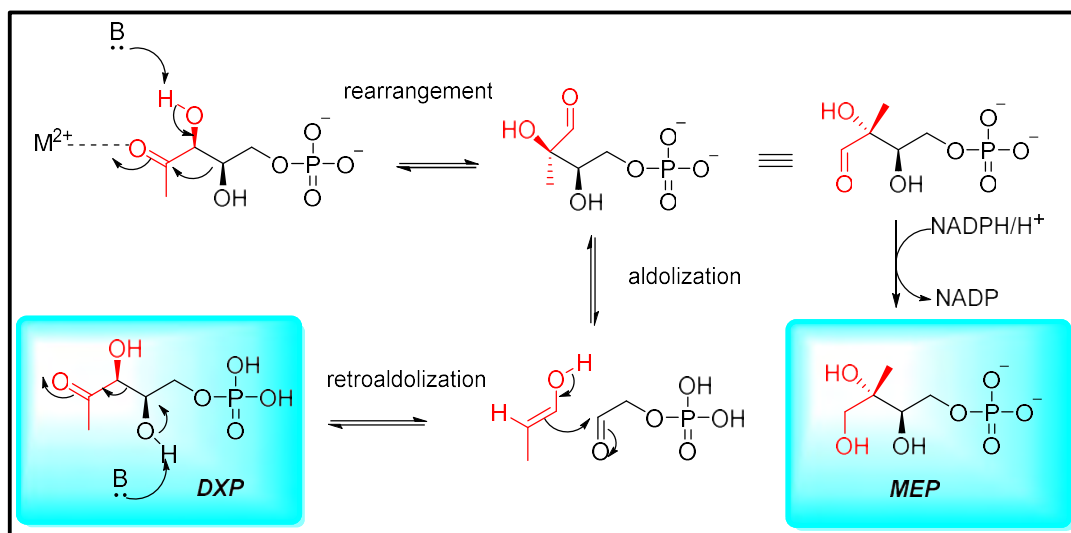


Fig. 2.3 Mechanism for conversion of DXP into MEP.

2.1.2.3 Structure of DXR:

The very first reported apo structure of the DXR was obtained from *E. coli* (*EcDXR*) in 2002.³⁷ Soon in 2006, *M. tuberculosis*-DXR (*MtDXR*) crystal structure was reported

by Henriksson *et al.*^{38,39} Later, more than 76 crystal structures of DXR from various organisms were reported in PDB to date, including several deadly pathogens like *P. Falciparum* (PDB codes 5JAZ and 4KP7),^{40,41} *M. tuberculosis* (PDB Codes 4OOE, 3ZHX),^{42,43} and *E. coli* (PDB code 3ANL and 1K5H)^{37,44} revealing the detailed structural architecture of the DXR protein and binding modes of DXP and NADPH in the presence of inhibitors and catalytic importance of the Mn²⁺. For instance, the crystal structure of *Mt*DXR in complex with NADPH is shown in Fig 2.4. DXR is a dynamic and highly flexible enzyme, the catalytic mechanism and overall protein structure of DXR remain the same, and the sequence is conserved across different species.^{31,35,36,39,45-48} Sequence alignment studies of DXR homologs from *E. coli*, *Mtb*, and *Zymomonas mobilis* revealed the highly conserved central catalytic domain with ~50% sequence identity of the enzymes. The residues interacting with substrate DXP were found to be conserved more strictly.³⁹ In 2007, the first quaternary complex of DXR with Mg²⁺, NADPH, and potent inhibitor fosmidomycin was published with PDB Code 2EGH.⁴⁸ Crystallographic studies revealed that all DXRs exist in a homodimer form, with each subunit of MW 39-47 kDa¹¹. Each monomeric subunit consists of three domains, the N-terminal domain, central domain, and C-terminal domain, connected between dimer interfaces by a varying number of salt bridges for each species. (Eight, four, and three for *M. tuberculosis*, *Z. mobilis*, and *E. coli* resp.).^{35,49} The larger N-terminal domain accounts for NADPH cofactor binding, and the central domain covers the residues involved in the lining of the active site. The C-terminal helical domain is involved in the structural and catalytic role.³⁶ A conserved flexible loop, part of a central domain, is lined with specific residues in different organisms. (207-215 from *E. Coli*, 198-206 from *Mtb*, and 291-299 in *Pf*). When N and C terminal domains move towards each other, the flexible loop closes by forming a deep cleft in the active site. This loop enables the substantial changes in the conformation upon binding of DXP or other strong binders like fosmidomycin, referred to as “open-loop” to “closed-loop” conformation change. This migrating loop functions as a lid that shelters the active site from being solvent-exposed and bulk solvent.^{26,47,50} Residues from flexible loops play an important role in substrate binding with the enzyme. Knock-out studies of the DXR enzyme have shown the essentiality of the *dxr* gene in many pathogens, including *E. coli*⁵¹ and *Mtb*.⁵² Thus, inhibiting the DXR enzyme will potentially lead to promising bactericidal agents.

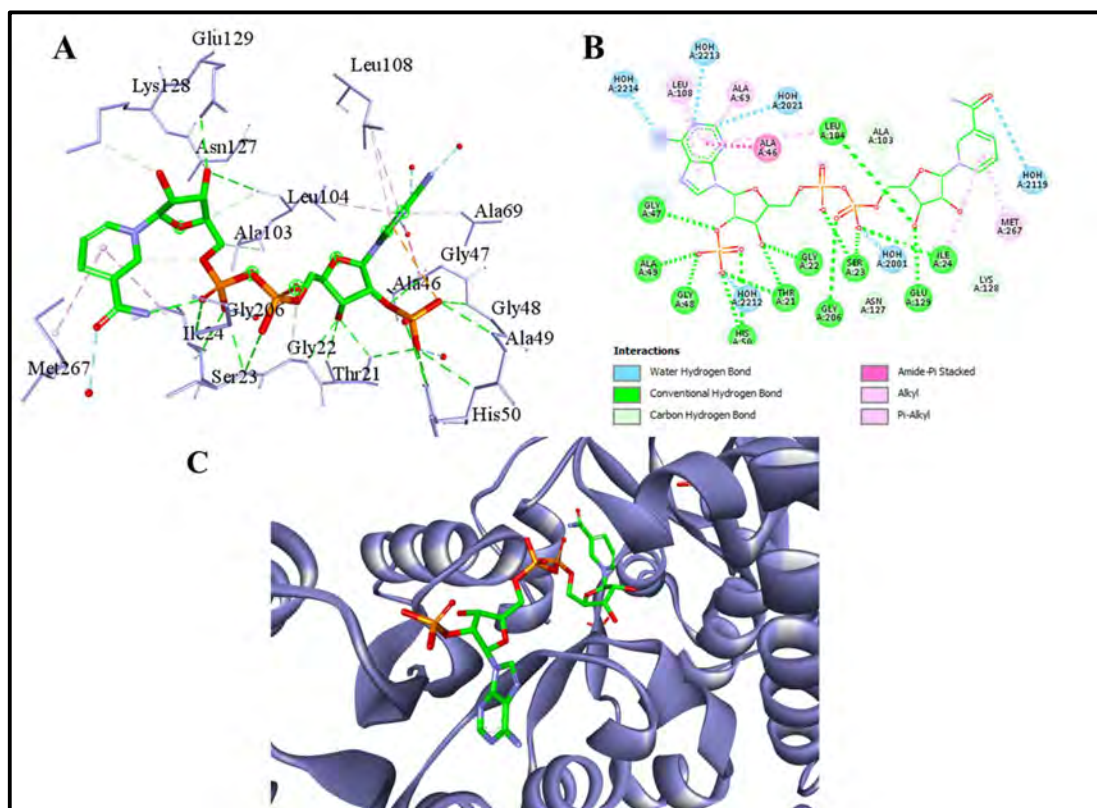


Fig. 2.4 Structure of *MtDXR* (PDB code: 2JD1) in complex with NADPH (A) Interactions of NADPH at the active site of *MtDXR*; (B) 2D view of interactions; (C) Bound NADPH with protein.

2.1.2.4 The structure of *PfDXR*

PfDXR complex with NADPH and Mn^{2+} in bound form reveals the presence of two asymmetric subunits forming homodimer molecular weight (MW) ≈ 47 kDa (each monomer consisting of 488 residues).⁵³ The monomer with two large domains is separated by a cleft forming a deep pocket, linker region, and C-terminal domain. The larger domain forming residues 77–230 was found responsible for the binding of NADPH, and the smaller domain with residues 231–369 forms a binding site for the divalent cation (Mg^{2+} or Mn^{2+}) and linker region site reserved for catalytic activity. The structure of *PfDXR* bound to NADPH and DXP is shown in Fig. 2.5.

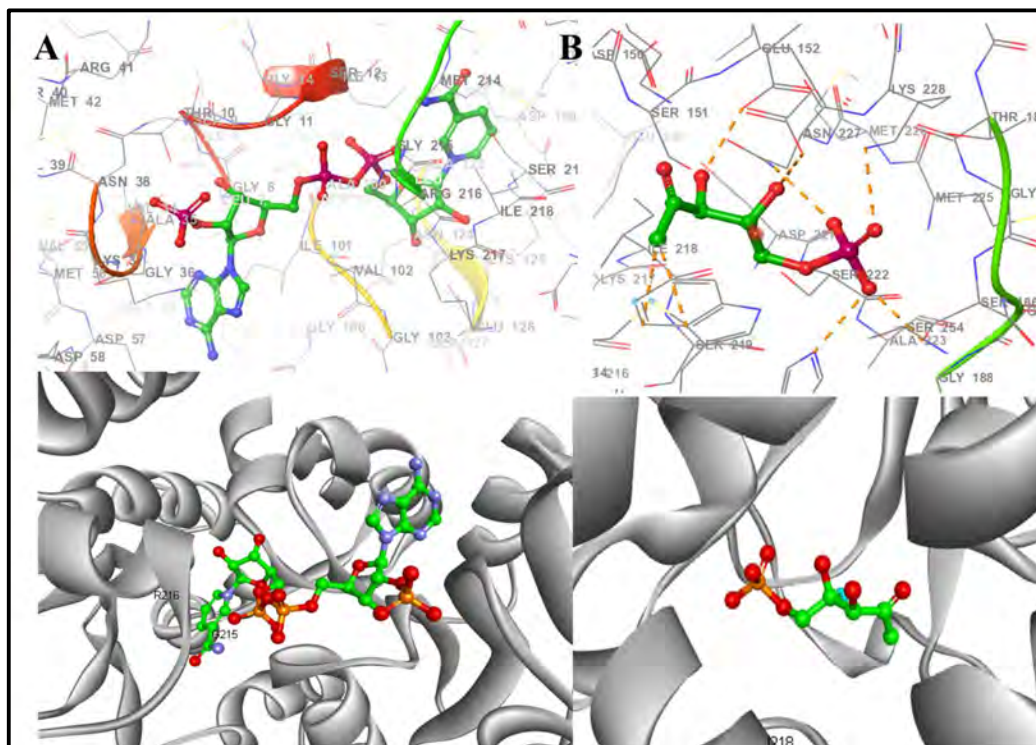


Fig. 2.5 Structure of *PfDXR* (PDB code 1Q0Q) with NADPH and DXP. (A) 2D and 3D structure of bound NADPH at the active site of *PfDXR*; (B) 2D and 3D structure of bound DXP substrate at the active site of *PfDXR*.

2.1.3 Fosmidomycin: A natural DXR Inhibitor

2.1.3.1 Discovery of fosmidomycin and its analogs

Fosmidomycin aka FR-31564 (FSM) or 3-(N-formyl-N-hydroxyamino)propylphosphonate and methyl analog of FSM, FR900098, as shown in Fig. 2.6, are the natural inhibitors of the DXR enzyme. FSM was isolated from actinobacterium *Streptomyces lavendulae*, whereas FR900098 was obtained from *Streptomyces rubellomurinus*.⁵⁴ Early research on FSM started in the 1970s by Fujisawa Pharmaceutical Co., and few analogs of FSM were reported. All the compounds were characterized by N-acylhydroxamino and phosphonic acid function.^{55–57} Medicinal chemistry efforts towards the design of DXR inhibitors started after these structurally related antibiotics successfully blocked the DXR function for their antibacterial action.

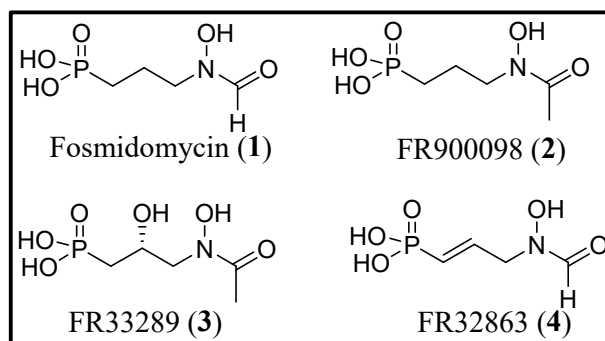


Fig. 2.6 Potent DXR inhibitors discovered in the early 1980s.

FSM and FR900098 have been reported with nanomolar activity against many clinical pathogens, gram-negative bacteria, and the protozoan parasite *P. falciparum*.^{58,59} Before the inhibitory action of FSM against DXR was evaluated, FSM was examined for the treatment of urinary tract infections (UTIs) in its early stages and then entered Phase I and II clinical trials in 1985.^{60,61} The non-existence of DXR enzyme in mammals and the significance of effective DXR inhibition by FSM has driven the research interest towards DXR enzyme inhibition as it seems a promising target. It became the most prevalent enzyme for inhibitor design in the MEP pathway. FSM shows potent inhibition of *EcDXR* with reported half maximal inhibitory concentration, $IC_{50} = 8.2$ nM, demonstrating the competitive binding with DXP (substrate) and non-competitive binding with NADPH cofactor.^{60,62} Since then, several analogs of FSM and FR900098 have been synthesized and evaluated, particularly against DXR enzymes of *E. Coli* (*EcDXR*), *M. tuberculosis* (*MtDXR*), and *P. falciparum* (*PfDXR*).^{54,63} FSM suppressed the growth of the multidrug-resistant *P. falciparum* parasite *in vitro* and successfully rescued infected mice *in vivo*.²⁶ In line with its potent *EcDXR* and *PfDXR* inhibition, FSM also inhibits the growth of *E. coli* and *P. falciparum* in whole-cell assays. Considering a high sequence identity of *MtDXR* to *EcDXR*, the FSM is expected to inhibit the *MtDXR* potentially, so it does, with an IC_{50} value of 80 nM. FSM displays potent inhibition of *PfDXR* as well with $IC_{50} = 36$ nM.^{50,64} FSM shows considerable efficacy against various clinical pathogens. *E. coli* shows $MIC_{90} = 0.78$ $\mu\text{g/mL}$ ⁵⁸ in *P. falciparum* $IC_{50} = 1$ μM ⁵⁰ and *Proteus mirabilis* with $MIC_{90} = 1.56$ $\mu\text{g/mL}$.⁵⁸ A high-resolution quaternary cocrystal structure was reported with the *MtDXR*, Mn^{2+} , and NADPH. (PDB code 2JCY).⁴⁵ Despite these promising efficacy and potent *MtDXR* inhibition, it is entirely inactive against whole cell *Mtb* activity,⁶⁵ probably due to the highly polar nature of FSM, which is unable to penetrate the highly

lipidic, waxy cell wall of *Mycobacteria*, which is responsible for the mycobacterial resistance to many antibiotics.⁶⁶ FSM is actively transported through glycerol-3-phosphate transporter (glpT).⁶⁷ Accordingly, organisms lacking glpT, such as Gram-positive bacteria, *M. tuberculosis*, and *Toxoplasma gondii*, are resistant to FSM due to its limited cellular permeation.^{66,68,69}

2.1.3.2 Binding mode of FSM and enzyme kinetics

Crystal structure of bound complexes of FSM/FR900098 with *Ec*DXR, *Mt*DXR⁷⁰, and *Pf*DXR reveals that FSM inhibits the conversion of DXP to MEP by mimicking the substrate DXP and its binding mode (Fig. 2.7). Inside the DXR active site, the FSM and its analogs enters in a crevice of the catalytic domain, where phosphonate group occupies the phosphate binding site. The phosphonate group interacts with multiple polar amino acid residues via hydrogen-bonds (H-bonds). The carbon backbone of FSM interacts with a hydrophobic patch, and hydroxamate (an anionic form of hydroxamic acid) acts as a metal-binding group (MBG) and chelates the divalent metal ion.^{36,45,71} Binding mode of the FSM analog in *Mt*DXR is described in Fig 2.7. Detailed structure-activity relationship (SAR) studies demonstrate the importance of both hydroxamate and phosphonate fragments and the length (3-carbon) of the linker chain that connects these moieties.

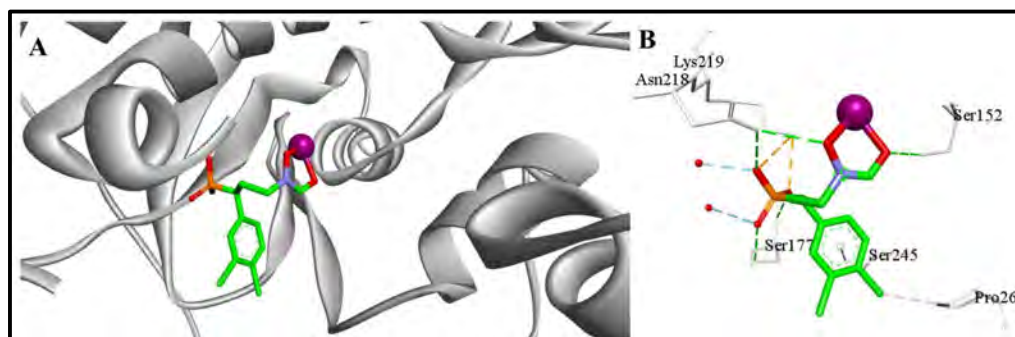


Fig. 2.7 3D structure of the FSM-bound quaternary complex of *Mt*DXR. (PDB Code: 2Y1D)

Various species show different extents of kinetics for DXR inhibition. Initially, FSM was described as a mixed inhibitor of *Ec*DXR,¹² and a competitive inhibitor of *Z. mobilis*.⁷⁴ Later, a thorough analysis of inhibition at the pre-steady-state phase revealed that FSM is a tight-binding, slow-onset inhibitor that follows a two-step binding.^{12,72} In the first phase, FSM competitively binds to DXR by inducing conformational changes characterized by inhibition constant K_i . For the tight binding, this conformational

change is necessary with the formation of the DXR-NADPH complex in advance. This DXR-inhibitor tight complex aligned with the non-competitive inhibition gives constant K_i' , where $K_i' < K_i$. Slow-onset can be avoided by pre-incubating enzyme with FSM and NADPH, and later substrate DXP is added. This slow-binding nature of FSM causes variations in the measured inhibition constant in the same enzyme/inhibitor complex with other contributory factors, including substrate, enzyme concentration, and inhibitor complex.⁷³ Despite sufficiently available crystal structures for DXR from different organisms, the prediction of the binding mechanism of the inhibitors is a big challenge. The dynamic nature and tragic conformational changes upon ligand binding and slow binding nature of DXR enzyme makes the rational design of inhibitors very challenging.

2.2 LITERATURE

2.2.1 Modifications around hydroxamate MBG

DXR has been validated clinically as a drug target. The success of FSM in combination with piperazine in clinical trials for the treatment of malaria has raised hope. It seems a promising strategy to block the MEP pathway for the treatment of deadly infectious diseases. Although FSM is a clinically safe antimalarial molecule, it suffers from a poor pharmacokinetic profile. It shows moderate bioavailability (with ~30% oral absorption), a short half-life, thus a speedy clearance rate (~1.5 hours), and malarial recrudescence, thus limiting its applicability as a therapeutic candidate. Many research groups have already reported nearly 76 crystal structures of DXR enzyme from different sources.^{37,38,74,75,35,63,64} The active site of DXR protein shows the induced flexibility by some molecules with amino acid residues, e.g., the indole ring of Tryptophan residue,⁷⁸ which poses a challenge in the design of molecules. Also, a conformational change is another challenge to inhibitor design.

Several efforts were made around FSM and FR900098 to improve the pharmacokinetic profile and develop more inhibitors. SAR studies were performed to understand the importance of the structural features of FSM required for the effective binding of the inhibitor (Fig. 2.8). Both hydroxamate and phosphonate groups with the length of the spacer (3-carbon) bridging them is required for effective binding. Altering any of these features leads to poor or no inhibition. Compound **5**, without any MBG, and compound **6**, with carboxylic acid instead of phosphonic acid, are reported to have low IC₅₀ values.^{79,80} Alteration in the chain length of molecule **7** and **8** also lead to poor enzyme inhibition.⁸¹ Thus, all structural features of FSM are required for enzyme inhibition.

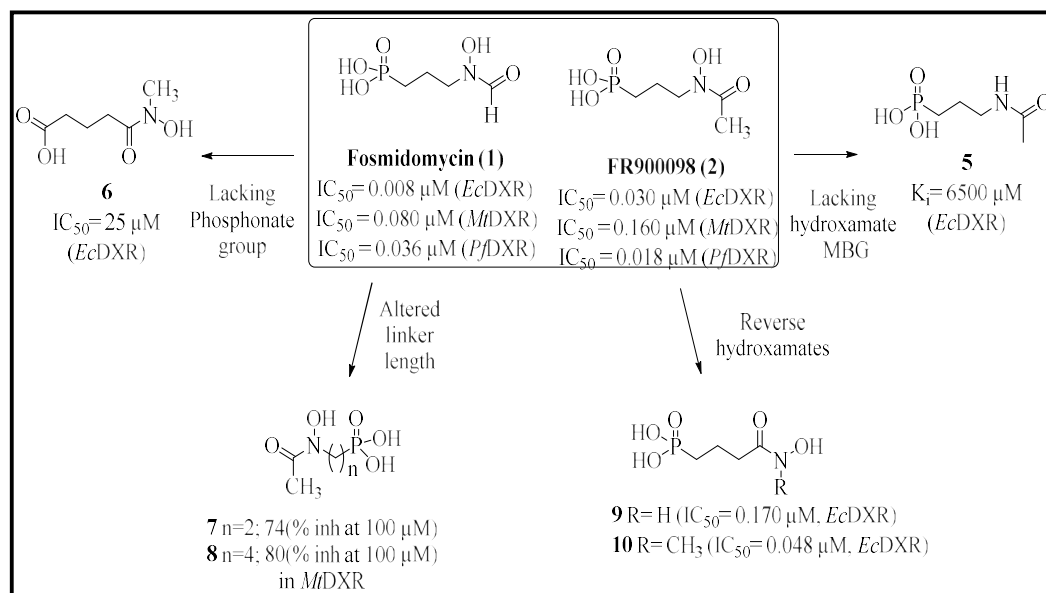


Fig. 2.8 Essential structural features of FSM, a natural DXR inhibitor

2.2.2 Reversal of Hydroxamate

The retrohydroxamate functionality of FSM coordinates the divalent cation in a similar fashion to β -hydroxyketone functionality from DXP. The studies with compounds **9** and **10** reveal that the swapping between the reverse hydroxamate and hydroxamate MBG is well tolerated with significant DXR inhibition.⁸² The N-methylated analog **10** demonstrated more potent *EcDXR* inhibition than the N-H analog **9**, with slow binding.⁷² Owing to the essential polar structural features of **1** (phosphonic acid and hydroxamate MBG),^{83–85} inhibitor design against DXR possesses severe challenges. Natural inhibitor **1** suffers from poor bioavailability and a short half-life attributed to its highly polar nature. Despite this, **1** is certified as a remarkably well-tolerated and safe candidate in human clinical trials.^{86–89} Overall, enzyme inhibition studies with **1–10** suggest that the relative position of carbonyl and N-hydroxy oxygen atoms does not significantly affect the potency as long as the phosphonate group is present.

The highly polar nature of FSM has been addressed by many research groups employing different structural modifications around the FSM. Due to the essentiality of polar structural features (hydroxamate and phosphonic acid), DXR inhibitors are extremely hydrophilic and lack ‘druglikeness.’^{84,85,90,91} FSM and its derivatives suffer from a short half-life and low bioavailability, severely hindering their clinical development. However, FSM is extremely safe and well-tolerated in clinical trials supporting the favorable safety profile of DXR inhibitors.^{86–88} Prodrug approaches have

been used to address the extreme hydrophilic nature of **1**, where ionizable phosphonic acid is masked with the bulky ester groups. Such prodrug molecules display higher lipophilicity and improved whole-cell activity due to the enhanced passive diffusion across the cell membrane.^{21,68,92–97} The second approach involves the substitution of linker carbons with hydrophobic substituents, often guided by SAR studies and a structure-based approach.^{40,43,75,98} Other strategies, guided by the SAR studies and structure-based approach,^{43,64,99,100} employed the substitution of linker carbons with hydrophobic groups/rings. Fig. 2.9 and Fig. 2.10 represents the different approaches used so far to improve the overall lipophilicity of the molecules to obtain the potential lead.

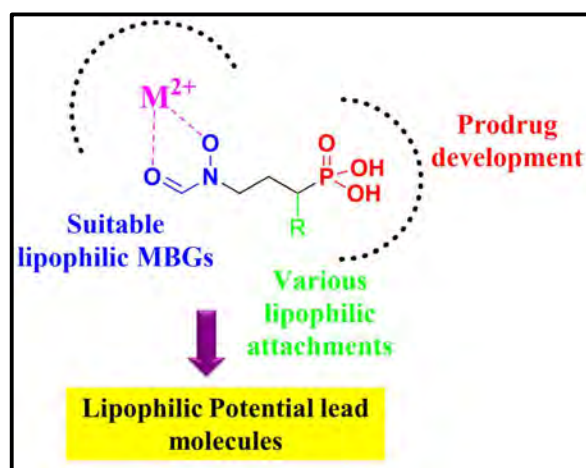


Fig. 2.9 Various modifications around FSM to develop a potent lipophilic inhibitor

Analogs **11**, **12** with aromatic substitution on alpha carbon to phosphonate exhibited better antimalarial activity ($IC_{50} = 0.028\text{--}0.09\ \mu\text{M}$) against *P. falciparum* (*in vitro* cultures) than FSM ($IC_{50} = 0.36\text{--}1.1\ \mu\text{M}$) (Fig. 2.10).¹⁰⁰ Sooriyaarachchi *et al.* synthesized a few β -Arylpropyl analogs of FSM with *Pf*DXR inhibition in nanomolar ranges.⁷⁷ The group revealed that arylpropyl attachments induced the displacement of important tryptophan residue of the active site, which successfully made favorable interactions with the reverse hydroxamate of FSM and its acetyl analog. They also mentioned the impact of smaller groups versus larger groups compared to potency, as larger lipophilic substituents like naphthyl and biphenyl resulted in poor potency. Some studies reported that the linker carbons substituted with heteroatoms such as *O* and *S* at varying carbon positions (α , β , and γ). These heteroatom-substituted analogs **13–19** exhibited significant DXR inhibition compared to **1** (Fig. 2.10).^{41,101,102} Compound **19**,

a β -thia-isostere of analog **12**, has shown 100-fold enhanced activity against the enzyme inhibition assay (all three organisms). Slight variation in the basic structure reflects significant variation in the activity, which signifies the importance of SAR analysis.⁴¹ Literature studies particularly highlight the modification of the phosphonate group and variation of the n-propyl linker chain. Most potent DXR inhibitors show close similarity to **1** and **2** with the same MBG hydroxamate (or retro-hydroxamate). FSM has also demonstrated significant growth inhibition in the whole-cell assays of *E. coli* with $MIC_{90} = 0.78 \mu\text{g/mL}$ ⁵⁸ and in *Proteus mirabilis* $MIC_{90} = 1.56 \mu\text{g/mL}$.⁵⁸ Despite the promising enzyme inhibition, **1** has failed to show significant growth inhibition in *M. tuberculosis* or *Toxoplasma gondii*, probably due to the absence of glpT in these organisms. GlpT carriers are usually involved in the transport of highly polar molecules in gram-negative bacteria (*E. coli*), whereas gram-positive bacteria (*M. tuberculosis*) usually lack them.^{66,69,103}

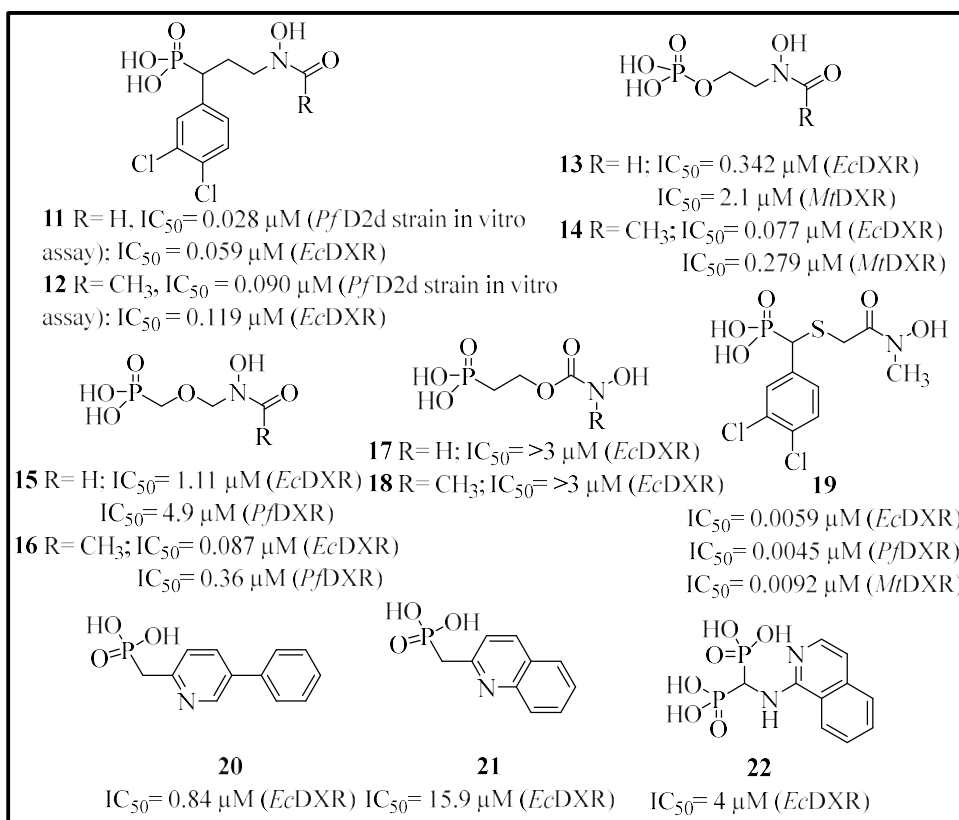


Fig 2.10 SAR analysis of hydroxamate-based DXR inhibitors

2.2.3 Attempts to design non-hydroxamate DXR inhibitors

Multiple studies across the world have attempted the design of non-hydroxamate DXR inhibitors. Song et al. designed pyridine/quinoline-based lipophilic phosphonate DXR

inhibitors **20**, **21** without any MBG (Fig. 2.10).⁴⁴ These electron-deficient rings showed the π - π stacking with the indole ring of Trp211(*E. coli* DXR). Compound **20** was reported with sub-micromolar activity due to its orientation, showing more π - π stacking with the indole ring of Trp211, with a 180° flip on the binding. The group also revealed two hydrophobic sub-pockets A and B, at the binding site. Pocket A is defined by Trp211, Met213, and Asn210, while pocket B is lined with the residue Trp211, Pro273, and Met275 as described in Fig. 2.11. The electron-deficient pyridine/quinoline ring of **20/21** was able to occupy the hydrophobic cavity A with the interaction between the lipophilic group of inhibitors and the indole ring of Trp211. In contrast, sub-pocket B is reported to occupy by bisphosphonates inhibitors **20** (PDB: 1T1R). *Mt*DXR and *Pf*DXR also show a similar conformation adaptation to Trp211 with bulky ligands.^{47,99,104} These examples highlight the potential of SBDD for the design of hydrophobic DXR inhibitors. In summary, while modification of the phosphonate and the n propyl linker has been extensively studied, most potent DXR inhibitors are structurally similar to **1** and **2**, especially considering the common hydroxamate MBG in all these analogs.

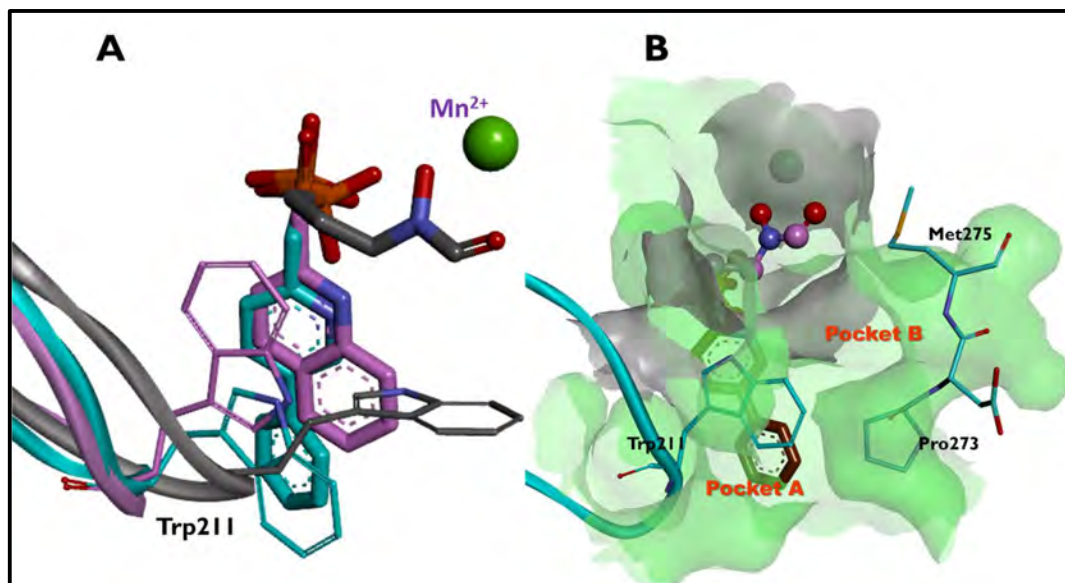


Fig. 2.11 (A) Binding mode comparison of hydrophobic inhibitors **20** (PDB 3ANM) and **21** (PDB 3ANN)¹⁰⁵ with FSM (**1**) (PDB 2EGH).⁴⁸ The indole ring of Trp211 (think sticks) moves considerably to accommodate bulky aromatic rings of **20** and **21**, exposing a lipophilic cavity. For clarity, only the Trp211-containing flexible loop of the respective DXR structures is displayed. The ligands **1**, **20**, and **21** and their respective flexible DXR loops are rendered in grey, cyan, and pink colors, respectively. (B) Solvent-accessible surface view of the active sites of 1-DXR (grey-colored) and 20-DXR (green-colored) complexes. The FSM (**1**) is displayed in pink ball-and-sticks, while **20** is shown as brown sticks. The hydrophobic sub-pocket A is occupied by the biphenyl ring of **20**, while pocket B is vacant. Due to the ‘closed’ Trp211 orientation,

lipophilic pockets are concealed in the 1-DXR complex. The DXR structures were superimposed using ChimeraX,¹⁰⁶ and surfaces were computed using Discovery Studio Visualizer (version 20.1.0).¹⁰⁷

In one of the earliest attempts to design non-hydroxamate DXR inhibitors, *Deng et al.* utilized the co-ordination chemistry-based approach to design a variety of small lipophilic MBGs. These MBGs were decorated with phenyl/benzyl rings around them to exploit the lipophilic pocket instead of the regular phosphonate moiety. They reported the catechol and N-hydroxy pyridone (NHP) based molecules (**23-25**) with *Ec*DXR inhibition at the micromolar level and metal chelation between Mn²⁺ DXR metal ion and N-hydroxy and carbonyl oxygen atoms of NHP of a ring of the **25** was observed in a molecular docking study (Fig. 2.12). The hydrophobic cavity was occupied by a 5-phenyl ring adjacent to the active site.¹⁰⁸ Molecule **25**, lacking a phosphonate group, showed moderate activity (MIC = 20 -100 μM) with considerable lipophilicity (clogP = 0.23) than **1** (clogP = -4.14) (computed using DataWarrior program),¹⁰⁹ owing to the absence of the phosphonate group.¹⁰⁹ Molecular docking study supported the expected metal chelation of the Mn²⁺ DXR metal ion through N-hydroxy and carbonyl oxygen atoms of the NHP ring of **25**, while the 5-phenyl ring occupied a hydrophobic pocket B as shown in Fig. 2.11. Even though follow-up studies with **25** were not reported, this study suggested that it is possible to design non-hydroxamate DXR inhibitors using *in silico* SBDD approach. However, it is important to note that the NHP ring of **25** can be considered a cyclized or rigidified hydroxamate group. This observation and the other reports from the same group indicated the possibility of designing hydrophobic inhibitors by excluding either the phosphonate or the hydroxamate moiety and targeting the hydrophobic sub-pockets with aryl rings.^{78,105,110}

Following these leads, *Andaloussi et al.* synthesized catechol and NHP-based molecules (**26** and **27**) with phosphonic acid, and these molecules were evaluated against *Mt*DXR (Fig. 2.12).¹¹¹ Despite having a phosphonic acid moiety, **26** and **27** displayed moderate enzyme inhibition with IC₅₀ values of 41 mM and 53 mM, respectively. Molecules based on other MBGs demonstrated weak *Mt*DXR inhibition, and none of the molecules significantly inhibited the growth of *M. tuberculosis*, presumably due to their reduced on-target activity and poor permeation. However, as

in the previous case,¹⁰⁸ detailed SAR analysis around the catechol and NHP rings were not carried out.

Bodill et al. synthesized a series of molecules replacing hydroxamate MBG with various heteroaryl carboxamide groups expecting ring heteroatom and carbonyl oxygen to coordinate with the DXR metal ion.¹¹² This attempt resulted in poor *Ec*DXR inhibition in all tested molecules (**28-30**), with the lowest IC₅₀ of 408 μM (Fig. 2.12).¹¹² In docking studies, co-ordination between the metal ion and the phosphonic acid was observed instead of metal chelation with the ring heteroatom and carbonyl oxygen. Heterocyclic rings occupied the region close to the phosphonate binding pocket. In a follow-up investigation, the group studied additional aryl/heteroaryl moieties and the effect of linker length on the *Ec/Pf*DXR inhibition.¹¹³ Except for hydroxyl-substituted aryl rings (with 40% inhibition at 250 μM), all analogs resulted in poor DXR inhibition, with the compound exhibiting only about 40% inhibition at 250 mM concentration (**31-36**, Fig. 2.12). SAR analysis revealed that hydroxyl-substituted aryl rings showed comparatively better *Ec/Pf*DXR inhibition, probably due to their metal coordination property. Later, the same group elaborated on evaluating N-benzylated (N-arylcarbamoyl)alkylphosphonic acid derivatives with heteroatoms attached to the aryl ring, expecting to behave as donors for metal cation at the active site. The benzyl group was predicted to cover the hydrophobic cavity nearer to the active site.¹¹⁴ However, complete inactivity was noted with these analogs (**37-39**, Fig. 2.12) when screened against *Pf*DXR in the enzyme inhibition assay.¹¹⁴ Certain analogs showed moderate activity against the *P. falciparum* growth assay, probably *via* some other mechanism that was not investigated.

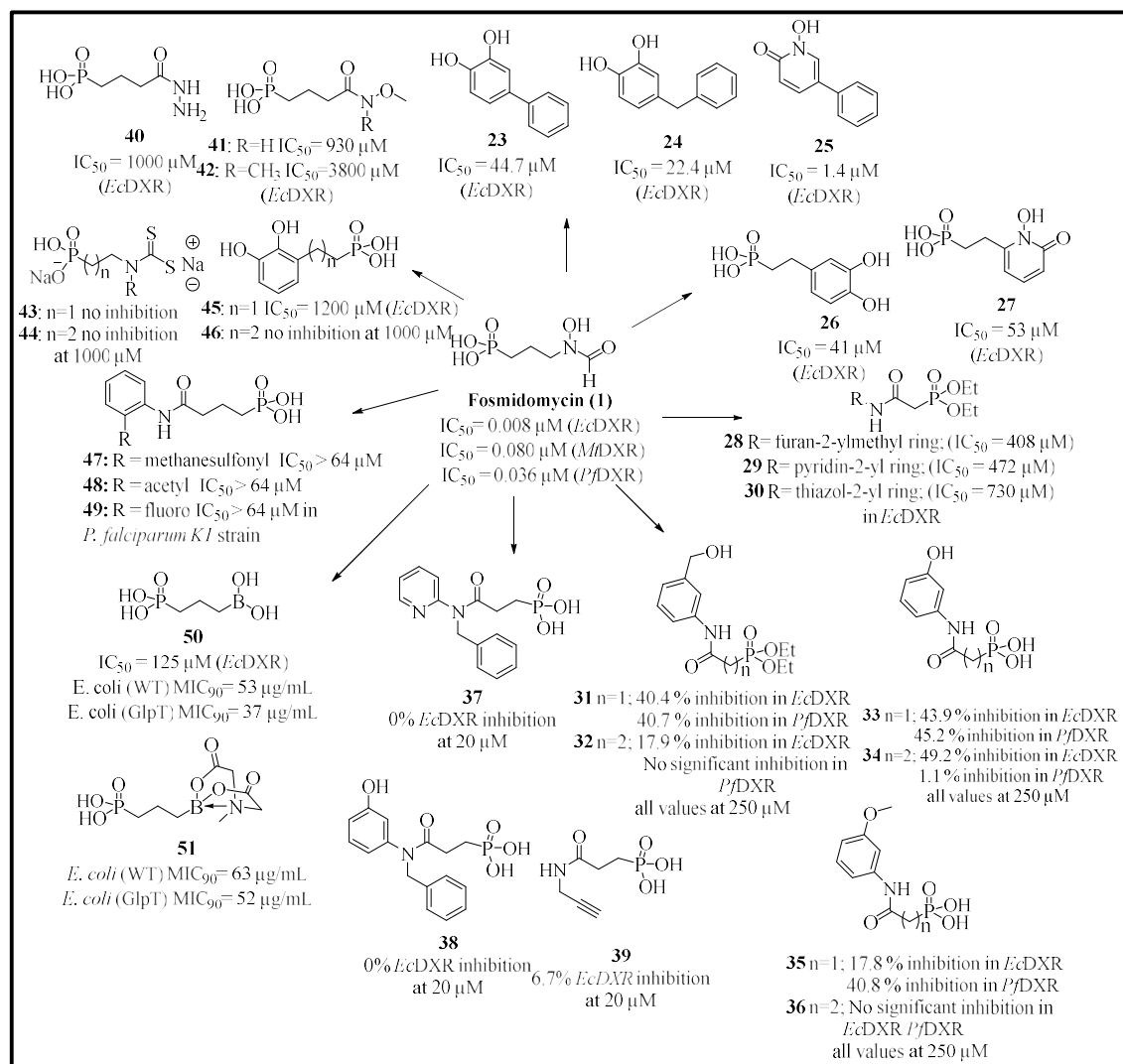


Fig. 2.12 Non-hydroxamate MBG-based DXR inhibitors from the literature

Zinglé *et al.* attempted the replacement of hydroxamate MBG with several other bidentate chelators, such as catechol, dithiocarbamate, and hydrazide group (Fig. 2.12).¹¹⁵ However, these MBGs resulted in weak *EcDXR* inhibition compared to **1**. Compound **40** with hydrazide group as metal chelator was found to be inactive, probably due to reduced chelation potency resulting from the protonation of hydrazide at (pH 7.5) under the assay conditions. Compound **41** (*O*-methylated hydroxamate) and **42** *O*, *N*-dimethylated derivative, exhibited moderate inhibition, whereas the others were completely inactive. The probable reason could be the steric bulk of the *O*-methyl group, affecting the ligand binding. Compound **45** with a catechol ring, similar to **26**,¹¹⁶ showed weak DXR inhibition. Dithiocarbamates (**43** and **44**) also resulted in complete inactivity at 1000 μM due to the soft base character of sulfur. Dithiocarbamate leads to

the formation of a less stable 4-membered chelate ring with the metal ion, as compared to the hydroxamate, which forms a stable 5-membered ring, thereby reducing its chelation capability. Furthermore, like the carboxylate ion, the thiocarboxylate group is also expected to form a strained four-membered chelate ring. Interestingly, compound **44** ($IC_{50} = 1200 \mu\text{M}$), based on the catechol MBG mentioned in Fig. 2.12, was found to be 30 times less potent than the previously described close analog **26** ($IC_{50} = 41 \mu\text{M}$).¹¹⁶ Compounds **26** and **45** differ only in the position of the linker containing the phosphonic acid moiety. This observation signifies the importance of relative positioning of the two pharmacophore features and calls for a detailed SAR study around the newly explored MBG.

Chofor et al. synthesized molecules **47-49**¹¹⁷ with ortho-substitution on an aryl ring possessing an arylamide as a hydroxamic acid replacement (Fig. 2.12). These compounds were expected to chelate metal ions in DXR active site but failed to inhibit *EcDXR* and *MtDXR* even at 100 μM concentration¹¹⁷ and did not inhibit the *P. falciparum* growth. *Mancini et al.* replaced the hydroxamate of FSM with boronic acid as a metal-chelator (Fig. 2.12).¹¹⁸ Four different γ -borono phosphonate analogs, including prodrug, were synthesized and evaluated against *EcDXR*. Compound **50** resulted in poor inhibition of *EcDXR* ($IC_{50} = 125 \mu\text{M}$) compared to **1** ($IC_{50} = 0.05 \mu\text{M}$). However, boronic acid carrying two potential oxygen donors failed to show metal coordination. Similar to carboxylate and dithiocarboxylate, it chelates with the metal ion, resulting in a strained four-membered ring and the inability to form a stable 5-membered ring-like interaction similar to the hydroxamate of FSM. Compound **51**, where boronic acid was masked with N-methyl iminodiacetic acid (MIDA) and/or phosphonic acid, was esterified to improve the. DXR inhibitors based on catechol as MBG (*Deng et al.*). Although compound **50** and its prodrug **51** showed remarkable activity against the different *E. coli* strains in the whole cell assay, suggesting the involvement of another target than DXR, confirmed by chemical rescue experiments. All these analogs were ineffective in the DXR inhibition assay and against the *M. smegmatis* in whole-cell assay. Nevertheless, **50** and **51** showed reasonable activity against two different strains of *E. coli*, suggesting different molecular mechanisms rather than the *EcDXR* inhibition. This observation was further confirmed by the fact that the extraneous supply of IPP, the end product of the MEP pathway, did not reverse the inhibition of *E. coli* by these two compounds.

This non-hydroxamate MBG rationale has been particularly explored by Cohen and group, contributing to the design of the non-hydroxamate molecules for several important targets.¹¹⁹⁻¹²² Following the ongoing medicinal chemistry strategies to design inhibitors against other metalloenzymes, there is an additional opportunity to develop the potential DXR inhibitors with different approaches,¹²⁰ including FBDD. The latter is emerging as a promising strategy, especially for the design of inhibitors of metalloenzymes like matrix metalloproteinases (MMPs), influenza endonuclease, carbonic anhydrase (CAs), and histone deacetylases (HDACs).^{120,121,123-127} We planned to screen a small library of various non-hydroxamate MBGs against the DXR enzymes using molecular docking and *in vitro* assay. The promising fragments would be further grown towards the phosphonate binding pocket or lipophilic cavities to foster further interactions with the enzyme.

2.3 GAPS IN THE EXISTING RESEARCH AND OBJECTIVES

Metalloenzymes rely on metal ions for their activity; thus, the metal chelation ability of the MBG plays a vital role in the design of inhibitors against metalloenzymes. Historically, hydroxamate has been widely used to design inhibitors of structurally diverse metalloenzymes due to its strong interactions with a wide range of metal ions.^{128–130} The hydroxamate MBG-based inhibitors of different metalloenzyme targets such as MMPs, HDACs, and CAs.^{119,131,132}

Although hydroxamate is a strong metal binder and is an ideal MBG, it poses certain challenges. It exhibits inferior pharmacokinetic profiles, toxicity issues, off-target effects, and metabolic instability.^{133,134} Even FDA-approved drugs containing a hydroxamate group suffer from these challenges. For instance, Panobinostat and Vorinostat display poor bioavailability, whereas Belinostat needs to be administered parenterally (Fig. 2.13).¹³⁴ The rate of clearance is also high in hydroxamate-based molecules due to the hydrolysis of this functional group. The carboxylesterases and arylesterases (in plasma) hydrolyze the hydroxamate functionality to carboxylates,¹³⁵ a weak ion chelator. Therefore, several hydroxamate-based molecules targeting HDACs, MMPs, and CAs faced rejection in clinical trials due to poor pharmacokinetics and toxicity issues.^{133,136–139} These serious drawbacks related to hydroxamates led researchers to pivot to the non-hydroxamate-based inhibitor design against several metalloenzymes. Seth et al. designed several non-hydroxamate inhibitors against multiple metalloenzyme targets by ‘*debunking the myth of hydroxamates*.’^{119–122} Following this trail, one recent study reported a significant drop in hydroxamate-based metalloenzyme inhibitors as evaluated in humans, with only 16 molecules possessing hydroxamic acid out of 74 molecules.¹³² Hence, the trend of DXR inhibitor design needs a shift towards non-hydroxamate-based inhibitors.

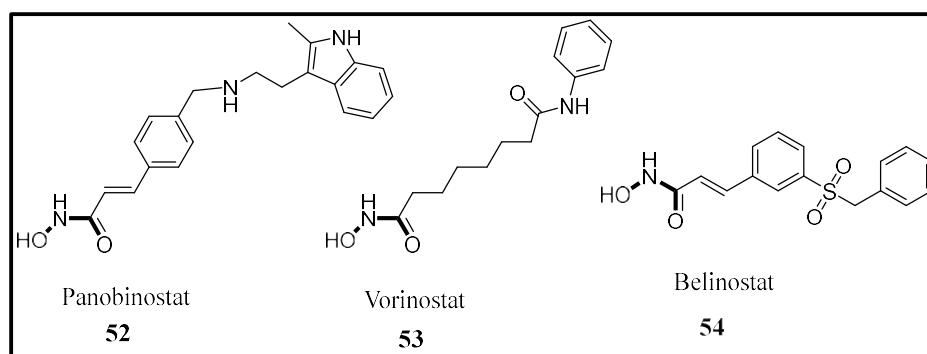


Fig. 2.13 HDAC inhibitors with hydroxamate group

Furthermore, the synthesis and purification of hydroxamate-based small molecules get tricky due to the high polarity of **1**. Replacement of highly polar hydroxamate moiety with different lipophilic non-hydroxamate MBGs might improve the overall hydrophobicity of the small molecules and add on feature to the structural diversity of the DXR inhibitors.

Based on binding interactions of **1** and general rules of co-ordination chemistry observed in the hydroxamate groups suggest the following characteristic features for the potent DXR inhibitors:

1. Hydroxamic acid forms a co-ordination bond with the ‘hard’ Mg^{2+}/Mn^{2+} ion present inside the DXR cavity *via* the ‘hard’ dioxygen (*O, O*) donor motif (Fig. 2.14) obtained from the deprotonation of hydroxyl and the carbonyl oxygen atoms.¹⁴⁰
2. *pKa* of hydroxamic acid varies based on the substituents;^{128,141} thus, dissociation is expected inside the DXR cavity forming the corresponding anion. Again, higher electron density on the carbonyl oxygen is anticipated due to the mesomeric effect from amide nitrogen. Both oxygens with high electron density may account for the strong metal-hydroxamate interactions.
3. *Cis* configuration adapted by both donor oxygens and the metal ion forms the five-membered chelate ring structure seems thermodynamically more stable comparatively than a monodentate binding, as shown in Fig 2.14.¹²⁸

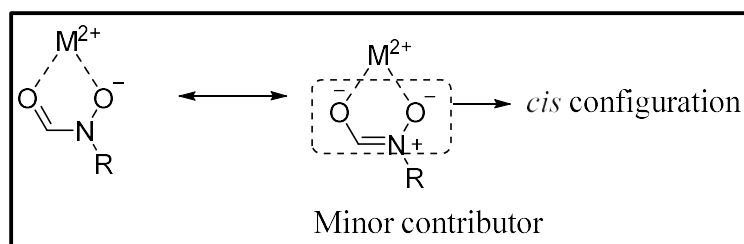


Fig. 2.14 Possible resonance of the hydroxamate group contributing to the metal coordination

As reviewed in the above sections, the non-hydroxamate DXR inhibitors reported in the literature lack one or more aforementioned features, resulting in poor potency. Also, detailed SAR studies are not reported for such inhibitors. In this chapter, we aim to fulfill this gap by exploring non-hydroxamate MBGs suitable for the coordination of the Mn^{2+} ion. The molecular modeling was used to assist the design of the ligands

targeting specific hydrophobic pockets with lipophilic fragments in conjugation with the MBG fragments.

2.3.1 OBJECTIVES

Since several quality X-ray structures of apo and ligand-bound DXR are available, we decided to proceed with a structure-guided drug design strategy. The rationale of the study included the replacement of polar hydroxamate functionality with lipophilic MBGs, which may extend to the inducible lipophilic pocket B (Fig. 2.14). As different substituents at the alpha position to phosphonate were well tolerated in terms of inhibition, attachment of lipophilic substituents at the alpha position to phosphonates was adopted. The combination of aliphatic and aromatic substituents was selected for lipophilic attachments from literature to explore the SAR study. Thus, combining an α -aminophosphonates fragment bearing lipophilic groups with a lipophilic MBG was conceived as a viable strategy for the design. Hence, the following objectives were proposed.

- Collection of lipophilic MBGs from literature and molecular docking studies to identify optimum interactions with the metal.
- *In vitro* screening of the selected fragments against DXR
- Merging of potent MBGs with the α -aminophosphonates guided by molecular docking studies.
- Synthesis, purification, and *in vitro* evaluation of the selected ligands to understand the SAR.
- Antibacterial and antitubercular screening of the selected molecules (in collaboration).

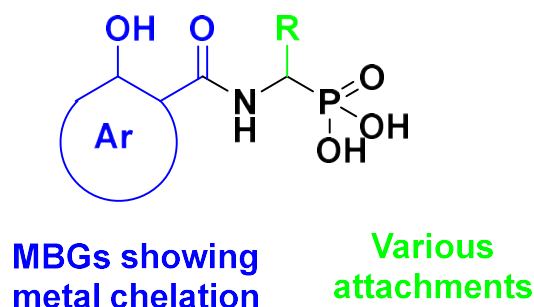


Fig. 2.15 Proposed structure for designed DXR inhibitors

2.4 RESULT AND DISCUSSION

2.4.1 Fragment selection and *in vitro* screening

To accomplish the proposed objectives, we surveyed the existing literature for reported potential lipophilic MBGs. A library reported by Cohen et al.¹²⁰ consisting of 96 small metal chelating fragments (Fig. 2.16), referred as a metal chelating library (MCL), was selected for the study. With a few exceptions, these fragments fit into the Rule of Three (Ro3) of fragment selection criteria. The MW for all the fragments is ≤ 300 , clogP is ≤ 3 , HBD, HBA, and rotatable bonds are ≤ 3 . (Table 2.1, Figure. 2.17). Since donor moiety is essential for effective metal chelation at the active site, we did not filter the fragments exceeding this criterion. The fragments with more HBA (> 4) showed lesser lipophilicity than those with lesser HBA (2-4). Apparently, the size of HBD did not affect lipophilicity; maximum fragments showed an HBA count of 2 or less. All the fragments showed MW less than 240, obeying the Ro3. Thus, we proceed further with the molecular docking study of the fragments.

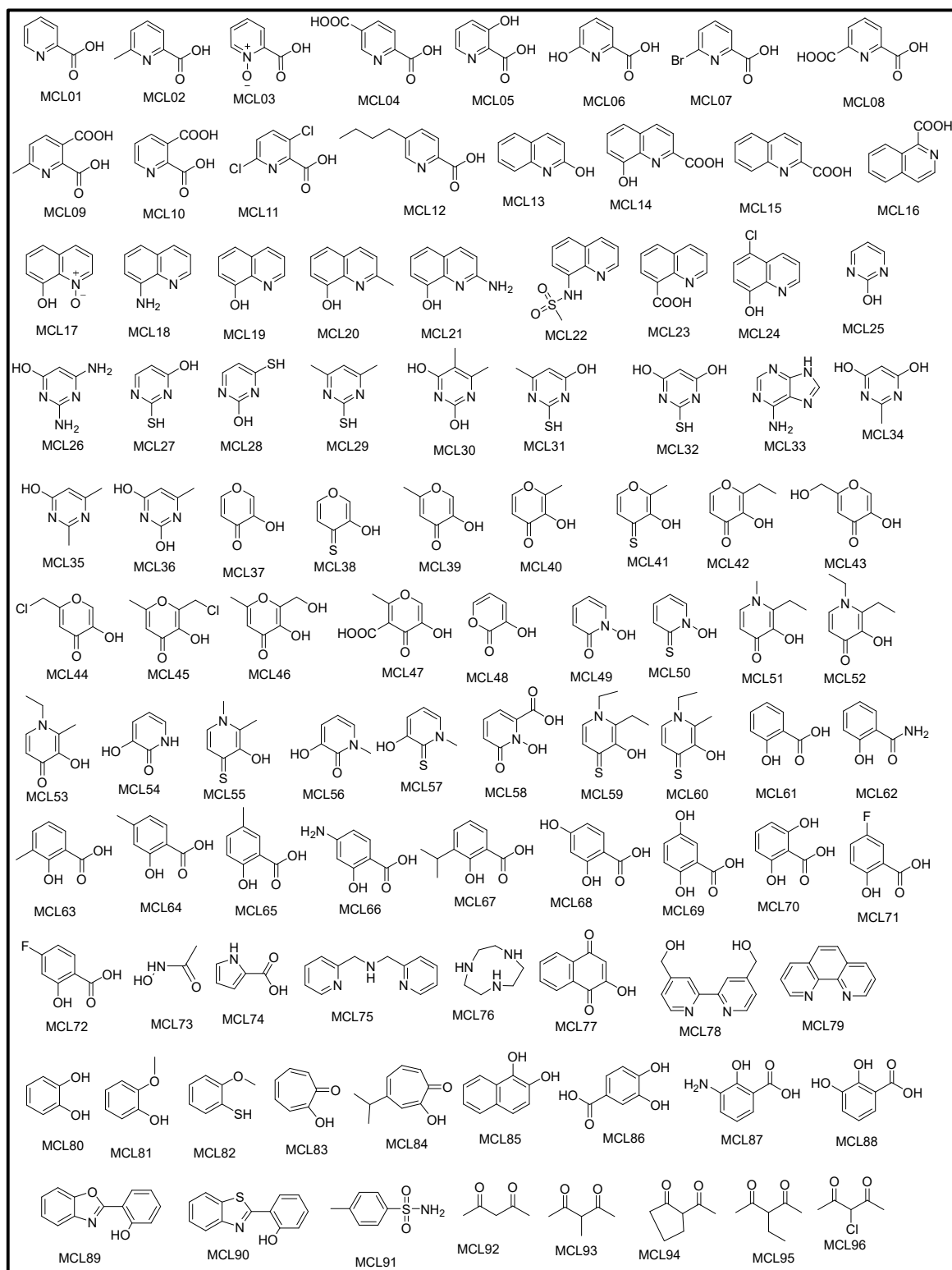


Fig. 2.16 Structure of fragments in MCL

Table 2.1: Metal chelators and their properties (calculated using DataWarrior)

Code	MW	clogP	clogS	HBD	HBA	Rotatable bonds
MCL01	123.1	0.2	-0.86	3	1	1
MCL02	137.1	0.6	-1.23	3	1	1
MCL03	139.1	-0.28	-3.24	4	1	1
MCL04	167.1	-0.32	-0.87	5	2	2
MCL05	139.1	-0.15	-0.56	4	2	1
MCL06	139.1	0.03	-1.09	4	2	1
MCL07	202	1.02	-1.46	3	1	1
MCL08	167.1	-0.26	-0.9	5	2	2
MCL09	181.2	0.08	-1.24	5	2	2
MCL10	167.1	-0.32	-0.87	5	2	2
MCL11	192	1.51	-2.09	3	1	1
MCL12	179.2	1.87	-1.9	3	1	4
MCL13	145.2	1.98	-2.55	2	1	0
MCL14	189.2	1.17	-2.06	4	2	1
MCL15	173.2	1.51	-2.36	3	1	1
MCL16	173.2	1.39	-2.46	3	1	1
MCL17	161.2	1.15	-4.41	3	1	0
MCL18	144.2	1.3	-2.4	2	1	0
MCL19	145.2	1.63	-2.03	2	1	0
MCL20	159.2	2.03	-2.39	2	1	0
MCL21	160.2	1.3	-2.63	3	2	0
MCL22	222.3	1.02	-3.41	4	1	1
MCL23	173.2	1.46	-2.34	3	1	1
MCL24	179.6	2.24	-2.76	2	1	0
MCL25	96.1	0.12	-0.59	3	1	0
MCL26	126.1	-0.53	-1.79	5	3	0
MCL27	128.2	0.29	-1.72	3	1	0
MCL28	128.2	0.16	-1.46	3	1	0
MCL29	140.2	1.08	-2.22	2	0	0
MCL30	140.1	0.87	-1.53	4	2	0
MCL31	142.2	0.68	-2.08	3	1	0
MCL32	144.2	0.29	-1.95	4	2	0
MCL33	135.1	-0.35	-2.27	5	2	0
MCL34	126.1	0.34	-0.7	4	2	0
MCL35	124.1	0.73	-0.84	3	1	0
MCL36	126.1	0.52	-1.18	4	2	0
MCL37	112.1	-0.86	-1.29	3	1	0

MCL38	128.2	-0.8	-0.28	2	1	0
MCL39	126.1	-0.19	-1.55	3	1	0
MCL40	126.1	-0.19	-1.55	3	1	0
MCL41	142.2	-0.13	-0.54	2	1	0
MCL42	140.1	0.27	-1.82	3	1	1
MCL43	142.1	-1.11	-1.04	4	2	1
MCL44	160.6	0.04	-1.95	3	1	1
MCL45	174.6	0.71	-2.21	3	1	1
MCL46	156.1	-0.44	-1.3	4	2	1
MCL47	170.1	-1.02	-1.15	5	2	1
MCL48	112.1	-0.72	-1.17	3	1	0
MCL49	111.1	-1.02	-0.88	3	1	0
MCL50	127.2	-0.81	-1.82	2	1	0
MCL51	153.2	0.38	-1.32	3	1	1
MCL52	167.2	0.78	-1.62	3	1	2
MCL53	153.2	0.33	-1.35	3	1	1
MCL54	111.1	-0.86	-1.03	3	2	0
MCL55	155.2	-0.02	-0.04	2	1	0
MCL56	125.1	-0.61	-0.67	3	1	0
MCL57	141.2	-0.39	-1.61	2	1	0
MCL58	155.1	-1.63	-0.61	5	2	1
MCL59	183.3	0.84	-0.61	2	1	2
MCL60	169.3	0.39	-0.34	2	1	1
MCL61	138.1	0.8	-1.33	3	2	1
MCL62	137.1	0.4	-1.41	3	2	1
MCL63	152.2	1.14	-1.68	3	2	1
MCL64	152.2	1.14	-1.68	3	2	1
MCL65	152.2	1.14	-1.68	3	2	1
MCL66	153.1	0.12	-1.41	4	3	1
MCL67	180.2	1.99	-2.2	3	2	2
MCL68	154.1	0.45	-1.04	4	3	1
MCL69	154.1	0.45	-1.04	4	3	1
MCL70	154.1	0.45	-1.04	4	3	1
MCL71	156.1	0.9	-1.65	3	2	1
MCL72	156.1	0.9	-1.65	3	2	1
MCL73	75.1	-0.81	-0.73	3	2	0
MCL74	111.1	-0.08	-0.68	3	2	1
MCL75	199.3	0.54	-1.27	3	1	4
MCL76	129.2	-1.7	0.12	3	3	0
MCL77	174.2	0.94	-2.77	3	1	0

MCL78	216.2	0.3	-1.26	4	2	3
MCL79	180.2	2.29	-3.03	2	0	0
MCL80	110.1	0.97	-1.02	2	2	0
MCL81	124.1	1.24	-1.34	2	1	1
MCL82	140.2	1.53	-2.74	1	0	1
MCL83	122.1	0.36	-1.32	2	1	0
MCL84	164.2	1.47	-1.87	2	1	1
MCL85	160.2	2.16	-2.63	2	2	0
MCL86	154.1	0.45	-1.04	4	3	1
MCL87	153.1	0.12	-1.41	4	3	1
MCL88	154.1	0.45	-1.04	4	3	1
MCL89	211.2	2.97	-4.31	3	1	1
MCL90	227.3	3.15	-2.88	2	1	1
MCL91	171.2	0.77	-1.86	3	1	1
MCL92	100.1	0.23	-1.1	2	0	2
MCL93	114.1	0.45	-1.26	2	0	2
MCL94	126.2	0.67	-1.61	2	0	1
MCL95	128.2	0.91	-1.53	2	0	3
MCL96	134.6	0.42	-1.43	2	0	2

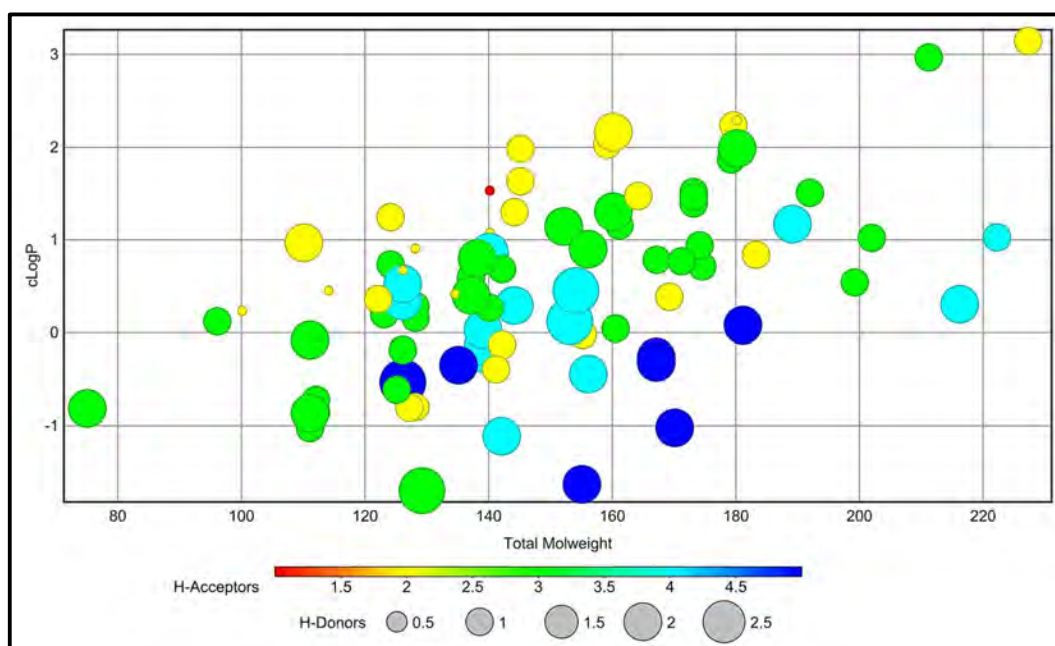


Fig. 2.17 The graphical representation of the calculated properties of the fragments from MCL. Y-axis indicates lipophilicity, and x-axis indicates MW. The count of HBA is colour coded, while the HBD count is proportional to the size of the data points.

A few other metal chelating fragments used earlier and not mentioned in the MCL were obtained from literature resulting in 103 MBG fragments. The curated library of fragments was docked within the DXR active site from different microorganisms (5JAZ⁷⁵ from *P. falciparum* 3D7, 2Y1D¹⁴² from *Mtb* H37Rv, and 3ANM¹⁰⁵ and 3R0I¹⁴³ from *E. coli* K-12) employing the Glide docking program. The respective co-crystallized ligands from protein 5JAZ, 3R0I, and 2Y1D were found to chelate metal ions by forming a 5-membered ring-like structure (Fig. 2.14). In contrast, protein 3ANM, complexed with compound **20** without MBG, interacted with the indole ring of Trp211. The indole ring of Trp211 was found flipped at a 180° angle due to extended lipophilic biphenyl substituent, revealing the presence of pocket A. The co-crystallized poses of all three ligands were successfully reproduced (RMSD < 2 Å) by the docking procedure used in Glide (Fig. 2.18 and Table 2.2). To corroborate our study with DXR enzyme inhibition assay, here we demonstrated the docking results obtained using a protein-ligand complex from *E. coli* (3R0I). The optimized docking protocol was then used to model the fragment binding poses within the *E. coli*. DXR pocket.

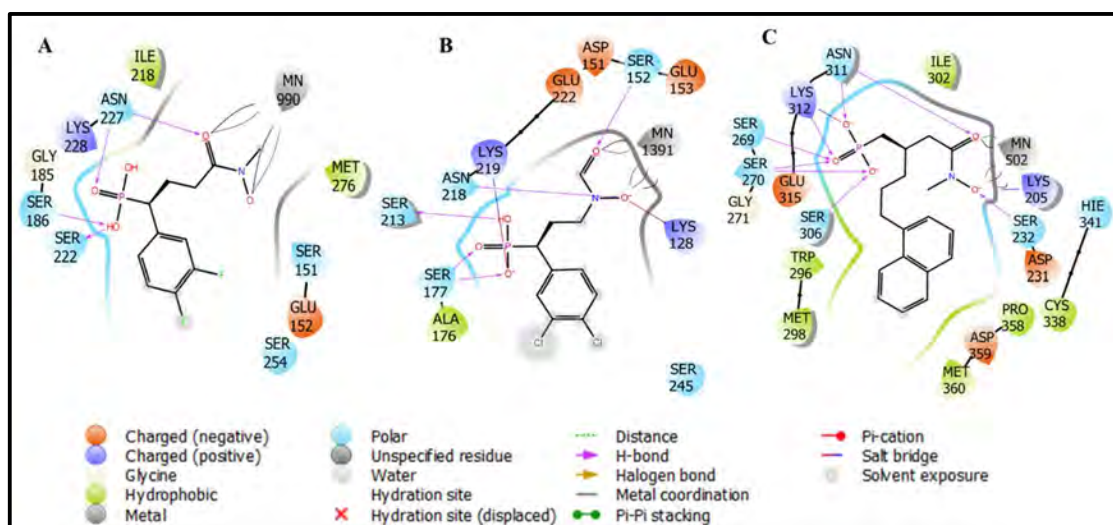


Fig. 2.18 Interactions of co-crystallized ligand at the binding site of 3R0I (A), 2Y1D (B), and 5JAZ (C)

Table 2.2: Interactions shown by cocrystallized ligand at the binding site

PDB ID	RMSD	Docking score	Hydrogen bond interactions	Metal coordination distance	co-ordination distance
5JAZ	0.37	-10.7	Ser232, Asn311	2.20 Å	2.23 Å
2Y1D	1.04	-3.9	Ser152, Asn218	2.21 Å	2.12 Å
3R0I	1.9	-3.86	Asn227	2.46 Å	2.09 Å

2.4.2 Docking studies on 5JAZ, 2Y1D and 3R0I protein

Among the diverse metal chelating fragments from MCL, the docked poses of several aromatic ring fragments containing MBG were found to interact with the metal ion by metal chelation. These ring fragments have MBG embedded in the aromatic ring itself, which offers an advantage of metal chelation along with increased lipophilicity and is expected to occupy lipophilic pocket A, found close to the hydroxamate binding pocket (Fig. 2.11). Since these fragments have MBG locked already in the *cis* configuration, unlike hydroxamate, more stable metal chelation can be achieved. The fragments with dioxygen moiety particularly showed the desired interactions and metal coordination in a bidentate fashion *via* their *O,O* motif, as observed in the case of the hydroxamate group of the co-crystallized ligand (Fig 2.19). Hydroxamic acid from FSM and its analogs demonstrates favorable interactions with the ‘hard’ Mg^{2+}/Mn^{2+} ion present inside the DXR active site *via* its ‘hard’ dioxygen (*O,O*) donor motif consisting of the deprotonated hydroxyl and the carbonyl oxygen atoms. The metal coordination distance between the fragments and dioxygen moiety was found in the range of 2.10-2.50 Å, which is important for effective metal coordination. This observation resembles the DXR enzyme complexes with FSM and its hydroxamate derivatives. The cocrystallized ligand of 3R0I shows 2.14 Å and 2.07 Å distance from the metal. A few, but not all, rings containing *N,O* as MBG demonstrated the effective metal coordination with bidentate metal ions at the active site (e.g., F1 and F8, Table 2.3). The other fragments lacking *O,O* moiety failed to show desired metal interactions in docking studies,¹⁴⁴ indicating the importance of hard donor motif for metal chelation. Expectedly, modelled binding poses of these aromatic ring-based MBGs were found to occupy pocket B. (Fig. 2.19). However, a few rings with MBG were flipped to another direction rather than oriented towards the phosphonic acid motif.

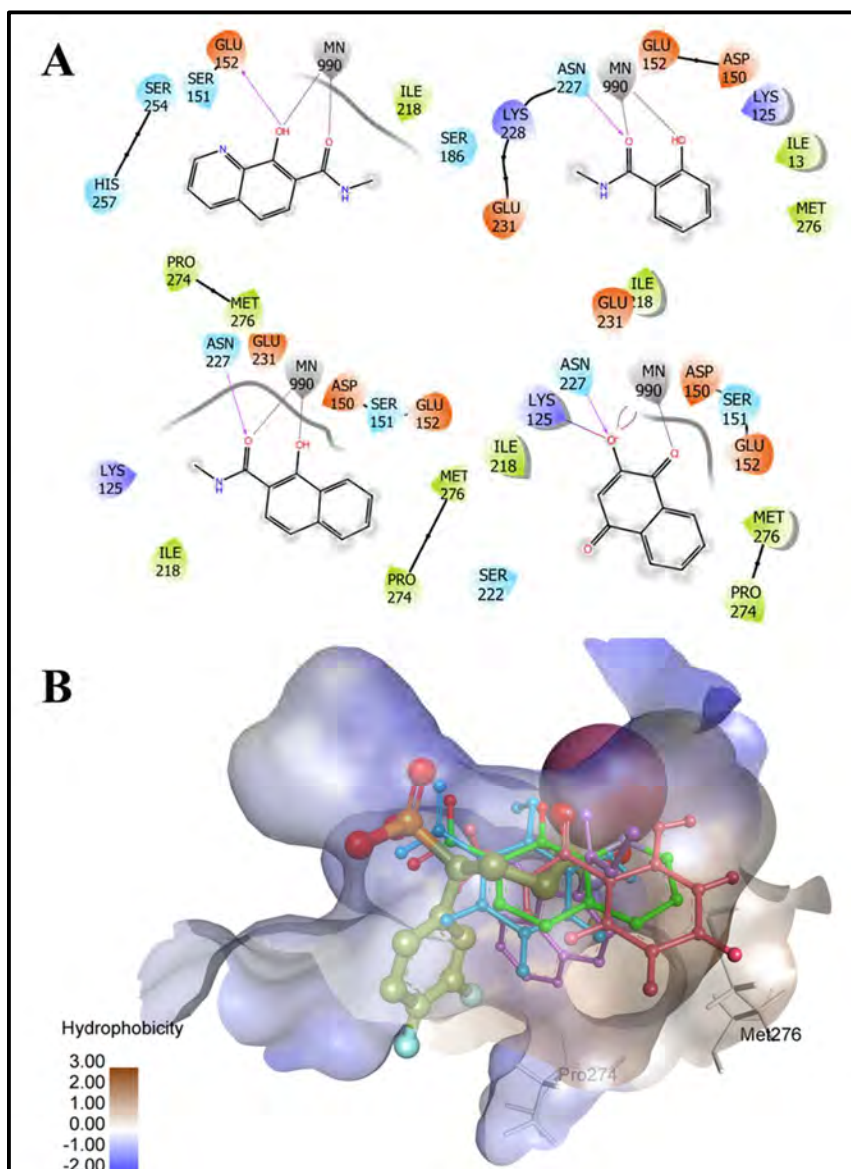


Fig. 2.19 (A) Ring fragments showing metal chelation. The metal ion is shown in pink colour. (B) Aromatic ring fragments occupying hydrophobic Pocket B (lined with Pro274 and Met276)

Since the *O,O* donor motifs from these aromatic ring fragments are locked in the *cis* configuration, these fragments are likely to have a thermodynamic advantage over the hydroxamate group since only the *trans* rotamer of the latter is expected to chelate metal (Fig. 2.14). The binding affinity for some of these fragments with Mn^{2+} ion is similar to acetohydroxamic acids calculated by quantum mechanics, which is already reported.¹⁴⁵

Overall, the *O,O* motif of several MBGs was found to overlap that of the hydroxamate group of the co-crystallized ligand (Fig. 2.20). In the case of docking with the 5JAZ

protein complex, aromatic rings showed the pi-pi stacking with the indole ring of Trp296 residue. Additionally, these MBG fragments possess higher clogP as these are part of the aromatic rings and hence, are expected to have improved cellular permeability compared to FSM. Also, due to hydrolases, the challenge of hydrolysis of the hydroxamate group to carboxylic acids can be avoided. Thus, we expect these rings to occupy pocket B and form H-bond interaction with the residues.

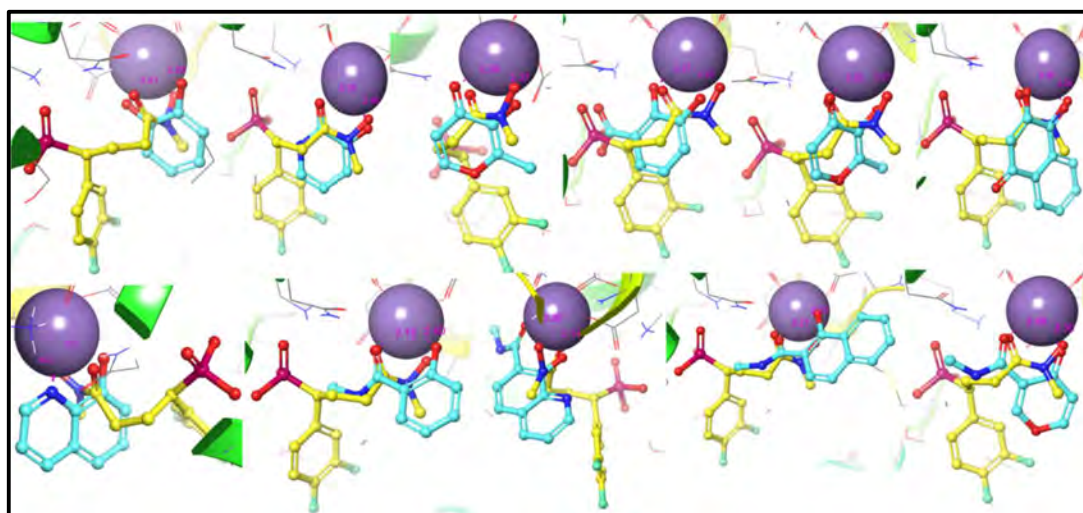


Fig. 2.20 Docking poses of MBGs (cyan balls and sticks) showing bidentate chelation of the Mn²⁺ ion (purple ball) inside the DXR pocket (PDB 3R0I). The cocrystallized ligand is shown in yellow balls and sticks.

We selected 13 fragments for *in vitro* enzyme inhibition assay based on the following criteria

- i) the desired metal chelation with divalent metal ion and oriented towards hydrophobic pocket B,
- ii) the overlap of MBG with the hydroxamate functionality of the cocrystallized ligand,
- iii) the presence of the *O,O* motif is required for strong chelation with the metal ion, and
- iv) synthetic tractability of the MBG derivatives.

These 13 fragments (F1-F13) were procured and screened against the recombinant *E. Coli* DXR, initially at a single concentration (100 μ M).¹⁴⁶ As expected, almost all fragments with the dioxygen moiety inhibited the enzyme at 100 μ M concentration (Fig. 2.21). Fragments F2, F5, F8, F12, F9, and F5 were selected for further SAR studies as these possess either a carboxylic acid or an aldehyde functionality as a vector to grow

molecules further toward phosphonate binding pocket and/or lipophilic pocket B. Table 2.3 shows the percentage of DXR enzyme activity at 100 μM .

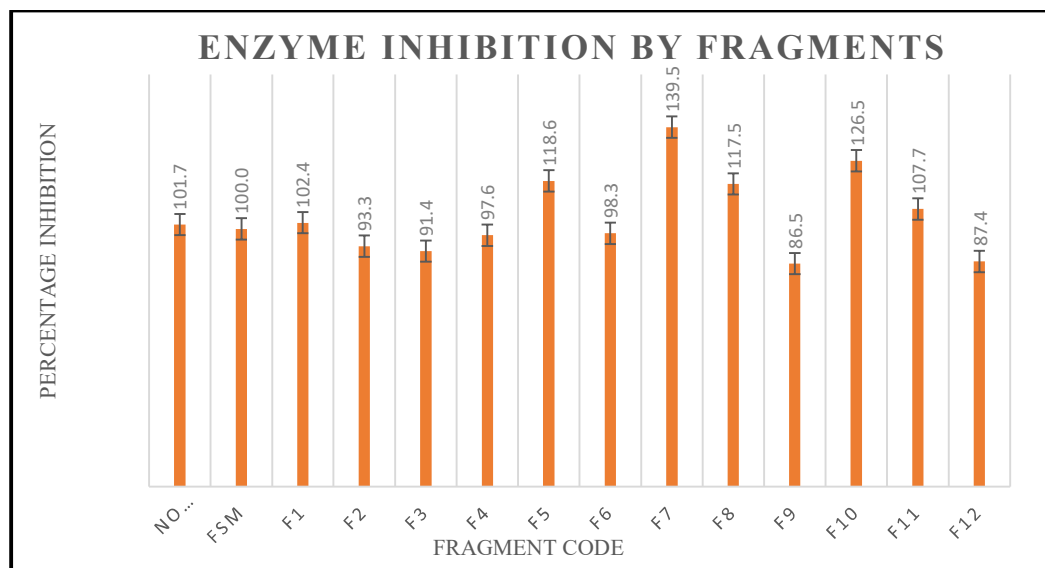
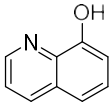
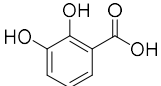
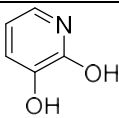
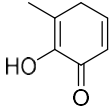
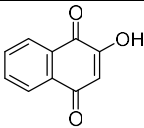
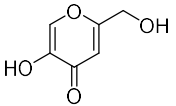
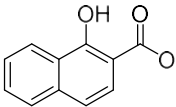
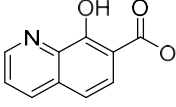
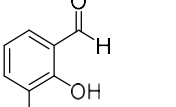
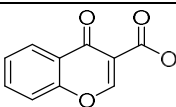
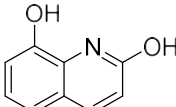
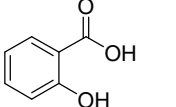
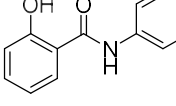


Fig. 2.21 Graphical representation of enzyme inhibition activity of fragments at 100 μM concentration. (NO represents the no reaction in the absence of enzyme or substrate)

Table 2.3: Percentage inhibition of the DXR enzyme by fragments in DXR inhibition assay

Fragment code	Structure of the Fragment	% Inhibition at 100 μM	Docking score (kcal/mol)	Distance from metal (\AA)		MMGBSA (kcal/mol)
F1		102.4	-5.08	2.20	2.40	-33.0
F2		93.3	-6.34	2.37	2.29	-32.6
F3		91.4	-4.52	2.19	2.46	-1.02
F4		97.6	-4.3	2.36	2.37	-15.0
F5		>100	-2.9	2.36	2.38	-19.7

F6		98.3	-4.4	2.36	2.07	-15.0
F7		>100	-4.5	2.33	2.11	-25.95
F8		>100	-4.76	2.37	2.21	-35.4
F9		86.5	-5.48	2.13	2.31	-15.7
F10		>100	-5.03	2.20	2.32	-17.4
F11		>100	-3.58	2.15	2.45	-33.9
F12		87.4	-4.47	2.40	2.19	-22.6
F13		>100%	3.24	2.21	2.31	-33.5

2.4.3 Design of inhibitors with selected MBGs

To further occupy the phosphonate binding pocket in the DXR active site, we adopted a fragment-linking strategy where the identified MBGs were linked to the α -aminophosphonates. These α -aminophosphonate moieties were found to be ideal as a source of required phosphonic acid function as they can be synthesized in a single step using Kabachnik–Fields multicomponent reaction.¹⁴⁷ Also, diverse lipophilic groups (R_1) can be added at the alpha position by choosing an appropriate aldehyde component. Initially, we selected MBGs with carboxylic acid groups (F2, F7, F8, F10, and F12), aiming to use amide coupling between the acidic and amine functionality of the α -aminophosphonates. These designed molecules were found to adopt similar

conformation as shown by the co-crystallized ligand. Also, as hypothesized, MBG fragments chelated metal ions and aromatic rings occupied pocket “B”. As proposed, the lipophilic R₁ group alpha to the phosphonate moiety occupied pocket “A” (Fig. 2.22). This observation was particularly noted in compounds with aromatic R₁ group as phenyl, naphthyl, 3,4-dichlorophenyl, and phenylpropyl attachments. Aliphatic R₁ attachments, propyl, and -H failed to enter pocket “A” mentioned in Fig. 2.23

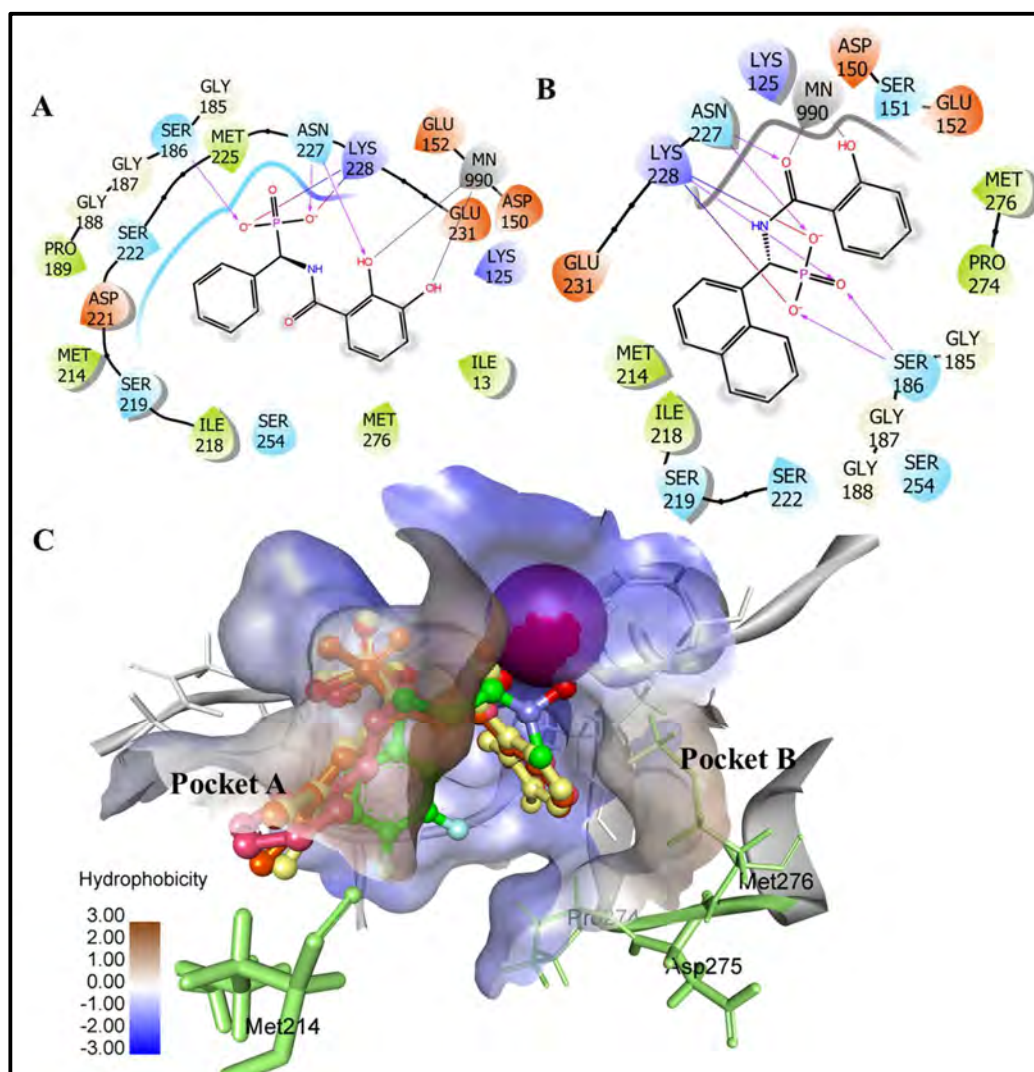


Fig. 2.22 Examples of designed molecules (A). Derivative of fragment F2 (B) Derivative of fragment F12 (C). 3D view of derivatives occupying pocket A by lipophilic R₁ attachments and aromatic rings attached to MBG occupying lipophilic pocket B lined by Pro274 and Met276 residues.

To design the derivatives of F5, we placed phosphonate attachments at C-3, which could be attached by a C-alkylation achieved *via* enolate formation.¹⁴⁸ About ~50 small molecules were designed using molecular docking studies based on the selected MBGs

linked to α -aminophosphonates. Few derivatives of fragments F2 (Fig. 2.22A) and F12 (Fig. 2.22B) were found to display the metal chelation by phenolic and amide oxygen atoms and occupation of pocket “A” and “B” by the lipophilic rings (Fig. 2.22C). Similarly, the derivatives of other MBGs such as Salicylic acid (SA, F12), 1-Hydroxy-2-naphthoic acid (NA, F7), 2,3-Dihydroxy benzoic acid (DHBA, F2), 8-Hydroxyquinoline-7-carboxylic acid (8-HQ, F8), Chromone-3-carboxylic acid (CCA, F10) and 2-Hydroxy-1,4-naphthoquinone (2-HNQ, F5) were found to chelate the metal ion at DXR active site in a similar fashion to the co-crystallized ligand. The following observations were noted from the modeling studies of the designed molecules (Fig. 2.23).

1. Metal coordination was observed by MBGs within the range of 2.10-2.50 Å.
2. Hydrogen bond interactions with the active site residues (Asn and Ser) were similar to the co-crystallized ligand.
3. Pi-pi stacking was observed between the indole ring of Trp296 and the aromatic ring (R₁) of the designed ligands in the *P. falciparum* DXR protein-ligand complex (5JAZ).
4. The phosphonate group occupied desired hydrophilic pocket similar to the co-crystallized ligand and fostered important H-bond interactions with Ser186, Asn222, Ser227, and Leu228 residues.
5. A lipophilic attachment (R₁) at the alpha carbon to phosphonate group was found to occupy a revealed lipophilic pocket A, similar to the co-crystallized ligand as in the case of PDB (3R0I, 5JAZ).

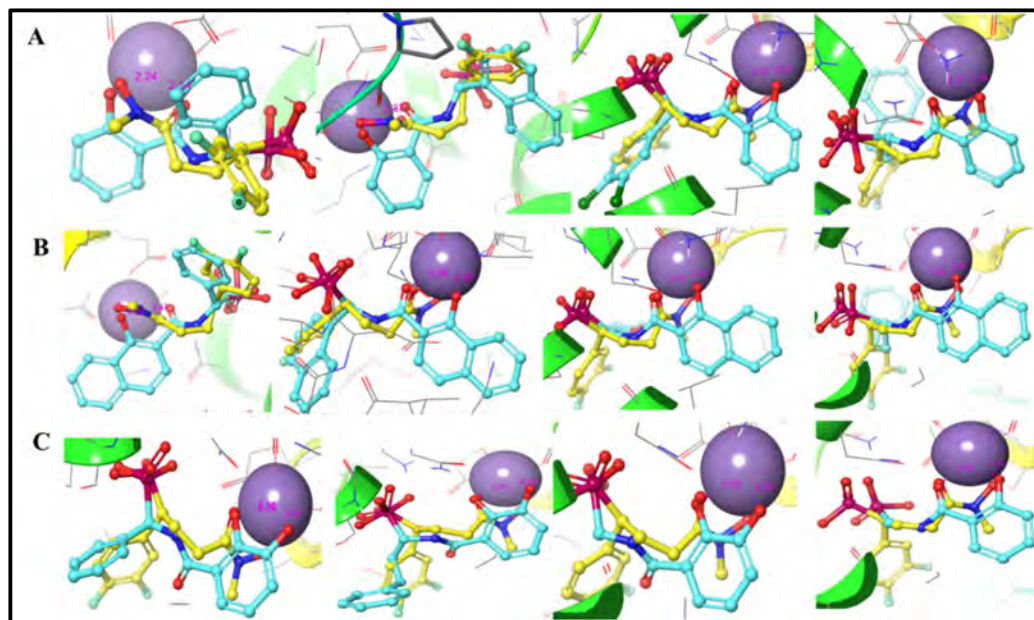


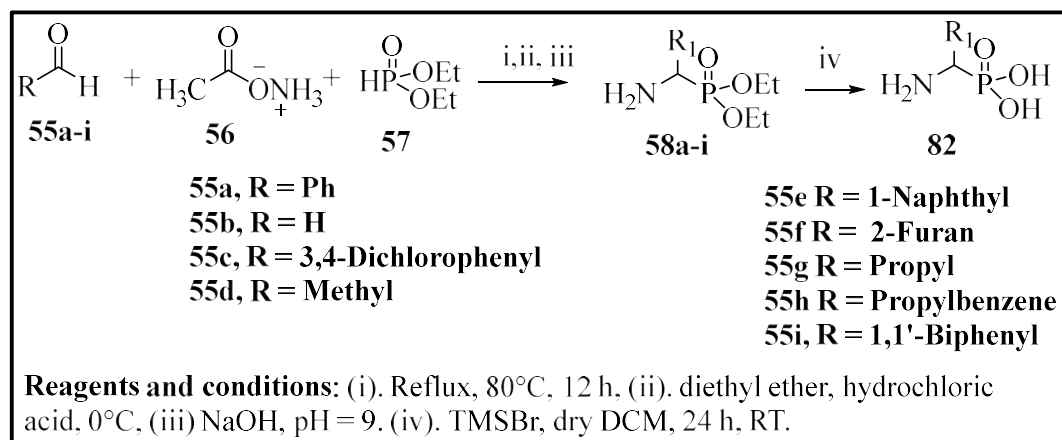
Fig. 2.23 Docking poses of MBG containing non-hydroxamate DXR inhibitors (cyan balls and sticks) showing bidentate chelation of the Mn^{2+} ion (purple ball) inside the DXR pocket (3R0I). The cocrystallized ligand is shown in the yellow balls and sticks model. (A) Designed inhibitors containing SA as MBG (F12) (B) Designed inhibitors containing NA as MBG (F7) (C) Designed inhibitors containing DHBA as MBG (F2).

However, in certain designed molecules, a few poses showed the metal chelation between the *O,O* of the phosphonic acid, and divalent metal, which is in accordance with the known metal chelation property of the phosphonic acid functionality. Overall, docking studies of the designed molecules supported the optimum metal chelation by MBGs and binding to hydrophobic sub-pockets. Thus, based on the docking poses, chemical synthesis of the ligands based on the fragments SA (F12), NA (F7), DBHA (F2), 8-HQ, and CCA (F10), Scheme 2.3-2.7 and Table 2.5) was initiated.

2.4.4 Chemical synthesis

2.4.4.1 Synthesis of α -aminophosphonates

Firstly, we optimized the synthesis of various α -aminophosphonates. using Kabachnik-fields condensation reaction (Scheme 2.1).¹⁴⁷ An aldehyde, ammonium acetate, and diethyl phosphite were used for the condensation reaction, with ammonium acetate being an amine source. This three-component reaction proceeds by an imine intermediate, followed by the addition of diethyl phosphite to the imine. Nine different α -aminophosphonates were synthesized using various aliphatic and aromatic aldehydes as per Scheme 2.1. To investigate the SAR studies, a few α -aminophosphonates were hydrolyzed to their respective acids.



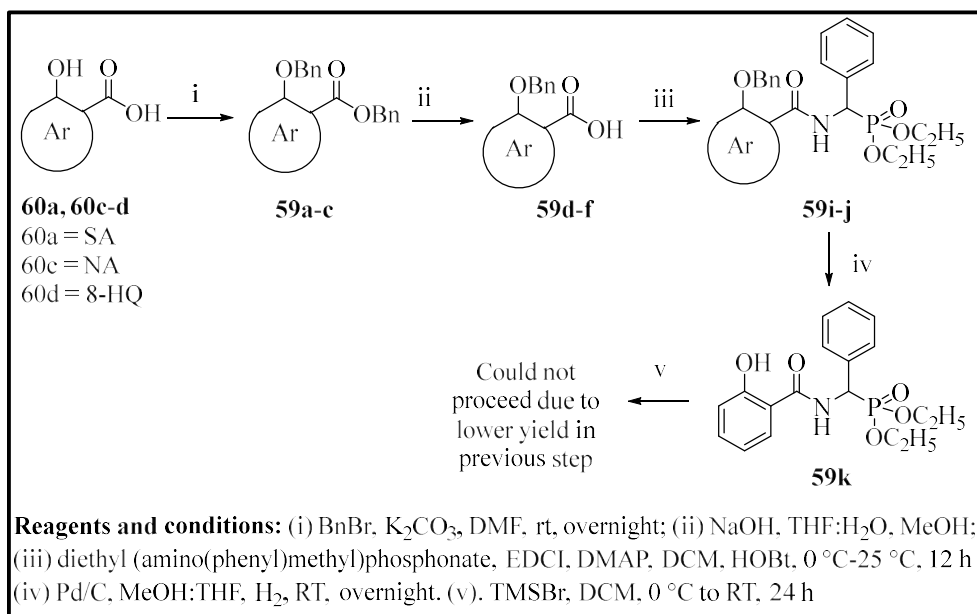
Scheme 2.1. Synthesis of different primary α -aminophosphonates

2.4.4.2 Synthesis of molecules based on SA (F12), NA (F7), 8-HQ (F8), DHBA (F2), and CCA (F10) as MBGs

To synthesize the derivatives of MBG containing fragments SA (F12), NA (F7), and 8-HQ (F8), we tried to optimize the reaction using two approaches to obtain the designed molecules. We particularly synthesized derivatives with MBGs NA (F7), SA (F12), and 8-HQ (F8) because the presence of aromatic rings makes them more lipophilic than hydroxamates. Moreover, the carboxylic acid function can be used to attach the phosphonate-containing linker. Also, derivatives of DHBA (F2) and CCA (F10) were synthesized (Scheme 2.4 and 2.7). Further, to study the SAR analysis of the synthesized molecules, eight different α -aminophosphonate (**55a-h**) attachments were used to couple with the fragments, including aromatic and aliphatic functionalities.

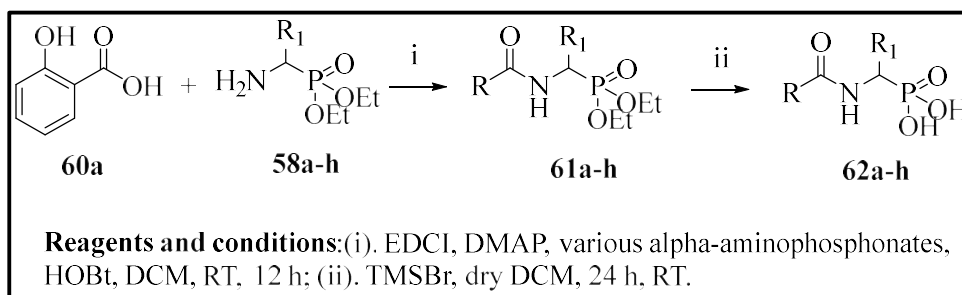
In the first approach (Scheme 2.2), we performed the *O*-benzylation to protect the phenolic and carboxylic OH groups of SA (F12), NA (F7), and 8-HQ (F8) MBGs (**59a-c**). Later, the hydrolysis of the ester group was performed to obtain the free carboxylic functionality (**59d-f**). Subsequently, the coupling reaction with the free carboxylic acid of MBG was attempted using various reagents, which, unfortunately, did not work at our hands. After extensive optimization using 1-(3-Dimethylaminopropyl)-3-ethylcarbodiimide hydrochloride (EDCI.HCl) and 1-Hydroxybenzotriazole (HOBt) as the coupling reagents, the products **59i-j** were obtained albeit in lower yields. In the next step, we attempted reductive debenylation of the benzyl group. However, starting material remained unconsumed under these conditions, and we obtained a debenzylated product (**59k**) with a very low yield. Our proposed next step was TMSBr-mediated

hydrolysis to remove ethyl esters to obtain the desired phosphonic acid product. However, the exceptionally low yield hindered our progression to the subsequent step.

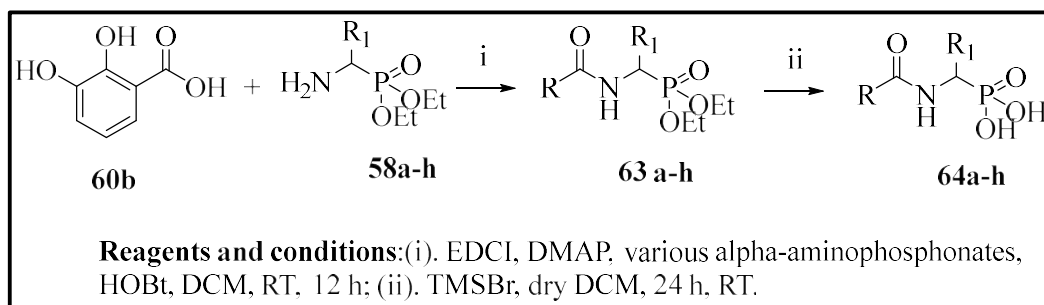


Scheme 2.2 Synthesis of the derivatives of F2, F7 and F8 MBGs using benzylation chemistry

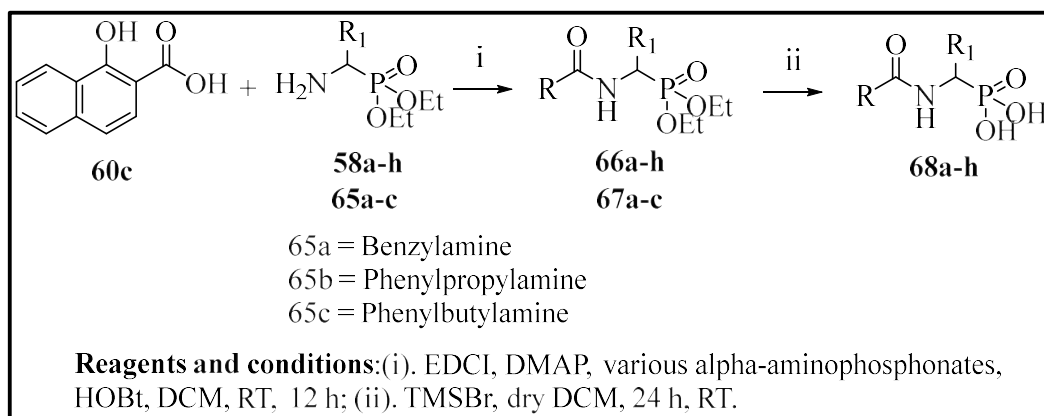
To avoid the protection-deprotections steps, we also tried direct coupling of unprotected MBGs with the synthesized α -aminophosphonates. Initial reactions resulted in a satisfactory yield of the desired products, and hence, we continued with this approach to reduce the overall synthetic steps. This approach resulted in the synthesis of total 28 esters (**61a-h**, **63a-h**, **66a-h**, **69a-c**, and **72a**), using primary α -aminophosphonates (Schemes 2.3-2.7) with satisfactory yield. To study the SAR, four compounds (**67a-c** and **70**), analogous to the designed inhibitors (**68a**, **68h**, and **71a**), were also synthesized using optimized conditions without phosphonate attachment (listed in Table 2.5). These synthesized phosphonate esters were further hydrolyzed to their respective acids by bromotrimethylsilane (TMSBr)-mediated hydrolysis, as shown in Scheme 2.3-2.7.



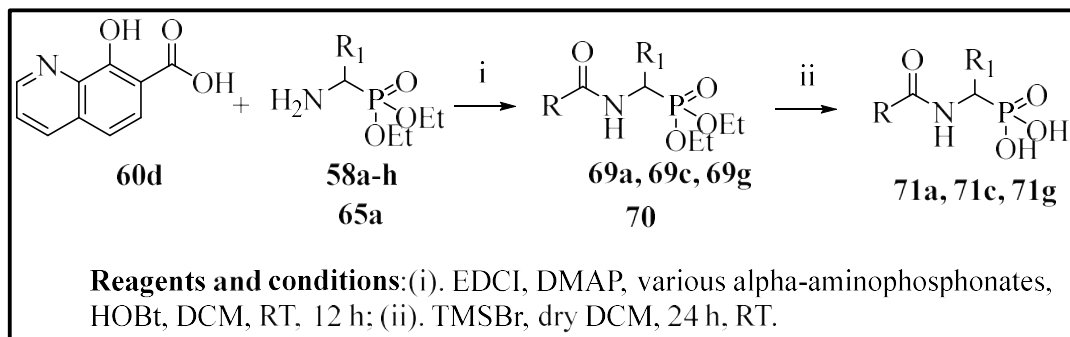
Scheme 2.3: General synthesis scheme for the derivatives of F12, salicylic acid (SA) MBG



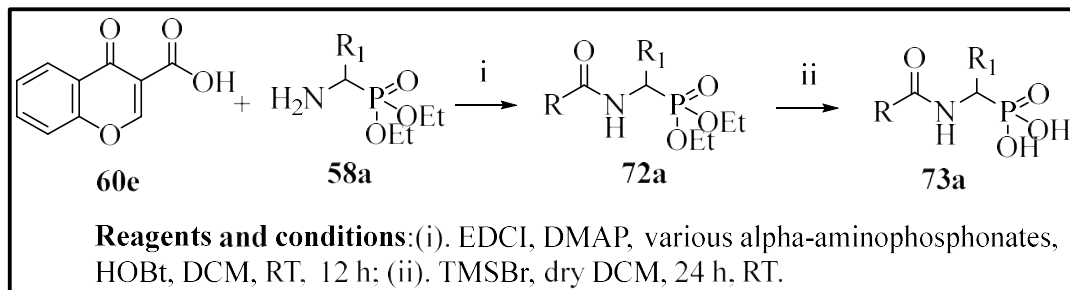
Scheme 2.4: General synthesis scheme for the derivatives of F2, 2,3-Dihydroxy benzoic acid (DHBA) MBG



Scheme 2.5: General synthesis scheme for the derivatives of F7, 1-Hydroxy-2-naphthoic acid (NA) MBG

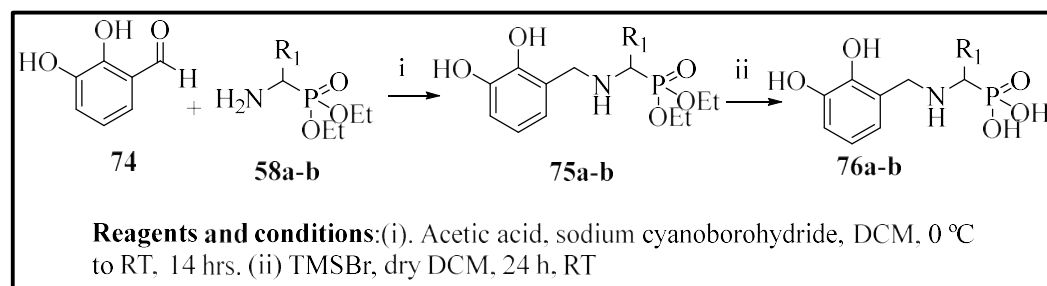


Scheme 2.6: General synthesis scheme for the derivatives of F8, 8-Hydroxyquinoline-7-carboxylic acid (8-HQ) MBG



Scheme 2.7: General synthesis scheme for the derivatives of F10, Chromone-3-carboxylic acid (CCA) MBG

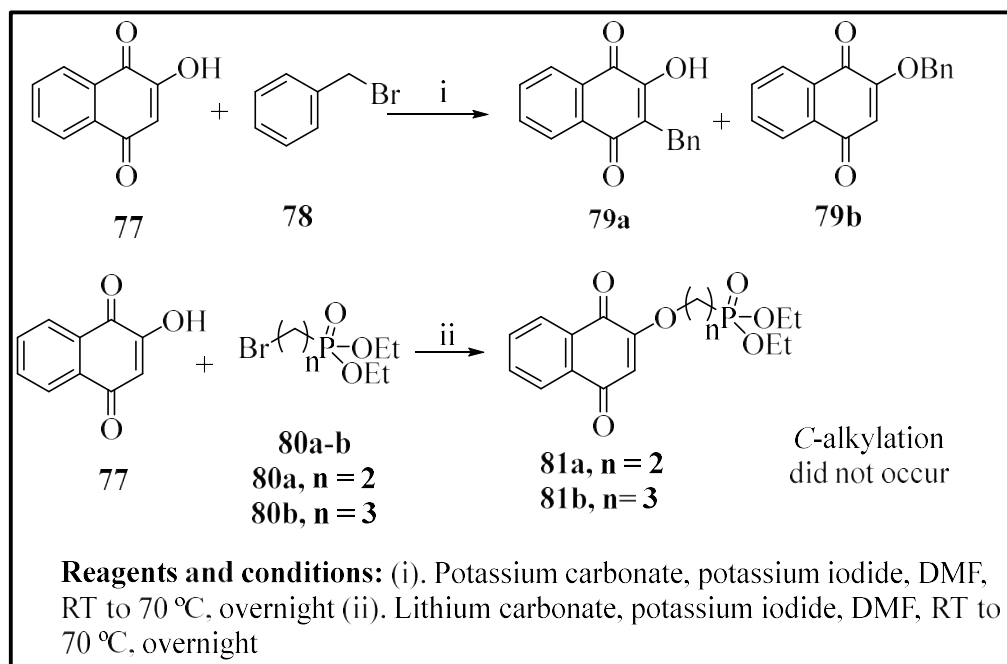
In docking studies, we observed that the designed molecules yielded only a few poses, presumably due to rigidity induced by the amide bond. Thus, to study the effect of flexibility, we also synthesized a few derivatives (**76a-b**, Table 2.5) by reductive amination of 2,3-Dihydroxy benzaldehyde (F9) with synthesized α -aminophosphonates, as per Scheme 2.8. These compounds do not contain an amide bond and have a flexible linkage between MBG and the phosphonate moiety. The docking studies also predicted these molecules to have optimum interactions with the metal ion and other active site residues. The ethyl ester derivatives of F9 (**75a-b**) were hydrolyzed by TMSBr-mediated hydrolysis to their respective phosphonic acids.



Scheme 2.8: General synthesis scheme for the derivatives of 2,3-Dihydroxy benzaldehyde (F9) MBG

2.4.4.3 Synthesis of 2-HNQ (F5) derivatives

We also attempted the *C*-alkylation of 2-HNQ (F5) (Scheme 2.9) with bromophosphonates under basic conditions to obtain the designed compounds. The F5 fragment, being enol-containing MBG, is expected to generate an enolate, which can be alkylated by bromophosphonate linkers. The resulting mixture of *C*- and *O*-alkylation products can be conveniently separated by chromatography.¹⁴⁸ Indeed, the expected results were obtained with the test reaction using benzyl bromide as an electrophile, where both *C*-alkylated (**79a**) and *O*-alkylated (**79b**) products were observed using potassium carbonate as a base. However, with bromophosphonates as an electrophile, *O*-alkylated products (**81a** and **81b**) were obtained exclusively under identical conditions. Changing the potassium carbonate base to lithium carbonate did not help to obtain the desired *C*-alkylated products. Most probably, under the given high-temperature conditions, the elimination reaction competes with the substitution leading to poor yields of only *O*-alkylated products **81a** and **81b**. Also, the *O*-alkylated product is expected to be thermodynamically more stable than the *C*-alkylated and is expected to be favoured under high temperatures. We did not attempt further optimization of the conditions.



Scheme 2.9: Attempts to obtain the *O*-alkylated and *C*-alkylated derivatives of 2-HNQ (F5).

Table 2.4: Structures of *O*-alkylated and *C*-alkylated derivatives of 2-HNQ.

Code	R	<i>C</i> -alkylation	<i>O</i> -alkylation	Product formed
79a		No	Yes	
79b		Yes	Yes	
81a		No	Yes	
81b		No	Yes	

2.4.5 *In-vitro* DXR enzyme inhibition and SAR analysis

A total of 34 molecules based on five (F2, F7, F8, F9, F10, and F12) fragments were synthesized (Schemes 2.3-2.8), out of which 21 displayed more than 50% inhibition (Table 2.5) when screened against *Ec*DXR at 50 μ M. For 8 molecules that exhibited more than 80% enzyme inhibition, IC_{50} values were determined.

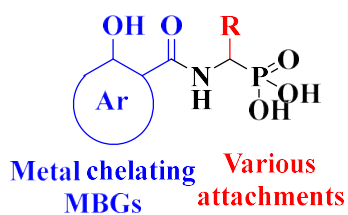
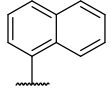
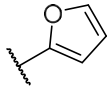
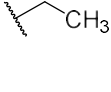
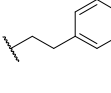
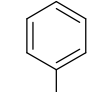
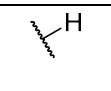
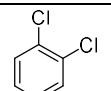
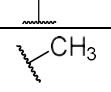
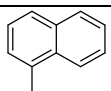
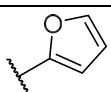
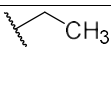
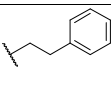
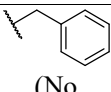
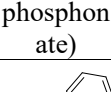


Table 2.5: IC₅₀ and enzyme inhibition data for non-hydroxamate synthesis derivatives.

SN	MBG fragment	R ₁ group	IC ₅₀ (μM)	% Inhibition at 50 μM	MMGBSA (kcal/mol)	Docking score (kcal/mol)	Distance from metal Å	
Scheme 2.3 compounds								
62a	Salicylic acid		33.2	94.6	-48.8	-6.45	2.14	2.24
62b	Salicylic acid		ND	ND	-43.7	-5.35	2.44	2.33
62c	Salicylic acid		ND	ND	-58.2	-6.45	2.24	2.30
62d	Salicylic acid		ND	ND	-52.9	-5.77	2.20	2.14
62e	Salicylic acid		32.9	81.3	-41.5	-6.76	2.19	2.37
62f	Salicylic acid		ND	ND	-59.9	-6.29	2.24	2.35
62g	Salicylic acid		ND	ND	-33.5	-6.00	2.47	2.44
62h	Salicylic acid		ND	ND	-38.2	-6.36	2.11	2.34
Scheme 2.4 compounds								
64a	2,3-dihydroxybenzoic acid		ND	66.5	-53.4	-6.43	2.20	2.47
64b	2,3-dihydroxybenzoic acid		ND	68.4	-29.3	-5.57	2.31	2.33
64c	2,3-dihydroxybenzoic acid		ND	ND	-59.0	-5.97	2.35	2.41
64d	2,3-dihydroxybenzoic acid		ND	60.13	-40.0	-5.59	2.35	2.17

64e	2,3-dihydroxybenzoic acid		ND	78.48	-51.1	-6.71	2.29	2.21
64f	2,3-dihydroxybenzoic acid		ND	ND	-48.7	-6.10	2.39	2.20
64g	2,3-dihydroxybenzoic acid		ND	ND	-33.8	-5.85	2.21	2.32
64h	2,3-dihydroxybenzoic acid		ND	ND	-49.5	-6.69	2.28	2.31
Scheme 2.5 compounds								
68a	1-hydroxy naphthoic acid		16.9	70.9	-72.4	-3.7	2.25	2.47
68b	1-hydroxy naphthoic acid		0.29	76.3	-38.3	-5.96	2.42	2.34
68c	1-hydroxy naphthoic acid		ND	ND	-68.5	-6.83	2.28	2.27
68d	1-hydroxy naphthoic acid		ND	84.2	-78.1	-6.46	2.25	2.26
68e	1-hydroxy naphthoic acid		4.44	73.7	-47.1	-6.62	2.26	2.25
68f	1-hydroxy naphthoic acid		ND	ND	-42.0	-6.31	2.18	2.28
68g	1-hydroxy naphthoic acid		ND	ND	-47.2	-5.91	2.19	2.26
68h	1-hydroxy naphthoic acid		ND	ND	-72.5	-6.5	2.29	2.44
67a	1-hydroxy naphthoic acid	 (No phosphonate)	ND	30.4	-44.0	-2.43	2.36	2.17
67b	1-hydroxy naphthoic acid	 (No phosphonate)	ND	4.69	-21.0	-4.56	2.26	2.24

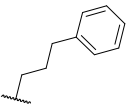
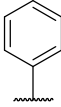
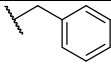
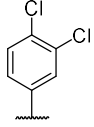
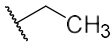
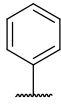
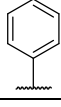
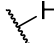
67c	1-hydroxy naphthoic acid		ND	31.3	-34.4	3.95	2.19	2.33
		(No phosphonate)						
Scheme 2.6 compounds								
71a	8-hydroxyquinoline-7-carboxylic acid		ND	58.5	-57.6	-5.99	2.30	2.24
70	8-hydroxyquinoline-7-carboxylic acid		ND	16.4	-64.7	-4.49	2.18	2.24
71c	8-hydroxyquinoline-7-carboxylic acid		ND	ND	ND	-6.45	2.36	2.24
71g	8-hydroxyquinoline-7-carboxylic acid		ND	ND	-58.0	-5.60	2.35	2.33
Scheme 2.7 compound								
73a	Chromone-3-carboxylic acid		6.09	79.8	-15.7	-6.72	2.33	2.17
Scheme 2.8 compounds								
76a	2,3-dihydroxybenzaldehyde		106	96.8	-38.7	-6.6	2.22	2.24
76b	2,3-dihydroxybenzaldehyde		10.8	74.1	-34.3	-5.80	2.21	2.31
ND: Not determined								

Table 2.6: Physicochemical Properties of the synthesized derivatives. Calculated using DataWarrior tool¹⁰⁹

Code	Molecular formula	MW	cLogP	HBA	HBD	LE	cLogS	TPSA
62a	C ₁₄ H ₁₄ NO ₅ P	307.2	-0.99	6	4	0.49	-1.5	116.7
62b	C ₈ H ₁₀ NO ₅ P	231.1	-2.86	6	4	NA	-1	116.7
62c	C ₁₄ H ₁₂ NO ₅ Cl ₂ P	376.1	0.22	6	4	NA	-3	116.7
62d	C ₉ H ₁₂ NO ₅ P	245.2	-2.63	6	4	NA	-0.6	116.7
62e	C ₁₈ H ₁₆ NO ₅ P	357.3	0.21	6	4	0.41	-3.1	116.7
62f	C ₁₂ H ₁₂ NO ₆ P	297.2	-1.8	7	4	NA	-1.2	129.8
62g	C ₁₀ H ₁₄ NO ₅ P	259.2	-2.18	6	4	NA	-0.9	116.7
62h	C ₁₆ H ₁₈ NO ₅ P	335.3	-0.73	6	4	NA	-2	116.2
64a	C ₁₄ H ₁₄ NO ₆ P	323.2	-1.33	7	5	NA	-1.2	136.9
64b	C ₈ H ₁₀ NO ₆ P	247.1	-3.21	7	5	NA	-0.7	136.9
64c	C ₁₄ H ₁₂ NO ₆ Cl ₂ P	392.1	-0.12	7	5	NA	-2.7	136.9
64d	C ₉ H ₁₂ NO ₆ P	261.2	-2.98	7	5	NA	-0.3	136.9
64e	C ₁₈ H ₁₆ NO ₆ P	373.3	-0.14	7	5	NA	-2.8	136.9
64f	C ₁₂ H ₁₂ NO ₇ P	313.2	-2.15	8	5	NA	-0.9	150.0
64g	C ₁₀ H ₁₄ NO ₆ P	275.2	-2.52	7	5	NA	-0.6	136.9
64h	C ₁₆ H ₁₈ NO ₆ P	351.3	-1.08	7	5	NA	-1.7	136.9
68a	C ₁₈ H ₁₆ NO ₅ P	357.3	0.21	6	4	0.43	-3.1	116.7
68b	C ₁₂ H ₁₂ NO ₅ P	281.2	-1.67	6	4	0.69	-2.6	116.7
68c	C ₁₈ H ₁₄ NO ₅ Cl ₂ P	426.2	1.418	6	4	NA	-4.6	116.7
68d	C ₁₃ H ₁₄ NO ₅ P	295.2	-1.44	6	4	1.26	-2.2	116.7
68e	C ₂₂ H ₁₈ NO ₅ P	407.4	1.4	6	4	0.4	-4.7	116.7
68f	C ₁₆ H ₁₄ NO ₆ P	347.3	-0.61	7	4	NA	-2.8	129.8
68g	C ₁₄ H ₁₆ NO ₅ P	309.3	-0.98	6	4	NA	-2.5	116.7
68h	C ₂₀ H ₂₀ NO ₅ P	385.4	0.46	6	4	NA	-3.6	116.7
71a	C ₁₇ H ₁₅ N ₂ O ₅ P	358.3	-0.67	7	4	NA	-2.2	129.6
71c	C ₁₇ H ₁₃ N ₂ O ₅ Cl ₂ P	427.2	0.54	7	4	NA	-3.7	129.6
71g	C ₁₃ H ₁₅ N ₂ O ₅ P	310.3	-1.86	7	4	NA	-1.6	129.6
76a	C ₁₄ H ₁₆ NO ₅ P	309.3	-2.81	6	5	0.46	-1.1	119.8
76b	C ₈ H ₁₂ NO ₅ P	233.2	-4.68	6	5	0.73	-0.6	119.8
73a	C ₁₇ H ₁₄ NO ₆ P	359.3	-1.21	7	3	0.45	-2.5	122.7

Among all the tested molecules, derivatives of NA (F7) (**68a-b**, **68d-e**, Table 2.5) demonstrated better inhibition compared to other synthesized molecules. Compound **68b** showed the highest potency ($IC_{50} = 0.29 \mu\text{M}$, which is closest to the potency of FSM ($IC_{50} = 0.13 \mu\text{M}$) tested under the same assay conditions (Fig. 2.24A). The compound **68b** closely resembles the binding mode of FSM (**1**), where the NA's *O,O* donor motif mimics the hydroxamate group of **1**. In addition, the NA (F7) ring of **68b** was found to occupy lipophilic pocket B, similar to its original fragment F7 (Fig. 2.24B), and expectedly displayed stronger predicted binding (-38.3 kcal/mol) than the NA (F7) (-26.0 kcal/mol).

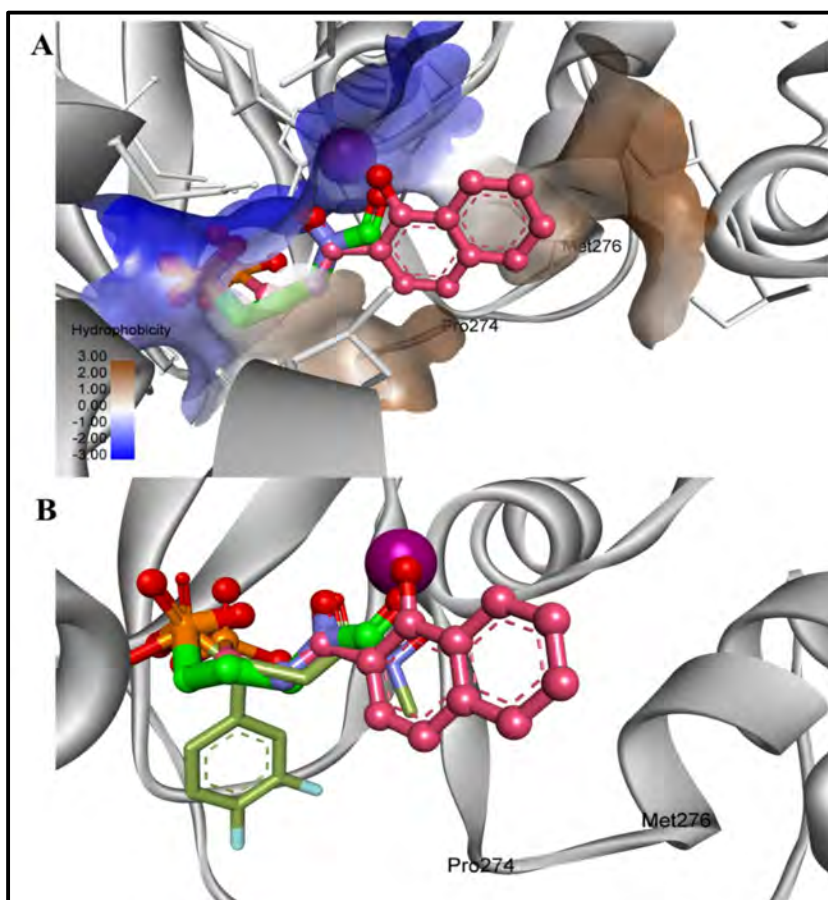


Fig. 2.24 Binding mode of **68b** and FSM (**1**). FSM is shown in the green-coloured ball and stick model, and **68b** is shown in the pink-coloured ball and stick model. Metal is shown in a magenta-coloured ball. (A) The surface view of DXR active site in complex with the calculated poses of **68b** and FSM. As hypothesized, NA (F7) occupies the hydrophobic pocket B lined by Pro274 and Met276 (orange coloured), whereas phosphonic acid of FSM and **68b** occupy the hydrophilic (blue coloured) region. (B) A closer view of **68b** overlaid with FSM and the co-crystallized ligand (PDB code 3R0I). The phosphonic groups and the linker atoms of **68b** and FSM are predicted to adapt a similar conformation. The surface was computed using Discovery Studio Visualizer (version 2017R2).¹⁰⁷

Compound **68a** ($R_1 = \text{Phenyl}$), a phenyl-substituted analogue of **68b**, showed ~57-fold lower potency ($IC_{50} = 16.9 \mu\text{M}$) (Fig. 2.25, green colour) despite having higher predicted binding energy (-72.4 kcal/mol) compared to **68b**. In docking studies, the NA ring of **68b** was found closer to the lipophilic pocket A, while the NA ring of **68a** was comparatively flipped in another direction (Fig. 2.25A). The phenyl substituent in **68a** might be affecting the optimum metal chelation. Indeed, the *O*-metal distances in **68a** and **68b** are considerably different (Table 2.5). However, when the naphthyl group was attached as a lipophilic substituent, a ~4-fold improved IC_{50} value ($4.44 \mu\text{M}$) was observed in compound **68e** ($R_1 = \text{naphthyl}$) compared to **68a**. The docking studies showed that naphthyl substituent alpha to the phosphonate of **68e** occupied pocket A. In contrast, the phenyl ring of **68a** failed to do so (Fig. 2.25, orange colour), which might be a plausible explanation for the betterer potency of **68e**. Also, unlike in **68a**, the orientation of the NA ring in both **68b** and **68e** allowed it to occupy pocket B (Fig. 2.25) in quite a similar way, which might be another explanation for their better potency than **68a**. Thus, the interaction of the NA ring with pocket B seems to improve overall binding as hypothesized. However, the results obtained from the binding energy analysis contradicted the findings, as compound **68e** exhibited a lower binding energy (-47.1 kcal/mol) compared to **68a** (-72.4 kcal/mol). Among the synthesized derivatives, compounds lacking the lipophilic group ($R_1 = \text{H}$), like **62b** (-43.7 kcal/mol), **64b** (-29.3 kcal/mol), and **68b** (-38.3 kcal/mol), displayed relatively weaker binding energies when compared to other synthesized molecules with the lipophilic R_1 group. The exceptions were compounds **62g** (-33.5 kcal/mol), **64g** (-33.8 kcal/mol), and **62h** (-38.2 kcal/mol).

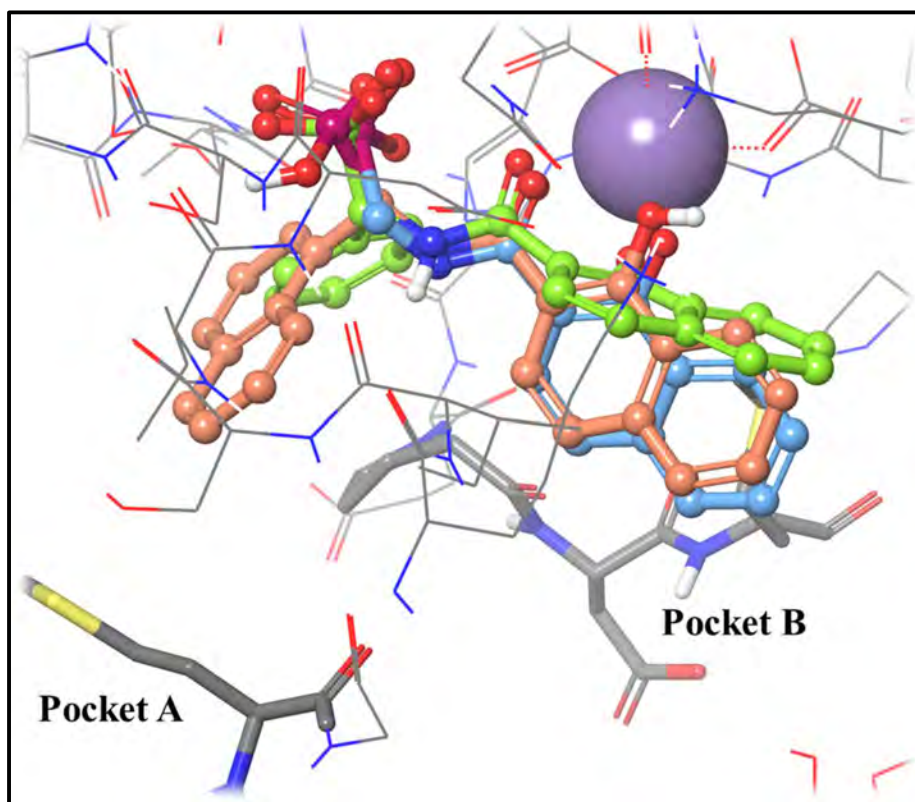


Fig. 2.25 Binding pose comparison of **68a** (green), **68b** (blue), and **68e** (orange). The naphthyl ring of **68a** shows considerable flipping compared to **68b** and **68e** resulting in poor metal chelation and lower potency than the other two analogs.

Compound **62e** ($R_1 = \text{naphthyl}$) containing SA (F12) as MBG with naphthyl substitution showed ~ 8 -fold less potency ($IC_{50} = 32.9 \mu\text{M}$) than **68e** ($IC_{50} = 4.44 \mu\text{M}$). In the top docking pose of **68e**, the distance between the metal and phenolic *O* and carboxylic *O* was found to be 2.25 Å and 2.26 Å. In contrast, in the case of **62e**, the distance between the metal and phenolic *O* and carboxylic *O* was found to be 2.19 Å and 2.37 Å, respectively. Also, the binding energy of **68e** (-47.1 kcal/mol) was found to be comparatively high than that of **62e** (-41.5 kcal/mol). The differences in distance between the metal and *O,O*, and the more lipophilic character of NA (F7) compared to SA (F12), led to better potency of **68e** than **62e**, despite having the same lipophilic attachment ($R_1 = \text{naphthyl}$).

Compound **68d** ($R_1 = \text{CH}_3$), a very close analogue of **68b** ($R_1 = \text{H}$), and compound **64d** ($R_1 = \text{CH}_3$) with DHBA as MBG displayed poor enzyme inhibition at 50 μM . Compound **64d** (-40.0 kcal/mol) possesses similar binding energy to the **68b** (-38.3 kcal/mol), whereas **68d** (-78.1 kcal/mol) possesses comparatively much better binding

energy of to **68b** (-38.3 kcal/mol). Still, these molecules showed less enzyme inhibition than **68b**, and the IC₅₀ value could not be determined for these derivatives.

The SA (F12) MBG derivative **62a** with the phenyl group as a lipophilic attachment, exhibited ~100-fold lower potency (IC₅₀ = 33.2 μM) than **68b** (IC₅₀ = 0.29 μM, Table 2.5). The docking pose of compound **62a** exhibits (Fig. 2.26, pink colour) a considerable difference compared to **68b** in terms of the orientation of the aromatic rings. The SA ring's plane is perpendicular to the plane of the NA ring of **68b**. The importance of NA as MBG is also evident while comparing **62a** (SA MBG) and **68a** (NA MBG), where both contain the same lipophilic attachment (R₁ = Phenyl). The NA derivative **68a** displays two-folds potency as compared to **62a** (**62a**, IC₅₀ = 33.17 μM vs **68a**, IC₅₀ 16.89 μM, respectively). Again, the inability of the SA ring to fully occupy pocket B might explain this difference in the potencies of the two analogs.

Compound **62a** (R₁ = phenyl) exhibited a potency (IC₅₀ = 33.2μM) that was almost identical to that of **62e** (R₁ = naphthyl) with a potency of (IC₅₀ = 32.9 μM). The similar docking scores (-6.45 and -6.76 kcal/mol, respectively) with slight variations in binding energies (-48.8 kcal/mol and -41.5 kcal/mol, respectively) supported their similar potencies. The docking poses of both **62a** (green) and **62e** (pink) revealed a perfect overlapping of the SA rings, justifying the equipotency of both compounds. However, the lipophilic attachments in these compounds were oriented in opposite directions. (Fig. 2.26). Despite **62e** displaying interaction with pocket A through its alpha-naphthyl substitution, it is equipotent to **62a**, suggesting the targeting of pocket A may not be very useful to improve the potency of this series.

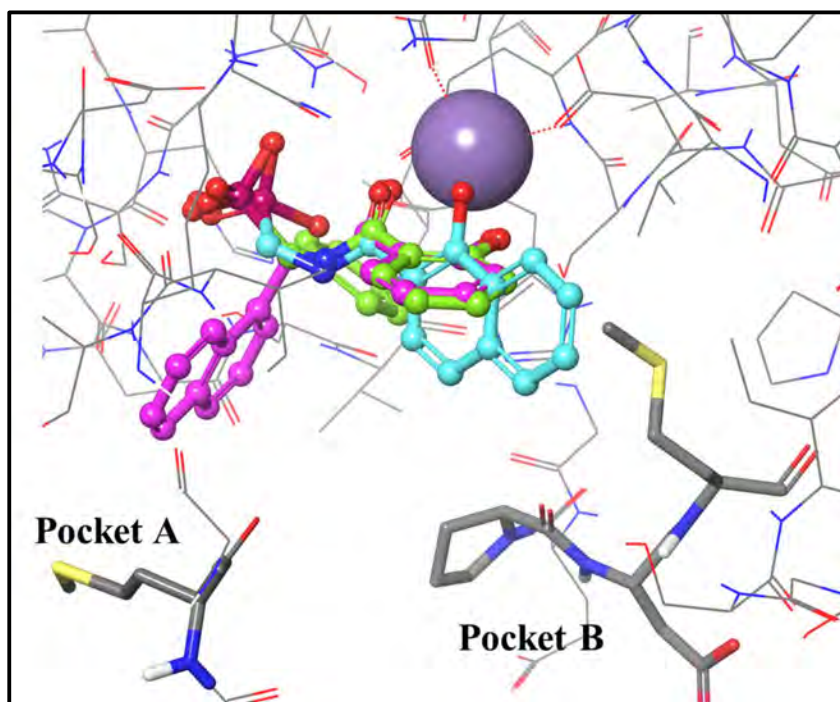


Fig. 2.26 The binding poses of **62e** (pink) and **62a** (green) shows flipped orientations compared to **68b** (cyan).

All compounds containing DHBA (F2) fragments were found to display poor enzyme inhibition (Table 2.4) at the highest concentration (50 μM); thus, IC_{50} was not determined for these compounds. The DHBA (F2) displayed two modes of metal chelation as per the modeling studies. In the first case, the amide and phenolic oxygen coordinate metal, while in the other case, metal is chelated by both phenolic OH functionalities. In the latter case, the MBG fragment occupied both pockets (Fig. 2.27A), unlike the former case, where **64e** occupied only pocket A (Fig. 2.27B). In **68e** ($\text{R}_1 = \text{naphthyl}$) with NA (F7) as MBG, pockets A and B were occupied (Fig. 2.25, orange colour), with considerable docking scores, and can be used for comparison.

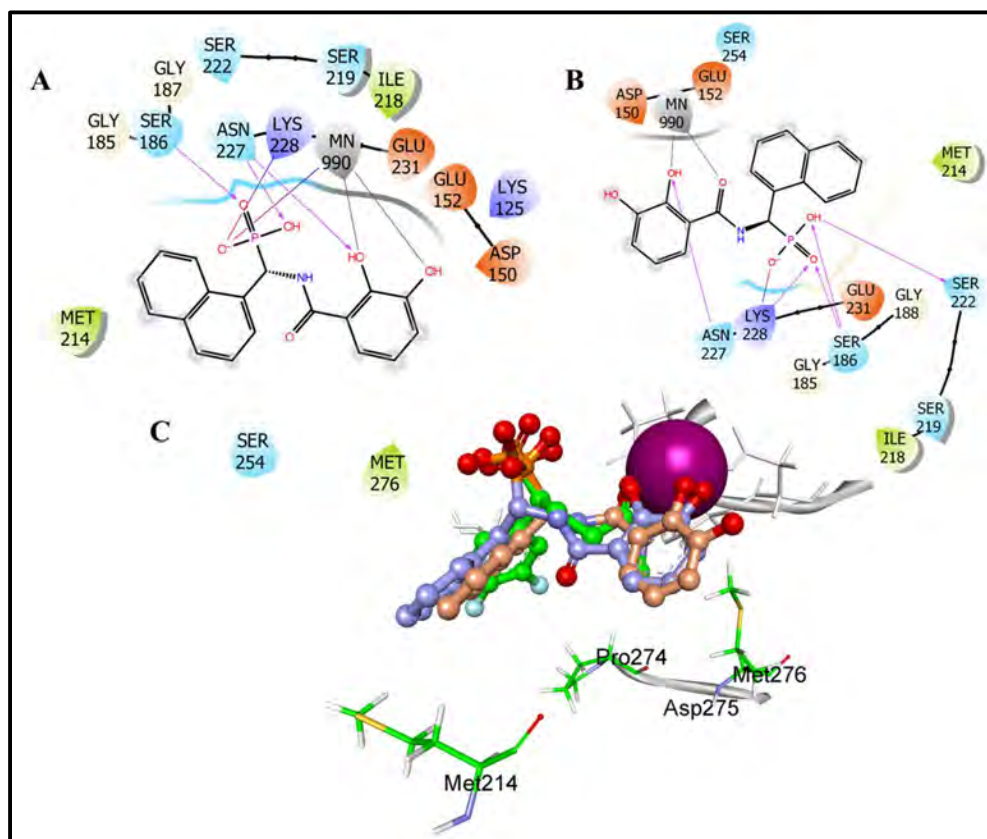


Fig. 2.27 Two different metal chelation modes observed in the DHBA (F2) series (A) Two phenolic OH showing metal chelation with Mn^{2+} (B) One phenolic OH and amide oxygen showing metal chelation with Mn^{2+} (C) 3D view of derivatives of DHBA (F2) MBG

We anticipated stronger inhibition from the DHBA (F2) series due to the presence of two phenolic oxygens and the precedence of catechol derivatives for DXR inhibition (cite our review). Surprisingly, none of the compounds in this series exhibited potent inhibition. In docking analysis, all derivatives of DHBA (F2) (**64a-b** and **64d**) exhibited metal chelation by two phenolic OH of DHBA, except **64e** (Fig. 2.28A). The latter displayed metal chelation with one phenolic OH and one amide oxygen. Despite having different metal binding modes, **64a** and **64e** displayed similar binding energies (-53.4 kcal/mol and -51.1 kcal/mol, respectively). This finding emphasizes the importance of metal chelation by amide oxygen, which holds more electronegativity resulting in strong metal chelation, thus leading to better DXR inhibition. For the other molecules, enzyme inhibition studies could not be performed due to the unavailability of the DXR enzyme kit. When comparing compounds **62e** (SA MBG), **64e** (DHBA MBG), and **68e**, all of which had a common alpha-lipophilic substitution ($R_1 =$ naphthyl) while differing

in MBG, **68e** (NA MBG) exhibited the highest potency ($IC_{50} = 4.44 \mu M$). Again, this may be due to the higher occupancy pocket B by the NA MBG of **68e**. The docking results revealed that the NA (**68e**) and DHBA (**64e**) rings exhibited overlapping in their orientations. At the same time, a slight flip was observed with the SA (**62e**) ring, in the computed poses of all three molecules displayed the remarkable overlapping of the alpha-naphthyl group. (Fig. 2.28B). However, similar docking scores of **64e** and **68e** (-6.71 kcal/mol and -6.62 kcal/mol resp.) and binding energies (-48.7 kcal/mol and -47.1 kcal/mol resp., Table 2.5) contradicted the experimental data. The ligand efficiency (LE) of these derivatives was calculated based on their IC_{50} values. The most potent compound, **68b**, showed the highest LE due to the lower IC_{50} and lower MW, as it lacks an alpha-substituent (R =H).

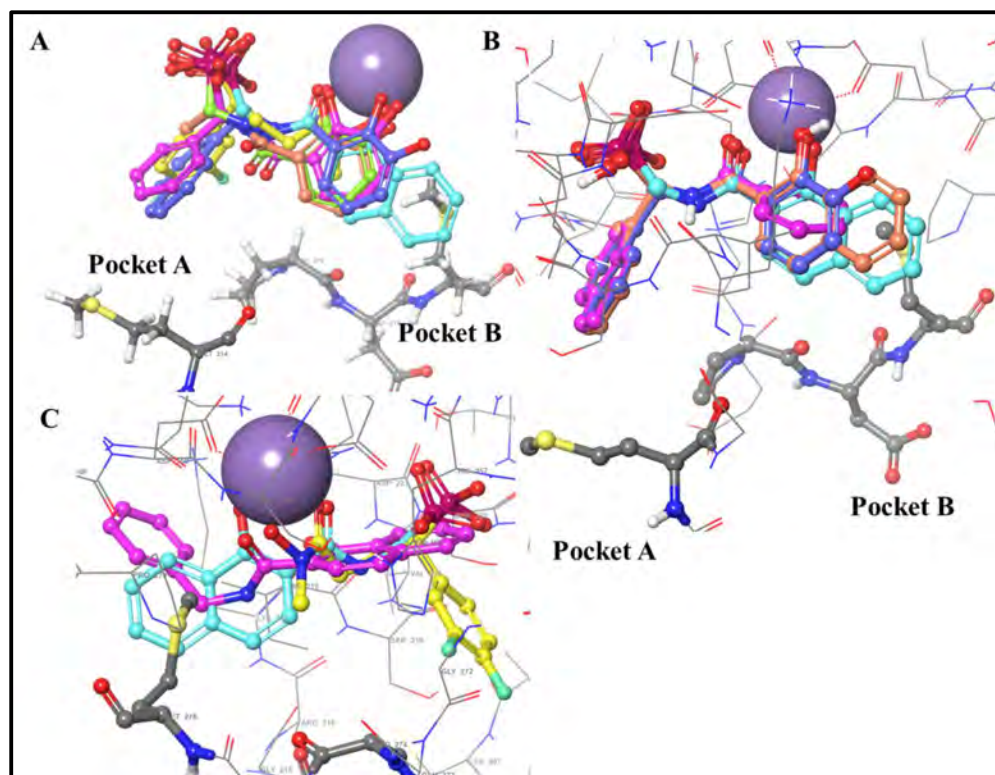


Fig. 2.28 Binding pose comparison for the fragment derivatives (A) Derivatives of DHBA, **64a** (pink), **64b** (green), **64d** (orange) showing metal chelation by two phenolic OH while **64e** (royal blue) showing metal chelation by one phenolic OH and amide O, similar to most potent compound **68b** (cyan). (B) Derivatives of SA, **62e** (pink), DHBA, **64e** (royal blue), and NA, **68e** (orange), showed overlapping of the naphthyl group near pocket A, while DHBA and NA of **64e** and **68e** showed overlapping near pocket B. However, the NA ring was found closer to pocket B. (C) Derivatives of NA, with phosphonic acid attachment, **68b** (cyan) and without phosphonic acid **67a** (pink). **68b** (cyan) showed a similar binding pose to the co-crystallized ligand (yellow), whereas the NA ring of **67a** was oriented towards the phosphonate binding motif.

Additionally, we synthesized analogs of **68a** by enhancing the lipophilic nature and flexibility of the R₁ group but without the inclusion of a phosphonate group (**67a-c**). The aim was to assess the significance of phosphonic acid functionality in this series. As anticipated, all such molecules demonstrated minimal or no enzyme inhibition. This observation highlights the critical role of the phosphonic acid group and is in agreement with the earlier studies with hydroxamate-based compounds. During the docking analysis, it was observed that compound **67a** exhibited a flipped pose, where the phenyl ring of benzylamine occupied pocket B instead of the NA ring (F7) (Fig. 2.28C, pink). Similarly, compound **70**, an analogue of **71a** but lacking the phosphonic acid group, also failed to inhibit the enzyme, similar to compound **67a-c**.

Compounds **64a** (DHBA as MBG) and **71a** (8-HQ as MBG) exhibited poor enzyme inhibition at a concentration of 50 μ M compared to their counterparts **62a** (SA as MBG) and **68a** (NA as MBG). Consequently, the determination of their IC₅₀ values was not feasible. Docking poses displayed the effective occupation of pocket B the bicyclic ring NA (F7), which is consistent with previous findings, led to derivatives of NA (F7) (**68a-b**, **68e**) displaying comparatively greater potency than other compounds in the series. Compound **73a**, a derivative of CCA (F10) containing phenyl substituent, exhibited ~5.5-fold and ~2.5-fold better potency (IC₅₀ value = 6.09 μ M) compared to its SA (**62a**) and NA (**68a**) counterparts. In docking analysis, **73a** exhibited a close resemblance to NA of **68b** and demonstrated better occupation of pocket B in comparison to compounds **62a** and **68a** (Fig. 2.29). It also showed the most favorable docking score (-6.72 kcal/mol) among all the synthesized compounds. However, it exhibited significantly weaker binding energy (-15.7 kcal/mol) compared to **68b**. However, being a chromone-based structure, CCA moiety is expected to display high UV absorbance and may interfere with the enzyme assay based on the absorbance signal. Indeed, strong inhibition (> 100%) with the CCA (F10) fragment was observed during the assay. Thus, we discontinued further studies of CCA derivatives despite promising results.

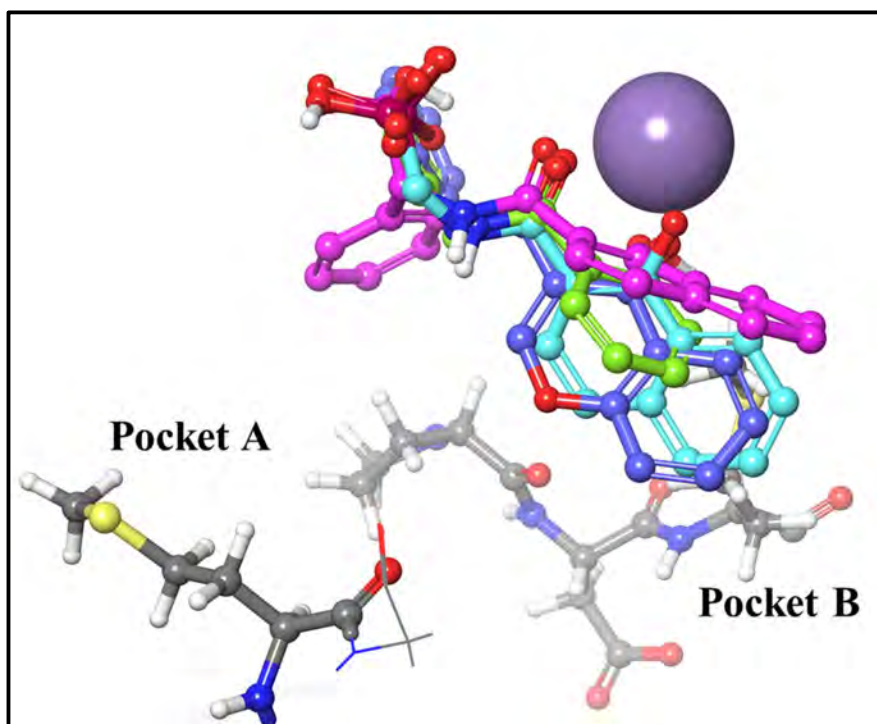


Fig. 2.29: Binding pose comparison for **73a** (blue), **68a** (pink), and **68b** (cyan). **73a** showed a close resemblance to the **68b** to occupy the pocket B compared to the NA ring of **68a**, which is comparatively away from the pocket B

Other synthesized compounds, such as **62c**, **64c**, **68c**, and **71c**, featuring 3,4-dichlorophenyl substitution, exhibited favorable docking scores and stronger binding energies. Earlier reports have shown that similar analogs of FSM with 3,4-dichlorophenyl substitution at the α -carbon displayed nanomolar activity in *PfDXR*. Thus, these compounds have the potential to serve as improved enzyme inhibitors. Within the SA (F12) series, compound **62f**, which includes a 2-furyl attachment, demonstrated a notably stronger binding energy (-59.9 kcal/mol) and a good docking score compared to its close analogs, **64f** (-48.7 kcal/mol) and **68f** (-42.0 kcal/mol).

The propyl-substituted derivatives (**62g**, **64g**, **68g**, and **71g**) displayed moderate to weak binding energies. Derivatives with smaller aromatic rings, such as SA (**62g**) and DHBA (**64g**), showed weaker binding energies, while derivatives NA (**68g**) and 8-HQ (**71g**) exhibited moderate binding energies. In the case of phenylpropyl substitution, slight improvements in binding energies were noted compared to propyl-substituted analogs. Compounds **62h** (-38.2 kcal/mol) and **64h** (-49.5 kcal/mol) showed moderate binding energy, while higher binding energy was noted for **68h** (-72.5 kcal/mol).

Similar binding energies were observed for the propyl and phenylpropyl substituents in the SA (F12) series and DHBA (F2) series (**62g** vs. **62h** and **64g** vs. **64h**). However, a significant difference in binding energies was noted in the case of NA (F7) series between **68g** (-47.2 kcal/mol) and **68h** (-72.5 kcal/mol). The docking scores of phenylpropyl-substituted derivatives were comparatively better than those of propyl-substituted derivatives of three fragments (F2, F7, and F12) due to more lipophilic character and flexibility of phenylpropyl substituent. The above findings suggest the need for optimization of the selection of rings with optimum bulk.

Compound **76a** ($IC_{50} = 106 \mu M$), a non-amide analog of **62a** and **68a**, showed ~3- folds and ~7-fold inferior enzyme inhibition compared to **62a** ($IC_{50} = 33.2 \mu M$) and **68a** ($IC_{50} = 16.9 \mu M$), respectively. Compound **76b** showed ~37-fold weak enzyme inhibition ($IC_{50} = 10.8 \mu M$) compared to **68b** ($IC_{50} = 0.29 \mu M$). Compounds **76a** and **76b** lack the amide bond and are expected to have a free conformational rotation than its amide analogs with restricted rotations, as shown in Fig. 2.30. The flexibility of these non-amide analogs is expected to have entropic cost compared to the amide analogs and a plausible reason for their lower potency. These molecules (**76a** and **76b**) are more hydrophilic than their amide analogs.

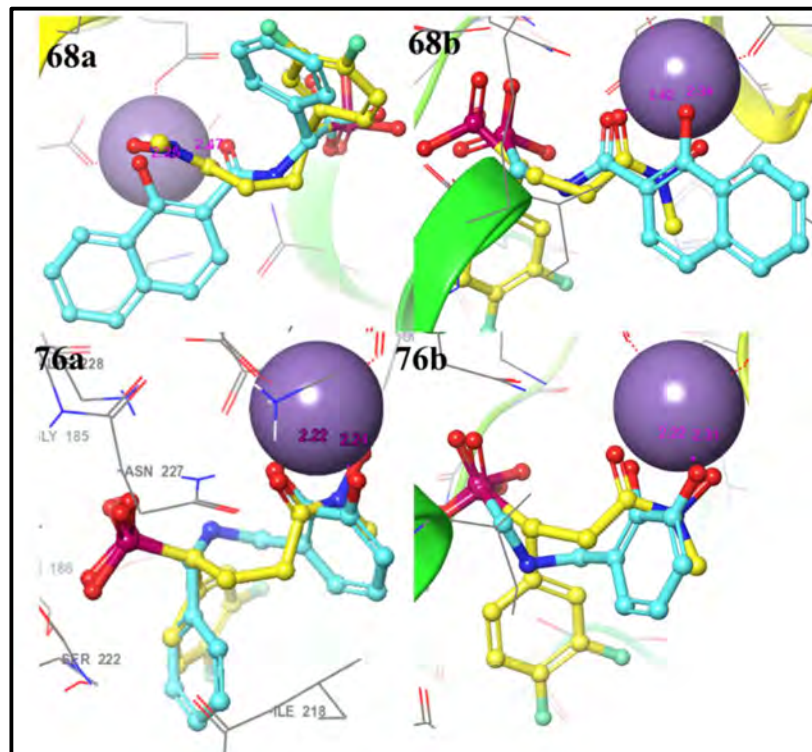


Fig. 2.30 Restricted rotation in **68a** vs. **68b** and **76a** vs. **76b**

A cell-based assay was conducted to evaluate the effects of the 17 compounds on gram-positive and gram-negative clinical pathogens, including *Acinetobacter baumannii*, *E. coli*, *Klebsiella pneumoniae*, *Pseudomonas aeruginosa*, *Salmonella typhimurium*, *Staphylococcus aureus*, and *Vibrio cholerae*. All the tested compounds were found to be inactive in all the tested pathogens except **76b**. Compound **76b** (F9 MBG) demonstrated successful cell growth inhibition in *A. baumannii*, *E. coli*, *S. typhimurium*, and *V. cholerae* at a higher concentration, 500 μM . Compound **71c** (HNQ MBG) showed some inhibition in cell growth with a MIC value $>500 \mu\text{M}$, which is very poor. The cell growth inhibition observed in compound **71c** could potentially involve other mechanisms. The observed inactivity of the other compounds may be due to their poor membrane permeability or metabolic instability and remains to be investigated.

These compounds were also tested against *M. tuberculosis*, initially at 200 μM (**62a**, **64a**, **68a**, **71a**, **73a** and **76a-b**) and 500 μM (**62c-e**, **64b**, **64d-e**, **68b**, **68d-e** and **71c**). At 200 μM concentration, the seven tested compounds (**62a**, **64a**, **68a**, **71a**, **73a**, and **76a-b**) were found inactive in *M. tuberculosis*. At 500 μM concentration, out of the ten tested compounds (**62c-e**, **64b**, **64d-e**, **68b**, **68d-e**, and **71c**), four compounds (**62c**, **62e**, **68b**, and **68e**) inhibited the cell growth in *Mtb*. MIC values for these compounds against *Mtb* were determined using Alamar Blue Assay (Fig. 2.31). Compound **68e**, based on NA MBG ($\text{IC}_{50} = 4.44 \mu\text{M}$ in against *EcDXR*), showed the most potent antimycobacterial activity (MIC = 125 μM), while three compounds **62c**, **62e**, and **68b** exhibited MIC higher than 125 μM . The most potent enzyme inhibitor, **68b** ($\text{IC}_{50} = 0.29 \mu\text{M}$ against *EcDXR*), showed a MIC value greater than 125 μM . This is not surprising as the DXR structure of both organisms has slightly different active sites and substantial differences in the cellular membrane composition. It should be noted that both analogs, although based on NA MBG, have different alpha-substituents (R = H in **68b** vs. R = naphthyl in **68e**) and hence, quite different lipophilicities affecting their cellular permeability. All these four compounds (**62c**, **62e**, **68b**, and **68e**) are more lipophilic compared to other analogs, in which **68e** has the highest lipophilicity.

Interestingly, like in enzymatic assays, the NA (F7) MBG derivatives also showed higher potency in the antibacterial assay.

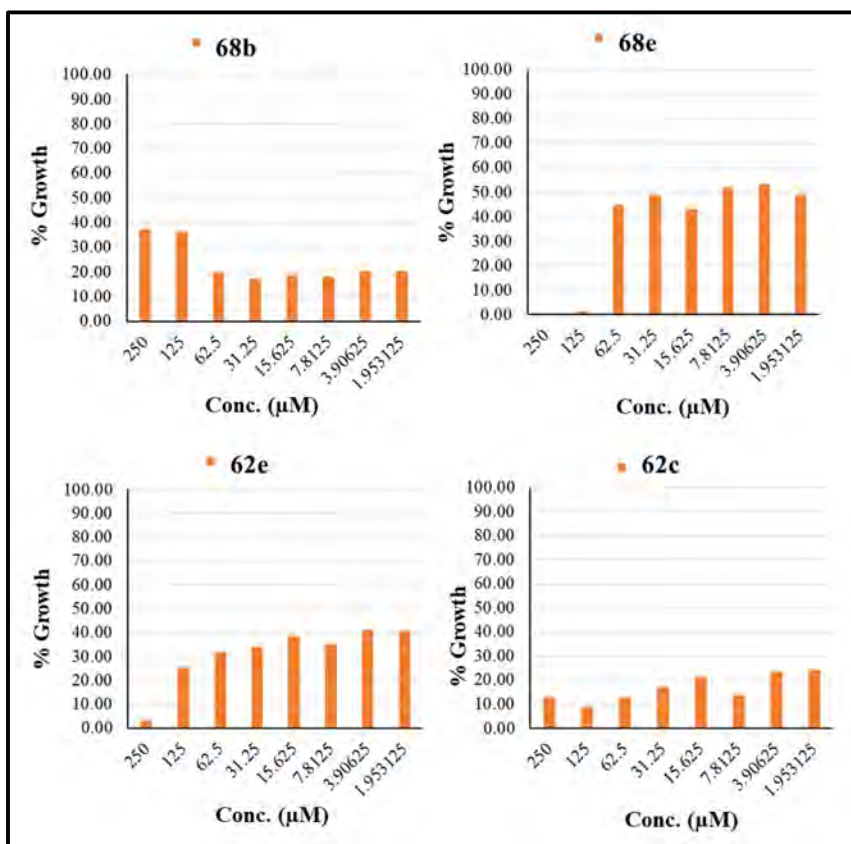


Fig. 2.31 Determination of MIC against Mtb (>80% inhibition by Alamar Blue Assay)

In conclusion, the findings highlight several important considerations for the design of compounds with inhibitory activity. Relying solely on docking scores or MMGBSA binding energies may not be a good approach for effective DXR inhibitor design. The effective metal chelation is more important, and the NA as MBG clearly shows an advantage over other fragments. The modeling study revealed the effective interaction of NA with pocket B compared to other monocyclic rings, such as SA. The enzyme inhibition data seems to be more sensitive to the occupancy of pocket B as opposed to pocket A. This is evident, in general, by the poor potency of compounds possessing a bulky lipophilic alpha-substituent that is expected to target pocket A. The notable differences in potencies between lipophilic substituted derivatives vs. H-containing analogs (**68a** vs. **68b** and **76a** vs. **76b**) demonstrate that the derivatives without lipophilic attachments showed better inhibition due to conformation flexibility. Moreover, the equipotency of **62a** and **62e** suggested that the targeting of pocket A may not be very useful in improving the potency of the SA series. Overall, this systematic screening of various MBG fragments and their derivatives presents NA as a promising

substitute to the hydroxamate group for designing novel DXR inhibitors. However, the cell-based antibacterial and antimycobacterial potencies of these compounds are not satisfactory and require further optimization.

2.5 METHODOLOGY

2.5.1 Fragment screen:

A donor motif is essentially required for metal-donor interaction for effective metal chelation at the active site of DXR. Thus, fragments possessing donor moieties were collected from the literature reported by Cohen, S., named this library MCL.¹²⁰ This library contains 96 small metal chelating fragments. A few other metal chelating fragments were obtained from literature considering the structural requirement. Different chemical properties of the fragments were calculated. Molecular docking studies for selected 103 fragments were performed using Glide within the DXR active site from different microorganisms (5JAZ from *P. falciparum* 3D7, 2Y1D from *M. tuberculosis* H37Rv and 3R0I and 3ANM from *E. coli* K-12). Schrodinger Suite was used for the docking using the following steps.

2.5.1.1 Protein Preparation:

The *Escherichia coli* K-12 DXR structure PDB code 3R0I was downloaded from the protein data bank and was prepared 'Protein Preparation Wizard.' All water molecules and ions (except active site Mn²⁺) were deleted; atom types and bond orders were corrected, and the hydrogen atoms were reassigned after deleting the original ones. The protonation states of acidic/basic amino acids were adjusted for pH 7.0. Restrained minimization of the protein was performed employing the OPLS-2005 force fields with the convergence criteria of RMSD of 0.3 Å for heavy atoms. A similar procedure was adapted for protein 2Y1D, 5JAZ, and 3ANM reported from other pathogens.

2.5.1.2 Ligand Preparation:

All molecules were prepared using the 'LigPrep wizard' of the Schrodinger Suite, which utilizes 'Epik 3.6' to generate energetically accessible protonation states and all possible stereoisomers. Metal binding states were generated using Epik.

2.5.1.3 Docking:

A receptor grid was generated using the centroid of the co-crystallized ligand with default settings for the size of the enclosing box. All other default settings were used. The ligands were docked into the prepared protein using the 'Glide' program implemented in Schrodinger Suite using the standard precision (SP) or extra precision (XP) mode. Amide bonds were penalized in their nonplanar conformation. Epik state

penalties were added to the final Glide score. A maximum of 15 poses per ligand were allowed, and post-docking minimization was allowed.

To these fragments, we performed an *in-vitro* DXR enzyme inhibition assay. For DXR enzyme inhibition screening, commercially available DXR enzyme inhibition assay kits were utilized. Assay was performed according to the given procedure provided with the assay kit. Initially, 13 fragments (F1-F13) were selected and purchased commercially. The samples were weighed, dilutions of 100 μ M were prepared, and *in-vitro* DXR enzyme inhibition for these fragments was performed. We used control samples as one without enzyme, without substrate, full reaction, and with strong inhibitor FSM at high concentration. Controls and prepared dilutions of the compounds were added in a 96-well plate according to the mentioned layout given with the assay procedure. All the concentrations of enzyme, substrate, and the final volume of the well were kept the same as described.

After pre-incubated with the DXR enzyme with shaking for 10 minutes, followed by the addition of (DXP substrate to initiate the reaction. The absorbance was recorded in kinetic mode at 340 nm. The DXR inhibitor screen monitors a decrease in β -NADPH levels which directly corresponds with the conversion of the DXP substrate to MEP product. Data were analyzed for each fragment's percentage inhibition at a given concentration. Docking analysis and *in-vitro* DXR enzyme inhibition assay was performed for the synthesized compounds at 100 μ M and 50 μ M.

2.5.2 Synthetic methodology

All starting materials were purchased from commercial sources and used as purchased without further purification unless stated otherwise or synthesized *via* literature procedures. Thin-layer chromatography was used to monitor the progress of the reactions and checked by pre-coated TLC plates (E. Merck Kieselgel 60 F254 with fluorescence indicator UV254). The components were visualized by irradiation with ultraviolet light (254 nm), using iodine vapors, or by staining in potassium permanganate solution followed by heating. Compounds were purified over a silica gel (230-400 mesh) column using distilled solvents. All final compounds were characterized by ^1H NMR spectroscopy using deuterated solvents, CDCl_3 or DMSO-d_6 . ^1H NMR spectra were recorded on a Bruker Advance 400 MHz spectrometer. Chemical shifts are given in parts per million (ppm) (δ relative to residual solvent peak for ^1H). High-resolution mass spectrometry (HRMS) analysis was performed using

Agilent Technologies 6545 Q-TOF Agilent system. If needed, the LC-MS of compounds was recorded using the Waters TQD system. Purity analysis for the synthesized compounds was performed using RP-HPLC (UFLC LC-1020C, Shimadzu Corporation, Japan).

Purity Analysis: The purity analysis of all the synthesized compounds was determined by analytical high-pressure liquid chromatography (HPLC) using a Shimadzu HPLC system (UFLC LC-1020C, Shimadzu Corporation, Japan) with a D2 detector. The chromatographic data acquisition and integration for the experiments were recorded using Lab Solution software. The chromatographic purification of the compound was performed at ambient temperature using stationary phase as Ascentis® C18 (50 mm × 4.6 mm, i.d. 3.0 μm) and mobile phase of acetonitrile and 10 mM phosphate buffer adjusted to pH 4.7 with orthophosphoric acid. Isocratic mode with a flow rate of 1 mL/min was used for the analysis. Purity of all final compounds determined by HPLC was 90% or higher.

2.5.2.1 General synthesis procedure of α -aminophosphonates (58a-i):

Synthetic route was followed according to Scheme 2.1. In a round bottom flask, ammonium acetate (1 eq.) and diethyl phosphite or triethyl phosphite (1 eq.) were dissolved in aromatic aldehyde (2 eq.) and stirred for 12 h at 60-80 °C. 20 mL of diethyl ether was added to the reaction mixture, cooled in an ice bath, and hydrochloric acid was gradually dropped into the reaction mixture to pH = 2. The resulting mixture was stirred for 2 h and extracted with water. The water layer was extracted with fresh diethyl ether, and then sodium hydroxide was added successively to the system to pH = 9. After stirring for additional 30 minutes, the mixture was extracted with ethyl acetate (x3). The combined ethyl acetate layer was dried over MgSO₄ and concentrated to dryness to afford desired α -aminophosphonates. Column chromatography was performed to obtain pure compounds.

Synthesis procedure for diethyl (amino(phenyl)methyl)phosphonate (58a):

Synthesized from benzaldehyde (212.2 mg, 2 mmol), ammonium acetate (77.09 mg, 1 mmol) and diethyl phosphite (129 μL, 1 mmol) according to general procedure 2.5.2.1. Yellowish semisolid, Yield: 57%. ¹H NMR (400 MHz, CDCl₃) δ 7.42 – 7.38 (dd, 2H), 7.30 (t, *J* = 7.6 Hz, 2H), 7.27 – 7.21 (td, 1H), 4.24 – 4.17 (d, 1H), 4.05 – 3.75 (m, 4H), 1.22 (t, *J* = 7.1 Hz, 3H), 1.12 (t, *J* = 7.1 Hz, 3H).

Synthesis procedure for diethyl (aminomethyl)phosphonate (58b): Synthesized from paraformaldehyde (600 mg, 20 mmol), ammonium acetate (770.9 mg, 10 mmol), and diethyl phosphite (1.29 mL, 10 mmol) according to general procedure 2.5.2.1. Yellowish oil, Yield: 66%. ¹H NMR (400 MHz, CDCl₃) δ 4.21 – 4.08 (m, 4H), 3.36 (d, *J* = 10.7 Hz, 2H), 1.31 (t, *J* = 7.1 Hz, 6H).

Synthesis procedure for diethyl (amino(3,4-dichlorophenyl)methyl)phosphonate (58c): Synthesized from 3,4-dichlorobenzaldehyde (350.02 mg, 2 mmol), ammonium acetate (77.09 mg, 1 mmol) and diethyl phosphite (129 μL, 10 mmol) according to general procedure 2.5.2.1. Yellowish semisolid, Yield: 73.4 %. ¹H NMR (400 MHz, CDCl₃) δ 7.58 (t, *J* = 2.2 Hz, 1H), 7.43 (t, *J* = 6.4 Hz, 1H), 7.32 (dt, *J* = 8.4, 2.1 Hz, 1H), 4.26 (d, *J* = 17.7 Hz, 1H), 4.13 – 3.97 (m, 4H), 1.27 (dd, *J* = 6.5, 2.5 Hz, 6H).

Synthesis procedure for diethyl (1-aminoethyl)phosphonate (58d): Synthesized from acetaldehyde (3.33 g, 83.32 mmol), ammonium acetate (3.21 g, 41.66 mmol), and triethyl phosphite (6.922 g, 41.66 mmol) according to general procedure 2.5.2.1. Dark brown liquid, Yield: 72%. ¹H NMR (400 MHz, CDCl₃) δ 5.26 (d, *J* = 49.3 Hz, 1H), 4.14 – 3.09 (m, 5H), 1.35 – 1.10 (m, 9H).

Synthesis procedure for diethyl (amino(naphthalen-1-yl)methyl)phosphonate (58e): Synthesized from Naphthaldehyde (4 g, 25.6 mmol), ammonium acetate (0.987g, 12.8 mmol) and triethyl phosphite (2.127 g, 12.8 mmol) according to general procedure 2.5.2.1. Creamy white powder, Yield: 88%. ¹H NMR (400 MHz, CDCl₃) δ 8.12 (d, *J* = 8.3 Hz, 1H), 7.89 (dd, *J* = 7.1, 3.3 Hz, 2H), 7.86 (d, *J* = 8.5 Hz, 1H), 7.61 – 7.48 (m, 3H), 4.15 – 3.74 (m, 4H), 3.65 (d, *J* = 20.3 Hz, 1H), 1.26 – 1.22 (m, 3H), 1.07 (t, *J* = 7.1 Hz, 3H).

Synthesis procedure for diethyl (amino(furan-2-yl)methyl)phosphonate (58f): Synthesized from 2-Furaldehyde (5.33 g, 55.52 mmol), ammonium acetate (2.14 g, 27.76 mmol) and diethyl phosphite (4.622 g, 27.76 mmol) according to general procedure 2.5.2.1. Dark brown semisolid, Yield: 74%. ¹H NMR (400 MHz, CDCl₃) δ 7.42 (dd, *J* = 1.7, 0.9 Hz, 1H), 6.51 (t, *J* = 2.9 Hz, 1H), 6.38 – 6.36 (m, 1H), 5.01 (d, *J* = 13.4 Hz, 1H), 4.22 – 4.09 (m, 4H), 1.31 (t, *J* = 7.0 Hz, 3H), 1.27 – 1.22 (m, 3H).

Synthesis procedure for diethyl (1-aminopropyl)phosphonate (58g): Synthesized from Propionaldehyde (2.62 g, 46 mmol), ammonium acetate (1.78 g, 23 mmol), and diethyl phosphite (3.822 g, 23mmol) according to general procedure 2.5.2.1. Yellowish

oil, Yield: 43%. ^1H NMR (400 MHz, CDCl_3) δ 4.23 – 4.05 (m, 4H), 4.02 – 3.83 (m, 2NH), 3.82 – 3.66 (m, 1H), 1.37 – 1.32 (m, 6H), 1.18 – 0.90 (m, 5H).

Synthesis procedure for diethyl (1-amino-3-phenylpropyl)phosphonate (58h):

Synthesized from 3-phenylpropanal (6 g, 44.72 mmol), ammonium acetate (1.725g, 22.36 mmol) and diethyl phosphite (3.715 g, 22.36 mmol) according to general procedure 2.5.2.1. Orange semisolid, Yield: 52%. ^1H NMR (400 MHz, CDCl_3) δ 7.32 (d, $J = 7.3$ Hz, 1H), 7.27 – 7.17 (m, 5H), 4.31 – 3.82 (m, 4H), 3.04 – 2.64 (m, 2H), 2.08 – 2.02 (m, 2H), 1.42 – 1.13 (m, 6H).

Synthesis procedure for diethyl ([1,1'-biphenyl]-4-yl(amino)methyl)phosphonate (58i):

Synthesized from biphenyl-4-carboxaldehyde (2 g, 11 mmol), ammonium acetate (424 mg, 5.5 mmol) and diethyl phosphite (0.914 g, 5.5 mmol) according to general procedure 2.5.2.1. Yellow solid, Yield: 42%. ^1H NMR (400 MHz, CDCl_3) δ 7.61 – 7.58 (dd, 4H), 7.53 (dd, $J = 8.3, 2.1$ Hz, 2H), 7.46 – 7.41 (ddd, 2H), 7.35 (ddd, $J = 9.4, 5.2, 3.5$ Hz, 1H), 4.32 (d, $J = 17.3$ Hz, 1H), 4.17 – 3.98 (m, 4H), 1.29 (t, $J = 7.1$ Hz, 3H), 1.23 – 1.19 (m, 3H).

Synthesis procedure for ([1,1'-biphenyl]-4-yl(amino)methyl)phosphonic acid (83):

The given ester derivative was hydrolyzed according to the general procedure. An ester, diethyl ([1,1'-biphenyl]-4-yl(amino)methyl)phosphonate (52 mg, 0.163 mmol) in DCM, was hydrolyzed using an excess of TMSBr (250 mg, 1.63 mmol) and purified according to the general procedure. Yield: 55%. ^1H NMR (400 MHz, DMSO) δ 7.68 (dt, $J = 8.6, 7.0$ Hz, 4H), 7.59 – 7.44 (m, 4H), 7.42 – 7.34 (m, 1H), 4.45 (d, $J = 17.2$ Hz, 1H).

2.5.2.2 General synthesis procedures for non-hydroxamate lipophilic DXR inhibitors using benzyl group protection and deprotection approach:

2.5.2.2.1 General synthesis procedure for benzyl group protection:

Synthetic route was followed according to Scheme 2.2. A mixture of carboxylic acid (60a, 60c-d) (1 eq.) and benzyl bromide (2 eq.) in DMF was suspended. Potassium carbonate (4 eq.) was added, and the reaction was stirred at room temperature overnight. After completion of the reaction, water was added to the reaction mixture, and the mixture was extracted with ethyl acetate (50 mL \times 3). The combined organic layers were dried over anhydrous sodium sulfate, filtered, and concentrated *in vacuo*. The crude product was purified by column chromatography.

Synthesis procedure for benzyl 2-(benzyloxy)benzoate (59a): Synthesized from salicylic acid (1g, 7.24 mmol), benzyl bromide (2.4g, 14.49 mmol) and potassium carbonate (4g, 28.98 mmol) in 10 mL DMF, according to general synthesis procedure 2.5.2.2.1. The crude product was purified by column chromatography (n-Hexane/ Ethyl acetate: 100:0 to 93:7) to yield the desired product (**59a**). Yield= 50%; ¹H NMR (400 MHz, CDCl₃) δ 7.91 – 7.84 (m, 1H), 7.50 – 7.29 (m, 11H), 7.02 (m, 2H), 5.45 – 5.32 (m, 2H), 5.29 – 5.13 (m, 2H).

Synthesis procedure of benzyl 1-(benzyloxy)-2-naphthoate (59b): Synthesized from 2-hydroxy naphthoic acid (752.78 g, 4 mmol), benzyl bromide (1.437 g, 8.4 mmol), and potassium carbonate (2.760 g, 63.72 mmol) in 10 mL DMF, according to general procedure 2.5.2.2.1. Yield = 95%. ¹H NMR (400 MHz, Chloroform-*d*) = δ 8.30 (dd, *J* = 8.7, 1.4 Hz, 1H), 7.98 (d, *J* = 8.7 Hz, 1H), 7.89 (dd, *J* = 8.0, 1.2 Hz, 1H), 7.68 (d, *J* = 8.7 Hz, 1H), 7.62 (ddd, *J* = 8.1, 6.8, 1.3 Hz, 1H), 7.58 – 7.48 (m, 5H), 7.41 (dddd, *J* = 13.3, 11.1, 8.2, 4.4 Hz, 6H), 5.45 (s, 2H), 5.19 (s, 2H).

Synthesis procedure of benzyl 8-(benzyloxy)quinoline-7-carboxylate (59c): Synthesized from 8-hydroxyquinoline-7-carboxylic acid (758 mg, 4 mmol, 1 eqv), benzyl bromide (1.437 mg, 8 mmol), and potassium carbonate (2.76 g, 20 mmol, 6 eqv) in 10 mL DMF, according to general procedure 2.5.2.2.1. Yield = 69%. ¹H NMR (400 MHz, Chloroform-*d*) δ 9.03 (dd, *J* = 4.1, 1.7 Hz, 1H), 8.19 (dd, *J* = 8.3, 1.8 Hz, 1H), 7.86 (d, *J* = 8.6 Hz, 1H), 7.67 – 7.62 (m, 2H), 7.60 (d, *J* = 8.6 Hz, 1H), 7.52 – 7.48 (m, 1H), 7.46 – 7.39 (m, 2H), 7.37 (d, *J* = 4.4 Hz, 6H), 7.33 – 7.26 (m, 1H), 5.56 (s, 2H), 4.69 (s, 3H).

2.5.2.2.2 General synthesis procedure for deprotection of benzyl carboxylate group

Synthetic route was followed according to Scheme 2.2 (step ii); a mixture of benzyl-protected carboxylates (**59a-c**) (1 eqv) was dissolved in a previously prepared 10 mL mixture of THF and water (1:1). The solution was treated with alcoholic 1N NaOH (3 eq.) and stirred at room temperature for 5 h. After completion of the reaction, the organic solvent was removed *in vacuo*, and the crude product was re-dissolved in water. The aqueous portion was washed with DCM and subsequently acidified to pH 4–5 with 1N HCl under an ice bath. The precipitates formed were collected by filtration and washed with DCM to yield the desired products (**59d-f**).

Synthesis procedure for 2-(benzyloxy)benzoic acid (59d): Synthesized from a mixture of benzyl 2-(benzyloxy)benzoate (0.5 g, 1.57 mmol) and 1N NaOH (0.8 mL) in 10 mL mixture of THF and water (1:1), according to general synthesis procedure Scheme 2.5.2.2.2. The precipitate was collected by filtration and washed with DCM to yield the desired product (59d). Yield = 75%; ¹H NMR (400 MHz, CDCl₃) δ 10.83 (s, 1H), 8.24 (dd, *J* = 7.8, 1.8 Hz, 1H), 7.62 – 7.55 (m, 1H), 7.50 – 7.41 (m, 6H), 7.23 – 7.12 (m, 2H), 5.28 (s, 2H).

Synthesis procedure of 1-(benzyloxy)-2-naphthoic acid (59e): Synthesized from benzyl 1-(benzyloxy)-2-naphthoate (368.432 mg, 1mmol) and 1N NaOH (0.8 mL) in 10 mL mixture of THF and water (1:1), according to general synthesis procedure Scheme 2.5.2.2.2. The precipitate was collected by filtration and washed with DCM to yield the desired product. Yield = 83%; ¹H NMR (400 MHz, Chloroform-*d*) δ 8.28 (dd, *J* = 7.8, 1.7 Hz, 1H), 8.13 (d, *J* = 8.7 Hz, 1H), 7.99 – 7.93 (m, 1H), 7.78 (d, *J* = 8.7 Hz, 1H), 7.72 – 7.62 (m, 2H), 7.60 – 7.54 (m, 2H), 7.51 – 7.44 (m, 2H), 7.29 (d, *J* = 0.9 Hz, 1H), 5.28 (s, 2H).

Synthesis procedure of 8-(benzyloxy)quinoline-7-carboxylic acid (59f): Synthesized from benzyl 8-(benzyloxy)quinoline-7-carboxylate (369.42 mg, 1mmol, 1eqv) and 1N NaOH (0.8 mL) in 10 mL mixture of THF and water (1:1), according to general synthesis procedure Scheme 2.5.2.2.2. The precipitate was collected by filtration and washed with DCM to yield the desired product. Yield: 72%; ¹H NMR (400 MHz, DMSO-*d*₆) δ 9.01 (dd, *J* = 4.1, 1.7 Hz, 1H), 8.42 (dd, *J* = 8.4, 1.7 Hz, 1H), 7.77 (d, *J* = 5.7 Hz, 2H), 7.64 (dd, *J* = 8.3, 4.2 Hz, 1H), 7.60 – 7.54 (m, 2H), 7.43 – 7.36 (m, 2H), 7.36 – 7.30 (m, 1H), 5.42 (s, 2H).

2.5.2.2.3 General synthesis procedure for amide coupling (59g-h):

Synthetic route was followed according to Scheme 2.2 (step iii), A mixture of an acid (1 eq.) and EDCI HCl (1.5 eq.) was added in dry DCM. A solution of DMAP (1eq.), triethylamine (1eq.) and diethyl (α -amino benzyl)phosphonate (**58a**) (1eq.) in dry DCM was added to reaction mixture after 15 minute at 0 °C. The reaction mixture was warmed to RT and stirred at room temperature under an inert N₂ atmosphere for 15 h. After completion of reaction, crude mixture was quenched with water and extract with DCM (25mL x 3. The combined layers were dried over anhydrous sodium sulphate and concentrated *in vacuo*. The residue was purified by column chromatography on silica gel yield the desired products (**59g-h**).

Synthesis procedure for diethyl ((2-(benzyloxy)benzamido)(phenyl)methyl)phosphonate (59g): Synthesized from mixture of 2-(benzyloxy)benzoic acid (0.2g, 0.87 mmol), EDCI HCl (0.251g, 1.31 mmol) in dry DCM (7mL). A solution of DMAP (0.107g, 0.87 mmol), triethylamine (0.88g, 0.87mmol) and diethyl (α -amino benzyl)phosphonate (0.244g, 0.87mmol) in DCM was added to the reaction mixture after 15 minute at 0 °C, and proceeded according to general synthesis procedure 2.5.2.2.3. The crude residue was purified by column chromatography on silica gel (DCM/Methanol= 92:8) to yield the desired product **59g**. Yield = 70%; ¹H NMR (400 MHz, CDCl₃) δ 8.85 (dd, J = 9.3, 3.2 Hz, 1H), 8.24 (dd, J = 8.0, 1.9 Hz, 1H), 7.55 (dd, J = 7.8, 1.5 Hz, 2H), 7.51 – 7.43 (m, 4H), 7.26 – 7.18 (m, 5H), 7.16 – 7.06 (m, 2H), 5.96 – 5.70 (m, 1H), 5.27 (dt, J = 26.1, 13.0 Hz, 2H), 4.07 – 3.91 (m, 3H), 3.85 – 3.76 (m, 1H), 1.21 (t, J = 7.1 Hz, 3H), 1.13 (t, J = 7.1 Hz, 3H).

Synthesis procedure for diethyl ((1-(benzyloxy)-2-naphthamido)(phenyl)methyl)phosphonate (59h): Synthesized from mixture of 1-(benzyloxy)-2-naphthoic acid (86 mg, 0.3 mmol) in dry DCM, diethyl (amino(phenyl)methyl)phosphonate (73 mg, 0.3 mmol), EDCI HCl (93.147 mg, 0.6 mmol), triethylamine (250 μ L, 1.8 mmol) and Hydroxybenztriazole (HOBT) (81 mg, 0.6 mmol) at 0 °C to RT overnight according to general procedure 2.5.2.2.3. ¹H NMR (400 MHz, CDCl₃) δ 8.88 (dd, J = 9.3, 3.7 Hz, 1H), 8.19 – 8.09 (m, 2H), 7.97 – 7.86 (m, 1H), 7.80 – 7.71 (m, 1H), 7.67 (td, J = 7.5, 1.5 Hz, 1H), 7.62 – 7.41 (m, 10H), 7.26 (d, J = 7.2 Hz, 2H), 5.88 (dd, J = 20.4, 9.4 Hz, 1H), 5.27 (t, J = 5.9 Hz, 2H), 4.99 (t, J = 10.1 Hz, 1H), 4.08 – 3.80 (m, 4H), 1.22 – 1.12 (m, 6H).

2.5.2.2.4 Synthesis procedure for phenolic benzyl deprotection (59i):

Synthesis procedure for diethyl ((2-hydroxybenzamido)(phenyl)methyl)phosphonate (59i): Synthetic route was followed according to Scheme 2.2, A mixture of diethyl ((2-(benzyloxy)benzamido)(phenyl)methyl)phosphonate (20 mg, 0.08 mmol, 1 eq.) and Pd/C 10% (3 mg, 0.028 mmol, 0.35 eq.) in MeOH:THF (2:5) stirred under H₂ for 12 h. The catalyst was filtered off using celite filtration and the solvent was removed *in vacuo*. The residue was purified by column chromatography on silica gel (15:85 EA/Hexane) to yield the desired product **59i**. ¹H NMR (400 MHz, CDCl₃) δ 8.85 (dd, J = 9.3, 3.2 Hz, 1H), 8.24 (dd, J = 8.0, 1.9 Hz, 1H), 7.55 (dd, J = 7.8, 1.5 Hz, 2H), 7.51

– 7.43 (m, 4H), 7.26 – 7.18 (m, 5H), 7.16 – 7.06 (m, 2H), 5.96 – 5.70 (m, 1H), 5.27 (dt, $J = 26.1, 13.0$ Hz, 2H), 4.07 – 3.91 (m, 3H), 3.85 – 3.76 (m, 1H), 1.21 (t, $J = 7.1$ Hz, 3H), 1.13 (t, $J = 7.1$ Hz, 3H).

2.5.2.3 General synthesis procedure for non-hydroxamate lipophilic DXR inhibitors

Synthetic route was followed according to Scheme 2.3, 2.4, 2.5, 2.6, and 2.7. To a solution of an acid (1 eq.) in dichloromethane, EDCI.HCl (1.5 eqv) and HOBT (0.5 eqv) were added under a nitrogen environment at 0 °C. The reaction mixture was charged with dimethylaminopyridine (DMAP) (1 eq.), followed by the addition of diethyl α -aminophosphonate (1 eq.) in a round bottom flask under nitrogen environment at 0 °C. The reaction mixture was stirred for an hour at 0 °C, then warmed to RT, and stirred at room temperature under an inert N₂ atmosphere for 15 hours. After completion of the reaction, the crude mixture was quenched with sodium bicarbonate solution and extracted with DCM (25mL x 3). Collected reaction mixture was dried over anhydrous sodium sulfate and concentrated *in a vacuo*. The crude residue was purified by column chromatography on silica gel to obtain the desired ester derivatives of non-hydroxamate compounds.

Synthesis procedure for diethyl ((2-hydroxybenzamido)(phenyl)methyl)phosphonate (61a): Synthesized by coupling Salicylic acid (26 mg, 0.185 mmol) and diethyl (amino(phenyl)methyl)phosphonate (45 mg, 0.185 mmol). EDCI.HCl (44 mg, 0.28 mmol) and HOBT (13 mg, 0.0925 mmol) were added under a nitrogen environment at 0 °C. The reaction mixture was charged with DMAP (23 mg, 0.185 mmol), according to general procedure 2.5.2.2. Yield: 47.6%. ¹H NMR (400 MHz, CDCl₃) δ 8.24 (dd, $J = 9.1, 4.0$ Hz, 1H), 7.79 (dd, $J = 8.0, 1.4$ Hz, 1H), 7.60 – 7.55 (m, 2H), 7.39 (tdd, $J = 8.2, 7.7, 1.3$ Hz, 3H), 7.05 – 6.97 (m, 1H), 6.91 – 6.86 (m, 1H), 5.86 – 5.75 (m, 1H), 4.28 – 3.69 (m, 4H), 1.34 (t, $J = 6.7$ Hz, 3H), 1.14 (t, $J = 7.1$ Hz, 3H).

Synthesis procedure for diethyl ((2-hydroxybenzamido)methyl)phosphonate (61b): Synthesized by coupling Salicylic acid (138.21, 1 mmol) and diethyl (aminomethyl)phosphonate (243.24 mg, 1 mmol). EDCI.HCl (233 mg, 1.5 mmol) and HOBT (68 mg, 0.5 mmol) were added under a nitrogen environment at 0 °C. The reaction mixture was charged with DMAP (122.17, 1 mmol), according to general

procedure 2.5.2.2. After performing the work-up, the crude residue was purified using column chromatography (2-20% ethyl acetate/hexane). Yield: 49%; ¹H NMR (400 MHz, CDCl₃) δ 8.11 (d, *J* = 8.4 Hz, 1H), 7.90 (d, *J* = 8.3 Hz, 1H), 7.64 – 7.59 (m, 1H), 7.50 (dd, *J* = 11.3, 4.0 Hz, 1H), 6.39 (s, 1H), 4.24 – 3.75 (m, 4H), 3.44 – 3.21 (m, 2H), 1.35 (t, *J* = 7.1 Hz, 3H), 1.28 (t, *J* = 9.3 Hz, 3H).

Synthesis procedure for diethyl ((3,4-dichlorophenyl)(2-hydroxybenzamido)methyl)phosphonate (61c): Synthesized by coupling Salicylic acid (138.21 mg, 1 mmol) and diethyl (amino(3,4-dichlorophenyl)methyl)phosphonate (312.13 mg, 1 mmol), EDCl.HCl (233 mg, 1.5 mmol) and HOBt (68 mg, 0.5 mmol) were added under a nitrogen environment at 0 °C. The reaction mixture was charged with DMAP (122.17 mg, 1 mmol), according to general procedure 2.5.2.2. After performing the work-up, the crude residue was purified using column chromatography (2-20% ethyl acetate/hexane). Yield: 37%; ¹H NMR (400 MHz, CDCl₃) δ 10.29 (s, 1O-H), 8.03 (dd, *J* = 8.0, 1.5 Hz, 1H), 7.66 (t, *J* = 1.9 Hz, 1H), 7.57 – 7.46 (m, 2H), 7.45 – 7.40 (m, 1H), 7.04 – 6.94 (m, 2H), 6.30 (d, *J* = 13.8 Hz, 1H), 4.26 – 4.01 (m, 4H), 1.29 (dd, *J* = 15.0, 7.2 Hz, 6H).

Synthesis procedure for diethyl (1-(2-hydroxybenzamido)ethyl)phosphonate (61d): Synthesized by coupling Salicylic acid (207 mg, 1.5 mmol) and diethyl (1-aminoethyl)phosphonate (272 mg, 1.5 mmol), EDCl.HCl (350 mg, 2.25 mmol) and HOBt (101.34, 0.75 mmol) were added under a nitrogen environment at 0 °C. The reaction mixture was charged with DMAP (183.25, 1.5 mmol), according to general procedure 2.5.2.2. After performing the work-up, the crude residue was purified using column chromatography (2-20% ethyl acetate/hexane). Yield: 46%; ¹H NMR (400 MHz, CDCl₃) δ 10.49 (s, 1O-H), 7.85 (d, *J* = 7.9 Hz, 1H), 7.45 (t, *J* = 7.7 Hz, 1H), 6.96 (d, *J* = 8.3 Hz, 1H), 6.87 (t, *J* = 7.5 Hz, 1H), 5.51 (p, *J* = 7.2 Hz, 1H), 4.25 – 4.12 (m, 4H), 1.58 (dd, *J* = 16.6, 7.0 Hz, 3H), 1.31 (t, *J* = 7.0 Hz, 6H).

Synthesis procedure for diethyl ((2-hydroxybenzamido)(naphthalen-1-yl)methyl)phosphonate: Synthesized by coupling Salicylic acid (207 mg, 1.5 mmol) and diethyl (amino(naphthalen-1-yl)methyl)phosphonate (440 mg, 1 mmol). EDCl.HCl (350 mg, 2.25 mmol) and HOBt (101.34 mg, 0.75 mmol) were added under a nitrogen environment at 0 °C. The reaction mixture was charged with DMAP (184 mg, 1.5 mmol), according to general procedure 2.5.2.2. After performing the work-up, the crude residue was purified using column chromatography (2-30% ethyl acetate/hexane).

Yield: 61%. ¹H NMR (400 MHz, CDCl₃) δ 8.37 (d, *J* = 8.6 Hz, 1H), 8.17 (dd, *J* = 8.4, 1.6 Hz, 1H), 7.93 (dd, *J* = 7.2, 2.9 Hz, 1H), 7.89 (d, *J* = 8.2 Hz, 2H), 7.68 – 7.61 (m, 1H), 7.57 – 7.52 (m, 2H), 7.52 – 7.48 (m, 1H), 7.23 (d, *J* = 13.9 Hz, 1H), 6.98 (dd, *J* = 11.5, 4.4 Hz, 2H), 4.24 – 3.73 (m, 4H), 1.28 (dd, *J* = 8.8, 5.4 Hz, 3H), 1.06 (t, *J* = 7.1 Hz, 3H).

Synthesis procedure for diethyl (furan-2-yl(2-hydroxybenzamido)methyl)phosphonate (61f): Synthesized by coupling Salicylic acid (138.12 mg, 1 mmol) and diethyl (amino(furan-2-yl)methyl)phosphonate (233 mg, 1 mmol). EDCI.HCl (233 mg, 1.5 mmol) and HOBt (68 mg, 0.5 mmol) were added under a nitrogen environment at 0 °C. The reaction mixture was charged with DMAP (122.17 mg, 1 mmol), according to general procedure 2.5.2.2. After performing the work-up, the crude residue was purified using column chromatography (2-20% ethyl acetate/hexane). Yield: 54%. ¹H NMR (400 MHz, CDCl₃) δ 10.41 (s, 1H), 7.95 (dd, *J* = 8.0, 1.6 Hz, 1H), 7.54 – 7.46 (m, 2H), 7.00 (d, *J* = 8.4 Hz, 1H), 6.92 (t, *J* = 7.6 Hz, 1H), 6.76 – 6.72 (m, 1H), 6.53 (d, *J* = 15.2 Hz, 1H), 6.46 – 6.42 (m, 1H), 4.32 – 4.08 (m, 4H), 1.34 (t, *J* = 7.1 Hz, 3H), 1.29 (t, *J* = 7.1 Hz, 3H).

Synthesis procedure for diethyl (1-(2-hydroxybenzamido)propyl)phosphonate (61g): Synthesized by coupling Salicylic acid (138.12 mg, 1 mmol) and (1-aminopropyl)phosphonate (195.1 mg, 1 mmol). EDCI.HCl (233 mg, 1.5 mmol) and HOBt (68 mg, 0.5 mmol) were added under a nitrogen environment at 0 °C. The reaction mixture was charged with DMAP (122.17 mg, 1 mmol), according to the general procedure 2.5.2.2. After performing the work-up, the crude residue was purified using column chromatography (2-20% ethyl acetate/hexane). Yield: 34%. ¹H NMR (400 MHz, CDCl₃) δ 10.57 (s, 1H), 7.92 (dd, *J* = 8.0, 1.7 Hz, 1H), 7.54 – 7.47 (m, 1H), 7.04 – 6.99 (m, 1H), 6.96 – 6.89 (m, 1H), 5.47 (ddd, *J* = 9.6, 8.3, 4.4 Hz, 1H), 4.24 – 4.14 (m, 4H), 2.16 – 1.97 (m, 2H), 1.33 (t, *J* = 7.1 Hz, 6H), 1.06 (t, *J* = 7.4 Hz, 3H).

Synthesis procedure for diethyl (1-(2-hydroxybenzamido)-3-phenylpropyl)phosphonate (61h): Synthesized by coupling Salicylic acid (138.121 eqv) and (1-amino-3-phenylpropyl)phosphonate (271.3 mg, 1 mmol). EDCI.HCl (233 mg, 1.5 mmol) and HOBt (68 mg, 0.5 mmol) were added under a nitrogen environment at 0 °C. The reaction mixture was charged with DMAP (122.17 mg, 1 mmol), according to general procedure 2.5.2.2. After performing the work-up, the crude residue was purified by using column chromatography (2-20% ethyl acetate/hexane). Yield: 44%.

¹H NMR (400 MHz, CDCl₃) δ 10.56 (s, 1H), 7.90 (dt, *J* = 7.8, 2.4 Hz, 1H), 7.53 (ddd, *J* = 8.8, 7.3, 1.7 Hz, 1H), 7.31 – 7.26 (m, 1H), 7.19 (dd, *J* = 7.2, 5.2 Hz, 3H), 7.04 (dd, *J* = 8.4, 0.9 Hz, 1H), 6.96 – 6.91 (m, 1H), 5.62 – 5.50 (m, 1H), 4.24 – 4.13 (m, 4H), 2.91 – 2.66 (m, 2H), 2.49 – 2.28 (m, 2H), 1.32 (t, *J* = 7.1 Hz, 6H).

Synthesis procedure for diethyl ((2,3-dihydroxybenzamido)(phenyl)methyl)phosphonate (63a): Synthesized by coupling 2,3-dihydroxybenzoic acid (204.2 mg, 1 mmol) and diethyl (amino(phenyl)methyl)phosphonate (243.24 mg, 1 mmol). EDCI.HCl (233 mg, 1.5 mmol) and HOBt (68 mg, 0.5 mmol) were added under a nitrogen environment at 0 °C. The reaction mixture was charged with DMAP (122.17 mg, 1 mmol), according to general procedure 2.5.2.2. After performing the work-up, the crude residue was purified using column chromatography (2-20% ethyl acetate/hexane). Yield: 27%. ¹H NMR (400 MHz, CDCl₃) δ 12.28 (s, 1H), 7.75 (dd, *J* = 8.8, 5.2 Hz, 1H), 7.54 (dt, *J* = 10.7, 5.5 Hz, 2H), 7.43 – 7.32 (m, 3H), 7.21 (dd, *J* = 8.2, 1.3 Hz, 1H), 7.07 (dd, *J* = 7.9, 1.3 Hz, 1H), 6.78 (t, *J* = 8.0 Hz, 1H), 5.76 – 5.62 (m, 1H), 4.27 – 3.68 (m, 5H), 1.37 – 1.31 (m, 3H), 1.18 – 1.09 (m, 3H).

Synthesis procedure for diethyl ((2,3-dihydroxybenzamido)methyl)phosphonate (63b): Synthesized by coupling 2,3-dihydroxybenzoic acid (204.2 mg, 1 mmol) and diethyl (aminomethyl)phosphonate (167 mg, 1 mmol). EDCI.HCl (233 mg, 1.5 mmol) and HOBt (68 mg, 0.5 mmol) were added under a nitrogen environment at 0 °C. The reaction mixture was charged with DMAP (122 mg, 1 mmol), according to general procedure 2.5.2.2. After performing the work-up, the crude residue was purified using column chromatography (2-20% ethyl acetate/hexane). Yield: 27%. ¹H NMR (400 MHz, CDCl₃) δ 10.54 (s, 1O-H), 7.43 (dd, *J* = 8.1, 1.5 Hz, 1H), 7.16 (dd, *J* = 7.9, 1.5 Hz, 1H), 6.85 (t, *J* = 8.0 Hz, 1H), 4.67 (d, *J* = 8.7 Hz, 2H), 4.32 – 4.21 (m, 4H), 1.41 – 1.36 (m, 6H).

Synthesis procedure for diethyl ((3,4-dichlorophenyl)(2,3-dihydroxybenzamido)methyl)phosphonate (63c): Synthesized by coupling 2,3-dihydroxybenzoic acid (204.2 mg, 1 mmol) and diethyl (amino(3,4-dichlorophenyl)methyl)phosphonate (312 mg, 1 mmol). EDCI.HCl (233 mg, 1.5 mmol) and HOBt (68 mg, 0.5 mmol) were added under a nitrogen environment at 0 °C. The reaction mixture was charged with DMAP (122 mg 1 mmol), according to the general procedure 2.5.2.2. After performing the work-up, the crude residue was purified using

column chromatography (2-20% ethyl acetate/hexane). Yield: 26%. ¹H NMR (400 MHz, CDCl₃) δ 10.37 (s, 1H), 7.65 (t, *J* = 2.0 Hz, 1H), 7.56 (dd, *J* = 8.1, 1.5 Hz, 1H), 7.49 (d, *J* = 8.4 Hz, 1H), 7.42 (dt, *J* = 8.4, 1.9 Hz, 1H), 7.18 (dd, *J* = 7.9, 1.5 Hz, 1H), 6.89 (t, *J* = 8.0 Hz, 1H), 6.29 (d, *J* = 13.8 Hz, 1H), 4.25 – 4.05 (m, 4H), 1.31 – 1.27 (m, 6H).

Synthesis procedure for diethyl (1-(2,3-dihydroxybenzamido)ethyl)phosphonate (63d): Synthesized by coupling 2,3-dihydroxybenzoic acid (204.2 mg, 1 mmol) and diethyl (1-aminoethyl)phosphonate (181 mg, 1 mmol). EDCI.HCl (233 mg, 1.5 mmol) and HOBt (68 mg, 0.5 mmol) were added under a nitrogen environment at 0 °C. The reaction mixture was charged with DMAP (122 mg, 1 mmol), according to general procedure 2.5.2.2. After performing the work-up, the crude residue was purified using column chromatography (2-20% ethyl acetate/hexane). Yield: 37%. ¹H NMR (400 MHz, CDCl₃) δ 10.61 (s, 1O-H), 7.40 (dd, *J* = 8.1, 1.5 Hz, 1H), 7.13 (dd, *J* = 7.9, 1.5 Hz, 1H), 6.79 (dd, *J* = 10.4, 5.6 Hz, 1H), 5.55 (dq, *J* = 14.2, 7.1 Hz, 1H), 4.29 – 4.16 (m, 4H), 1.65 – 1.58 (m, 3H), 1.35 (dd, *J* = 9.5, 4.6 Hz, 6H).

Synthesis procedure for diethyl ((2,3-dihydroxybenzamido)(naphthalen-1-yl)methyl)phosphonate (63e): Synthesized by coupling 2,3-dihydroxybenzoic acid (306 mg, 1.5 mmol) and diethyl (amino(naphthalen-1-yl)methyl)phosphonate (440 mg, 1.5 mmol), EDCI.HCl (350 mg, 2.25 mmol) and HOBt (101 mg, 0.75 mmol) were added under a nitrogen environment at 0 °C. The reaction mixture was charged with DMAP (184 mg, 1.5 mmol), according to general procedure 2.5.2.2. After performing the work-up, the crude residue was purified using column chromatography (2-20% ethyl acetate/hexane). Yield: 61%. ¹H NMR (400 MHz, CDCl₃) δ 10.43 (s, 1O-H), 8.32 (d, *J* = 8.6 Hz, 1H), 7.89 (dd, *J* = 13.5, 5.7 Hz, 3H), 7.70 – 7.62 (m, 2H), 7.54 (dd, *J* = 18.0, 7.8 Hz, 2H), 7.21 (d, *J* = 13.9 Hz, 1H), 7.16 (dd, *J* = 7.9, 1.1 Hz, 1H), 6.90 (t, *J* = 8.0 Hz, 1H), 4.38 – 3.70 (m, 4H), 1.28 (t, *J* = 7.0 Hz, 3H), 1.07 (t, *J* = 7.1 Hz, 3H).

Synthesis procedure for diethyl ((2,3-dihydroxybenzamido)(furan-2-yl)methyl)phosphonate (63f): Synthesized by coupling 2,3-dihydroxybenzoic acid (204 mg, 1 mmol) and diethyl (amino(furan-2-yl)methyl)phosphonate (233 mg, 1 mmol). EDCI.HCl (233 mg, 1.5 eqv) and HOBt (68 mg, 0.5 eqv) were added under a nitrogen environment at 0 °C. The reaction mixture was charged with DMAP (122 mg, 1 mmol), according to general procedure 2.5.2.2. After performing the work-up, the crude residue was purified using column chromatography (2-40% ethyl

acetate/hexane). Yield: 25%. ¹H NMR (400 MHz, CDCl₃) δ 10.48 (s, 1O-H), 7.52 – 7.45 (m, 2H), 7.14 (dd, *J* = 7.9, 1.5 Hz, 1H), 6.82 (t, *J* = 8.0 Hz, 1H), 6.75 – 6.72 (m, 1H), 6.52 (d, *J* = 15.2 Hz, 1H), 6.46 – 6.41 (m, 1H), 5.94 (s, 1H), 4.33 – 4.11 (m, 4H), 1.37 – 1.33 (m, 3H), 1.32 – 1.28 (m, 3H).

Synthesis procedure for diethyl (1-(2,3-dihydroxybenzamido)propyl)phosphonate (63g): Synthesized by coupling 2,3-dihydroxybenzoic acid (204 mg, 1 mmol) and (1-aminopropyl)phosphonate (195 mg, 1 mmol). EDCI.HCl (233 mg, 1.5 mmol) and HOBT (68 mg, 0.5 mmol) were added under a nitrogen environment at 0 °C. The reaction mixture was charged with DMAP (122 mg, 1 mmol), according to the general procedure 2.5.2.2. After performing the work-up, the crude residue was purified using column chromatography (2-25% ethyl acetate/hexane). Yield: 27%. ¹H NMR (400 MHz, CDCl₃) δ 10.66 (s, 1H), 7.45 – 7.41 (m, 1H), 7.19 – 7.10 (m, 1H), 6.88 – 6.79 (m, 1H), 5.47 (ddd, *J* = 9.6, 8.3, 4.3 Hz, 1H), 4.26 – 4.16 (m, 4H), 2.17 – 1.94 (m, 2H), 1.33 (td, *J* = 7.2, 4.4 Hz, 6H), 1.06 (t, *J* = 7.4 Hz, 3H).

Synthesis procedure for diethyl (1-(2,3-dihydroxybenzamido)-3-phenylpropyl)phosphonate (63h): Synthesized by coupling 2,3-dihydroxybenzoic acid (204 mg, 1 mmol) and (1-amino-3-phenylpropyl)phosphonate (271 mg, 1 mmol). EDCI.HCl (233 mg, 1.5 eqv) and HOBT (68 mg, 0.5 mmol) were added under a nitrogen environment at 0 °C. The reaction mixture was charged with DMAP (122 mg, 1 mmol), according to general procedure 2.5.2.2. After performing the work-up, the crude residue was purified using column chromatography (2-20% ethyl acetate/hexane). ¹H NMR (400 MHz, CDCl₃) δ 10.64 (s, 1O-H), 7.42 (dt, *J* = 6.4, 3.2 Hz, 1H), 7.28 (dd, *J* = 8.0, 6.8 Hz, 2H), 7.22 – 7.14 (m, 4H), 6.82 (dd, *J* = 13.6, 5.5 Hz, 1H), 5.61 – 5.53 (m, 1H), 4.27 – 4.14 (m, 4H), 2.88 – 2.70 (m, 2H), 2.41 – 2.32 (m, 2H), 1.33 (dd, *J* = 8.9, 5.2 Hz, 6H).

Synthesis procedure for diethyl ((1-hydroxy-2-naphthamido)(phenyl)methyl)phosphonate (66a): Synthesized by coupling 2-hydroxy naphthoic acid (188.18 mg, 1 mmol) and diethyl (amino(phenyl)methyl)phosphonate (243.2 mg, 1 mmol). EDCI.HCl (233 mg, 1.5 mmol) and HOBT (68 mg, 0.5 mmol) were added under a nitrogen environment at 0 °C. The reaction mixture was charged with DMAP (122.17mg, 1 mmol), according to general procedure 2.5.2.2. After performing the work-up, the crude residue was purified using column chromatography (2-20% ethyl acetate/hexane). White powder. Yield:

58%. ¹H NMR (400 MHz, DMSO) δ 8.26 (d, *J* = 8.2 Hz, 1H), 8.13 (d, *J* = 8.9 Hz, 1H), 7.89 (d, *J* = 8.2 Hz, 1H), 7.72 – 7.60 (m, 3H), 7.55 (dd, *J* = 14.0, 7.1 Hz, 1H), 7.40 (dd, *J* = 12.0, 8.2 Hz, 3H), 7.36 – 7.32 (m, 1H), 5.79 (d, *J* = 22.1 Hz, 1H), 4.13 – 3.82 (m, 4H), 1.15 (t, *J* = 7.0 Hz, 3H), 1.08 (t, *J* = 7.0 Hz, 3H).

Synthesis procedure for diethyl ((1-hydroxy-2-naphthamido)methyl)phosphonate (66b): Synthesized by coupling 2-hydroxy naphthoic acid (188.18 mg, 1 mmol) and diethyl (aminomethyl)phosphonate (167 mg, 1 mmol). EDCI.HCl (233 mg, 1.5 mmol) and HOBT (68 mg, 0.5 mmol) were added under a nitrogen environment at 0 °C. The reaction mixture was charged with DMAP (122 mg, 1 mmol), according to general procedure 2.5.2.2. After performing the work-up, the crude residue was purified using column chromatography (2-50% ethyl acetate/hexane). Yield: 32.5%; ¹H NMR (400 MHz, CDCl₃) δ 11.67 (s, 1O-H), 8.44 (d, *J* = 7.8 Hz, 1H), 7.81 (dd, *J* = 8.5, 6.2 Hz, 2H), 7.69 – 7.62 (m, 1H), 7.60 – 7.54 (m, 1H), 7.33 (d, *J* = 8.8 Hz, 1H), 5.37 (t, *J* = 4.7 Hz, 1H), 4.72 (d, *J* = 8.6 Hz, 2H), 4.40 – 4.17 (m, 4H), 1.40 (t, *J* = 7.1 Hz, 6H).

Synthesis procedure for diethyl ((3,4-dichlorophenyl)(1-hydroxy-2-naphthamido)methyl)phosphonate (66c): Synthesized by coupling 2-hydroxy naphthoic acid (188.18 mg, 1 mmol) and diethyl (amino(3,4-dichlorophenyl)methyl)phosphonate (312 mg, 1 mmol). EDCI.HCl (1.5mmol) and HOBT (68 mg, 0.5 mmol) were added under a nitrogen environment at 0 °C. The reaction mixture was charged with DMAP (122 mg, 1 mmol), according to general procedure 2.5.2.2. After performing the work-up, the crude residue was purified using column chromatography (2-20% ethyl acetate/hexane). Yield: 25%. ¹H NMR (400 MHz, CDCl₃) δ 11.53 (s, 1H), 8.41 (d, *J* = 8.3 Hz, 1H), 7.94 (d, *J* = 8.8 Hz, 1H), 7.80 (d, *J* = 8.1 Hz, 1H), 7.71 (s, 1H), 7.64 (dd, *J* = 14.2, 6.1 Hz, 1H), 7.55 (dd, *J* = 13.1, 5.7 Hz, 1H), 7.48 (d, *J* = 3.2 Hz, 2H), 7.36 (d, *J* = 8.9 Hz, 1H), 6.39 (d, *J* = 14.0 Hz, 1H), 4.30 – 4.04 (m, 4H), 1.30 (dd, *J* = 12.6, 7.0 Hz, 6H).

Synthesis procedure for diethyl (1-(1-hydroxy-2-naphthamido)ethyl)phosphonate (66d): Synthesized by coupling 2-hydroxy naphthoic acid (188.18 mg, 1mmol) and diethyl (1-aminoethyl)phosphonate (185 mg, 1 mmol). EDCI.HCl (233 mg, 1.5 mmol) and HOBT (68 mg, 0.5 mmol) were added under a nitrogen environment at 0 °C. The reaction mixture was charged with DMAP (122 mg, 1 mmol), according to general procedure 2.5.2.2. After performing the work-up, the crude residue was purified using column chromatography (2-20% ethyl acetate/hexane). Yield: 30%. ¹H NMR (400

MHz, CDCl₃) δ 11.78 (s, 1O-H), 8.44 (d, J = 8.3 Hz, 1H), 7.81 (dd, J = 11.1, 8.6 Hz, 2H), 7.70 – 7.61 (m, 1H), 7.60 – 7.53 (m, 1H), 7.32 (d, J = 8.8 Hz, 1H), 5.62 (dq, J = 14.3, 7.1 Hz, 1H), 4.32 – 4.16 (m, 4H), 1.67 (dd, J = 16.6, 7.1 Hz, 3H), 1.36 (td, J = 7.1, 1.8 Hz, 6H).

Synthesis procedure for diethyl ((1-hydroxy-2-naphthamido)(naphthalen-1-yl)methyl)phosphonate (66e): Synthesized by coupling 2-hydroxy naphthoic acid (188.18 mg, 1 mmol) and diethyl (amino(naphthalen-1-yl)methyl)phosphonate (293.3 mg, 1 mmol). EDCI.HCl (233 mg, 1.5 mmol) and HOBt (68 mg, 0.5 mmol) were added under a nitrogen environment at 0 °C. The reaction mixture was charged with DMAP (122 mg, 1 mmol), according to general procedure 2.5.2.2. After performing the work-up, the crude residue was purified using column chromatography (2-20% ethyl acetate/hexane). Yield: 66%. ¹H NMR (400 MHz, CDCl₃) δ 11.63 (s, 1H), 8.42 (t, J = 9.2 Hz, 2H), 8.10 (d, J = 8.8 Hz, 1H), 8.00 (dd, J = 6.9, 2.5 Hz, 1H), 7.95 – 7.88 (m, 2H), 7.79 (d, J = 8.1 Hz, 1H), 7.72 – 7.65 (m, 1H), 7.64 – 7.59 (m, 1H), 7.59 – 7.49 (m, 3H), 7.38 (d, J = 8.8 Hz, 1H), 7.32 (d, J = 13.9 Hz, 1H), 4.31 – 3.79 (m, 4H), 1.32 – 1.30 (m, 3H), 1.09 (t, J = 7.1 Hz, 3H).

Synthesis procedure for diethyl (furan-2-yl(1-hydroxy-2-naphthamido)methyl)phosphonate (66f): Synthesized by coupling 2-hydroxy naphthoic acid (188.18 mg, 1 mmol) and diethyl (amino(furan-2-yl)methyl)phosphonate (233 mg, 1 mmol). EDCI.HCl (233 mg, mmol 1.5 eqv) and HOBt (68 mg, 0.5 mmol) were added under a nitrogen environment at 0 °C. The reaction mixture was charged with DMAP (122 mg, 1 mmol), according to general procedure 2.5.2.2. After performing the work-up, the crude residue was purified using column chromatography (2-20% ethyl acetate/hexane). Yield: 71%. ¹H NMR (400 MHz, CDCl₃) δ 11.63 (s, 1O-H), 8.42 (d, J = 8.3 Hz, 1H), 7.89 – 7.86 (m, 1H), 7.78 (d, J = 8.1 Hz, 1H), 7.66 – 7.61 (m, 1H), 7.57 – 7.50 (m, 2H), 7.31 (d, J = 8.8 Hz, 1H), 6.80 – 6.76 (m, 1H), 6.61 (d, J = 15.3 Hz, 1H), 6.48 – 6.44 (m, 1H), 4.34 – 4.13 (m, 4H), 1.33 (dt, J = 16.6, 7.1 Hz, 6H).

Synthesis procedure for diethyl (1-(1-hydroxy-2-naphthamido)propyl)phosphonate (66g): Synthesized by coupling 2-hydroxy naphthoic acid (188.18 mg, 1 mmol) and (1-aminopropyl)phosphonate (195 mg, 1 mmol). EDCI.HCl (233 mg, 1.5 mmol) and HOBt (68 mg, 0.5 mmol) were added under a nitrogen environment at 0 °C. The reaction mixture was charged with DMAP (122

mg, 1 mmol), according to the general procedure 2.5.2.2. After the work-up, the crude residue was purified using column chromatography (2-20% ethyl acetate/hexane). Yield: 52%; ¹H NMR (400 MHz, CDCl₃) δ 11.78 (d, *J* = 25.1 Hz, 1H), 8.44 (d, *J* = 8.3 Hz, 1H), 7.84 (d, *J* = 8.8 Hz, 1H), 7.79 (d, *J* = 8.1 Hz, 1H), 7.67 – 7.61 (m, 1H), 7.59 – 7.52 (m, 1H), 7.32 (d, *J* = 8.8 Hz, 1H), 5.54 (ddd, *J* = 9.4, 8.3, 4.5 Hz, 1H), 4.28 – 4.13 (m, 4H), 2.28 – 1.86 (m, 2H), 1.33 (td, *J* = 7.1, 2.9 Hz, 6H), 1.09 (t, *J* = 7.4 Hz, 3H).

Synthesis procedure for diethyl (1-(1-hydroxy-2-naphthamido)-3-phenylpropyl)phosphonate (66h): Synthesized by coupling 2-hydroxy naphthoic acid (188.18 mg, 1 mmol) and (1-amino-3-phenylpropyl)phosphonate (271 mg, 1 mmol). EDCI.HCl (233 mg, 1.5 mmol) and HOBt (68 mg, 0.5 mmol) were added under a nitrogen environment at 0 °C. The reaction mixture was charged with DMAP (122 mg, 1 mmol), according to general procedure 2.5.2.2. After performing the work-up, the crude residue was purified using column chromatography (2-20% ethyl acetate/hexane). Yield: 29%. ¹H NMR (400 MHz, CDCl₃) δ 11.80 (s, 1O-H), 8.49 – 8.44 (m, 1H), 7.83 (t, *J* = 9.3 Hz, 2H), 7.66 (ddd, *J* = 8.2, 6.9, 1.3 Hz, 1H), 7.57 (ddd, *J* = 8.2, 6.9, 1.2 Hz, 1H), 7.34 (d, *J* = 8.8 Hz, 1H), 7.32 – 7.27 (m, 2H), 7.23 – 7.17 (m, 3H), 5.68 – 5.59 (m, 1H), 4.29 – 4.15 (m, 4H), 2.83 (dtd, *J* = 22.0, 14.1, 7.7 Hz, 2H), 2.45 – 2.36 (m, 2H), 1.33 (t, *J* = 7.0 Hz, 6H).

Synthesis procedure for N-benzyl-1-hydroxy-2-naphthamide (67a): Synthesized by coupling 2-hydroxy naphthoic acid (94.1 mg, 0.5 mmol) and benzylamine (53.6 mg, 0.5 mmol eqv), and EDCI.HCl (116.5 mg, 0.75 mmol) was added under a nitrogen environment at 0 °C. The reaction mixture was charged with DMAP (61 mg, 0.5 mmol), according to general procedure 2.5.2.2. After performing the work-up, the crude residue was purified using column chromatography (hexane/ethyl acetate = 95:5) to yield the desired product. Yield: 56%. ¹H NMR (400 MHz, CDCl₃) δ 13.81 (s, 1H), 8.46 (ddd, *J* = 8.3, 4.5, 3.8 Hz, 1H), 7.77 (d, *J* = 7.5 Hz, 1H), 7.58 (dd, *J* = 22.2, 8.2, 6.9, 1.3 Hz, 2H), 7.45 – 7.37 (m, 4H), 7.35 – 7.24 (m, 3H), 6.62 (s, 1H), 4.72 (d, *J* = 5.6 Hz, 2H).

Synthesis procedure for 1-hydroxy-N-phenethyl-2-naphthamide (67b): Synthesized by coupling 2-hydroxy naphthoic acid (94.1 mg, 0.5 mmol) and phenylethylamine (61 mg, 0.5 mmol), and EDCI.HCl (116.5 mg, 0.75 mmol) were added under a nitrogen environment at 0 °C. The reaction mixture was charged with DMAP (61 mg, 0.5 mmol), according to general procedure 2.5.2.2. After performing the work-up, the crude residue was purified using column chromatography

(hexane/ethyl acetate = 95:5) to yield the desired product. Yield: 62%. ¹H NMR (400 MHz, CDCl₃) δ 13.84 (s, 1H), 8.47 – 8.42 (m, 1H), 7.76 (d, J = 7.7 Hz, 1H), 7.57 (dd, J = 22.1, 8.1, 6.9, 1.3 Hz, 2H), 7.41 – 7.36 (m, 2H), 7.33 – 7.29 (m, 2H), 7.28 (s, 1H), 7.25 (d, J = 8.7 Hz, 1H), 7.16 (d, J = 8.8 Hz, 1H), 6.36 (s, 1H), 3.80 (dd, J = 12.8, 6.9 Hz, 2H), 3.00 (t, J = 6.9 Hz, 2H).

Synthesis procedure for 1-hydroxy-N-(3-phenylpropyl)-2-naphthamide (67c):

Synthesized by coupling 2-hydroxy naphthoic acid (94.1 mg, 0.5 mmol) and phenylpropylamine (66.5 mg, 0.5 mmol), and EDCI.HCl (116.5 mg, 0.75 mmol) were added under a nitrogen environment at 0 °C. The reaction mixture was charged with DMAP (61 mg, 0.5 mmol), according to general procedure 2.5.2.2. After performing the work-up, the crude residue was purified using column chromatography (hexane/ethyl acetate = 95:5) to yield the desired product. Yield: 55%. ¹H NMR (400 MHz, CDCl₃) δ 13.86 (s, 1H), 8.45 (d, J = 8.2 Hz, 1H), 7.76 (d, J = 7.9 Hz, 1H), 7.57 (dd, J = 23.6, 8.2, 6.9, 1.3 Hz, 2H), 7.34 (ddd, J = 17.1, 10.7, 6.1 Hz, 2H), 7.29 – 7.21 (m, 4H), 7.06 (dd, J = 8.5, 4.1 Hz, 1H), 6.25 (s, 1H), 3.58 (dd, J = 12.7, 6.9 Hz, 2H), 2.80 (t, J = 7.4 Hz, 2H), 2.12 – 2.00 (m, 2H).

Synthesis procedure for N-benzyl-8-hydroxyquinoline-7-carboxamide (70):

Synthesized by coupling 8-hydroxyquinoline-7-carboxylic acid (95 mg, 0.5 mmol) and benzylamine (53.6 mg, 0.5 mmol), and EDCI.HCl (116.5 mg, 0.75 mmol) were added under a nitrogen environment at 0 °C. The reaction mixture was charged with DMAP (61 mg, 0.5 mmol), according to general procedure 2.5.2.2. After performing the work-up, the crude residue was purified using column chromatography (hexane/ethyl acetate = 90:10) to yield the desired product. Yield: 72%. ¹H NMR (400 MHz, CDCl₃) δ 8.86 (dd, J = 4.2, 1.5 Hz, 1H), 8.28 – 8.15 (m, 2H), 7.55 (dd, J = 8.3, 4.2 Hz, 1H), 7.42 (ddd, J = 15.4, 8.3, 3.8 Hz, 4H), 7.32 (dd, J = 8.4, 6.0 Hz, 1H), 4.79 (d, J = 5.6 Hz, 2H).

Synthesis procedure for diethyl ((8-hydroxyquinoline-7-

carboxamido)(phenyl)methyl)phosphonate (71a): Synthesized by coupling 8-hydroxyquinoline-7-carboxylic acid (189.17 mg, 1 mmol) and diethyl (amino(phenyl)methyl)phosphonate (1 mmol). EDCI.HCl (1.5 mmol) and HOBT (0.5 mmol) were added under a nitrogen environment at 0 °C. The reaction mixture was charged with DMAP (1 mmol), according to general procedure 2.5.2.2. After performing the work-up, the crude residue was purified using column chromatography (2-20% ethyl acetate/hexane). Yield: 28%. ¹H NMR (400 MHz, CDCl₃) δ 9.06 (s, 1H),

8.88 (d, $J = 3.4$ Hz, 1H), 8.19 (dd, $J = 8.1, 3.6$ Hz, 2H), 7.59 (d, $J = 7.4$ Hz, 2H), 7.57 – 7.52 (m, 1H), 7.39 (t, $J = 7.2$ Hz, 2H), 7.34 – 7.29 (m, 1H), 5.86 (dd, $J = 20.8, 9.1$ Hz, 1H), 4.26 – 3.80 (m, 4H), 1.36 – 1.30 (m, 3H), 1.18 (t, $J = 7.0$ Hz, 3H).

Synthesis procedure for diethyl ((3,4-dichlorophenyl)(8-hydroxyquinoline-7-carboxamido)methyl)phosphonate (71c): Synthesized by coupling 8-hydroxyquinoline-7-carboxylic acid (189.17 mg, 1 mmol) and diethyl (amino(3,4-dichlorophenyl)methyl)phosphonate (312 mg, 1 mmol), EDCI.HCl (233 mg, 1.5 mmol) and HOBt (68 mg, 0.5 eqv) were added under a nitrogen environment at 0 °C. The reaction mixture was charged with DMAP (122 mg, 1 mmol), according to the general procedure 2.5.2.2. After performing the work-up, the crude residue was purified using column chromatography (2-20% ethyl acetate/hexane). Yield: 67%. ¹H NMR (400 MHz, CDCl₃) δ 9.00 (dd, $J = 4.1, 1.5$ Hz, 1H), 8.17 (dd, $J = 8.3, 1.5$ Hz, 1H), 8.06 (d, $J = 8.8$ Hz, 1H), 7.72 (d, $J = 1.8$ Hz, 1H), 7.58 (dd, $J = 8.3, 4.2$ Hz, 1H), 7.49 (dd, $J = 3.8, 2.1$ Hz, 1H), 7.37 (d, $J = 8.9$ Hz, 1H), 6.39 (d, $J = 13.7$ Hz, 1H), 4.28 – 4.05 (m, 4H), 1.30 (q, $J = 7.1$ Hz, 6H).

Synthesis procedure for diethyl (1-(8-hydroxyquinoline-7-carboxamido)propyl)phosphonate (71g): Synthesized by coupling 8-hydroxyquinoline-7-carboxylic acid (189.17 mg, 1 mmol) and (1-aminopropyl)phosphonate (195 mg, 1 mmol). EDCI.HCl (233 mg, 1.5 mmol) and HOBt (67 mg, 0.5 mmol) were added under a nitrogen environment at 0 °C. The reaction mixture was charged with DMAP (122 mg, 1 mmol), according to the general procedure 2.5.2.2. After performing the work-up, the crude residue was purified using column chromatography (2-20% ethyl acetate/hexane). Yield: 29%. ¹H NMR (400 MHz, CDCl₃) δ 9.00 – 8.89 (m, 1H), 8.10 (dd, $J = 8.4, 1.2$ Hz, 1H), 7.92 – 7.81 (m, 1H), 7.55 – 7.47 (m, 1H), 7.31 – 7.22 (m, 1H), 5.50 (td, $J = 9.0, 4.5$ Hz, 1H), 4.23 – 4.02 (m, 4H), 2.10 – 2.01 (m, 2H), 1.27 (td, $J = 7.0, 4.7$ Hz, 6H), 1.07 – 1.00 (m, 3H).

Synthesis procedure for diethyl ((4-oxo-4H-chromene-3-carboxamido)(phenyl)methyl)phosphonate (73a): Synthesized by coupling Chromone-3-carboxylic acid (95.0 mg, 0.5 mmol) and diethyl (amino(phenyl)methyl)phosphonate (134 mg, 0.5 mmol), EDCI.HCl (116.5 mg, 0.75 mmol) and HOBt (35 mg, 0.25 mmol) were added under a nitrogen environment at 0 °C. The reaction mixture was charged with DMAP (61 mg, 0.5 mmol), according to general procedure 2.5.2.2. After performing the work-up, the crude residue was purified

using column chromatography (2-20% ethyl acetate/hexane). Yield: 25%. ^1H NMR (400 MHz, CDCl_3) δ 11.93 (s, 1H), 7.95 (d, $J = 3.5$ Hz, 1H), 7.70 (d, $J = 7.4$ Hz, 1H), 7.57 (d, $J = 7.5$ Hz, 2H), 7.36 (tt, $J = 14.3, 7.0$ Hz, 3H), 6.98 (d, $J = 8.3$ Hz, 1H), 6.85 (t, $J = 7.5$ Hz, 1H), 5.73 (dd, $J = 21.3, 9.2$ Hz, 1H), 4.29 – 3.68 (m, 4H), 1.33 (t, $J = 7.1$ Hz, 3H), 1.14 (t, $J = 7.0$ Hz, 3H).

2.5.2.4 Synthesis procedure for hydrolysis of non-hydroxamate lipophilic DXR inhibitors:

Synthetic route was followed according to Scheme 2.3-2.7. To a mixture of ester derivatives of non-hydroxamate compounds (1 eq.), synthesized in the previous step in dry dichloromethane, TMSBr (10 eq.) was added at 0 °C dropwise. After 1 h, the solution was allowed to warm to room temperature and stirred for an additional 23 h. After completion of the reaction, the solvent was removed under reduced pressure, and the remaining residue was dissolved in a mixture of tetrahydrofuran and water (9:1). After 30 min, the solvent was evaporated and washed with dichloromethane to remove nonpolar impurities and remaining TMSBr. The resulting residue dried *in vacuo* overnight and was characterized further by NMR and mass spectroscopy.

Synthesis procedure for ((2-hydroxybenzamido)(phenyl)methyl)phosphonic acid (62a): The respective ester derivative was hydrolyzed according to the given general procedure 2.5.2.3. ^1H NMR (400 MHz, DMSO) δ 7.90 (d, $J = 7.5$ Hz, 1H), 7.39 (d, $J = 5.1$ Hz, 3H), 7.32 (t, $J = 7.3$ Hz, 2H), 7.29 – 7.22 (m, 1H), 7.01 – 6.90 (m, 2H), 5.34 (d, $J = 21.1$ Hz, 1H). ^{31}P NMR (162 MHz, DMSO) δ 16.58 (d, $J = 19.9$ Hz). HRMS (ESI) for $\text{C}_{14}\text{H}_{14}\text{NO}_5\text{P}$ ($[\text{M}+\text{H}]^+$): calculated 307.061, found 307.0625. Purity 89.3 % [Mobile Phase, ACN: Buffer (70:30); RT: 3.087 min].

Synthesis procedure for ((2-hydroxybenzamido)methyl)phosphonic acid (62b): The respective ester derivative was hydrolyzed according to the given general procedure 2.5.2.3. ^1H NMR (400 MHz, DMSO) δ 7.93 (t, $J = 12.9$ Hz, 1H), 7.64 (dd, $J = 14.1, 6.0$ Hz, 1H), 7.07 (dd, $J = 12.1, 7.9$ Hz, 2H), 4.51 (d, $J = 6.9$ Hz, 2H).

Synthesis procedure for ((3,4-dichlorophenyl)(2-hydroxybenzamido)methyl)phosphonic acid (62c): The respective ester derivative was hydrolyzed according to the given general procedure 2.5.2.3. ^1H NMR (400 MHz, DMSO) δ 7.99 (dd, $J = 7.9, 1.6$ Hz, 1H), 7.73 (t, $J = 1.8$ Hz, 1H), 7.66 (d, $J = 8.4$ Hz, 1H), 7.60 – 7.53 (m, 1H), 7.47 (dt, $J = 8.4, 1.8$ Hz, 1H), 7.05 – 6.99 (m, 2H), 6.12 (d, J

= 13.6 Hz, 1H). ³¹P NMR (162 MHz, DMSO) δ 11.06 (s). HRMS (ESI) for C₁₄H₁₂Cl₂NO₅P ([M+H]⁺): calculated 374.983, found 374.9815. Purity 91.9% [Mobile Phase, ACN: Buffer (55:45); RT: 4.873 min].

Synthesis procedure for (1-(2-hydroxybenzamido)ethyl)phosphonic acid (62d):

The respective ester derivative was hydrolyzed according to the given general procedure 2.5.2.3. ¹H NMR (400 MHz, DMSO) δ 7.84 (dd, *J* = 7.9, 1.6 Hz, 1H), 7.54 (ddd, *J* = 8.8, 5.7, 1.7 Hz, 1H), 7.05 – 6.94 (m, 2H), 5.22 (d, *J* = 1.2 Hz, 1H), 1.45 (dd, *J* = 15.4, 7.0 Hz, 3H). ¹³C NMR (101 MHz, DMSO) δ 168.16 (d, *J* = 7.4 Hz, C=O), 160.53 (s), 130.78 (s), 119.82 (s), 117.83 (s), 113.42 (s), 67.76 (s), 66.14 – 65.46 (m). ³¹P NMR (162 MHz, DMSO) δ 16.17 – 15.59 (m). Purity 94.2% [Mobile Phase, ACN: Buffer (70:30); RT: 2.982 min].

Synthesis procedure for ((2-hydroxybenzamido)(naphthalen-1-yl)methyl)phosphonic acid (62e):

The respective ester derivative was hydrolyzed according to the given general procedure 2.5.2.3. ¹H NMR (400 MHz, MeOD) δ 8.38 (d, *J* = 8.5 Hz, 1H), 8.24 (dd, *J* = 8.0, 1.5 Hz, 1H), 7.90 (dt, *J* = 10.4, 4.2 Hz, 3H), 7.63 (t, *J* = 7.2 Hz, 1H), 7.58 – 7.51 (m, 3H), 7.19 (d, *J* = 13.7 Hz, 1H), 7.05 – 7.00 (m, 1H), 6.95 (s, 1H). ³¹P NMR (162 MHz, DMSO) δ 12.28 (d, *J* = 13.0 Hz) HRMS (ESI) for C₁₈H₁₆NO₅P ([M+H]⁺): calculated 357.0766, found 357.075. Purity 99.7% [Mobile Phase, ACN: Buffer (70:30); RT: 3.43 min].

Synthesis procedure for (furan-2-yl(2-hydroxybenzamido)methyl)phosphonic acid (62f):

The respective ester derivative was hydrolyzed according to the given general procedure 2.5.2.3. ¹H NMR (400 MHz, DMSO) δ 10.22 (s, 1H), 8.01 (td, *J* = 8.0, 1.6 Hz, 1H), 7.80 (dd, *J* = 7.9, 1.7 Hz, 1H), 7.55 – 7.51 (m, 1H), 7.40 (d, *J* = 8.1 Hz, 1H), 7.08 – 6.90 (m, 5H). ³¹P NMR (162 MHz, DMSO) δ 14.30 (s).

Synthesis procedure for (1-(2-hydroxybenzamido)propyl)phosphonic acid (62g):

The respective ester derivative was hydrolyzed according to the given general procedure 2.5.2.3. ¹H NMR (400 MHz, DMSO) δ 8.16 – 7.31 (m, 3H), 6.97 (dd, *J* = 38.0, 14.9 Hz, 1H), 4.99 (s, 1H), 1.98 – 1.53 (m, 2H), 0.90 (td, *J* = 47.9, 36.2 Hz, 3H).

Synthesis procedure for (1-(2-hydroxybenzamido)-3-phenylpropyl)phosphonic acid (62h):

The respective ester derivative was hydrolyzed according to the given general procedure 2.5.2.3. ¹H NMR (400 MHz, DMSO) δ 7.82 (d, *J* = 7.7 Hz, 1H), 7.51 (dd, *J* = 11.3, 4.3 Hz, 1H), 7.27 – 7.22 (m, 3H), 7.16 (dd, *J* = 17.8, 6.8 Hz, 4H), 6.95

(dd, $J = 13.6, 7.7$ Hz, 3H), 5.16 (dd, $J = 8.8, 5.6$ Hz, 2H), 2.72 – 2.60 (m, 3H), 2.12 (dd, $J = 23.6, 13.5$ Hz, 3H).

Synthesis procedure for ((2,3-dihydroxybenzamido)(phenyl)methyl)phosphonic acid (64a): The respective ester derivative was hydrolyzed according to the given general procedure 2.5.2.3. ^1H NMR (400 MHz, MeOD) δ 7.88 (s, 1H), 7.43 (d, $J = 61.3$ Hz, 5H), 6.84 (d, $J = 77.8$ Hz, 2H), 5.40 (d, $J = 40.6$ Hz, 2H). LCMS (-ESI): m/z calculated for $\text{C}_{14}\text{H}_{14}\text{NO}_6\text{P}$: 323.2408, found: 322.22. Purity 94.8% [Mobile Phase, ACN: Buffer (60:40); RT: 3.02 min].

Synthesis procedure for ((2,3-dihydroxybenzamido)methyl)phosphonic acid (64b): The respective ester derivative was hydrolyzed according to the given general procedure 2.5.2.3. ^1H NMR (400 MHz, MeOD) δ 7.95 (s, 1H), 7.69 – 7.39 (m, 1H), 7.21 – 7.00 (m, 1H), 6.82 (d, $J = 30.0$ Hz, 1H), 4.62 (s, 2H). ^{31}P NMR (162 MHz, DMSO) δ 17.20 – 17.13 (m).

Synthesis procedure for ((3,4-dichlorophenyl)(2,3-dihydroxybenzamido)methyl)phosphonic acid (64c): The respective ester derivative was hydrolyzed according to the given general procedure 2.5.2.3. ^1H NMR (400 MHz, DMSO) δ 7.70 (s, 1H), 7.67 (d, $J = 8.4$ Hz, 1H), 7.46 (dd, $J = 8.1, 1.5$ Hz, 2H), 7.08 (dd, $J = 7.8, 1.4$ Hz, 1H), 6.83 (t, $J = 7.9$ Hz, 1H), 6.12 (d, $J = 13.5$ Hz, 1H). ^{31}P NMR (162 MHz, DMSO) δ 11.21 (s).

Synthesis procedure for 1-(2,3-dihydroxybenzamido)ethyl)phosphonic acid (64d): The respective ester derivative was hydrolyzed according to given general procedure 2.5.2.3. ^1H NMR (400 MHz, DMSO) δ 7.28 (d, $J = 7.4$ Hz, 1H), 7.04 (d, $J = 7.0$ Hz, 1H), 6.77 (t, $J = 7.9$ Hz, 1H), 5.25 – 5.16 (m, 1H), 1.43 (dd, $J = 15.4, 6.9$ Hz, 3H). ^{31}P NMR (162 MHz, DMSO) δ 20.56 (s), 13.18 (s). ^{13}C NMR (101 MHz, DMSO) δ 173.12 – 172.44 (m), 169.03 – 168.51 (m), 150.40 – 150.14 (m), 149.85 (s), 146.44 (s), 121.53 – 121.12 (m), 120.47 – 120.40 (m), 119.39 (s), 113.72 – 113.32 (m), 67.88 – 67.49 (m), 15.66 (s). Purity 85.7% [Mobile Phase, ACN: Buffer (60:40); RT: 2.729 min].

Synthesis procedure for (2,3-dihydroxybenzamido)(naphthalen-1-yl)methyl)phosphonic acid (64e): The respective ester derivative was hydrolyzed according to the given general procedure 2.5.2.3. ^1H NMR (400 MHz, MeOD) δ 8.38 (d, $J = 8.5$ Hz, 1H), 7.87 (dd, $J = 15.3, 7.1$ Hz, 4H), 7.78 – 7.73 (m, 1H), 7.59 (t, $J = 7.5$ Hz, 1H), 7.49 (dd, $J = 15.8, 8.4$ Hz, 3H), 7.23 (t, $J = 12.2$ Hz, 1H), 7.10 – 7.05 (m, 1H), 6.85 (t, $J = 8.0$ Hz, 1H). ^{31}P NMR (162 MHz, DMSO) δ 18.07 (s), 11.74 (s). ^{13}C

NMR (101 MHz, DMSO) δ 149.85 (s), 146.54 (s), 133.59 (s), 131.06 (s), 128.87 (s), 126.64 (s), 126.17 (s), 125.84 – 125.73 (m), 125.67 – 125.59 (m), 124.67 (s), 121.53 (s), 120.68 (s), 119.58 (s), 113.46 (s). HRMS (ESI) for $C_{18}H_{16}NO_5P$ ($[M+H]^+$): calculated 357.0766, found 357.0766. Purity 96.4% [Mobile Phase, ACN: Buffer (60:40); RT: 3.189 min].

Synthesis procedure for ((2,3-dihydroxybenzamido)(furan-2-yl)methyl)phosphonic acid (64f): The respective ester derivative was hydrolyzed according to the given general procedure 2.5.2.3. 1H NMR (400 MHz, DMSO) δ 12.70 (s, 1H), 8.31 (d, $J = 8.3$ Hz, 1H), 7.93 (d, $J = 8.1$ Hz, 1H), 7.81 – 7.56 (m, 3H), 7.42 (d, $J = 8.8$ Hz, 1H). Purity 90.9% [Mobile Phase, ACN: Buffer (60:40); RT: 4.882 min].

Synthesis procedure for (1-(2,3-dihydroxybenzamido)propyl)phosphonic acid (64g): The respective ester derivative was hydrolyzed according to the given general procedure 2.5.2.3. 1H NMR (400 MHz, DMSO) δ 11.25 (s, 1H), 7.24 (d, $J = 7.7$ Hz, 1H), 7.01 (d, $J = 7.7$ Hz, 1H), 6.72 (t, $J = 7.8$ Hz, 1H), 2.97 (d, $J = 19.0$ Hz, 2H), 2.38 (d, $J = 6.6$ Hz, 3H).

Synthesis procedure for (1-(2,3-dihydroxybenzamido)-3-phenylpropyl)phosphonic acid (64h): The respective ester derivative was hydrolyzed according to the given general procedure 2.5.2.3. 1H NMR (400 MHz, DMSO) δ 9.62 – 9.16 (m, 1H), 7.30 – 7.23 (m, 2H), 7.20 – 7.13 (m, 2H), 7.03 (dd, $J = 7.8, 1.5$ Hz, 1H), 6.75 (t, $J = 7.9$ Hz, 1H), 5.18 (td, $J = 9.2, 4.0$ Hz, 1H), 2.74 – 2.67 (m, 1H), 2.60 (dd, $J = 13.7, 7.1$ Hz, 1H), 2.22 – 2.03 (m, 2H).

Synthesis procedure for ((1-hydroxy-2-naphthamido)(phenyl)methyl)phosphonic acid (68a): The respective ester derivative was hydrolyzed according to the given general procedure 2.5.2.3. 1H NMR (400 MHz, DMSO) δ 8.24 (d, $J = 8.1$ Hz, 1H), 8.11 (d, $J = 8.1$ Hz, 1H), 7.95 – 7.81 (m, 1H), 7.70 – 7.61 (m, 1H), 7.55 (s, 4H), 7.49 – 7.24 (m, 4H), 5.52 (d, $J = 21.6$ Hz, 1H). ^{13}C NMR (101 MHz, DMSO) δ 159.61 (s), 137.53 (s), 136.39 (s), 129.39 (s), 128.87 (s), 128.45 (s), 127.92 (s), 127.66 – 127.57 (m), 126.24 (s), 125.01 (s), 123.99 (s), 123.50 (s), 118.12 (s), 107.98 – 107.87 (m). ^{31}P NMR (162 MHz, DMSO) δ 15.94 (d, $J = 21.9$ Hz). HRMS (ESI) for $C_{18}H_{16}NO_5P$ ($[M+H]^+$): calculated 357.0766, found 357.0756. Purity 97.2% [Mobile Phase, ACN: Buffer (70:30); RT: 4.300 min].

Synthesis procedure for ((1-hydroxy-2-naphthamido)methyl)phosphonic acid (68b): The respective ester derivative was hydrolyzed according to the given general

procedure 2.5.2.3. ^1H NMR (400 MHz, DMSO) δ 8.31 (d, $J = 8.3$ Hz, 1H), 7.93 (d, $J = 8.1$ Hz, 1H), 7.84 (d, $J = 8.8$ Hz, 1H), 7.72 (t, $J = 7.2$ Hz, 1H), 7.62 (t, $J = 7.5$ Hz, 1H), 7.47 (d, $J = 8.8$ Hz, 1H), 4.50 (d, $J = 8.6$ Hz, 2H). ^{13}C NMR (101 MHz, DMSO) δ 159.90 (s), 137.26 (s), 130.28 (s), 128.17 (s), 126.75 (s), 124.85 (s), 124.44 – 124.38 (m), 123.66 (s), 119.32 (s), 105.92 – 105.71 (m). ^{31}P NMR (162 MHz, DMSO) δ 12.31 (s). HRMS (ESI) for $\text{C}_{12}\text{H}_{12}\text{NO}_5\text{P}$ ($[\text{M}+\text{H}]^+$): calculated 281.0453, found 281.0462, Purity 98.2% [Mobile Phase, ACN: Buffer (70:30); RT: 3.973 min].

Synthesis procedure for diethyl ((3,4-dichlorophenyl)(1-hydroxy-2-naphthamido)methyl)phosphonate (68c): The respective ester derivative was hydrolyzed according to the given general procedure 2.5.2.3. ^1H NMR (400 MHz, DMSO) δ 11.47 (s, 1H), 8.31 (d, $J = 8.3$ Hz, 1H), 8.01 (d, $J = 8.8$ Hz, 1H), 7.96 (d, $J = 8.1$ Hz, 1H), 7.76 (s, 1H), 7.73 (d, $J = 7.1$ Hz, 1H), 7.68 (d, $J = 8.4$ Hz, 1H), 7.62 (t, $J = 7.2$ Hz, 1H), 7.53 (dd, $J = 11.9, 8.7$ Hz, 2H), 6.22 (d, $J = 13.4$ Hz, 1H). ^{31}P NMR (162 MHz, DMSO) δ 10.90 (d, $J = 13.3$ Hz).

Synthesis procedure for (1-(1-hydroxy-2-naphthamido)ethyl)phosphonic acid (68d): The respective ester derivative was hydrolyzed according to the given general procedure 2.5.2.3. ^1H NMR (400 MHz, DMSO) δ 11.76 (s, 1H), 8.32 (d, $J = 8.2$ Hz, 1H), 7.94 (d, $J = 8.1$ Hz, 1H), 7.82 (d, $J = 8.8$ Hz, 1H), 7.73 (dd, $J = 11.0, 4.0$ Hz, 1H), 7.63 (t, $J = 7.6$ Hz, 1H), 7.48 (d, $J = 8.8$ Hz, 1H), 5.35 – 5.26 (m, 1H), 1.50 (dd, $J = 15.4, 7.0$ Hz, 3H). ^{13}C NMR (101 MHz, DMSO) δ 159.99 (s), 137.28 – 137.09 (m), 130.32 (s), 128.20 (s), 126.79 (s), 124.88 (s), 124.44 – 124.35 (m), 123.66 (s), 106.04 (s), 68.22 – 68.09 (m), 66.60 – 66.48 (m), 15.80 (s). ^{31}P NMR (162 MHz, CDCl_3) δ 20.38 (dd, $J = 15.2, 8.4$ Hz). Purity 85.7% [Mobile Phase, ACN: Buffer (70:30); RT: 2.729 min].

Synthesis procedure for ((1-hydroxy-2-naphthamido)(naphthalen-1-yl)methyl)phosphonic acid (68e): The respective ester derivative was hydrolyzed according to the given general procedure 2.5.2.3. ^1H NMR (400 MHz, DMSO) δ 11.47 (s, 1H), 8.35 (d, $J = 8.5$ Hz, 1H), 8.28 (d, $J = 8.3$ Hz, 1H), 8.10 (d, $J = 8.8$ Hz, 1H), 8.01 – 7.88 (m, 3H), 7.80 (dd, $J = 7.1, 1.7$ Hz, 1H), 7.76 – 7.69 (m, 1H), 7.64 (dd, $J = 13.5, 7.0$ Hz, 2H), 7.60 – 7.55 (m, 3H), 6.99 (d, $J = 13.6$ Hz, 1H). ^{13}C NMR (101 MHz, DMSO) δ 169.30 (d, $J = 9.5$ Hz), 160.12 (s), 137.38 (s), 133.65 (s), 132.05 (s), 130.47 (s), 129.00 (d, $J = 10.2$ Hz), 126.81 (d, $J = 9.6$ Hz), 126.27 (s), 125.84 (s), 124.90 (s), 124.55 (s), 124.38 (s), 123.71 (s), 119.58 (s), 105.81 (s), 70.61 (s), 69.01 (s). ^{31}P NMR

(162 MHz, DMSO) δ 12.15 (d, $J = 13.4$ Hz). HRMS (ESI) for $C_{18}H_{16}NO_5P$ ($[M+H]^+$): calculated 357.0766, found 357.0766. Purity 96.4% [Mobile Phase, ACN: Buffer (60:40); RT: 3.189 min].

Synthesis procedure for (furan-2-yl(1-hydroxy-2-naphthamido)methyl)phosphonic acid (68f): The respective ester derivative was hydrolyzed according to the given general procedure 2.5.2.3. 1H NMR (400 MHz, DMSO) δ 12.67 (s, 1H), 8.35 (d, $J = 8.2$ Hz, 1H), 8.28 (d, $J = 8.2$ Hz, 1H), 8.08 (d, $J = 8.3$ Hz, 1H), 7.94 – 7.82 (m, 2H), 7.77 – 7.64 (m, 3H), 7.58 (t, $J = 7.8$ Hz, 1H), 7.39 (d, $J = 8.7$ Hz, 1H). ^{31}P NMR (162 MHz, DMSO) δ 14.48 (m). Purity 90.9% [Mobile Phase, ACN: Buffer (60:40); RT: 4.882 min].

Synthesis procedure for (1-(1-hydroxy-2-naphthamido)propyl)phosphonic acid (68g): The respective ester derivative was hydrolyzed according to the given general procedure 2.5.2.3. 1H NMR (400 MHz, DMSO) δ 11.78 (s, 1H), 8.31 (d, $J = 8.3$ Hz, 1H), 7.93 (d, $J = 8.1$ Hz, 1H), 7.83 (d, $J = 8.7$ Hz, 1H), 7.74 – 7.69 (m, 1H), 7.65 – 7.59 (m, 1H), 7.48 (d, $J = 8.7$ Hz, 1H), 5.24 (s, 1H), 1.89 (d, $J = 12.2$ Hz, 2H), 0.95 (t, $J = 18.2$ Hz, 3H). ^{31}P NMR (162 MHz, DMSO) δ 14.93 (s).

Synthesis procedure for (1-(1-hydroxy-2-naphthamido)-3-phenylpropyl)phosphonic acid (68h): The respective ester derivative was hydrolyzed according to the given general procedure 2.5.2.3. 1H NMR (400 MHz, DMSO) δ 8.32 (d, $J = 8.3$ Hz, 1H), 7.94 (d, $J = 7.7$ Hz, 1H), 7.83 (d, $J = 8.5$ Hz, 1H), 7.75 – 7.69 (m, 1H), 7.65 – 7.59 (m, 1H), 7.47 (d, $J = 8.9$ Hz, 1H), 7.28 – 7.13 (m, 6H), 5.32 (s, 1H), 2.77 – 2.61 (m, 4H), 2.23 (s, 3H).

Synthesis procedure for ((3,4-dichlorophenyl)(8-hydroxyquinoline-7-carboxamido)methyl)phosphonic acid (71c): The respective ester derivative was hydrolyzed according to the given general procedure 2.5.2.3. 1H NMR (400 MHz, DMSO) δ 9.05 (d, $J = 3.7$ Hz, 1H), 8.70 (d, $J = 8.2$ Hz, 1H), 8.14 (d, $J = 8.8$ Hz, 1H), 7.91 (dd, $J = 8.2, 4.4$ Hz, 1H), 7.78 (s, 1H), 7.68 (d, $J = 8.4$ Hz, 2H), 7.53 (d, $J = 8.8$ Hz, 1H), 6.20 (d, $J = 13.5$ Hz, 1H).

Synthesis procedure for ((4-oxo-4H-chromene-3-carboxamido)(phenyl)methyl)phosphonic acid (73a): The respective ester derivative was hydrolyzed according to the given general procedure 2.5.2.3. 1H NMR (400 MHz, MeOD) δ 7.98 (d, $J = 7.5$ Hz, 1H), 7.54 (d, $J = 7.4$ Hz, 2H), 7.38 (dd, $J = 15.6, 7.9$ Hz, 3H), 7.30 (t, $J = 7.2$ Hz, 1H), 6.96 (dd, $J = 16.1, 7.9$ Hz, 2H), 5.66 (t, $J = 17.3$ Hz, 1H).

^{31}P NMR (162 MHz, DMSO) δ 16.72 (d, $J = 20.8$ Hz). Purity 97.17% [Mobile Phase, ACN: Buffer (70:30); RT: 4.3 min].

2.5.2.5 General procedure followed for the synthesis of 2,3-dihydroxybenzaldehyde derivatives:

A solution of diethyl α -aminophosphonate **58a-b** (1 eq.) in methylene chloride (5 mL) in a round bottom flask equipped with a stir bar and placed on an ice bath. The solution was treated dropwise with acetic acid (1 eq.). To this mixture, 2,3-dihydroxybenzaldehyde (**74**) (1 eq.) was added as a solution in methylene chloride (1 mL), followed by, slow addition of sodium cyanoborohydride (1.5 eq) in small portions. The reaction mixture was stirred at ambient temperature for 14 h. After this, methanol was added to the mixture and all contents transferred to a separatory funnel. The mixture was partitioned (DCM and saturated NaHCO_3). Once neutralized, the organic phase was washed with brine ($\text{NaCl}/\text{H}_2\text{O}$), dried over Na_2SO_4 and concentrated in vacuo to give the reaction mixture. The mixture was purified by flash column chromatography to obtain the desired product **75a-b**.

Synthesis procedure for diethyl (((2,3-dihydroxybenzyl)amino)(phenyl)methyl)phosphonate (75a): Synthesized by using 2,3-dihydroxybenzaldehyde (207.18 mg, 1.5 mmol), diethyl (amino(phenyl)methyl)phosphonate (365 mg, 1.5 mmol), acetic acid (90 mg, 1.5 eqv) and sodium cyanoborohydride (141 mg, 2.25 mmol) according to general procedure 2.5.2.4. After performing the work-up, the crude residue was purified using column chromatography (2-50% ethyl acetate/hexane). Yield: 61%. ^1H NMR (400 MHz, CDCl_3) δ 7.45 – 7.34 (m, 5H), 6.87 (dd, $J = 8.0, 1.4$ Hz, 1H), 6.68 (td, $J = 7.8, 4.1$ Hz, 1H), 6.39 (dd, $J = 7.6, 1.2$ Hz, 1H), 4.21 – 3.87 (m, 5H), 3.76 – 3.62 (m, 2H), 1.38 – 1.32 (m, 3H), 1.09 (t, $J = 7.1$ Hz, 3H).

Synthesis procedure for diethyl (((2,3-dihydroxybenzyl)amino)methyl)phosphonate (75b): Synthesized by using 2,3-dihydroxybenzaldehyde (207.18 mg, 1.5 mmol), diethyl (aminomethyl)phosphonate (250 mg, 1.5 mmol), acetic acid (90 mg, 1.5 eqv) and sodium cyanoborohydride (141 mg, 2.25 mmol) according to general procedure 2.5.2.4. After performing the work-up, the crude residue was purified using column chromatography (2-50% ethyl acetate/hexane). ^1H NMR (400 MHz, CDCl_3) δ 7.00 – 6.56 (m, 3H), 4.22 – 4.12 (m, 4H), 3.44 – 3.06 (m, 2H), 2.29 – 1.99 (m, 2H), 1.37 – 1.34 (m, 6H).

2.5.2.6 Synthesis procedure for hydrolyzed derivatives (76a-b):

Synthetic route was followed according to Scheme 2.8. To a mixture of ester derivatives **75a-b** (1 eq.), synthesized in the previous step, in dry dichloromethane (2 mL), TMSBr (10 eq.) was added at 0 °C dropwise. After 1 h, the solution was allowed to warm to room temperature and stirred for an additional 23 h. After completion of the reaction, the solvent was removed under reduced pressure, and the remaining residue was dissolved in mixture of tetrahydrofuran and water (9:1). After 30 min the solvent was evaporated and washed with dichloromethane to remove nonpolar impurities and remaining TMSBr. The resulting residue dried *in vacuo* overnight and characterized further by NMR and mass spectroscopy.

Synthesis procedure for (((2,3-dihydroxybenzyl)amino)(phenyl)methyl)phosphonic acid (76a): The respective ester derivative was hydrolyzed according to the given general procedure 2.5.2.5. ¹H NMR (400 MHz, CD₃OD_SPE) δ 7.52 (d, *J* = 19.8 Hz, 5H), 6.89 (d, *J* = 7.7 Hz, 1H), 6.72 (t, *J* = 7.8 Hz, 1H), 6.60 (d, *J* = 7.4 Hz, 1H), 4.49 (d, *J* = 17.1 Hz, 1H), 4.20 (dd, *J* = 52.2, 13.1 Hz, 2H).

Synthesis procedure for (((2,3-dihydroxybenzyl)amino)methyl)phosphonic acid (76b): The respective ester derivative was hydrolyzed according to the given general procedure 2.5.2.5. ¹H NMR (400 MHz, MeOD) δ 6.81 – 6.21 (m, 3H), 3.76 (d, *J* = 12.8 Hz, 2H), 3.27 (d, *J* = 46.1 Hz, 2H).

2.5.2.7 Synthesis procedure of compounds 79a-b:

Synthetic route was followed according to Scheme 2.9; a mixture of 2-Hydroxy-1,4-naphthoquinone (1 eq.) and benzyl bromide (0.8 eq.) was suspended in DMF. Potassium carbonate (2 eq.) and potassium iodide (0.5 mmol) were added, and the reaction was stirred at 70 °C for overnight. After the reaction, water was added to the reaction mixture, and the mixture was extracted in ethyl acetate (50 mL × 3). The combined organic layers were dried over anhydrous sodium sulfate, filtered, and concentrated *in vacuo*. The crude alkylated products were purified using ethyl acetate-hexane solvent by column chromatography (1:9 – 3:7 v/v).

C-alkylated product 2-benzyl-3-hydroxynaphthalene-1,4-dione (79a): ¹H NMR (400 MHz, CDCl₃) δ 8.14 (dd, *J* = 7.7, 0.9 Hz, 1H), 8.09 (dd, *J* = 7.6, 1.0 Hz, 1H), 7.77 (td, *J* = 7.6, 1.4 Hz, 1H), 7.70 (td, *J* = 7.5, 1.4 Hz, 1H), 7.45 – 7.40 (m, 3H), 7.44 – 7.39 (m, 3H), 7.30 (d, *J* = 1.7 Hz, 1H), 7.20 (t, *J* = 7.3 Hz, 1H), 3.97 (s, 2H), 3.97 (s, 2H).

O-alkylated product 2-(benzyloxy)naphthalene-1,4-dione (79b): ^1H NMR (400 MHz, CDCl_3) δ 8.17 (dt, $J = 6.4, 4.2$ Hz, 1H), 8.13 – 8.08 (m, 1H), 7.79 – 7.73 (m, 2H), 7.48 – 7.37 (m, 4H), 6.25 (s, 1H), 5.17 (s, 2H).

Synthesis procedure of diethyl (2-((1,4-dioxo-1,4-dihydronaphthalen-2-yl)oxy)ethyl)phosphonate (81a): Synthetic route was followed according to Scheme 2.9, A mixture of 2-Hydroxy-1,4-naphthoquinone (100 mg, 0.58 mmol, 1 eq.) and Diethyl(2-bromoethyl)phosphonate (127.4 mg, 0.52 mmol, 0.9 eq.) was suspended in DMF. Lithium carbonate (66 mg, 1.74 mmol, 3 eq.) and potassium iodide (97 mg, 0.58 mmol, 1 eq.) were added, and the reaction was stirred at 70 °C overnight. The crude alkylated product was purified by column chromatography 1:99-5:95 v/v (MeOH/DCM) solvent system. Two different purified compounds were collected and analyzed by NMR spectroscopy. ^1H NMR (400 MHz, CDCl_3) δ 8.09 – 8.00 (m, 2H), 7.78 – 7.62 (m, 2H), 6.16 (s, 1H), 4.32 – 4.02 (m, 4H), 3.35 (dd, $J = 8.8, 5.4$ Hz, 4H), 2.39 – 2.30 (m, 3H), 1.99 – 1.93 (m, 3H).

Synthesis procedure for diethyl (3-((1,4-dioxo-1,4-dihydronaphthalen-2-yl)oxy)propyl)phosphonate (81b): Synthetic route was followed according to **scheme 8**, A mixture of 2-Hydroxy-1,4-naphthoquinone (49 mg, 0.25 mmol, 1 eq.) and Diethyl(3-bromopropyl)phosphonate (65 mg, 0.25 mmol, 0.1 eq.) was suspended in DMF. Lithium carbonate (33 mg, 0.75 mmol, 3 eq.) was added, and the reaction was stirred at 70 °C overnight according to general synthesis procedure 14. The crude alkylated product was purified by column chromatography 1:99-5:95 (MeOH/DCM) solvent system. *O*-alkylated product was formed. ^1H NMR (400 MHz, CDCl_3) δ 8.11 (ddt, $J = 23.2, 22.3, 11.6$ Hz, 2H), 7.82 – 7.67 (m, 2H), 6.18 (s, 1H), 4.22 – 4.05 (m, 4H), 2.31 – 2.17 (m, 2H), 2.05 – 1.87 (m, 2H), 1.35 (t, $J = 7.1$ Hz, 6H).

2.5.3 Biological evaluation:

2.5.3.1 DXR enzyme inhibition screening

For DXR enzyme inhibition screening, commercially available DXR enzyme inhibition assay kits from Echelon Biosciences (Product Number: K-2000C) were utilized. Assay was performed according to the given protocol provided with the assay kit. Initially, 13 commercially obtained fragments were selected, weighed, and diluted to a concentration of 100 μM . Percentage inhibition for DXR enzyme was calculated for each fragment at given concentration. A few derivatives of the 6 fragments were synthesized based on the inhibition obtained. Out of these, 17 compounds were

selected, weighed, and dilutions of 50 μM were made and plated in duplicates in a 96-well plate format for screening. Controls and plated compounds were pre-incubated with the DXR enzyme with shaking for 10 minutes, followed by the addition of a Deoxy-xylulose Phosphate (DXP) substrate to initiate the reaction. The absorbance was recorded in kinetic mode at 340 nm. The DXR Inhibitor Screen monitors a decrease in β -NADPH levels which directly corresponds with the conversion of the DXP substrate to MEP product. Data were analyzed for the percentage inhibition at a given concentration. Further, the compounds showing more than 80% inhibition at 50 μM were selected, and 5 different diluted concentrations, i.e., 100 μM , 50 μM , 10 μM , 1 μM , and 0.1 μM were prepared and tested for IC_{50} evaluation of the selected compounds according to the earlier mention procedure for DXR enzyme inhibition.

A few compounds were sent to collaborators to perform cell-based DXR inhibition. A total of 7 compounds were tested for cell growth inhibition in different gram-positive and gram-negative pathogens. Kanamycin was used as a positive control. Various pathogens included in the study were *Acinetobacter baumannii*, *E. coli*, *Klebsiella pneumoniae*, *Pseudomonas aeruginosa*, *Salmonella typhimurium*, *Staphylococcus aureus*, and *Vibrio cholerae* at 500 μM concentration. The percentage of cell viability of the pathogens was noted.

2.5.3.2 Screening of compounds against *M. tuberculosis* and ESKAPE pathogens.

Bacterial cultures were diluted to OD 600 of 0.02 in the culture medium, and 200 μL of each of these cultures was dispensed in the 96-well plate. For initial screening, bacteria were incubated with 500 μM drugs, freshly dissolved in DMSO, and growth was visually monitored after 24 hours (ESKAPE pathogens) or two weeks (*M. tuberculosis*) of incubation at 37 $^{\circ}\text{C}$. Bacteria cultured in the presence of DMSO were simultaneously used as controls. After initial screening, minimum inhibitory concentration (MIC) was determined for molecules that exhibit suppression at 500 μM . For this, bacterial cultures at OD 600 of 0.02 were incubated with a serial dilution of molecules ranging from 500- 7.8 μM followed by the analysis of viability by Alamar Blue cell viability assay (Thermo Fisher), as suggested by the manufacturer. The concentration at which growth is reduced by \sim 85-90% was considered as MIC against a particular pathogen.

REFERENCES

- (1) Gershenzon, J.; Dudareva, N. The Function of Terpene Natural Products in the Natural World. *Nature Chemical Biology*. Nature Publishing Group 2007, pp 408–414. <https://doi.org/10.1038/nchembio.2007.5>.
- (2) Duke, S. O.; Dayan, F. E.; Romagni, J. G.; Rimando, A. M. Natural Products as Sources of Herbicides: Current Status and Future Trends. *Weed Res.* **2000**, *40* (1), 99–111. <https://doi.org/10.1046/j.1365-3180.2000.00161.x>.
- (3) Dickschat, J. S. Bacterial Terpene Cyclases. *Nat. Prod. Rep.* **2016**, *33* (1), 87–110. <https://doi.org/10.1039/c5np00102a>.
- (4) Frank, A.; Groll, M. The Methylerythritol Phosphate Pathway to Isoprenoids. *Chem. Rev.* **2017**, *117* (8), 5675–5703. <https://doi.org/10.1021/acs.chemrev.6b00537>.
- (5) Sacchettini, J. C.; Poulter, C. D. Creating Isoprenoid Diversity. **1997**, *2* (September).
- (6) Ajikumar, P. K.; Tyo, K.; Carlsen, S.; Mucha, O.; Phon, T. H.; Stephanopoulos, G. Terpenoids: Opportunities for Biosynthesis of Natural Product Drugs Using Engineered Microorganisms. *Mol. Pharm.* **2008**, *5* (2), 167–190. <https://doi.org/10.1021/mp700151b>.
- (7) Rohmer, M.; Knani, M.; Simonin, P.; Sutter, B.; Sahm, H. Isoprenoid Biosynthesis in Bacteria: A Novel Pathway for the Early Steps Leading to Isopentenyl Diphosphate. *Biochem. J.* **1993**, *295* (2), 517–524. <https://doi.org/10.1042/bj2950517>.
- (8) Rohmer, M.; Seemann, M.; Horbach, S.; Bringer-Meyer, S.; Sahm, H. Glyceraldehyde 3-Phosphate and Pyruvate as Precursors of Isoprenic Units in an Alternative Non-Mevalonate Pathway for Terpenoid Biosynthesis. *J. Am. Chem. Soc.* **1996**, *118* (11), 2564–2566. <https://doi.org/10.1021/ja9538344>.
- (9) Rohdich, F.; Kis, K.; Bacher, A.; Eisenreich, W. Genes, Enzymes and Intermediates. *Curr. Opin. Chem. Biol.* **2001**, *5* (5), 535–540.
- (10) Zhao, L.; Chang, W.; Xiao, Y.; Liu, H.; Liu, P. Methylerythritol Phosphate Pathway of Isoprenoid Biosynthesis. *Annu. Rev. Biochem.* **2013**, *82* (1), 497–530. <https://doi.org/10.1146/annurev-biochem-052010-100934>.
- (11) Proteau, P. J. 1-Deoxy-D-Xylulose 5-Phosphate Reductoisomerase: An Overview. *Bioorg. Chem.* **2004**, *32* (6), 483–493.

<https://doi.org/10.1016/j.bioorg.2004.08.004>.

- (12) Takahashi, S.; Kuzuyama, T.; Watanabe, H.; Seto, H. A 1-Deoxy-d-Xylulose 5-Phosphate Reductoisomerase Catalyzing the Formation of 2-C-Methyl-d-Erythritol 4-Phosphate in an Alternative Nonmevalonate Pathway for Terpenoid Biosynthesis. *Proc. Natl. Acad. Sci.* **1998**, *95* (17), 9879–9884. <https://doi.org/10.1073/PNAS.95.17.9879>.
- (13) Wang, X.; Dowd, C. S. The Methylerythritol Phosphate Pathway: Promising Drug Targets in the Fight against Tuberculosis. *ACS Infect. Dis.* **2018**, *4* (3), 278–290. <https://doi.org/10.1021/acsinfecdis.7b00176>.
- (14) *biorender*. <https://app.biorender.com/biorender-templates>.
- (15) Masini, T.; Hirsch, A. K. H. Development of Inhibitors of the 2C-Methyl-D-Erythritol 4-Phosphate (MEP) Pathway Enzymes as Potential Anti-Infective Agents. *J. Med. Chem.* **2014**, *57* (23), 9740–9763. <https://doi.org/10.1021/jm5010978>.
- (16) Singh, N.; Chev e, G.; Avery, M. A.; McCurdy, C. R. Targeting the Methyl Erythritol Phosphate (MEP) Pathway for Novel Antimalarial, Antibacterial and Herbicidal Drug Discovery: Inhibition of 1-Deoxy-D-Xylulose-5-Phosphate Reductoisomerase (DXR) Enzyme. *Curr. Pharm. Des.* **2007**, *13* (11), 1161–1177. <https://doi.org/10.2174/138161207780618939>.
- (17) Imlay, L.; Odom, A. R. Isoprenoid Metabolism in Apicomplexan Parasites. *Current Clinical Microbiology Reports*. Springer December **2014**, pp 37–50. <https://doi.org/10.1007/s40588-014-0006-7>.
- (18) Heuston, S.; Begley, M.; Gahan, C. G. M.; Hill, C. Isoprenoid Biosynthesis in Bacterial Pathogens. *Microbiol. (United Kingdom)* **2012**, *158* (6), 1389–1401. <https://doi.org/10.1099/mic.0.051599-0>.
- (19) Wang, S.; Li, M.; Luo, X.; Yu, L.; Nie, Z.; Liu, Q.; An, X.; Ao, Y.; Liu, Q.; Chen, J.; Tian, Y.; Zhao, J.; He, L. Inhibitory Effects of Fosmidomycin Against Babesia Microti in Vitro. *Front. Cell Dev. Biol.* **2020**, *8*, 247. <https://doi.org/10.3389/fcell.2020.00247>.
- (20) Edwards, R. L.; Heueck, I.; Lee, S. G.; Shah, I. T.; Miller, J. J.; Jezewski, A. J.; Mikati, M. O.; Wang, X.; Brothers, R. C.; Heidel, K. M.; Osbourn, D. M.; Burnham, C.-A. D.; Alvarez, S.; Fritz, S. A.; Dowd, C. S.; Jez, J. M.; Odom John, A. R. Potent, Specific MEPicides for Treatment of Zoonotic

- Staphylococci. *PLOS Pathog.* **2020**, *16* (6), e1007806. <https://doi.org/10.1371/journal.ppat.1007806>.
- (21) Jackson, E. R.; Dowd, C. S. Inhibition of 1-Deoxy-D-Xylulose-5-Phosphate Reductoisomerase (Dxr): A Review of the Synthesis and Biological Evaluation of Recent Inhibitors. *Curr. Top. Med. Chem.* **2012**, *12* (7), 706–728.
- (22) Bhutta, Z. A.; Salam, R. A.; Das, J. K.; Lassi, Z. S. Tackling the Existing Burden of Infectious Diseases in the Developing World: Existing Gaps and the Way Forward. *Infect. Dis. Poverty* **2014**, *3* (1), 1–6. <https://doi.org/10.1186/2049-9957-3-28>.
- (23) Rodriguez-Concepcion, M. The MEP Pathway: A New Target for the Development of Herbicides, Antibiotics and Antimalarial Drugs. *Curr. Pharm. Des.* **2005**, *10* (19), 2391–2400. <https://doi.org/10.2174/1381612043384006>.
- (24) Seto, H.; Watanabe, H.; Furihata, K. Simultaneous Operation of the Mevalonate and Non-Mevalonate Pathways in the Biosynthesis of Isopentenyl Diphosphate in *Streptomyces Aeriouvifer*. *Tetrahedron Lett.* **1996**, *37* (44), 7979–7982. [https://doi.org/10.1016/0040-4039\(96\)01787-X](https://doi.org/10.1016/0040-4039(96)01787-X).
- (25) Argyrou, A.; Blanchard, J. S. Kinetic and Chemical Mechanism of Mycobacterium Tuberculosis 1-Deoxy-D-Xylulose-5-Phosphate Isomeroreductase. *Biochemistry* **2004**, *43* (14), 4375–4384. <https://doi.org/10.1021/bi049974k>.
- (26) Jomaa, H.; Wiesner, J.; Sanderbrand, S.; Altincicek, B.; Weidemeyer, C.; Hintz, M.; Türbachova, I.; Eberl, M.; Zeidler, J.; Lichtenthaler, H. K.; Soldati, D.; Beck, E. Inhibitors of the Nonmevalonate Pathway of Isoprenoid Biosynthesis as Antimalarial Drugs. *Science* (80-.). **1999**, *285* (5433), 1573–1576. <https://doi.org/10.1126/science.285.5433.1573>.
- (27) Hoeffler, J. F.; Tritsch, D.; Grosdemange-Billiard, C.; Rohmer, M. Isoprenoid Biosynthesis via the Methylerythritol Phosphate Pathway. Mechanistic Investigations of the 1-Deoxy-D-Xylulose 5-Phosphate Reductoisomerase. *Eur. J. Biochem.* **2002**, *269* (18), 4446–4457. <https://doi.org/10.1046/j.1432-1033.2002.03150.x>.
- (28) Wong, U.; Cox, R. J. The Chemical Mechanism OfD-1-Deoxyxylulose-5-Phosphate Reductoisomerase FromEscherichia Coli. *Angew. Chemie* **2007**, *119* (26), 5014–5017. <https://doi.org/10.1002/ange.200700647>.

- (29) Wang, X.; Ahn, Y. M.; Lentscher, A. G.; Lister, J. S.; Brothers, R. C.; Kneen, M. M.; Gerratana, B.; Boshoff, H. I.; Dowd, C. S. Design, Synthesis, and Evaluation of Substituted Nicotinamide Adenine Dinucleotide (NAD⁺) Synthetase Inhibitors as Potential Antitubercular Agents. *Bioorganic Med. Chem. Lett.* **2017**, *27* (18), 4426–4430. <https://doi.org/10.1016/j.bmcl.2017.08.012>.
- (30) Munos, J. W.; Pu, X.; Mansoorabadi, S. O.; Kim, H. J.; Liu, H. W. A Secondary Kinetic Isotope Effect Study of the 1-Deoxy-D-Xylulose-5- Phosphate Reductoisomerase-Catalyzed Reaction: Evidence for a Retroaldol-Aldol Rearrangement. *J. Am. Chem. Soc.* **2009**, *131* (6), 2048–2049. <https://doi.org/10.1021/ja807987h>.
- (31) Murkin, A. S.; Manning, K. A.; Kholodar, S. A. Mechanism and Inhibition of 1-Deoxy-d-Xylulose-5-Phosphate Reductoisomerase. *Bioorg. Chem.* **2014**, *57*, 171–185. <https://doi.org/10.1016/j.bioorg.2014.06.001>.
- (32) Lauw, S.; Illarionova, V.; Bacher, A.; Rohdich, F.; Eisenreich, W. Biosynthesis of Isoprenoids - Studies on the Mechanism of 2C-Methyl-d-Erythritol-4-Phosphate Synthase. *FEBS J.* **2008**, *275* (16), 4060–4073. <https://doi.org/10.1111/j.1742-4658.2008.06547.x>.
- (33) Wong, A.; Munos, J. W.; Devasthali, V.; Johnson, K. A.; Liu, H. W. Study of 1-Deoxy-D-Xylulose-5-Phosphate Reductoisomerase: Synthesis and Evaluation of Fluorinated Substrate Analogues. *Org. Lett.* **2004**, *6* (20), 3625–3628. <https://doi.org/10.1021/ol048459b>.
- (34) Li, H.; Tian, J.; Sun, W.; Qin, W.; Gao, W. Y. Mechanistic Insights into 1-Deoxy- d -Xylulose 5-Phosphate Reductoisomerase, a Key Enzyme of the MEP Terpenoid Biosynthetic Pathway. *FEBS J.* **2013**, *280* (22), 5896–5905. <https://doi.org/10.1111/febs.12516>.
- (35) Sweeney, A. Mac; Lange, R.; Fernandes, R. P. M.; Schulz, H.; Dale, G. E.; Douangamath, A.; Proteau, P. J.; Oefner, C. The Crystal Structure of E. Coli 1-Deoxy-D-Xylulose-5-Phosphate Reductoisomerase in a Ternary Complex with the Antimalarial Compound Fosmidomycin and NADPH Reveals a Tight-Binding Closed Enzyme Conformation. *J. Mol. Biol.* **2005**, *345* (1), 115–127. <https://doi.org/10.1016/j.jmb.2004.10.030>.
- (36) Steinbacher, S.; Kaiser, J.; Eisenreich, W.; Huber, R.; Bacher, A.; Rohdich, F.

- Structural Basis of Fosmidomycin Action Revealed by the Complex with 2-C-Methyl-D-Erythritol 4-Phosphate Synthase (IspC). Implications for the Catalytic Mechanism and Anti-Malaria Drug Development. *J. Biol. Chem.* **2003**, 278 (20), 18401–18407. <https://doi.org/10.1074/jbc.M300993200>.
- (37) Reuter, K.; Sanderbrand, S.; Jomaa, H.; Wiesner, J.; Steinbrecher, I.; Beck, E.; Hintz, M.; Klebe, G.; Stubbs, M. T. Crystal Structure of 1-Deoxy-D-Xylulose-5-Phosphate Reductoisomerase, a Crucial Enzyme in the Non-Mevalonate Pathway of Isoprenoid Biosynthesis. *J. Biol. Chem.* **2002**, 277 (7), 5378–5384. <https://doi.org/10.1074/jbc.M109500200>.
- (38) Henriksson, L. M.; Unge, T.; Carlsson, J.; Åqvist, J.; Mowbray, S. L.; Jones, T. A. Structures of Mycobacterium Tuberculosis 1-Deoxy-D-Xylulose-5-Phosphate Reductoisomerase Provide New Insights into Catalysis. *J. Biol. Chem.* **2007**, 282 (27), 19905–19916. <https://doi.org/10.1074/jbc.M701935200>.
- (39) Henriksson, L. M.; Björkelid, C.; Mowbray, S. L.; Unge, T. The 1.9 Å Resolution Structure of Mycobacterium Tuberculosis 1-Deoxy-D-Xylulose 5-Phosphate Reductoisomerase, a Potential Drug Target. *Acta Crystallogr. Sect. D Biol. Crystallogr.* **2006**, 62 (7), 807–813. <https://doi.org/10.1107/S0907444906019196>.
- (40) Chofor, R.; Sooriyaarachchi, S.; Risseeuw, M. D. P.; Bergfors, T.; Pouyez, J.; Johny, C.; Haymond, A.; Everaert, A.; Dowd, C. S.; Maes, L.; Coenye, T.; Alex, A.; Couch, R. D.; Jones, T. A.; Wouters, J.; Mowbray, S. L.; Van Calenbergh, S. Synthesis and Bioactivity of β -Substituted Fosmidomycin Analogues Targeting 1-Deoxy-D-Xylulose-5-Phosphate Reductoisomerase. *J. Med. Chem.* **2015**, 58 (7), 2988–3001. <https://doi.org/10.1021/jm5014264>.
- (41) Kunfermann, A.; Lienau, C.; Illarionov, B.; Held, J.; Gräwert, T.; Behrendt, C. T.; Werner, P.; Hähn, S.; Eisenreich, W.; Riederer, U.; Mordmüller, B.; Bacher, A.; Fischer, M.; Groll, M.; Kurz, T. IspC as Target for Antiinfective Drug Discovery: Synthesis, Enantiomeric Separation, and Structural Biology of Fosmidomycin Thia Isosters. *J. Med. Chem.* **2013**, 56 (20), 8151–8162. <https://doi.org/10.1021/jm4012559>.
- (42) Kholodar, S. A.; Tomblin, G.; Liu, J.; Tan, Z.; Allen, C. L.; Gulick, A. M.; Murkin, A. S. Alteration of the Flexible Loop in 1-Deoxy- d -Xylulose-5-Phosphate Reductoisomerase Boosts Enthalpy-Driven Inhibition by

- Fosmidomycin. *Biochemistry* **2014**, *53* (21), 3423–3431. <https://doi.org/10.1021/bi5004074>.
- (43) Jansson, A. M.; Wiećkowska, A.; Björkelid, C.; Yahiaoui, S.; Sooriyaarachchi, S.; Lindh, M.; Bergfors, T.; Dharavath, S.; Desroses, M.; Suresh, S.; Andaloussi, M.; Nikhil, R.; Sreevalli, S.; Srinivasa, B. R.; Larhed, M.; Jones, T. A.; Karlén, A.; Mowbray, S. L. DXR Inhibition by Potent Mono- and Disubstituted Fosmidomycin Analogues. *J. Med. Chem.* **2013**, *56* (15), 6190–6199. <https://doi.org/10.1021/jm4006498>.
- (44) Deng, L.; Endo, K.; Kato, M.; Cheng, G.; Yajima, S.; Song, Y. Structures of 1-Deoxy-D-Xylulose-5-Phosphate Reductoisomerase/Lipophilic Phosphonate Complexes. *ACS Med. Chem. Lett.* **2011**, *2* (2), 165–170. <https://doi.org/10.1021/ml100243r>.
- (45) Henriksson, L. M.; Unge, T.; Carlsson, J.; Åqvist, J.; Mowbray, S. L.; Jones, T. A. Structures of Mycobacterium Tuberculosis 1-Deoxy-D-Xylulose-5-Phosphate Reductoisomerase Provide New Insights into Catalysis. *J. Biol. Chem.* **2007**, *282* (27), 19905–19916. <https://doi.org/10.1074/jbc.M701935200>.
- (46) Umeda, T.; Tanaka, N.; Kusakabe, Y.; Nakanishi, M.; Kitade, Y.; Nakamura, K. T. Crystallization and Preliminary X-Ray Crystallographic Study of 1-Deoxy-d-Xylulose 5-Phosphate Reductoisomerase from Plasmodium Falciparum. *Acta Crystallogr. Sect. F Struct. Biol. Cryst. Commun.* **2010**, *66* (3), 330–332. <https://doi.org/10.1107/S1744309110001739>.
- (47) Yajima, S.; Nonaka, T.; Kuzuyama, T.; Seto, H.; Ohsawa, K. Crystal Structure of 1-Deoxy-D-Xylulose 5-Phosphate Reductoisomerase Complexed with Cofactors: Implications of a Flexible Loop Movement upon Substrate Binding. *J. Biochem.* **2002**, *131* (3), 313–317. <https://doi.org/10.1093/oxfordjournals.jbchem.a003105>.
- (48) Yajima, S.; Hara, K.; Iino, D.; Sasaki, Y.; Kuzuyama, T.; Ohsawa, K.; Seto, H. Structure of 1-Deoxy-D-Xylulose 5-Phosphate Reductoisomerase in a Quaternary Complex with a Magnesium Ion, NADPH and the Antimalarial Drug Fosmidomycin. *Acta Crystallogr. Sect. F Struct. Biol. Cryst. Commun.* **2007**, *63* (6), 466–470. <https://doi.org/10.1107/S1744309107024475>.
- (49) Takenoya, M.; Ohtaki, A.; Noguchi, K.; Endo, K.; Sasaki, Y.; Ohsawa, K.; Yajima, S.; Yohda, M. Crystal Structure of 1-Deoxy-d-Xylulose 5-Phosphate

- Reductoisomerase from the Hyperthermophile *Thermotoga Maritima* for Insights into the Coordination of Conformational Changes and an Inhibitor Binding. *J. Struct. Biol.* **2010**, *170* (3), 532–539. <https://doi.org/10.1016/j.jsb.2010.03.015>.
- (50) Edwards, R. L.; Brothers, R. C.; Wang, X.; Maron, M. I.; Ziniel, P. D.; Tsang, P. S.; Kraft, T. E.; Hruz, P. W.; Williamson, K. C.; Dowd, C. S.; John, A. R. O. MEPicides: Potent Antimalarial Prodrugs Targeting Isoprenoid Biosynthesis. *Sci. Rep.* **2017**, *7* (1), 1–11. <https://doi.org/10.1038/s41598-017-07159-y>.
- (51) Rodríguez-Concepción, M.; Campos, N.; María Lois, L.; Maldonado, C.; Hoeffler, J. F.; Grosdemange-Billiard, C.; Rohmer, M.; Boronat, A. Genetic Evidence of Branching in the Isoprenoid Pathway for the Production of Isopentenyl Diphosphate and Dimethylallyl Diphosphate in *Escherichia Coli*. *FEBS Lett.* **2000**, *473* (3), 328–332. [https://doi.org/10.1016/S0014-5793\(00\)01552-0](https://doi.org/10.1016/S0014-5793(00)01552-0).
- (52) Brown, A. C.; Parish, T. Dxr Is Essential in *Mycobacterium Tuberculosis* and Fosmidomycin Resistance Is Due to a Lack of Uptake. *BMC Microbiol.* **2008**, *8*, 1–9. <https://doi.org/10.1186/1471-2180-8-78>.
- (53) Umeda, T.; Tanaka, N.; Kusakabe, Y.; Nakanishi, M.; Kitade, Y.; Nakamura, K. T. Molecular Basis of Fosmidomycin's Action on the Human Malaria Parasite *Plasmodium Falciparum*. *Sci. Rep.* **2011**, *1*, 1–8. <https://doi.org/10.1038/srep00009>.
- (54) Masini, T.; Hirsch, A. K. H. Development of Inhibitors of the 2C-Methyl-D-Erythritol 4-Phosphate (MEP) Pathway Enzymes as Potential Anti-Infective Agents. *J. Med. Chem.* **2014**, *57* (23), 9740–9763. <https://doi.org/10.1021/jm5010978>.
- (55) OKUHARA, M.; KURODA, Y.; GOTO, T.; OKAMOTO, M.; TERANO, H.; KOHSAKA, M.; AOKI, H.; IMANAKA, H. Studies on New Phosphonic Acid Antibiotics. I. FR-900098, Isolation and Characterization. *J. Antibiot. (Tokyo)*. **1980**, *33* (1), 13–17. <https://doi.org/10.7164/antibiotics.33.13>.
- (56) Okuhara, M.; Kuroda, Y.; Goto, T.; Okamoto, M.; Terano, H.; Kohsaka, M.; Aoki, H.; Imanaka, H. Studies on New Phosphonic Acid Antibiotics III. Isolation and Characterization of Fr-31564, FR-32863 and FR-33289. *J. Antibiot. (Tokyo)*. **1980**, *33* (1), 24–28. <https://doi.org/10.7164/antibiotics.33.24>.

- (57) Iguchi, E.; Okuhara, M.; Kohsaka, M.; Aoki, H.; Imanaka, H. Studies on New Phosphonic Acid Antibiotics. II. Taxonomic Studies on Producing Organisms of the Phosphonic Acid and Related Compounds. *J. Antibiot. (Tokyo)*. **1980**, *33*, 19–23.
- (58) Neu, H. C.; Kamimura, T. In Vitro and in Vivo Antibacterial Activity of FR-31564, a Phosphonic Acid Antimicrobial Agent. *Antimicrob. Agents Chemother.* **1981**, *19* (6), 1013–1023. <https://doi.org/10.1128/AAC.19.6.1013>.
- (59) Antibiotics, O. F. To FR-315643'. Drugs Recently Similar. **1981**, 876–883.
- (60) Kuzuyama, T.; Shimizu, T.; Takahashi, S.; Seto, H. Fosmidomycin, a Specific Inhibitor of 1-Deoxy-D-Xylulose 5-Phosphate Reductoisomerase in the Nonmevalonate Pathway for Terpenoid Biosynthesis. *Tetrahedron Lett.* **1998**, *39* (43), 7913–7916. [https://doi.org/10.1016/S0040-4039\(98\)01755-9](https://doi.org/10.1016/S0040-4039(98)01755-9).
- (61) Armstrong, C. M.; Meyers, D. J.; Imlay, L. S.; Meyers, C. F.; Odom, A. R. Resistance to the Antimicrobial Agent Fosmidomycin and an FR900098 Prodrug through Mutations in the Deoxyxylulose Phosphate Reductoisomerase Gene (Dxr). *Antimicrob. Agents Chemother.* **2015**, *59* (9), 5511–5519. <https://doi.org/10.1128/AAC.00602-15>.
- (62) Koppisch, A. T.; Fox, D. T.; Blagg, B. S. J.; Poulter, C. D. E. Coli MEP Synthase: Steady-State Kinetic Analysis and Substrate Binding. *Biochemistry* **2002**, *41* (1), 236–243. <https://doi.org/10.1021/bi0118207>.
- (63) Jackson, E. R.; Dowd, C. S. Inhibition of 1-Deoxy-D-Xylulose-5-Phosphate Reductoisomerase (Dxr): A Review of the Synthesis and Biological Evaluation of Recent Inhibitors. *Curr. Top. Med. Chem.* **2012**, *12* (7), 706–728.
- (64) Chofer, R.; Sooriyaarachchi, S.; Risseeuw, M. D. P.; Bergfors, T.; Pouyez, J.; Johny, C.; Haymond, A.; Everaert, A.; Dowd, C. S.; Maes, L.; Coenye, T.; Alex, A.; Couch, R. D.; Jones, T. A.; Wouters, J.; Mowbray, S. L.; Van Calenbergh, S. Synthesis and Bioactivity of β -Substituted Fosmidomycin Analogues Targeting 1-Deoxy-D-Xylulose-5-Phosphate Reductoisomerase. *J. Med. Chem.* **2015**, *58* (7), 2988–3001. <https://doi.org/10.1021/jm5014264>.
- (65) Brown, A. C.; Parish, T. Dxr Is Essential in Mycobacterium Tuberculosis and Fosmidomycin Resistance Is Due to a Lack of Uptake. *BMC Microbiol.* **2008**, *8*, 1–9. <https://doi.org/10.1186/1471-2180-8-78>.
- (66) Dhiman, R. K.; Schaeffer, M. L.; Bailey, A. M.; Testa, C. A.; Scherman, H.;

- Crick, D. C. 1-Deoxy-D-Xylulose 5-Phosphate Reductoisomerase (IspC) from *Mycobacterium Tuberculosis*: Towards Understanding Mycobacterial Resistance to Fosmidomycin. *J. Bacteriol.* **2005**, *187* (24), 8395–8402. <https://doi.org/10.1128/JB.187.24.8395-8402.2005>.
- (67) Sakamoto, Y.; Furukawa, S.; Ogihara, H.; Yamasaki, M. Fosmidomycin Resistance in Adenylate Cyclase Deficient (Cya) Mutants of *Escherichia Coli*. *Biosci. Biotechnol. Biochem.* **2003**, *67* (9), 2030–2033. <https://doi.org/10.1271/bbb.67.2030>.
- (68) Uh, E.; Jackson, E. R.; San Jose, G.; Maddox, M.; Lee, R. E.; Lee, R. E.; Boshoff, H. I.; Dowd, C. S. Antibacterial and Antitubercular Activity of Fosmidomycin, FR900098, and Their Lipophilic Analogs. *Bioorganic Med. Chem. Lett.* **2011**, *21* (23), 6973–6976. <https://doi.org/10.1016/j.bmcl.2011.09.123>.
- (69) Nair, S. C.; Brooks, C. F.; Goodman, C. D.; Sturm, A.; McFadden, G. I.; Sundriyal, S.; Anglin, J. L.; Song, Y.; Moreno, S. N.; Striepen, B. Apicoplast Isoprenoid Precursor Synthesis and the Molecular Basis of Fosmidomycin Resistance in *Toxoplasma Gondii*. *J. Exp. Med.* **2011**, *208* (7), 1547–1559. <https://doi.org/10.1084/jem.20110039>.
- (70) Björkelid, C.; Bergfors, T.; Unge, T.; Mowbray, S. L.; Jones, T. A. Structural Studies on *Mycobacterium Tuberculosis* DXR in Complex with the Antibiotic FR-900098. *Acta Crystallogr. Sect. D Biol. Crystallogr.* **2012**, *68* (2), 134–143. <https://doi.org/10.1107/S0907444911052231>.
- (71) Mac Sweeney, A.; Lange, R.; Fernandes, R. P. M.; Schulz, H.; Dale, G. E.; Douangamath, A.; Proteau, P. J.; Oefner, C. The Crystal Structure of *E. Coli* 1-Deoxy-D-Xylulose-5-Phosphate Reductoisomerase in a Ternary Complex with the Antimalarial Compound Fosmidomycin and NADPH Reveals a Tight-Binding Closed Enzyme Conformation. *J. Mol. Biol.* **2005**, *345* (1), 115–127. <https://doi.org/10.1016/j.jmb.2004.10.030>.
- (72) Woo, Y. H.; Fernandes, R. P. M.; Proteau, P. J. Evaluation of Fosmidomycin Analogs as Inhibitors of the *Synechocystis* Sp. PCC6803 1-Deoxy-D-Xylulose 5-Phosphate Reductoisomerase. *Bioorganic Med. Chem.* **2006**, *14* (7), 2375–2385. <https://doi.org/10.1016/j.bmc.2005.11.012>.
- (73) Mercklé, L.; Andrés-Gómez, A. De; Dick, B.; Cox, R. J.; Godfrey, C. R. A. A Fragment-Based Approach to Understanding Inhibition of 1-Deoxy-D-

- Xylulose-5-Phosphate Reductoisomerase. *ChemBioChem* **2005**, *6* (10), 1866–1874. <https://doi.org/10.1002/cbic.200500061>.
- (74) Hunsche, S.; Wienecke, K.; Kurz, H. Rapid Communication. *J. Biochem.* **2002**, *131* (3), 313–317. <https://doi.org/https://doi.org/10.1093/oxfordjournals.jbchem.a003105>.
- (75) Sooriyaarachchi, S.; Chofor, R.; Risseeuw, M. D. P.; Bergfors, T.; Pouyez, J.; Dowd, C. S.; Maes, L.; Wouters, J.; Jones, T. A.; Van Calenbergh, S.; Mowbray, S. L. Targeting an Aromatic Hotspot in Plasmodium Falciparum 1-Deoxy-d-Xylulose-5-Phosphate Reductoisomerase with β -Arylpropyl Analogues of Fosmidomycin. *ChemMedChem* **2016**, 2024–2036. <https://doi.org/10.1002/cmhc.201600249>.
- (76) Hunsche, S.; Wienecke, K.; Kurz, H. Rapid Communication. *J. Biochem.* **2002**, *131* (3), 313–317. <https://doi.org/https://doi.org/10.1093/oxfordjournals.jbchem.a003105>.
- (77) Sooriyaarachchi, S.; Chofor, R.; Risseeuw, M. D. P.; Bergfors, T.; Pouyez, J.; Dowd, C. S.; Maes, L.; Wouters, J.; Jones, T. A.; Van Calenbergh, S.; Mowbray, S. L. Targeting an Aromatic Hotspot in Plasmodium Falciparum 1-Deoxy-d-Xylulose-5-Phosphate Reductoisomerase with β -Arylpropyl Analogues of Fosmidomycin. *ChemMedChem* **2016**, 2024–2036. <https://doi.org/10.1002/cmhc.201600249>.
- (78) Xue, J.; Diao, J.; Cai, G.; Deng, L.; Zheng, B.; Yao, Y.; Song, Y. Antimalarial and Structural Studies of Pyridine-Containing Inhibitors of 1-Deoxyxylulose-5-Phosphate Reductoisomerase. *ACS Med. Chem. Lett.* **2013**, *4* (2), 278–282. <https://doi.org/10.1021/ml300419r>.
- (79) Zinglé, C.; Kuntz, L.; Tritsch, D.; Grosdemange-Billiard, C.; Rohmer, M. Isoprenoid Biosynthesis via the Methylerythritol Phosphate Pathway: Structural Variations around Phosphonate Anchor and Spacer of Fosmidomycin, a Potent Inhibitor of Deoxyxylulose Phosphate Reductoisomerase. *J. Org. Chem.* **2010**, *75* (10), 3203–3207. <https://doi.org/10.1021/jo9024732>.
- (80) Mercklé, L.; De Andrés-Gómez, A.; Dick, B.; Cox, R. J.; Godfrey, C. R. A. A Fragment-Based Approach to Understanding Inhibition of 1-Deoxy-D-Xylulose-5-Phosphate Reductoisomerase. *ChemBioChem* **2005**, *6* (10), 1866–1874. <https://doi.org/10.1002/cbic.200500061>.

- (81) Jackson, E. R.; San Jose, G.; Brothers, R. C.; Edelstein, E. K.; Sheldon, Z.; Haymond, A.; Johny, C.; Boshoff, H. I.; Couch, R. D.; Dowd, C. S. The Effect of Chain Length and Unsaturation on Mtb Dxr Inhibition and Antitubercular Killing Activity of FR900098 Analogs. *Bioorg. Med. Chem. Lett.* **2014**, *24* (2), 649–653. <https://doi.org/10.1016/j.bmcl.2013.11.067>.
- (82) Kuntz, L.; Tritsch, D.; Grosdemange-Billiard, C.; Hemmerlin, A.; Willem, A.; Bach, T. J.; Rohmer, M. Isoprenoid Biosynthesis as a Target for Antibacterial and Antiparasitic Drugs: Phosphonohydroxamic Acids as Inhibitors of Deoxyxylulose Phosphate Reducto-Isomerase. *Biochem. J.* **2005**, *386* (1), 127–135. <https://doi.org/10.1042/BJ20041378>.
- (83) Lipinski, C. A.; Lombardo, F.; Dominy, B. W.; Feeney, P. J. Experimental and Computational Approaches to Estimate Solubility and Permeability in Drug Discovery and Development Settings IPII of Original Article: S0169-409X(96)00423-1. The Article Was Originally Published in *Advanced Drug Delivery Reviews* 23 (1997) . *Adv. Drug Deliv. Rev.* **2002**, *46* (1–3), 3–26. [https://doi.org/10.1016/s0169-409x\(00\)00129-0](https://doi.org/10.1016/s0169-409x(00)00129-0).
- (84) Lipinski, C. A. Drug-like Properties and the Causes of Poor Solubility and Poor Permeability. *J. Pharmacol. Toxicol. Methods* **2000**, *44* (1), 235–249. [https://doi.org/10.1016/S1056-8719\(00\)00107-6](https://doi.org/10.1016/S1056-8719(00)00107-6).
- (85) Franco, I.; Lipinski, A.; Dominy, B. W.; Feeney, P. J. Experimental and Computational Approaches to Estimate Solubility and Permeability in Drug Discovery and Development Settings. **1997**, *23*, 3–25. [https://doi.org/10.1016/S0169-409X\(96\)00423-1](https://doi.org/10.1016/S0169-409X(96)00423-1).
- (86) Mombo-Ngoma, G.; Remppis, J.; Sievers, M.; Zoleko Manego, R.; Endamne, L.; Kabwende, L.; Veletzky, L.; Nguyen, T. T.; Groger, M.; Lötsch, F.; Mischlinger, J.; Flohr, L.; Kim, J.; Cattaneo, C.; Hutchinson, D.; Duparc, S.; Moehrle, J.; Velavan, T. P.; Lell, B.; Ramharter, M.; Adegnika, A. A.; Mordmüller, B.; Kremsner, P. G. Efficacy and Safety of Fosmidomycin–Piperaquine as Nonartemisinin-Based Combination Therapy for Uncomplicated Falciparum Malaria: A Single-Arm, Age De-Escalation Proof-of-Concept Study in Gabon. *Clin. Infect. Dis.* **2017**, *66* (12), 1823–1830. <https://doi.org/10.1093/cid/cix1122>.
- (87) Borrmann, S.; Adegnika, A. A.; Matsiegui, P.; Issifou, S.; Schindler, A.; Mawili-

- Mboumba, D. P.; Baranek, T.; Wiesner, J.; Jomaa, H.; Kremsner, P. G. Fosmidomycin-Clindamycin for Plasmodium Falciparum Infections in African Children. *J. Infect. Dis.* **2004**, *189* (5), 901–908. <https://doi.org/10.1086/381785>.
- (88) Oyakhirome, S.; Issifou, S.; Pongratz, P.; Barondi, F.; Ramharter, M.; Kun, J. F.; Missinou, M. A.; Lell, B.; Kremsner, P. G. Randomized Controlled Trial of Fosmidomycin-Clindamycin versus Sulfadoxine-Pyrimethamine in the Treatment of Plasmodium Falciparum Malaria. *Antimicrob. Agents Chemother.* **2007**, *51* (5), 1869–1871. <https://doi.org/10.1128/AAC.01448-06>.
- (89) Wiesner, J.; Borrmann, S.; Jomaa, H. Fosmidomycin for the Treatment of Malaria. *Parasitology Research.* 2003. <https://doi.org/10.1007/s00436-002-0770-9>.
- (90) Leeson, P. D. Molecular Inflation, Attrition and the Rule of Five. *Adv. Drug Deliv. Rev.* **2016**, *101*, 22–33. <https://doi.org/10.1016/j.addr.2016.01.018>.
- (91) Leeson, P. D.; Young, R. J. Molecular Property Design: Does Everyone Get It? *ACS Med. Chem. Lett.* **2015**, *6* (7), 722–725. <https://doi.org/10.1021/acsmedchemlett.5b00157>.
- (92) Brücher, K.; Illarionov, B.; Held, J.; Tschan, S.; Kunfermann, A.; Pein, M. K.; Bacher, A.; Gräwert, T.; Maes, L.; Mordmüller, B.; Fischer, M.; Kurz, T. α -Substituted β -Oxa Isosteres of Fosmidomycin: Synthesis and Biological Evaluation. *J. Med. Chem.* **2012**, *55* (14), 6566–6575. <https://doi.org/10.1021/jm300652f>.
- (93) Haemers, T.; Wiesner, J.; Gießmann, D.; Verbrugghen, T.; Hillaert, U.; Ortmann, R.; Jomaa, H.; Link, A.; Schlitzer, M.; Van Calenbergh, S. Synthesis of β - and γ -Oxa Isosteres of Fosmidomycin and FR900098 as Antimalarial Candidates. *Bioorganic Med. Chem.* **2008**, *16* (6), 3361–3371. <https://doi.org/10.1016/j.bmc.2007.12.001>.
- (94) Ponaire, S.; Zinglé, C.; Tritsch, D.; Grosdemange-Billiard, C.; Rohmer, M. Growth Inhibition of Mycobacterium Smegmatis by Prodrugs of Deoxyxylulose Phosphate Reducto-Isomerase Inhibitors, Promising Anti-Mycobacterial Agents. *Eur. J. Med. Chem.* **2012**, *51*, 277–285. <https://doi.org/10.1016/j.ejmech.2012.02.031>.
- (95) Wang, X.; Edwards, R. L.; Ball, H.; Johnson, C.; Haymond, A.; Girma, M.; Manikkam, M.; Brothers, R. C.; McKay, K. T.; Arnett, S. D.; Osbourn, D. M.;

- Alvarez, S.; Boshoff, H. I.; Meyers, M. J.; Couch, R. D.; Odom John, A. R.; Dowd, C. S. MEPicides: α,β -Unsaturated Fosmidomycin Analogues as DXR Inhibitors against Malaria. *J. Med. Chem.* **2018**, *61* (19), 8847–8858. <https://doi.org/10.1021/acs.jmedchem.8b01026>.
- (96) Kurz, T.; Behrendt, C.; Pein, M.; Kaula, U.; Bergmann, B.; Walter, R. D. γ -Substituted Bis(Pivaloyloxymethyl)Ester Analogues of Fosmidomycin and FR900098. *Arch. Pharm. (Weinheim)*. **2007**, *340* (12), 661–666. <https://doi.org/10.1002/ardp.200700107>.
- (97) Jose, G. S.; Jackson, E. R.; Haymond, A.; Johny, C.; Edwards, R. L.; Wang, X.; Brothers, R. C.; Edelstein, E. K.; Odom, A. R.; Boshoff, H. I.; Couch, R. D.; Dowd, C. S. Structure-Activity Relationships of the MEPicides: N-Acyl and O-Linked Analogs of FR900098 as Inhibitors of Dxr from Mycobacterium Tuberculosis and Yersinia Pestis. *ACS Infect. Dis.* **2016**, *2* (12), 923–935. <https://doi.org/10.1021/acsinfecdis.6b00125>.
- (98) Haemers, T.; Wiesner, J.; Van Poecke, S.; Goeman, J.; Henschker, D.; Beck, E.; Jomaa, H.; Van Calenbergh, S. Synthesis of α -Substituted Fosmidomycin Analogues as Highly Potent Plasmodium Falciparum Growth Inhibitors. *Bioorganic Med. Chem. Lett.* **2006**, *16* (7), 1888–1891. <https://doi.org/10.1016/j.bmcl.2005.12.082>.
- (99) Sooriyaarachchi, S.; Chofor, R.; Risseeuw, M. D. P.; Bergfors, T.; Pouyez, J.; Dowd, C. S.; Maes, L.; Wouters, J.; Jones, T. A.; Van Calenbergh, S.; Mowbray, S. L. Targeting an Aromatic Hotspot in Plasmodium Falciparum 1-Deoxy-d-Xylulose-5-Phosphate Reductoisomerase with β -Arylpropyl Analogues of Fosmidomycin. *ChemMedChem* **2016**, 2024–2036. <https://doi.org/10.1002/cmdc.201600249>.
- (100) Haemers, T.; Wiesner, J.; Van Poecke, S.; Goeman, J.; Henschker, D.; Beck, E.; Jomaa, H.; Van Calenbergh, S. Synthesis of Alpha-Substituted Fosmidomycin Analogues as Highly Potent Plasmodium Falciparum Growth Inhibitors. *Bioorg. Med. Chem. Lett.* **2006**, *16* (7), 1888–1891. <https://doi.org/10.1016/j.bmcl.2005.12.082>.
- (101) Munier, M.; Tritsch, D.; Krebs, F.; Esque, J.; Hemmerlin, A.; Rohmer, M.; Stote, R. H.; Grosdemange-Billiard, C. Synthesis and Biological Evaluation of Phosphate Isosters of Fosmidomycin and Analogs as Inhibitors of Escherichia

- Coli and Mycobacterium Smegmatis 1-Deoxyxylulose 5-Phosphate Reductoisomerases. *Bioorganic Med. Chem.* **2017**, *25* (2), 684–689. <https://doi.org/10.1016/j.bmc.2016.11.040>.
- (102) Haemers, T.; Wiesner, J.; Gießmann, D.; Verbrugghen, T.; Hillaert, U.; Ortmann, R.; Jomaa, H.; Link, A.; Schlitzer, M.; Van Calenbergh, S. Synthesis of β - and γ -Oxa Isosteres of Fosmidomycin and FR900098 as Antimalarial Candidates. *Bioorganic Med. Chem.* **2008**, *16* (6), 3361–3371. <https://doi.org/10.1016/j.bmc.2007.12.001>.
- (103) Uh, E.; Jackson, E. R.; San Jose, G.; Maddox, M.; Lee, R. E.; Lee, R. E.; Boshoff, H. I.; Dowd, C. S. Antibacterial and Antitubercular Activity of Fosmidomycin, FR900098, and Their Lipophilic Analogs. *Bioorg. Med. Chem. Lett.* **2011**, *21* (23), 6973–6976. <https://doi.org/10.1016/j.bmcl.2011.09.123>.
- (104) Xue, J.; Diao, J.; Cai, G.; Deng, L.; Zheng, B.; Yao, Y.; Song, Y. Antimalarial and Structural Studies of Pyridine-Containing Inhibitors of 1-Deoxyxylulose-5-Phosphate Reductoisomerase. *ACS Med. Chem. Lett.* **2013**, *4* (2), 278–282. <https://doi.org/10.1021/ml300419r>.
- (105) Deng, L.; Endo, K.; Kato, M.; Cheng, G.; Yajima, S.; Song, Y. Structures of 1-Deoxy-D-Xylulose-5-Phosphate Reductoisomerase/Lipophilic Phosphonate Complexes. *ACS Med. Chem. Lett.* **2011**, *2* (2), 165–170. <https://doi.org/10.1021/ml100243r>.
- (106) Goddard, T. D.; Huang, C. C.; Meng, E. C.; Pettersen, E. F.; Couch, G. S.; Morris, J. H.; Ferrin, T. E. UCSF ChimeraX: Meeting Modern Challenges in Visualization and Analysis. *Protein Sci.* **2018**, *27* (1), 14–25. <https://doi.org/10.1002/pro.3235>.
- (107) BIOVIA, Dassault Systèmes, Discovery Studio Visualizer, 20.1.0, San Diego: Dassault Systèmes, 2020.
- (108) Deng, L.; Sundriyal, S.; Rubio, V.; Shi, Z. Z.; Song, Y. Coordination Chemistry Based Approach to Lipophilic Inhibitors of 1-Deoxy-D-Xylulose-5-Phosphate Reductoisomerase. *J. Med. Chem.* **2009**, *52* (21), 6539–6542. <https://doi.org/10.1021/jm9012592>.
- (109) Sander, T.; Freyss, J.; von Korff, M.; Rufener, C. DataWarrior: An Open-Source Program for Chemistry Aware Data Visualization and Analysis. *J. Chem. Inf. Model.* **2015**, *55* (2), 460–473. <https://doi.org/10.1021/ci500588j>.

- (110) Deng, L.; Diao, J.; Chen, P.; Pujari, V.; Yao, Y.; Cheng, G.; Crick, D. C.; Prasad, B. V. V.; Song, Y. Inhibition of 1-Deoxy-d-Xylulose-5-Phosphate Reductoisomerase by Lipophilic Phosphonates: SAR, QSAR, and Crystallographic Studies. *J. Med. Chem.* **2011**, *54* (13), 4721–4734. <https://doi.org/10.1021/jm200363d>.
- (111) Andaloussi, M.; Lindh, M.; Bjorkelid, C.; Suresh, S.; Wieckowska, A.; Iyer, H.; Karlen, A.; Larhed, M. Substitution of the Phosphonic Acid and Hydroxamic Acid Functionalities of the DXR Inhibitor FR900098: An Attempt to Improve the Activity against Mycobacterium Tuberculosis. *Bioorg. Med. Chem. Lett.* **2011**, *21* (18), 5403–5407. <https://doi.org/10.1016/j.bmcl.2011.07.005>.
- (112) Bodill, T.; Conibear, A. C.; Blatch, G. L.; Lobb, K. A.; Kaye, P. T. Bioorganic & Medicinal Chemistry Synthesis and Evaluation of Phosphonated N - Heteroarylcarboxamides as DOXP-Reductoisomerase (DXR) Inhibitors. *Bioorg. Med. Chem.* **2011**, *19* (3), 1321–1327. <https://doi.org/10.1016/j.bmc.2010.11.062>.
- (113) Bodill, T.; Conibear, A. C.; Mutorwa, M. K. M.; Goble, J. L.; Blatch, G. L.; Lobb, K. A.; Klein, R.; Kaye, P. T. Exploring DOXP-Reductoisomerase Binding Limits Using Phosphonated N-Aryl and N-Heteroarylcarboxamides as DXR Inhibitors. *Bioorganic Med. Chem.* **2013**, 4332–4341. <https://doi.org/10.1016/j.bmc.2013.04.076>.
- (114) Adeyemi, C. M.; Faridoun; Isaacs, M.; Mnkandhla, D.; Hoppe, H. C.; Krause, R. W. M.; Kaye, P. T. Synthesis and Antimalarial Activity of N-Benzylated (N-Arylcarbamoyl)Alkylphosphonic Acid Derivatives. *Bioorganic Med. Chem.* **2016**, *24* (23), 6131–6138. <https://doi.org/10.1016/j.bmc.2016.04.021>.
- (115) Zinglé, C.; Kuntz, L.; Tritsch, D.; Grosdemange-Billiard, C.; Rohmer, M. Modifications around the Hydroxamic Acid Chelating Group of Fosmidomycin, an Inhibitor of the Metalloenzyme 1-Deoxyxylulose 5-Phosphate Reductoisomerase (DXR). *Bioorganic Med. Chem. Lett.* **2012**, *22* (21), 6563–6567. <https://doi.org/10.1016/j.bmcl.2012.09.021>.
- (116) Andaloussi, M.; Lindh, M.; Björkelid, C.; Suresh, S.; Wieckowska, A.; Iyer, H.; Karlén, A.; Larhed, M. Substitution of the Phosphonic Acid and Hydroxamic Acid Functionalities of the DXR Inhibitor FR900098: An Attempt to Improve the Activity against Mycobacterium Tuberculosis. *Bioorganic Med. Chem. Lett.*

- 2011, 21 (18), 5403–5407. <https://doi.org/10.1016/j.bmcl.2011.07.005>.
- (117) Chofor, R.; Risseeuw, M. D. P.; Pouyez, J.; Johny, C.; Wouters, J.; Dowd, C. S.; Couch, R. D.; Van Calenbergh, S. Synthetic Fosmidomycin Analogues with Altered Chelating Moieties Do Not Inhibit 1-Deoxy-d-Xylulose 5-Phosphate Reductoisomerase or Plasmodium Falciparum Growth in Vitro. *Molecules* **2014**, 19 (2), 2571–2587. <https://doi.org/10.3390/molecules19022571>.
- (118) Mancini, G.; Bouda, M.; Gamrat, J. M.; Tomsho, J. W. Synthesis and Antimicrobial Evaluation of γ -Borono Phosphonate Compounds in Escherichia Coli and Mycobacterium Smegmatis. *ACS Omega* **2019**, 14551–14559. <https://doi.org/10.1021/acsomega.9b01774>.
- (119) Chen, A. Y.; Adamek, R. N.; Dick, B. L.; Credille, C. V.; Morrison, C. N.; Cohen, S. M. Targeting Metalloenzymes for Therapeutic Intervention. *Chem. Rev.* **2019**, 119 (2), 1323–1455. <https://doi.org/10.1021/acs.chemrev.8b00201>.
- (120) Cohen, S. M. A Bioinorganic Approach to Fragment-Based Drug Discovery Targeting Metalloenzymes. **2017**, 2007–2016. <https://doi.org/10.1021/acs.accounts.7b00242>.
- (121) Perez, C.; Barkley-Levenson, A. M.; Dick, B. L.; Glatt, P. F.; Martinez, Y.; Siegel, D.; Momper, J. D.; Palmer, A. A.; Cohen, S. M. Metal-Binding Pharmacophore Library Yields the Discovery of a Glyoxalase 1 Inhibitor. *J. Med. Chem.* **2019**, 62 (3), 1609–1625. <https://doi.org/10.1021/acs.jmedchem.8b01868>.
- (122) Dick, B. L.; Cohen, S. M. Metal-Binding Isosteres as New Scaffolds for Metalloenzyme Inhibitors. *Inorg. Chem.* **2018**, 57 (15), 9538–9543. <https://doi.org/10.1021/acs.inorgchem.8b01632>.
- (123) Credille, C. V.; Dick, B.; Morrison, C. N.; Stokes, R. W.; Adamek, R.; Wu, N. C.; Wilson, I. A.; Cohen, S. M. Structure-Activity Relationships in Metal-Binding Pharmacophores for Influenza Endonuclease. **2018**. <https://doi.org/10.1021/acs.jmedchem.8b01363>.
- (124) Adamek, R. N.; Credille, C. V.; Dick, B. L.; Cohen, S. M. Isosteres of Hydroxypyridinethione as Drug-like Pharmacophores for Metalloenzyme Inhibition. *J. Biol. Inorg. Chem.* **2018**, 23 (7), 1129–1138. <https://doi.org/10.1007/s00775-018-1593-1>.
- (125) Agrawal, A.; Johnson, S. L.; Jacobsen, J. A.; Miller, M. T.; Chen, L.; Pellecchia,

- M.; Cohen, S. M. Chelator Fragment Libraries for Targeting Metalloproteinases. **2010**, 195–199. <https://doi.org/10.1002/cmdc.200900516>.
- (126) Johnson, S.; Barile, E.; Farina, B.; Purves, A.; Chen, L.; Shiryaev, S.; Zhang, Z.; Rodionova, I.; Cohen, S. M.; Strongin, A. Targeting Metalloproteins by Fragment-Based Lead Discovery. **2011**, 211–223. <https://doi.org/10.1111/j.1747-0285.2011.01136.x>.
- (127) Erlanson, D. A.; Fesik, S. W.; Hubbard, R. E.; Jahnke, W.; Jhoti, H. Twenty Years on: The Impact of Fragments on Drug Discovery. *Nature Reviews Drug Discovery*. Nature Publishing Group August 2016, pp 605–619. <https://doi.org/10.1038/nrd.2016.109>.
- (128) Codd, R. Traversing the Coordination Chemistry and Chemical Biology of Hydroxamic Acids. *Coordination Chemistry Reviews*. Elsevier July 2008, pp 1387–1408. <https://doi.org/10.1016/j.ccr.2007.08.001>.
- (129) Brown, D. A.; McKeith (née Byrne), D.; Glass, W. K. Transition Metal Complexes of Monohydroxamic Acids. *Inorganica Chim. Acta* **1979**, 35 (C), 5–10. [https://doi.org/10.1016/S0020-1693\(00\)93409-1](https://doi.org/10.1016/S0020-1693(00)93409-1).
- (130) Brown, D. A.; McKeith (née Byrne), D.; Glass, W. K. The Infrared Spectra of Monohydroxamic Acid Complexes of Copper, Iron and Nickel. *Inorganica Chim. Acta* **1979**, 35 (C), 57–60. [https://doi.org/10.1016/S0020-1693\(00\)93417-0](https://doi.org/10.1016/S0020-1693(00)93417-0).
- (131) Jacobsen, F. E.; Lewis, J. A.; Cohen, S. M. The Design of Inhibitors for Medicinally Relevant Metalloproteins. *ChemMedChem* **2007**, 2 (2), 152–171. <https://doi.org/10.1002/cmdc.200600204>.
- (132) Jiang, Z.; You, Q.; Zhang, X. Medicinal Chemistry of Metal Chelating Fragments in Metalloenzyme Active Sites: A Perspective. *Eur. J. Med. Chem.* **2019**, 165, 172–197. <https://doi.org/10.1016/j.ejmech.2019.01.018>.
- (133) Shen, S.; Kozikowski, A. P. Why Hydroxamates May Not Be the Best Histone Deacetylase Inhibitors-What Some May Have Forgotten or Would Rather Forget? *ChemMedChem* **2016**, 11 (1), 15–21. <https://doi.org/10.1002/cmdc.201500486>.
- (134) McClure, J. J.; Li, X.; Chou, C. J. Advances and Challenges of HDAC Inhibitors in Cancer Therapeutics. In *Advances in Cancer Research*; Academic Press Inc., 2018; Vol. 138, pp 183–211. <https://doi.org/10.1016/bs.acr.2018.02.006>.

- (135) Hermant, P.; Bosc, D.; Piveteau, C.; Gealageas, R.; Lam, B.; Ronco, C.; Roignant, M.; Tolojanahary, H.; Jean, L.; Renard, P. Y.; Lemdani, M.; Bourotte, M.; Herledan, A.; Bedart, C.; Biela, A.; Leroux, F.; Deprez, B.; Deprez-Poulain, R. Controlling Plasma Stability of Hydroxamic Acids: A MedChem Toolbox. *J. Med. Chem.* **2017**, *60* (21), 9067–9089. <https://doi.org/10.1021/acs.jmedchem.7b01444>.
- (136) Vandenbroucke, R. E.; Libert, C. Is There New Hope for Therapeutic Matrix Metalloproteinase Inhibition? *Nature Reviews Drug Discovery*. Nature Publishing Group December 2014, pp 904–927. <https://doi.org/10.1038/nrd4390>.
- (137) Peterson, J. T. The Importance of Estimating the Therapeutic Index in the Development of Matrix Metalloproteinase Inhibitors. *Cardiovascular Research*. Cardiovasc Res February 2006, pp 677–687. <https://doi.org/10.1016/j.cardiores.2005.11.032>.
- (138) Summers, J. B.; Gunn, B. P.; Mazdiyasi, H.; Goetze, A. M.; Young, P. R.; Bouska, J. B.; Dyer, R. D.; Brooks, D. W.; Carter, G. W. In Vivo Characterization of Hydroxamic Acid Inhibitors of 5-Lipoxygenase. *J. Med. Chem.* **1987**, *30* (11), 2121–2126. <https://doi.org/10.1021/jm00394a032>.
- (139) Sanderson, L.; Taylor, G. W.; Aboagye, E. O.; Alao, J. P.; Latigo, J. R.; Coombes, R. C.; Vigushin, D. M. Plasma Pharmacokinetics and Metabolism of the Histone Deacetylase Inhibitor Trichostatin A after Intraperitoneal Administration to Mice. *Drug Metab. Dispos.* **2004**, *32* (10), 1132–1138. <https://doi.org/10.1124/dmd.104.000638>.
- (140) Pearson, R. G. Hard and Soft Acids and Bases. *J. Am. Chem. Soc.* **1963**, *85* (22), 3533–3539. <https://doi.org/10.1021/ja00905a001>.
- (141) Mock, W. L.; Cheng, H. Principles of Hydroxamate Inhibition of Metalloproteases: Carboxypeptidase A. *Biochemistry* **2000**, *39* (45), 13945–13952. <https://doi.org/10.1021/bi001497s>.
- (142) Andaloussi, M.; Henriksson, L. M.; Więckowska, A.; Lindh, M.; Björkelid, C.; Larsson, A. M.; Suresh, S.; Iyer, H.; Srinivasa, B. R.; Bergfors, T.; Unge, T.; Mowbray, S. L.; Larhed, M.; Jones, T. A.; Karlén, A. Design, Synthesis, and X-Ray Crystallographic Studies of α -Aryl Substituted Fosmidomycin Analogues as Inhibitors of Mycobacterium Tuberculosis 1-Deoxy-d-Xylulose 5-Phosphate

- Reductoisomerase. *J. Med. Chem.* **2011**, *54* (14), 4964–4976. <https://doi.org/10.1021/jm2000085>.
- (143) Behrendt, C. T.; Kunfermann, A.; Illarionova, V.; Matheussen, A.; Pein, M. K.; Gräwert, T.; Kaiser, J.; Bacher, A.; Eisenreich, W.; Illarionov, B.; Fischer, M.; Maes, L.; Groll, M.; Kurz, T. Reverse Fosmidomycin Derivatives against the Antimalarial Drug Target IspC (Dxr). *J. Med. Chem.* **2011**, *54* (19), 6796–6802. <https://doi.org/10.1021/jm200694q>.
- (144) Kesharwani, S.; Sundriyal, S. Non-Hydroxamate Inhibitors of 1-Deoxy-D-Xylulose 5-Phosphate Reductoisomerase (DXR): A Critical Review and Future Perspective. *Eur. J. Med. Chem.* **2021**, *213*, 113055. <https://doi.org/10.1016/j.ejmech.2020.113055>.
- (145) Williams, S. L.; Oliveira, C. A. F. De; Vazquez, H.; McCammon, J. A. From Zn to Mn: The Study of Novel Manganese-Binding Groups in the Search for New Drugs against Tuberculosis. *Chem. Biol. Drug Des.* **2011**, *77* (2), 117–123. <https://doi.org/10.1111/j.1747-0285.2010.01060.x>.
- (146) Deng, L.; Sundriyal, S.; Rubio, V.; Shi, Z. Z.; Song, Y. Coordination Chemistry Based Approach to Lipophilic Inhibitors of 1-Deoxy-d-Xylulose-5-Phosphate Reductoisomerase. *J. Med. Chem.* **2009**, *52* (21), 6539–6542. <https://doi.org/10.1021/jm9012592>.
- (147) He, S.; Ouyang, X.; Huang, X.; Hu, W.; Dai, W.; Tian, X.; Pan, Y.; Huang, S.; Wang, H. Synthesis of Derivatives of Artesunate α-Aminophosphonate and Their Antimicrobial Activities. *Lett. Drug Des. Discov.* **2015**, *12* (5), 408–416. <https://doi.org/10.2174/1570180812666141125004502>.
- (148) Sundriyal, S.; Viswanad, B.; Bharathy, E.; Ramarao, P.; Chakraborti, A. K.; Bharatam, P. V. New PPAR γ Ligands Based on 2-Hydroxy-1,4-Naphthoquinone: Computer-Aided Design, Synthesis, and Receptor-Binding Studies. *Bioorganic Med. Chem. Lett.* **2008**, *18* (11), 3192–3195. <https://doi.org/10.1016/j.bmcl.2008.04.072>.

CHAPTER 3

Design and Synthesis of *Mycobacterium tuberculosis* Uracil DNA Glycosylase (*MtUng*)

Inhibitors

3.1 INTRODUCTION AND BACKGROUND

Another key target for the antimicrobial drug design is UDG (or UNG), which is involved in the Base excision repair pathway (BER). The genome of *M. tuberculosis* containing high content of G, C genomes is usually at high risk of cytosine deamination owing to reactive oxygen species (ROS) and reactive nitrogen intermediates (RNI) present in the macrophages in the latent bacteria. *MtUng* helps to restore genomic integrity by removing deaminated cytosines from DNA prior to replication to avoid further detrimental consequences and propagation of mutations in transcription and translation processes. *MtUng* is the first and an important enzyme in the base excision repair mechanism, which removes uracil by hydrolyzing the N-glycosidic bond between uracil and deoxyribose from single-stranded and double-stranded DNA. This makes *MtUng* an important target for the search and design of inhibitors. Additionally, UNG has a well-defined uracil-binding pocket (UBP) that can be targeted for computational drug design.

3.1.1 Base excision repair pathway (BER):

DNA is genetically unstable and decomposes readily by several exogenous and endogenous factors, including x-rays, radiations, gamma rays, cancer chemotherapy, plant toxins, viruses, and man-made mutagenic and environmental chemicals.^{1,2} DNA damage occurs at the rate of thousands to a million lesions per cell on a daily basis. The genomic integrity of DNA is under constant threat due to a broad range of constant chemical modifications, such as alkylation, oxidation, deamination, and depurination. ROS and water are the major contributing factors for spontaneous DNA damage. Damaged bases could be miscoding or cytotoxic.³ To maintain the regular functioning of the cells, all organisms rely on various DNA repair pathways to analyze and correct damages in the molecules. Various DNA repair mechanisms, such as mismatch repair (MMR), nucleotide excision repair (NER), and BER, are present in all domains of life.⁴⁻⁶ BER is one such pathway in a critical protective system that accounts for countering the cytotoxic and mutagenic effects of damage occurring to the nucleotide bases of DNA, as shown in Fig. 3.1. BER is a central core repair mechanism and highly conserved pathway which plays a critical role in maintaining the genomic integrity of the DNA. The nucleotides of DNA are exposed to different chemical modifications, including alkylation by exogenous and endogenous electrophiles, oxidation by several ROS, and hydrolytic deamination of exocyclic amino groups. Several examples include

the deamination of cytosine base to uracil, methylation of adenine to 3-methyladenine, and oxidation of guanine to 8-oxoguanine.⁷ If these modifications are left unrepaired, lesions may lead to mutations that hinder the process of DNA replication and transcriptions, triggering apoptosis and causing cell death. Unrepaired base damage is expressed in cancers and premature aging.⁸ The presence of uracil in DNA is deleterious for living organisms, including yeast, bacteria, and humans.

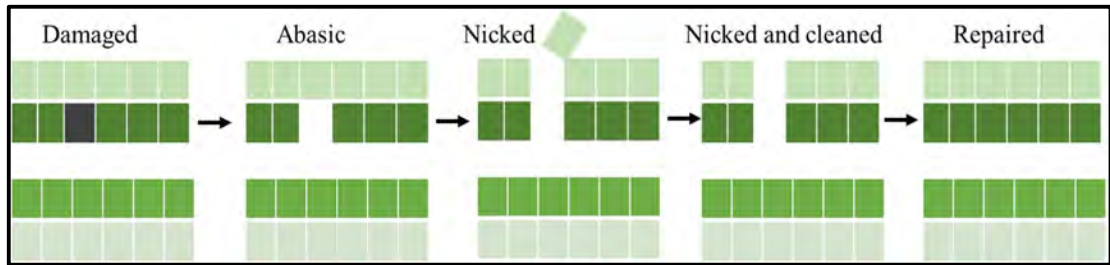


Fig. 3.1 General representation of Base Excision Repair Mechanism⁹

The basic process of BER is highly conserved for all organisms despite variations in detailed chemical reactions. The process initiates by searching the lesions by DNA glycosylase in DNA. Further, the process occurs in five steps mentioned in Fig. 3.2.⁷

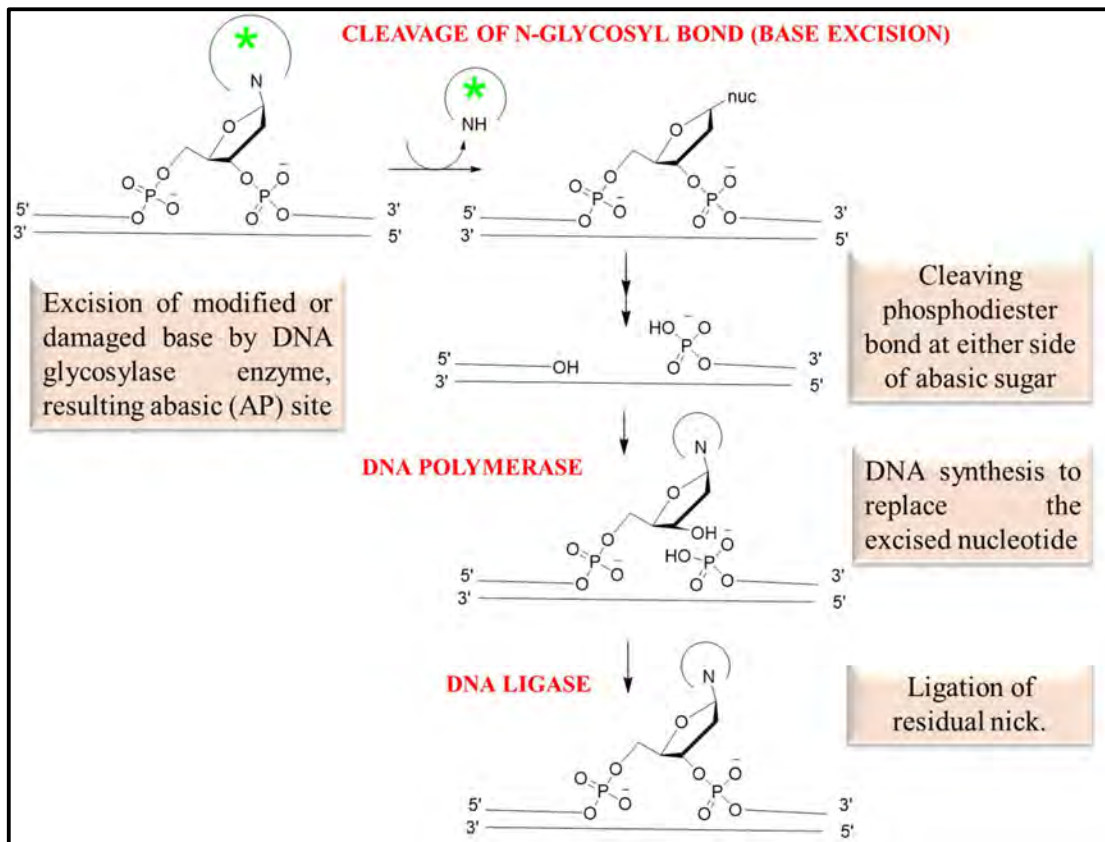


Fig. 3.2 The stepwise BER process

3.1.2 DNA glycosylases

DNA glycosylases play a critical role in the BER process by finding the damaged bases and excising them to initiate BER. Tomas Lindahl identified *Escherichia coli*-DNA glycosylase (*EcUng*), encoded by *ung* gene, in 1975 as the first DNA glycosylase.⁶ Mammals, including humans, show 11 different glycosylases.⁵ Out of these, four are devoted to the removal of mismatched thymine and uracil, one to removing alkylated bases, and six enzymes are devoted to repairing oxidative damage.⁴ These are positively charged, relatively small, and usually single-domain proteins. DNA glycosylase recognizes base lesions selectively. Some recognize inappropriate or damaged bases in a mismatch, base pair, and single-stranded ss-DNA (UDG), while others are very specific to base lesions in double-stranded ds-DNA, remaining inactive in ss-DNA.^{10,11} Few glycosylases, such as uracil DNA glycosylases, operate predominantly on one type of lesion, whereas others remove various modified bases.

DNA glycosylases can be classified as monofunctional and bifunctional DNA glycosylases.¹² They are monofunctional if they show only glycosylase activity (UNG), generating apurinic/apyrimidinic (AP) sites. Monofunctional glycosylases recognize thymine, uracil, and alkylated bases and cleave the N-glycosidic bond of the target base and deoxyribose. For cleaving, it uses water as a source of a nucleophile, releasing a free base and forming an abasic site, also called an AP site. Bifunctional DNA glycosylase shows other activities, such as β -lyase activity or β , δ - lyase activity to cleave DNA strands, besides the glycosylase activity. It utilizes amino groups from enzymes as a source of nucleophiles to form an intermediate called Schiff's base.¹³ The generated abasic sites are highly cytotoxic; thus, the action of glycosylases is immediately pursued by other enzymes to initiate the repair. The reaction products obtained by monofunctional and bifunctional glycosylases can be cytotoxic and mutagenic; therefore, it is crucial to be recognized and processed further by following BER enzymes. DNA glycosylases function via a nucleotide-flipping mechanism to identify damaged and modified DNA bases and eliminate them by cleavage of the N-glycosyl bond between the base and 2-deoxyribose sugar.⁷ Base flipping mechanism aids the searching for lesions and provides access to the C-N bond. Various DNA glycosylases are required to handle the many base lesions identified in organisms.

3.1.3 Uracil DNA Glycosylase (UDG/UNG)

UDGs are the primary DNA repair enzymes involved in BER. These monofunctional glycosylases remove uracil from DNA. Uracil is usually a unit of RNA, but sometimes it may appear in DNA too. It may be present in DNA due to two reasons.

1. Chemical modification of residues such as spontaneous or hydrolytic deamination of cytosine (Cyt) or UV-induced deamination of Cyt.
2. Mistaken incorporation of dUMP in DNA instead of dTMP.^{14,15}

UDG enzymes are found in archaea, eubacteria, large DNA viruses, and eukaryotes. Examples are mentioned in Fig. 3.3.

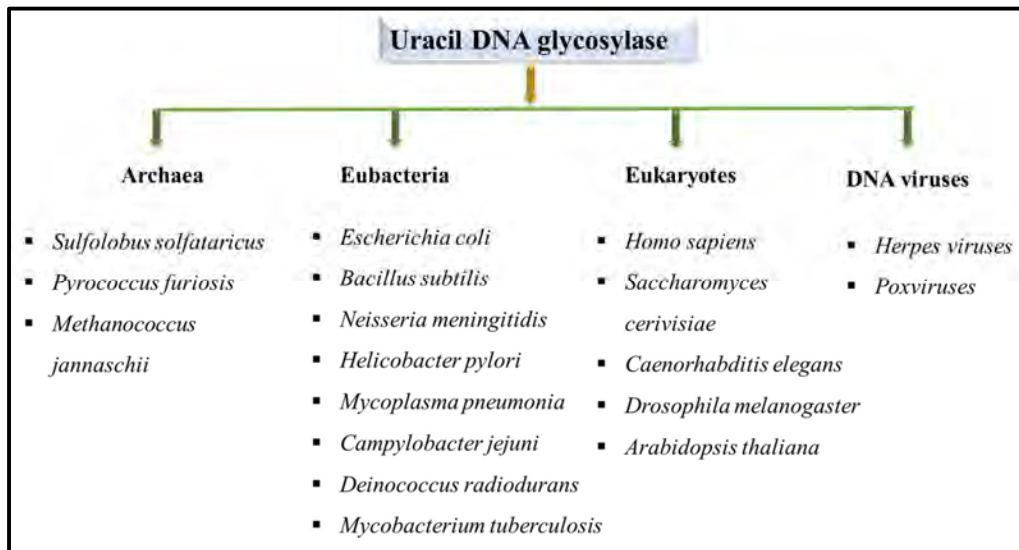


Fig. 3.3 Species showing the presence of UDG

UDGs are classified into six families based on two conserved motifs, A and B, and substrate specificity.¹⁶⁻¹⁸ The family I UDGs (UNGs) are the most conserved and extensively explored enzymes (specifically from *E. coli* and human UNG proteins) within the UDG superfamily. UNG shows high specificity for uracil (Ura) by excising Ura from single-stranded DNA and double-stranded DNA. Apart from Ura, it cleaves 5-fluorouracil (5-fU) at a three-magnitude slower rate and does not excise any other bases, not even 5-substituted uracil.^{19,20} It prefers ssU followed by U:G and U:A.

3.1.4 Properties and structure of UNG

The C-terminal domain of UNGs is highly conserved, including the catalytic domain, which consists of 200 amino acid residues. UNGs possess diverse N-terminal extensions varying in length and composition and are involved in protein-protein

interactions, regulation, and subcellular localization. Overall structures, motifs, and amino acid sequences in UNGs from all organisms are well conserved, except in poxvirus UNGs. Human UNG (hUng) shows close amino acid identity with pathogenic organisms such as *E. coli* (56%), yeast (54%), *B. subtilis* (49%), and Herpes simplex virus (40%).¹⁴ UNGs were considered a single-domain protein; later, it was described that it has two domains,²¹ consisting of eight α -helices and four parallel β -strands with a twist in the central part (residues 62–65, 123–127, 163–168, and 184–189).^{22–25} They show five stretches of conserved motifs mentioned in Fig. 3.4.^{14,26}

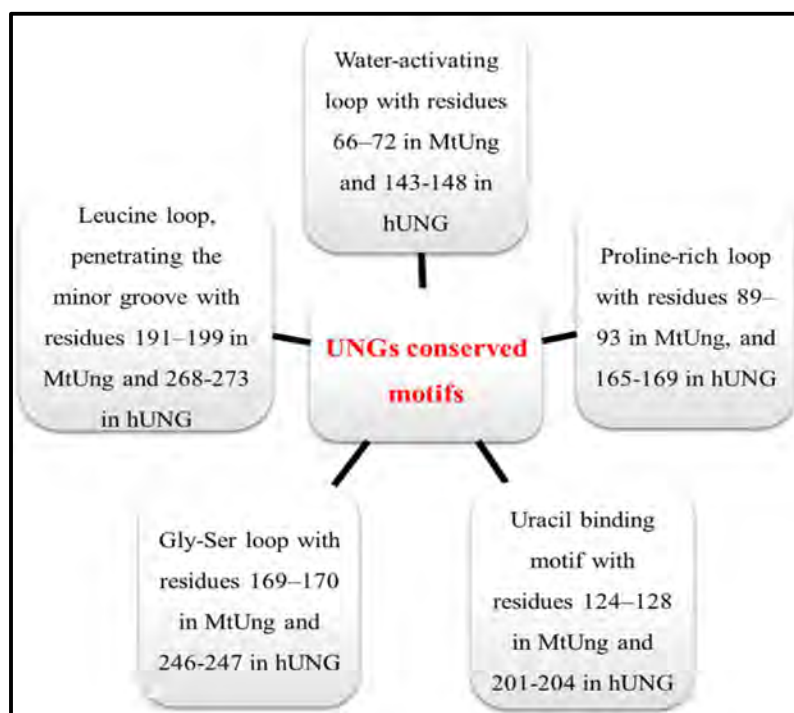


Fig. 3.4 Five stretches of conserved motifs in UNG

Water-activating loop (66-72) and uracil binding motif (124-128) constitute domain one, while the remaining three motifs constitute domain two. The Leucine loop is the most variable element in the structure and plays a significant role in UNG–Ugi and UNG–DNA interactions. The DNA-binding region shows few positively charged residues located at the C-terminal end of the β -sheet. A tapered and deep UBP is placed at the edge of the DNA binding groove. UBP consists of residues from catalytic water-activating loops such as Gln, Asp, and Tyr, a Phe residue, a Ser residue of the Pro-rich loop, the Asn residue of Ura-binding motif, and His residue from the Leu-intercalation loop. The size and shape of UBP depend on the number of hydrophobic residues (Phe, Ala, Leu, Tyr) residing near the active site. It includes aromatic residues stacking

against the DNA base, as shown in Fig. 3.5. The specificity is attributed to the smaller size of UBP, excluding the larger purine bases. The base should be flipped out to accommodate uracil in the groove.^{23,27-29} Only dU can be accessed into the groove with suitable conformation in the conserved active site for cleaving the N-glycosidic bond.^{3,15} UNG represents two conformational states, a closed conformation interacting with the DNA phosphate backbone and an open conformation with low affinity for DNA.³⁰ It releases a free uracil base by hydrolyzing the N-glycosidic bond bridging the base and the deoxyribose sugar of the DNA backbone and generating an abasic site in the DNA strand.³¹ These are specific to ssDNA but also repair dsDNA. The helical structure of DNA is critical for the action of UNGs.^{32,33}

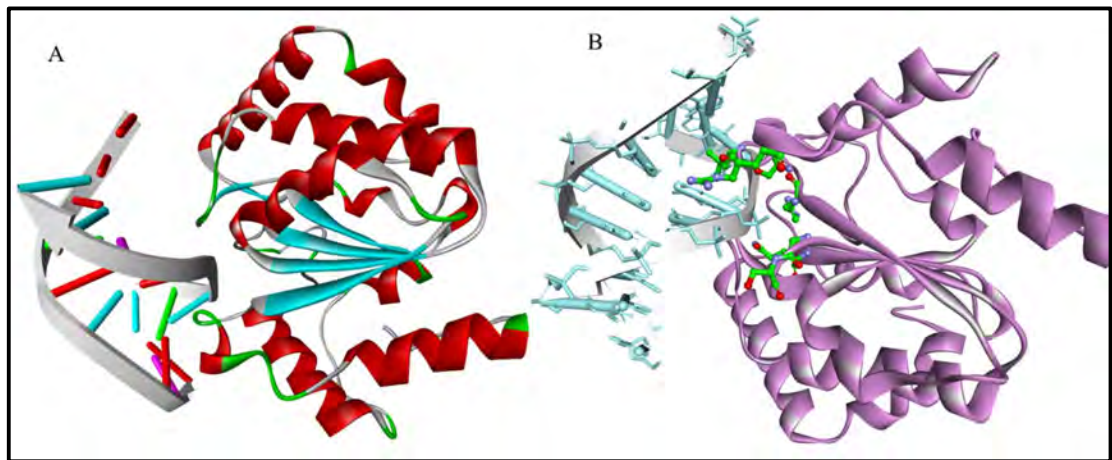


Fig. 3.5 (A) Crystal structure of UNG:DNA complex (PDBxxx) from *E. coli* showing the seven α -helices and four parallel β -strands (B) Image showing the interacting residues of UNG (pink ribbons) and DNA (cyan ladder) interface (green balls and sticks)

3.2 LITERATURE

3.2.1 UNG Inhibitor

Uracil-DNA glycosylase inhibitor (Ugi) is a well-known protein inhibitor of UNG proteins. Ugi is encoded by the bacteriophages PBS-I and PBS-II, part of their defense mechanism against host UNG.³⁴⁻³⁶ Ugi, being well characterized structurally and biochemically, has been used extensively to understand the structural aspects of UNG. It mimics the UNG:DNA complex. It is heat stable and acidic polypeptide with 84 amino acids that inactivates the UNG^{34,37,38} from various organisms, including *E. coli*, *B. subtilis*, *S. cerevisiae*, HSV, *Homo sapiens*, and rat liver. It binds in a specific way to inactivate the enzyme. The secondary structure of Ugi is made up of two α -helices and five anti-parallel β -strands. This irreversible UNG:Ugi complex in a 1:1 stoichiometry inhibits *EcUng*.³⁹ UNG bound to ugi complexes is reported from various sources shown in Fig. 3.6. UNGs are inhibited by uracil, generated from the enzymatic reaction, derivative of uracil, and its analogs, though the extent of inhibition varies.⁴⁰⁻⁴⁵ A few complexes of UNG bound to uracil and its derivatives are reported. However, the binding mode and interactions of the Ugi:UNG complex are not much explored, despite the detailed understanding of the biochemical aspects of inhibition.³³ The structures of the complexes of UNG with uracil, uracil analogs, and some of its derivatives have also been reported^{43,44,46-48} (1UDI, 1UGH, 1EUG, 1SSP, 1EMG, 1FLZ). The protein p56 from *Bacillus subtilis* phage ϕ 29 (PDB 3ZOQ) with 56 amino acids was identified as another natural inhibitor of UNG.⁴⁹⁻⁵¹ *Staphylococcus aureus* uracil-DNA glycosylase inhibitor (SAUGI) from *S. aureus* was also identified as a third inhibitor of UNG, showing high binding affinity to human UNG.⁵²

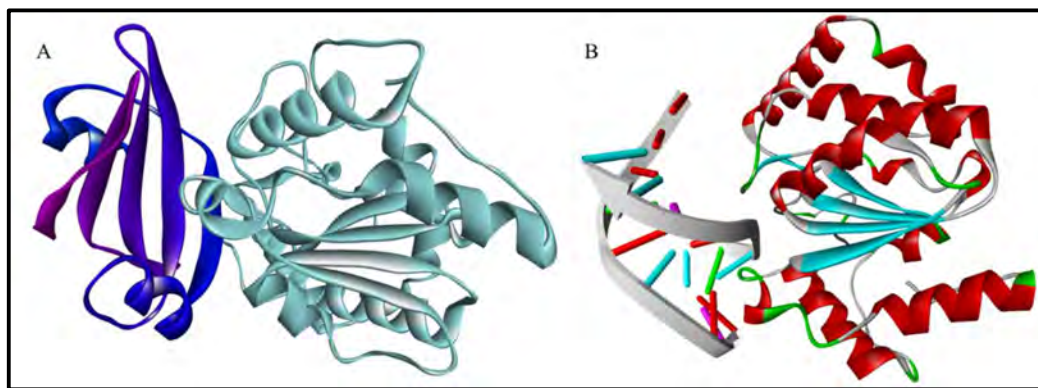


Fig. 3.6 (A) Ugi:UNG complex. The structure of Ugi is represented in dark blue-purple color. It shows two α -helices and five anti-parallel β -strands. UNG is represented in Cyan color. (B) UNG-DNA complex. DNA is bound to the left side of the UNG. In Ugi:UNG complex, Ugi mimic the DNA backbone interactions by targeting the DNA binding surface of UNG, thus inhibiting the enzyme.

UNG is well characterized structurally and biochemically. Many protein-inhibitor complex crystal structures reveal detailed insights into the UNG's uracil binding pocket and extended binding region. The specificity of the enzyme to selectively excise the uracil provides the add-on benefit to design the inhibitors towards UNG. Taking advantage of this, various inhibitors of UNG from different species, including humans, *Plasmodium*, and multiple viruses, are reported in the literature. Several uracil analogs were evaluated for inhibitory activity towards UNG enzyme, including 5-azauracil and 6-aminouracil displaying IC_{50} values in micromolar ranges (1-2 mM). Recently, our collaborators reported several uracil analogs with substitution at the 4 and 5 positions, displaying IC_{50} values between the 1-50 mM range mentioned in Fig. 3.7.⁵³

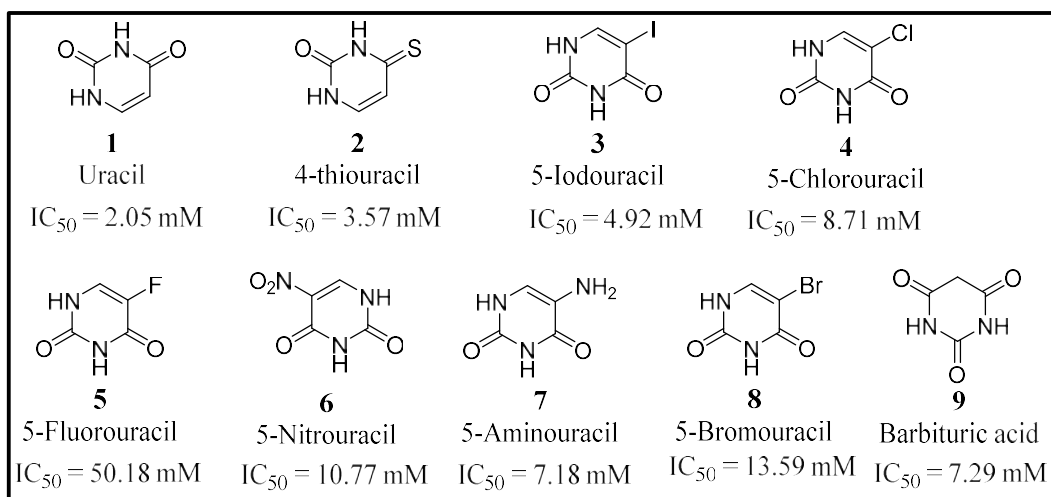


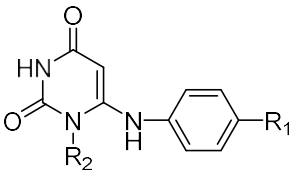
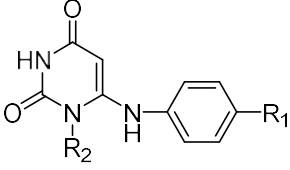
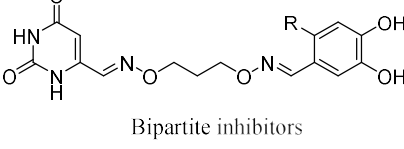
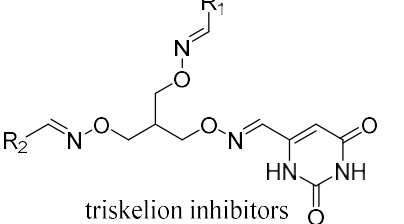
Fig. 3.7 Various 4 and 5 position substituted uracil derivatives and their reported IC_{50} values in mM

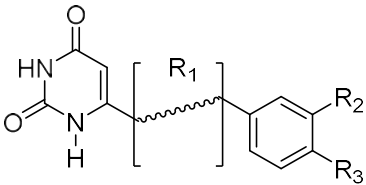
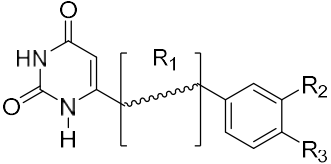
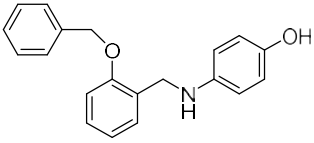
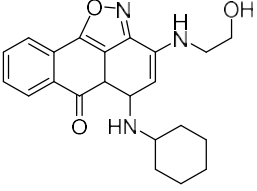
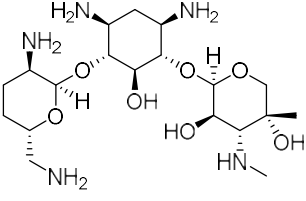
Several other approaches have been explored to inhibit the UNG enzyme. To these attempts, uracil-directed ligand tethering has been shown to be an efficient strategy for inhibitor development of UNG.^{42-44,54} The search in the ChEMBL database resulted in 89 unique inhibitors tested mostly against the human and *Vaccinia virus* UNG. The representative structures are mentioned in Table 2.1. One of the early attempts was made by *Focher et al.* to develop selective uracil-derived inhibitors of UNG. They synthesized several 6-(p-alkylanilino)uracil analogs and screened them against the isolated HSV1 UNG and human HeLa UNG enzyme. The group reported compound **10** holding the n-octyl chain, with the lowest IC₅₀ value in the series, inhibiting HSV1 isolated UNG. Three more compounds in series with n-heptyl, n-hexyl, and n-pentyl chains showed IC₅₀ values in the 10-30 μM range inhibiting the HSV1 enzyme. These same compounds showed comparatively higher IC₅₀ values in human UNG, with compound **10** with ~37-fold higher IC₅₀. N-heptyl substituted compound showed minimum IC₅₀ = 140 μM in human UNG⁴⁵. In a follow-up study, various R₂ substitutions were employed to earlier reported compound **10**. Out of 12 compounds in the series, only two compounds showed effective inhibition of the isolated *Pf*Ung. Compound **11** showed the lowest IC₅₀ = 17 μM, with another analog showing ~5-fold increased IC₅₀ value (78 μM). The other compounds in that series failed to show UNG inhibition at 400 μM. Surprisingly, all these compounds successfully inhibited the parasite growth with an IC₅₀ value in a range of 5-17 μM. Again, all these compounds failed to inhibit human UNG.⁵⁵

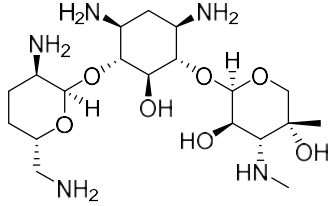
Jiang et al. reported bipartite inhibitors using uracil directed ligand tethering approach to inhibit the human UNG. This approach used the HTP platform to discover the small molecule inhibitors and utilized the extrahelical uracil recognition mechanism. Using oxime chemistry to explore the peripheral binding pockets, the group tethered the uracil aldehyde ligand with an alkyloxyamine linker. Using this approach, the group reported the first small molecule inhibitors (compounds **12-17**) of human UNG. The IC₅₀ values and binding affinities were reported in the micromolar and submicromolar range. These compounds were found to bind not only to the active site but also bind to the second uncompetitive site, suggesting the existence of a transitory binding site.⁴² The same group, a year later, identified another set of tethered molecules using a similar HTS strategy with a substrate fragment tethering library. The library was generated by linking 6-formyl uracil with a library of 215 various aldehyde binding elements using

O,O'-diaminoalkanediol linkers and tested against human UNG.⁴⁴ In an extended study, the group later reported the importance of an optimized selection of linkers. Unlike earlier studies, this time, more flexible amine linkers were used to study the connectivity effects. They adopted amine linker Monoamine 1 on the uracil side, monoamine 2 on the fragment side, and diamine on both sides. This study demonstrated the impact of linker flexibility and strain on binding affinity to achieve the effective inhibition of the enzyme. Inhibitor-bound protein complexes are available with different linkers (3FCF, 3FCI, 3FCK, and 3FCL). These complexes revealed that the uracil part occupied the UBP part, whereas the linking fragment part occupied the DNA binding groove.⁴³ Further, the triskelion library represented the presence of three different functional groups by derivatizing the vacant linker positions with aldehydes. HTS screening of these molecules yielded the more potent inhibitors of the human UNG with strong binding affinities and compounds 19 and 21 with the lowest IC₅₀ as 0.9 μM.⁵⁴ A summary of these inhibitors is given in Table 3.1.

Table 3.1: Summary of uracil-derived compounds reported as UNG inhibitors

General structures	R group	IC ₅₀ (μM)	Species	Reference
	10 , R ₁ = n-octyl R ₂ = H	8	HSV1	45
		>300	human	
	11 , R ₁ = n-octyl R ₂ = 1-methoxyethyl	17	<i>P. falciparum</i>	55
		>160	human	
 <p>Bipartite inhibitors</p>	12 , H	1.1	human	42
	13 , OH	0.26		
	14 , F	2.7		
	15 , Cl	16		
	16 , Br	40		
	17 , NO ₂	40		
 <p>triskelion inhibitors</p>	18 , R ₁ = R ₂ = 3,4-dihydroxyphenyl	1.6	human	54
	19 , R ₁ = 6-uracil R ₂ = 3,4-dihydroxyphenyl	0.9		
	20 , R ₁ = R ₂ = 3-carboxyphenyl	1.7		

	21 , R ₁ = 6-uracil R ₂ = 3- carboxyphenyl	0.9		
 <p>Bipartite inhibitors</p>	$R_1 = \text{N}(\text{O})\text{O}(\text{O})\text{N}$ $R_2 = \text{COOH}$, $R_3 = \text{H}$ 22	40	human	56
	$R_1 = \text{N}(\text{H})\text{O}(\text{O})\text{N}$ $R_2 = \text{COOH}$, $R_3 = \text{H}$ 23	1.6		
	$R_1 = \text{N}(\text{O})\text{O}(\text{O})\text{N}(\text{H})$ $R_2 = \text{COOH}$, $R_3 = \text{H}$ 24	100		
	$R_1 = \text{N}(\text{H})\text{O}(\text{O})\text{N}(\text{H})$ $R_2 = \text{COOH}$, $R_3 = \text{H}$ 25	315		
 <p>Bipartite inhibitors</p>	$R_1 = \text{N}(\text{O})\text{O}(\text{O})\text{N}$ $R_2 = \text{H}$, $R_3 = \text{COOH}$ 26	6		44
	27	5.1*	<i>Vaccinia virus</i>	57
	28	34*	<i>Vaccinia virus</i>	57
 <p>Gentamicin</p>	29	1500	Not defined	58
	30	420	<i>E. coli</i>	59

 <p style="text-align: center;">Gentamicin</p>				
<p>*IC₅₀ for DNA polymerase activity in the presence of the D4 (UNG in <i>Vaccinia virus</i>) A20 (Processing factor in <i>V. virus</i>) complex</p>				

Nuth et al., while searching the molecules that would block the *Vaccinia virus* infection, identified compounds **27** and **28** inhibiting the DNA polymerase activity in the micromolar range in a rapid plate assay. The remaining compounds showed moderate to low IC₅₀ values ranging from 50-200 μM. These two compounds were found effective against viral infection with EC₅₀ values of 7.1 and 8.1 μM, respectively.⁵⁷ In 2015, *Tao et al.* reported a label-free fluorescent method for detecting UNG activity. The group determined the inhibitory activity of Ugi and gentamycin using this assay and reported an IC₅₀ value of 420 μM. All these reported derivatives are uracil-based and developed using the tethering approach in most cases.⁵⁹

3.2.2 *Mycobacterium* UNG

Molecular genetics studies have shown the importance of UNG in *Mycobacteria*. Indeed, mutation rates were substantially elevated in the absence of this enzyme.^{60,61} Another study displayed the importance of *MtUng* in the survival of bacteria inside the host cell.⁶² Therefore, *MtUng* inhibitors may help treat TB alone or in combination with other antitubercular drugs. Given the critical role of UNG in various organisms, this enzyme is an important target for drug discovery for various therapeutic areas.⁹ *MtUng* has been well-characterized biochemically and structurally.^{63,64} The crystal structures of the native enzyme in various forms and in complex with different small molecules, namely, citrate, uracil, and uracil derivatives, are known. These structures comprehensively describe the UBP and the extended binding site.^{26,64,65} The extended binding pocket involves the region which interacts with the sugars and phosphates of DNA. The element which leads to the enzyme's specificity is primarily its UBP, making it an ideal target for drug design. The products formed from the UNG action on uracil-containing DNA are known to act as its inhibitors.⁶⁶ The product, uracil, binds to the enzyme's active site and serves as its inhibitor.^{66,67} The enzyme is also inhibited to various extents by uracil analogs.^{40,41,45}

3.3 GAPS IN THE RESEARCH AND OBJECTIVES

Inhibitors of UNG from different species, including humans, *Plasmodium*, and *Herpes virus*, have been reported in the literature.⁹ However, most of these inhibitors are essentially based on the uracil pharmacophore in which two or more uracil moieties are tethered through linkers, which possess moderate UNG inhibition in the higher μM to mM range. Thus, the reported UNG inhibitors are large, non-drug-like, and rely on the uracil ring for interaction with the target.

For *MtUng*, nearly 19 crystal structures complexed with uracil and its derivative are reported.²² To our knowledge, there is no systematic study to design non-uracil drug-like *MtUng* inhibitors. There is an opportunity to use SBDD for *MtUng* since this protein is amenable to crystallization.^{22,26,68} Recently, we reported diverse drug-like inhibitors of *MtUng* employing structure-based virtual screening suggesting the validity of the computational approach for the design of non-uracil inhibitors.⁶⁹ Thus, we planned to employ SBDD and a standard medicinal chemistry approach to identify uracil-mimicking compounds.

Objectives

1. To identify the uracil mimicking ring fragments from the literature based on the 2D structural similarity to uracil and molecular docking studies.
2. To solve crystal structures of various fragments in complex with *MtUng* (in collaboration) to guide the design of non-uracil inhibitors.
3. To design and synthesize derivatives of at least one fragment for establishing the SAR of the series.

3.4 RESULTS AND DISCUSSION

3.4.1 Selection, molecular docking, and *in-vitro* evaluation of ring fragments

Currently, *MtUng* inhibitors lack structural diversity. Thus, to identify new chemotypes, small ring fragments possessing hydrogen bond donor/acceptor motifs similar to the uracil ring were identified from the commercial vendors. A few rings were procured and tested *in vitro* to evaluate their *MtUng* inhibition potential. These rings were selected based on their 2D structural similarity to uracil, molecular docking results, and commercial availability.

Meanwhile, our collaborators developed the fluorescence-based assay of uracil excision by *MtUng* using a novel molecular beacon. The assay provides real-time activity detection and can be adopted for the HTS of small molecules to identify potential *MtUng* inhibitors.

The IC_{50} values of several uracil ring derivatives and the procured non-uracil fragments were estimated using the fluorescence-based assay (Table 3.2). Among various rings Interestingly, the barbituric acid (BA) ring, owing to its similarity to uracil, displayed *MtUng* inhibition ($IC_{50} = 1$ mM) comparable to several uracil derivatives.

The molecular docking of these ring fragments was performed using SwissDock, a web server-based docking program based on EADock DSS engine R. The *MtUng* binds uracil in a well-defined UBP, mostly lined with the hydrophilic residues shown in Fig. 3.10A. The molecular docking of the ring fragments with *MtUng* (PDB ID 4WPL) suggested that these rings interact with the UBP in a manner similar to uracil. All ring fragments foster a network of short-distanced hydrogen bonds with His191, Gln67, Asn127, and Phe81, displayed in Fig. 3.8. In addition, pi-pi interactions with Phe81 and Tyr70 and ion-pi bonding with Asp68 are also evident with most of these aromatic rings shown in Fig 3.8. Several of these fragments, such as BA (**9**), 5-fluoroorotic acid (**34**), and 5-Hydroxy 2,4 (1H,3H) pyrimidinedione (**37**), displayed IC_{50} values in the lower mM range in the fluorescence-based assay (Table 3.2). In addition, the activity of these fragments was also corroborated using the conventional radioactivity-based UNG assay.⁷⁰

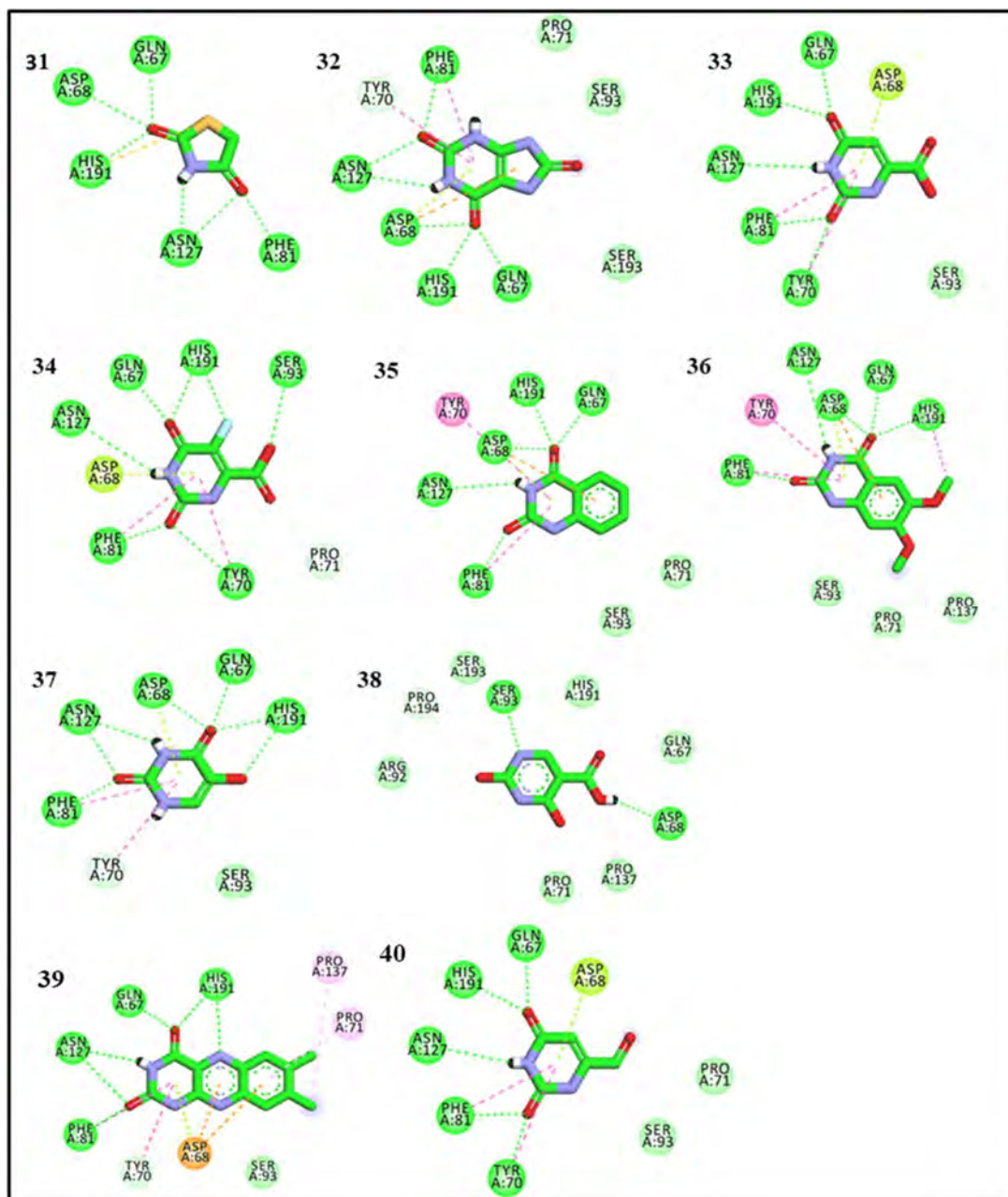


Fig. 3.8 Molecular interactions shown by ring fragments in docking studies

Our collaborators disclosed the crystal structures of *MtUng* with the ring fragments to understand their binding modes that could further assist in structure-based inhibitor design, as shown in Fig 3.9. These *MtUng* co-crystals with ring fragments could serve as an excellent starting point using SBDD for the development of non-uracil based *MtUng* inhibitors.

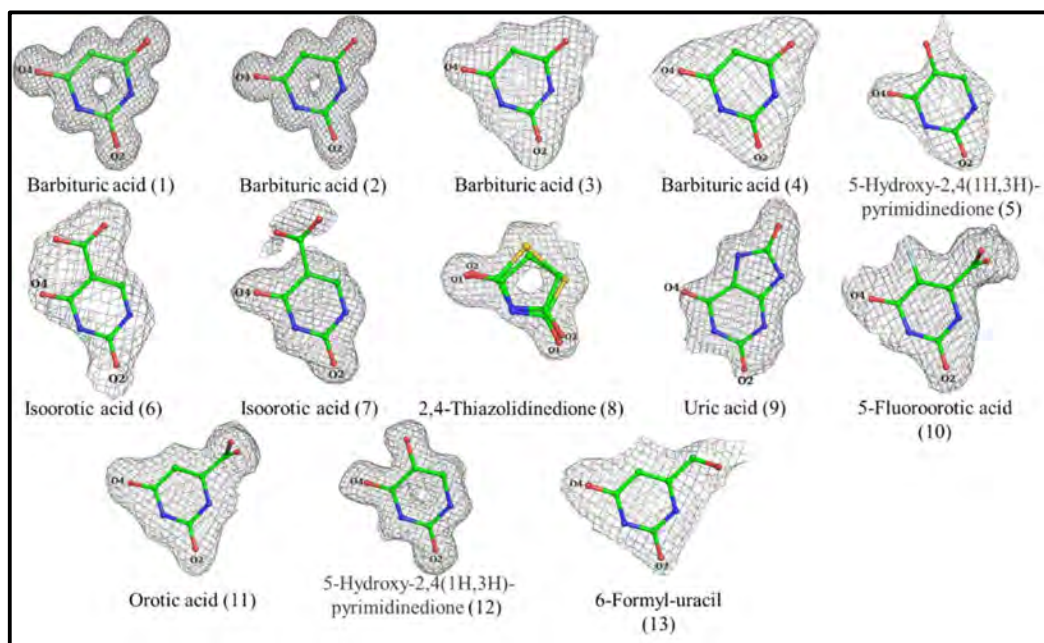
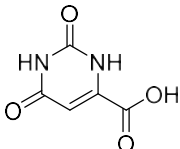
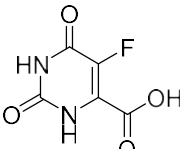
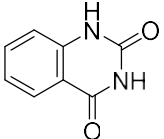
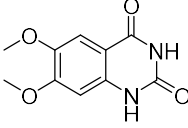
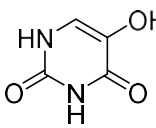
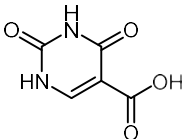
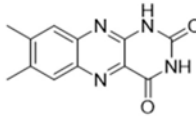
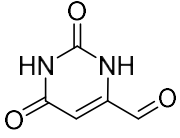


Fig. 3.9 *MtUng* co-crystals with the uracil-mimicking ring fragments

Table 3.2 IC_{50} values and predicted binding energies of uracil and similar ring fragments

Sr. no	Code	Structure	IC_{50} (mM) Radioactivity-based assay	IC_{50} (mM) (Fluorescence-based assay)	SwissDock Docking score (kcal/mol)	MM-GBSA ΔG (kcal/mol)
1	Uracil		0.8	2.05 ± 0.308^a	-6.76	-30.39
9	Barbituric acid (BA)		1.0	7.29 ± 0.32^a	-6.88	-24.86
31	2,4-Thiazolidine dione		ND	17.35 ± 0.64	-6.84	-32.77
32	Uric Acid		1.7	16.45 ± 1.79	-7.10	-37.80

33	Orotic Acid monohydrate		2.3	14.20 ± 1.20	-6.56	-15.43
34	5-Fluororotic Acid monohydrate		2.8	2.93 ± 0.19	-6.94	-16.42
35	Benzoyleneurea		ND	4.93 ± 0.54	-6.75	-24.68
36	6,7-Dimethoxyquinazoline-2,4(1H,3H)-dione		ND	0.93 ± 0.04	-7.18	-44.49
37	5-Hydroxy 2,4 (1H,3H) pyrimidinedione		1.2	2.80 ± 0.44	-6.99	-35.57
38	Isoorotic acid		2.4	15.92 ± 0.29	-6.52	-15.73
39	7,8-Dimethylalloxazine		1.5	ND	-8.09	-49.86
40	Uracil-6-carboxaldehyde monohydrate		1.0	6.51 ± 0.37	-6.61	-33.42
a IC ₅₀ values earlier reported ⁷⁰						

While BA (**9**) displayed ~3.5 less potency than uracil in the fluorescence-based assay, the radioactivity-based assay did not show much difference in the potency of the two rings. The predicted binding pose of BA overlays its hydrogen bond acceptor/donor

atoms perfectly with the uracil ring (Fig 3.10 B). It exhibits similar close contacts with UBP residues (Fig 3.10C and D).

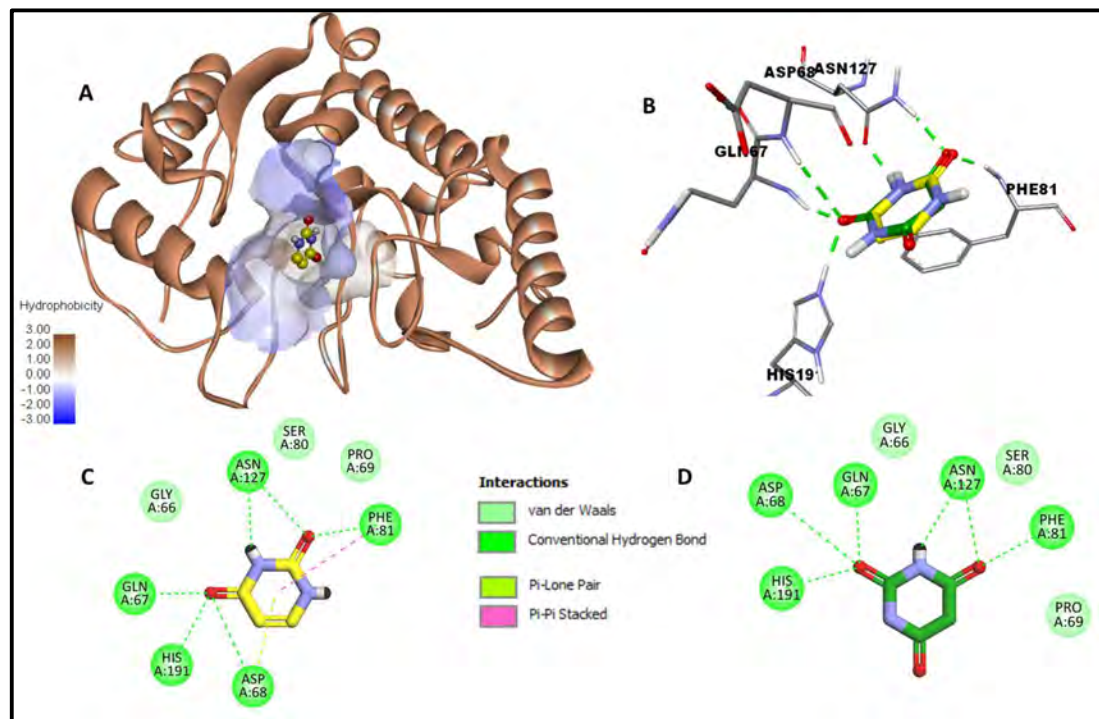


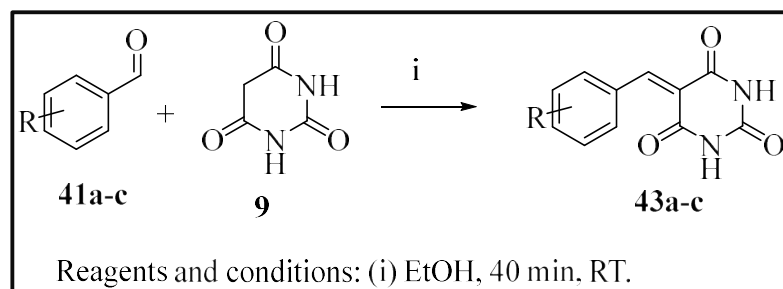
Fig. 3.10 A) 3D view of *MtUng* bound to uracil (**1**) (yellow ball and sticks) in the UBP (PDB ID 4WLP). The solvent-accessible surface is color-coded based on the hydrophobicity. B) overlay of cocrystallized uracil **1** (yellow sticks) and docked pose of barbituric acid (**9**) (green sticks) within the UBP. C) 2D view of interactions of **1** within the UBP. D) 2D view of **9** within the UBP. Colored boxes depict the interactions displayed by the ligands with *MtUng* residues.

3.4.2 Design, synthesis, and *in-vitro* evaluation of BA derivatives

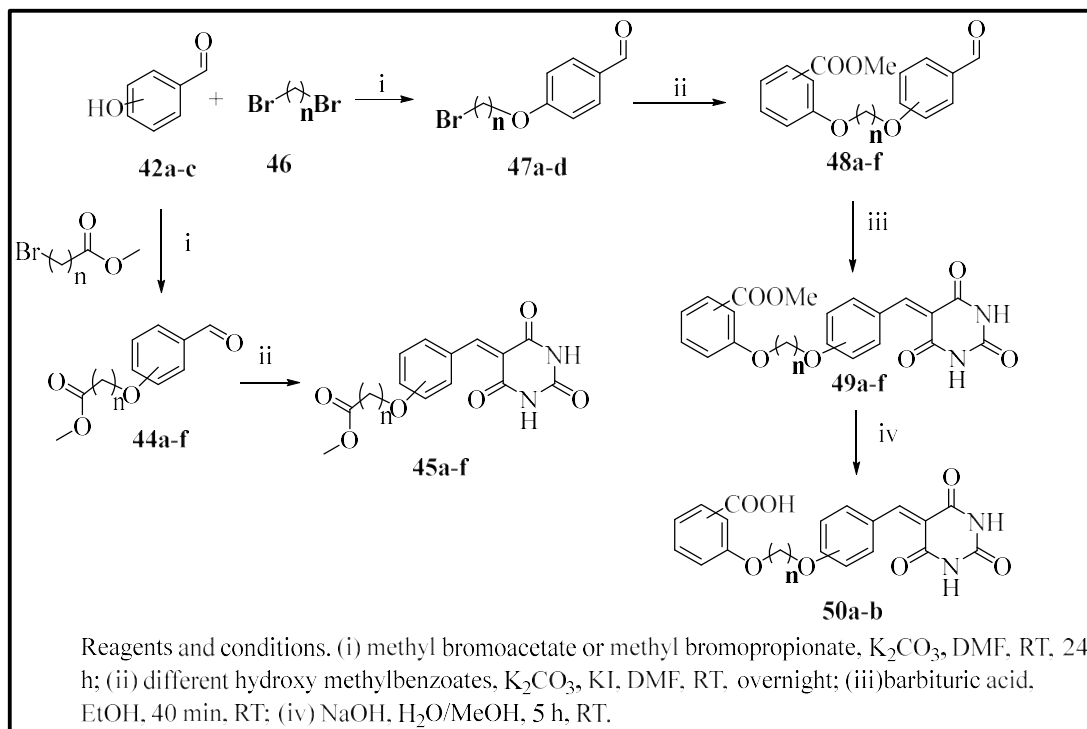
Hence, we selected the BA ring for further derivatization to design more potent *MtUng* inhibitors and understand the structure-activity relationship of this series. The BA ring bears high structural similarity to uracil, and its derivatives possess excellent synthetic tractability and wide medicinal chemistry applications.^{71–74} Different crystal forms of BA in complex with *MtUng* suggest that BA displays a variety of orientations in UBP while maintaining key H-bonds like uracil. The methylene carbon of BA provides a convenient handle for synthesizing benzylidene analogs such as **45a-c** via Knoevenagel condensation using aldehydes.

The synthetic route to molecules **43a-c** is displayed in Scheme 3.1, which involves Knoevenagel condensation of commercially available benzaldehydes derivatives with BA.⁷³ For the synthesis of molecules **49a-f**, Williamson ether synthesis was employed

using different commercially available hydroxy-substituted benzaldehydes (**42d-f**) and bromo esters, followed by Knoevenagel condensation of the resulting intermediates **48a-f** with BA (Scheme 3.2). The molecules **49a-f** were synthesized with a similar approach where mono-alkylation of hydroxy-substituted benzaldehydes (**42**) with 1,2-bromoethane (**46b**) or 1,3-bromopropane (**46a**) yielded benzaldehyde derivatives **47a-c** with an appended alkyl bromide chain. The latter was used to alkylate different hydroxybenzoates to obtain substituted benzaldehyde intermediates **48a-f**. Subsequent condensation of the latter with BA resulted in derivatives **49a-f**. The acid analogs **50a** and **50b** were obtained from **49a** and **49b**, respectively, by the basic hydrolysis of the ester group (Scheme 3.2). All Knoevenagel condensation products precipitated from the reaction solvent in good yields and did not require chromatographic purification.



Scheme 3.1 Synthesis of barbituric acid derivatives **43a-c**.



Scheme 3.2 Synthesis of barbituric acid derivatives **45a-f**, **49a-f**, and **50a-b**.

The effect of attaching a substituted phenyl ring to BA was initially studied by synthesizing benzylidene derivatives **45a-c** (Scheme 3.1). These analogs were predicted to have stronger binding affinities based on the docking and MMGBSA binding energies (Table 3). A variety of benzylidene derivatives of BA have been reported earlier against other biological targets. Initial docking results with **43a-c** suggested that BA can be grown at this vector without disturbing the required H-bond pattern of the BA ring, and additional contacts can be gained by the substituted aromatic ring (Fig. 3.11). Also, **43a-c** displayed higher MMGBSA energies compared to the uracil ring (**1**) and BA ring (**9**). This is further reflected in the docking scores of **43a-c** (-8.15 to -8.21 kcal/mol, Table 3.3) as compared to unsubstituted BA (-6.88 kcal/mol, $\Delta G = -24.86$ kcal/mol, Table 3.2). However, the **43a-c** did not display the corresponding improvement in enzyme inhibition in comparison to uracil (**1**) or BA (**9**) as assessed by the radioactivity-based assay (Table 3.3). While the BA head group in these molecules maintained the H-bonding network like the unsubstituted BA (**9**) ring, the docking studies did not predict the gain of any significant new interactions by these compounds with other residues. (Fig. 3.11).

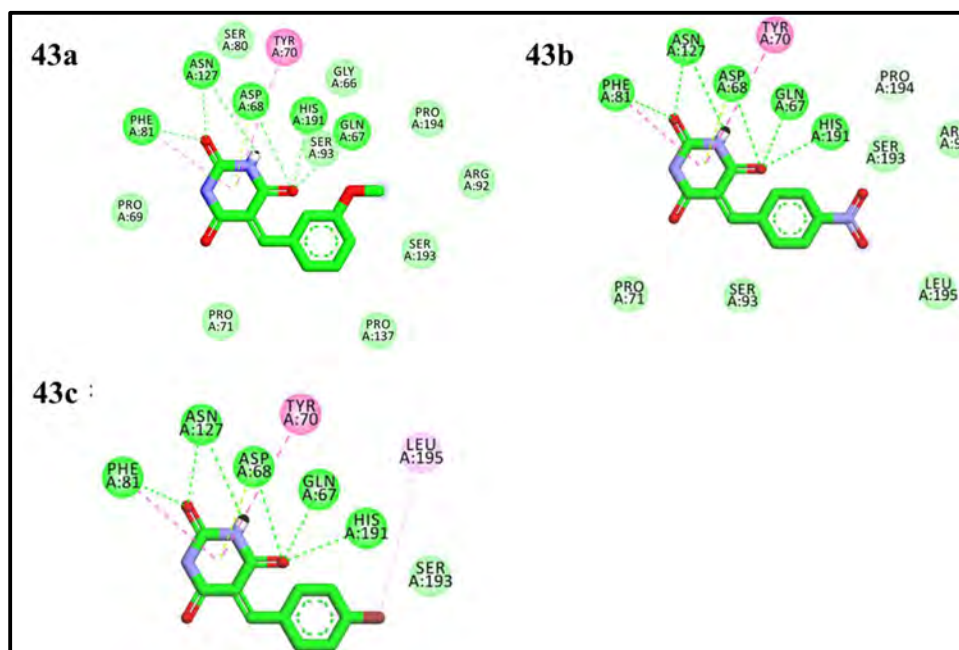


Fig. 3.11 Predicted binding pose of analogs **43a-c**

To capture further interactions with the surrounding residues, it was decided to substitute the benzylidene ring with an extended flexible substituent capable of fostering both hydrophobic as well as hydrophilic interactions. To this end, methyl ester

function was tethered to the hydroxy group of the phenyl ring with varying chain length and position (**45a-f**). Among these analogs, **45a** with the para-substitution displayed the highest potency in both assays (Table 3.3). According to the fluorescence-based assay, compound **45a** displayed ~7- and ~24-fold better inhibition than uracil (**1**) and unsubstituted BA ring (**9**), respectively. Changing the position of methyl ester substituent to ortho (**45b**) or meta (**45c**) position had a detrimental effect on the activity. Top-ranked docking pose of **45a-c** showed a perfect overlap of the BA ring of these analogs with the underivatized BA ring (**9**). However, different conformations of the ester function bearing tail region were evident (Fig. 3.12) in the highest-ranked docked poses of these analogs. The top-ranked pose of **45a** exhibited additional hydrophobic interaction with Leu195. On the other hand, **45b** and **45c** were predicted to capture an additional H-bond with Ser193 and Arg92 (Fig. 3.12B and 3.12C), respectively, although this did not translate into enhanced enzyme inhibition. Predicted binding energies of **45a-c** did not correlate with their IC₅₀, which aligns with the known limitation of molecular docking programs. Among these, **45c** showed the lowest binding energy compared to **45a** and **45b** (-66.76 kcal/mol vs. -54.71 kcal/mol and 55.60 kcal/mol, respectively), probably due to extra alkyl interactions with His75 and Pro91 with methoxy carbon (Fig. 3.12B and 3.12C). Nonetheless, binding energies of **45a-c** are higher (more negative) when compared to the analogs **43a-c**, thus supporting the rationale of substituent selection for enhancing binding strength in **45a-c**.

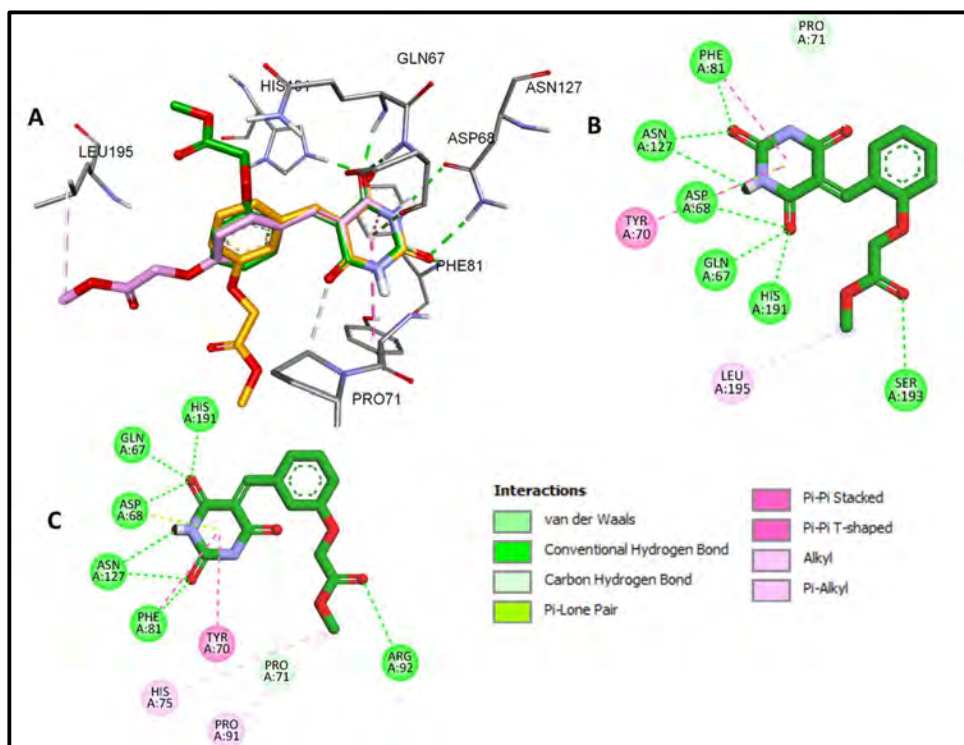
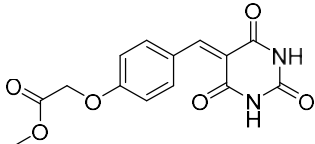
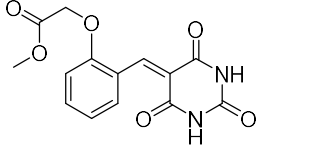
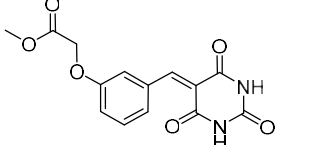
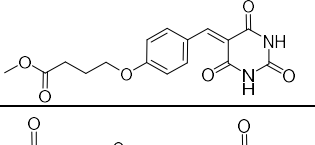
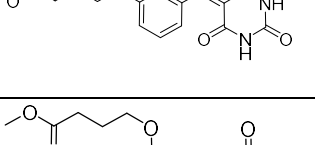
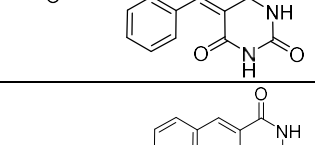
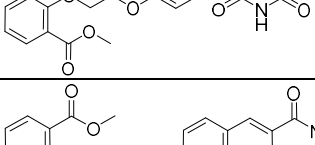
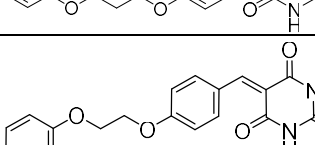
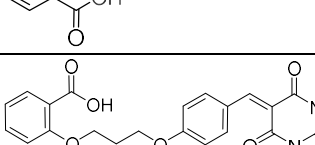
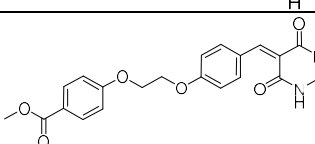

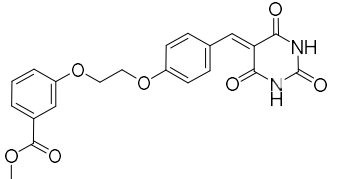
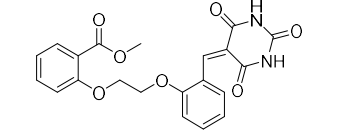
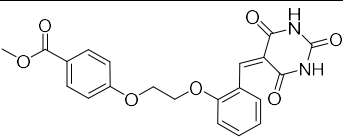


Fig. 3.12 A) Docked poses of BA derivatives **45a** (pink sticks), **45b** (orange sticks), and **45c** (green sticks) with *MtUng*. For clarity, interactions of only **45a** are shown B) 2D view of the interactions of **45b** C) 2D view of the interactions of **45c**. Colored boxes depict the type of interactions displayed by the ligands with *MtUng* residues.

Table 3.3 IC₅₀ values and predicted binding energies for the BA-based molecules

Cod e	Structure	IC ₅₀ (mM) Radioact ivity-based assay	IC ₅₀ (mM) (Fluoresce nce-based assay)	SwissDo ck Binding energy ΔG (kcal/mol)	MMGBS A ΔG binding energy (kcal/mol)
43a	<chem>COc1ccc(cc1)/C=C/C(=O)NC(=O)N</chem>	1.9	ND	-8.22	-52.19
43b	<chem>O=[N+]([O-])c1ccc(cc1)/C=C/C(=O)NC(=O)N</chem>	1.0	ND	-8.15	-44.60
43c	<chem>Brc1ccc(cc1)/C=C/C(=O)NC(=O)N</chem>	1.5	ND	-8.16	-52.13

45a		0.5	0.33 ± 0.036	-8.67	-54.71
45b		ND	5.55 ± 0.34	-8.59	-55.60
45c		ND	10.4 ± 0.7	-8.89	-66.76
45d		3.0	ND	-9.08	-71.64
45e		ND	4.20 ± 1.3	-9.36	-66.30
45f		ND	0.99 ± 0.28	-8.64	-66.00
49a		0.1	ND	-9.35	-89.82
49b		1.6	ND	-9.45	-68.62
50a		1.9	1.10 ± 0.49	-8.98	-61.74
50b		0.7	ND	-9.71	-85.90
49c		1.2	ND	-9.09	-75.33

49d		2.4	ND	-9.58	-75.68
49e		ND	1.06 ± 0.31	-9.56	-58.55
49f		3.5	ND	-9.62	-61.42
ND = not determined due to intrinsic fluorescence					

Increasing the size of the ester-bearing substituent at the para position by one carbon (**45a** vs. **45d**) led to the decrease in activity in the radioactivity-based assay, despite the predicted MMGBSA binding energy to be higher for **45d** (-54.71 kcal/mol vs. -71.64 kcal/mol). However, similar changes for the ortho (**45b** vs. **45f**) and meta (**45c** vs. **45e**) resulted in the improvement in the *MtUng* inhibition as found using the fluorescence-based assay (Table 3.3). However, increasing the size of the ester-bearing substituent at the ortho (**45b** vs. **45f**) and meta (**45c** vs. **45e**) resulted in the improvement in the *MtUng* inhibition as found using the fluorescence-based assay (Table 3.3). All analogs with longer ester-based substituents (**45-45f**) resulted in improved *MtUng* inhibition than the unsubstituted BA ring fragment by capturing more H-bond interactions, found using the fluorescence-based assay. Overall, these results show the importance of substituent-size and its position relative to the BA ring in determining the activity.

The ortho-substituted analog **45f** ($IC_{50} = 0.99$ mM) was found to possess ~4-fold higher potency in the fluorescence-based assay compared to the meta-substituted compound **45e** ($IC_{50} = 4.2$ mM) despite having nearly the same binding energies. As in the case of **45b**, the highest-ranked pose of **45f** ester-bearing tail of the molecule is oriented in a direction opposite to that of **45d** and **45e** (Fig. 3.13) towards Arg170. While **45f** displays hydrophobic interactions with Arg170, **45d** and **45e** foster additional H-bonds with Arg92 and hydrophobic interaction with His75 and Pro9 (Fig. 3.13B and 3.13C).

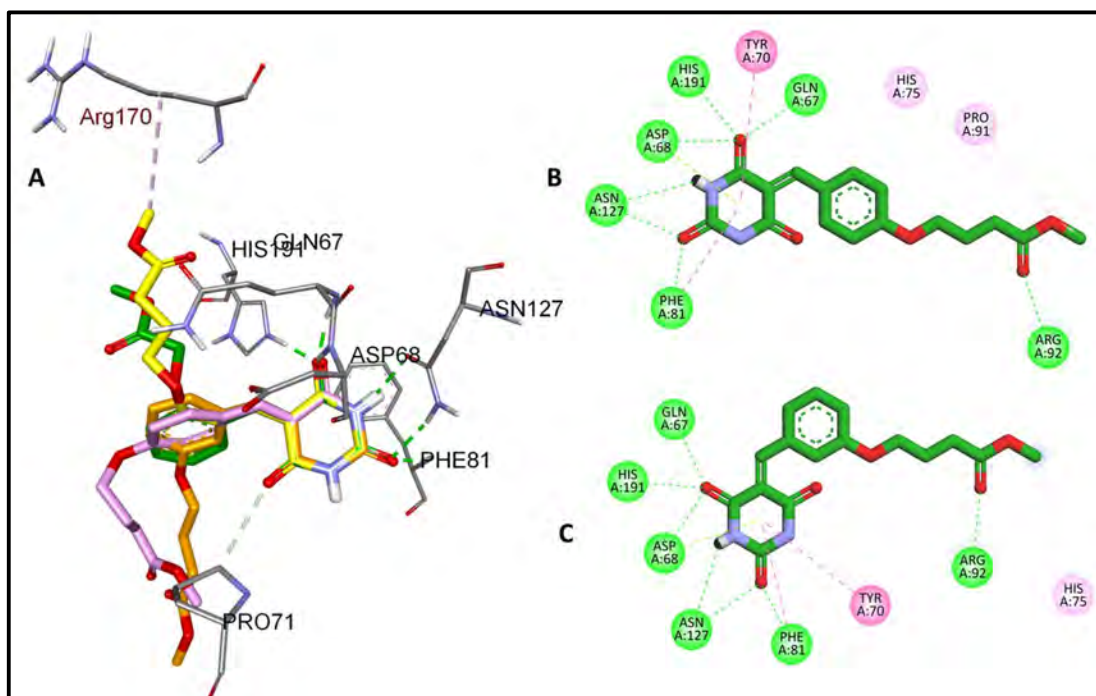


Fig. 3.13 A) Docked poses of BA derivatives **45d** (pink sticks), **45e** (orange sticks), **45f** (yellow sticks), and **45a** (green sticks) with *MtUng*. For clarity, interactions of only **45f** are shown B) 2D view of the interactions of **45d** C) 2D view of the interactions of **45e**. See Fig 3.12 for the color codes of ligand-protein interactions.

Given the positive impact of substitution at para (**45a**) and ortho position (**45f**), in addition to the short linear substituents, we synthesized analogs with an additional aromatic ring at these positions, thus, mimicking the previously reported uracil-based human UNG analogs. Overall, such molecules were predicted to have higher binding affinities for the enzyme due to the presence of an aromatic ring, which could offer more H-bond interactions in the active site. Thus **49a-f** and **50a-b** were synthesized and evaluated against *MtUng* (Table 3.3).

In this series, molecule **49a**, with a two-carbon linker between the two aromatic rings, was found to be the most potent derivative with IC_{50} of 0.1 mM in the radioactivity-based assay. Compound **49a** is about ~10 and ~5-fold more potent than BA (**9**) and **45a**, respectively, as per the same assay. Interestingly, **49a** also showed the highest binding affinity for *MtUng* as per the MMGBSA score. Increasing the chain length in **49a** from two to three carbons lowered the activity and binding energy of the resulting analog **49b** significantly. This suggests that increasing the flexibility of the linker region is not favorable for enzyme inhibition. This result is also reflected by the lower MMGBSA score of **49b** (-68.62 kcal/mol) compared to **49a** (-89.82 kcal/mol). As expected, the

phenyl ring in the tail region of both **49a** and **49b** exhibited additional hydrophobic interactions, albeit they are oriented in the opposite direction within the pocket (Fig. 3.14A). The analog **49a** displays hydrophobic interactions with Pro137 and Pro71 (Fig 3.14A), while **49b** interacts with Ala138, Pro137, and Leu195 (Fig 3.14B).

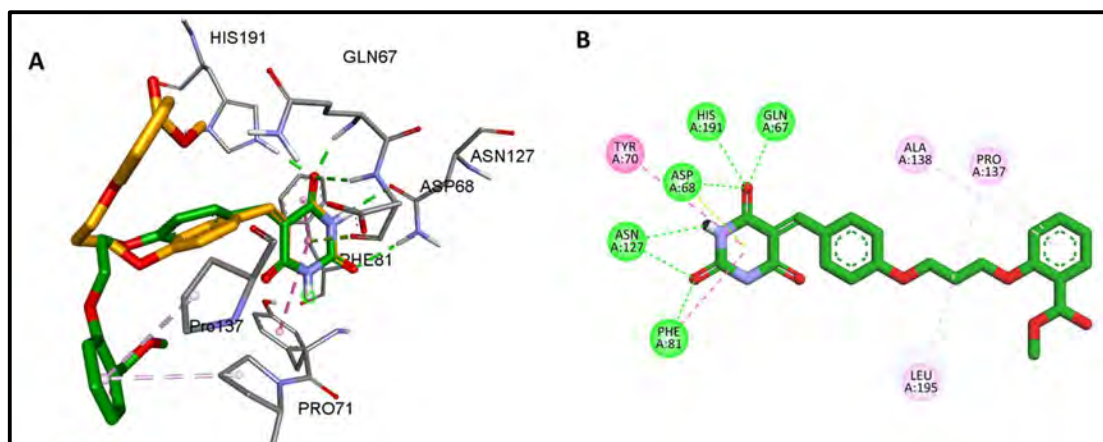


Fig. 3.14 A) Docked poses of BA derivatives **49a** (green sticks) and **49b** (orange sticks). For clarity, interactions of only **49a** are shown. B) 2D view of the interactions of **49b**. See Fig. 3.14 for the color codes of ligand-protein interactions.

Conversion of the ester group in **49a** to carboxylic acid in **50a** resulted in a ~19-fold decrease in the activity based on radioactivity assay as binding energy decreased. In contrast, **50b**, the corresponding acid analog of **49b**, showed ~2.2-fold better inhibition of *MtUng* in the radioactivity-based assay supported by the significant increase in binding energy in **50b**. These contrasting results may be due to the different orientations of the tail regions of both compounds resulting in different interactions. Indeed, MMGBSA binding data is in accordance with the observed experimental data. The acid derivative **50a** is predicted to have lower ΔG (-61.74 kcal/mol) compared to its ester analogs **49a** (-89.82 kcal/mol), while derivative **50b** displays higher binding affinity (-85.90 kcal/mol) than the corresponding ester analogs **49b** (-68.62 kcal/mol). The compounds **49c** and **49d** were synthesized to see the effect of moving the ester group from ortho to para (**49c**) or meta (**49d**) position. Unfortunately, both analogs showed lower potency compared to **43a** suggesting the ortho-position to be optimum for the ester group. The lower IC_{50} data is supported by, the lower MMGBSA energy of **49c** and **49d** compared to **49a**. Changing the position of the linker on the benzylidene ring in **49a** from para to ortho position while restricting the ester group to ortho position resulted in analog **49e** with IC_{50} of about 1 mM in the fluorescence-based assay, which

could not be compared with **49a** due to the unavailability of inhibition data of latter in the same assay. However, the similar potency of **50a** (the acid analog of **49a**) compared to **49e** in the fluorescence-based assay, and their comparable MMGBSA energies, suggest **50a** should be less potent than **49a**. Similarly, an attempt to measure the effect of switching the position of the ester group from ortho (**49e**) to the para position of the phenyl ring could not be measured in **49f**. However, both compounds **49e** and **49f** displayed nearly similar binding energies (-58.55 kcal/mol and -61.42 kcal/mol resp.). Nevertheless, in comparison to BA, **49e** displayed ~7-fold better potency. Similarly, a comparison of **49f** ($IC_{50} = 3.5$ mM) to **49c** ($IC_{50} = 1.2$ mM) also suggests that the ortho substitution of the linker to the benzylidene moiety is detrimental to the *MtUng* inhibition. The MMGBSA binding affinities also support the latter results. Thus, the SAR study and molecular docking suggest that the ester-bearing lipophilic chain/aromatic ring at the para position of the benzylidene ring is favorable for the *MtUng* inhibition. Conversely, a polar carboxylate function was found to be relatively unfavorable.

3.5 METHODOLOGY

3.5.1 Fragment selection

Fragment screening and identification of the ring fragments selected based on their 2D structural similarity to uracil, modeling studies, and commercial availability of the compounds. A molecular docking study was performed for these fragments, followed by a screening of ring fragments for their inhibitor potential of *MtUng* activity (Table 3.2).

3.5.2 Docking and MMGBSA calculations:

The molecular docking of all compounds was performed using SwissDock, a web server-based docking program based on EADock DSS engine^{75,76} with *MtUng* protein (PDB ID 4WPL). The protein was prepared using the DockPrep Plugin in Chimera 1.13⁷⁷ by removing the solvent molecules. The hydrogen atoms and charges were added to the protein. All the cofactors and heteroatoms were removed, and energy minimization was performed using an Amber99 forcefield. The ligand was prepared by adding all hydrogen atoms and saved in MOL2 format. The prepared protein and ligands were docked using the 'blind docking' and 'accurate' options available on the web server. The residue side chains were kept rigid. The default setting for docking includes the number of binding modes = 5000, SD minimization steps = 100, ABNR minimization steps = 250, and NB seeds = 250.⁷⁵ The resulting chimerax file was opened in Chimera, and the lowest energy pose for each ligand was exported to Biovia Discovery studio 2017 R2⁷⁸ to visualize interactions and create images. The MMGBSA calculations for binding energy were performed using Prime MM-GBSA (Schrodinger Suite Maestro 13.2 version). After generating the output ligands from SwissDock, separate protein and ligand structures were saved in PDB format and used to estimate the binding free energy. For the calculations with the OPLS_2005 force field, VSGB 2.0 solvation model was used, which uses water as a solvent. ΔG_{bind} energy was calculated using the following equation.

$$\Delta G_{\text{bind}} = G_{\text{RL}} - G_{\text{R}} - G_{\text{L}}$$

Where ΔG_{bind} is the free energy of binding; G_{RL} is the energy of receptor-ligand complex; G_{R} is the energy of receptor; G_{L} is the energy of ligand.

3.5.3 Chemistry

All starting materials were purchased from commercial sources and used as purchased without further purification unless stated otherwise or synthesized *via* literature procedures. Thin-layer chromatography was used to monitor the progress of the reactions and checked by pre-coated TLC plates (E. Merck Kieselgel 60 F254 with fluorescence indicator UV254). The components were visualized by irradiation with ultraviolet light (254 nm), using iodine vapors, or by staining in potassium permanganate solution followed by heating. Compounds were purified over a silica gel (230-400 mesh) column using distilled solvents. All final compounds were characterized by ¹H NMR spectroscopy using deuterated solvents, CDCl₃ or DMSO-d₆. ¹H NMR spectra were recorded on a Bruker Advance 400 MHz spectrometer. Chemical shifts are given in parts per million (ppm) (δ relative to residual solvent peak for ¹H). High-resolution mass spectrometry (HRMS) analysis was performed using a Q-TOF Agilent system. The purity of the sample was checked by Quantitative NMR protocol using maleic acid as an internal standard.

The synthesized benzylidene molecules were found to have stability issues in the presence of DMSO upon storage for a long time. Thus, purity analysis was performed using quantitative NMR with maleic acid.

General procedure for quantitative NMR: Accurately weighed the internal standard maleic acid and sample, dissolved in 500 μL DMSO, and sample submitted for ¹H NMR. NMR spectra were integrated, and percentage purity was calculated using the standard formula.

$$\%Purity(x) = \frac{MW(x)}{MW(std)} * \frac{nH(std)}{nH(x)} * \frac{A(x)}{A(std)} * \frac{m(std)}{(mx)} * Purity(std)$$

Where P(x) and P(std) are the purities in percent, m(x) and m(std) are the weights in mg, nH(x) and nH(std) are the number of protons generating the selected signals for integration, MW(x) and MW(std) are the molecular weights in g/mol, A(x) and A(std) are the areas for the selected peaks of the sample and the internal standard, all respectively.

The general procedure for the synthesis of compounds and compound characterization data are given below.

3.5.3.1 General synthesis procedure of compound (43a-c):

A mixture of various substituted benzaldehydes (**41a-c**) and barbituric acid (**9**) (0.8 eq.) was suspended in ethanol, and the reaction mixture was stirred for 40 min at room temperature. After completion of the reaction, yellow-colored precipitate was formed. The precipitate was filtered and washed with dichloromethane 3-4 times to remove unreacted aldehydes. The solid was dried and collected as a compound (**43a-c**).

5-(3-methoxybenzylidene)pyrimidine-2,4,6(1H,3H,5H)-trione (43a). Synthesized from 3-methoxybenzaldehyde (**41a**) (100 mg, 0.5 mmol) and barbituric acid (**9**) (76 mg, 0.4 mmol) according to general procedure 3.5.3.1. Yellow solid, Yield = 44% (79.5 mg); Quantitative NMR Purity = 97.4%; ¹H NMR (400 MHz, DMSO) δ 11.41 (s, 1H), 11.26 (s, 1H), 8.26 (s, 1H), 7.85 (s, 1H), 7.62 (d, *J* = 7.7 Hz, 1H), 7.40 (t, *J* = 8.0 Hz, 1H), 7.13 (dd, *J* = 8.0, 2.3 Hz, 1H), 3.80 (s, 3H). HRMS (ESI) for C₁₂H₁₀N₂O₄ ([M+H]⁺): calculated 246.0641, found 246.0651.

5-(4-nitrobenzylidene)pyrimidine-2,4,6(1H,3H,5H)-trione (43b). Synthesized from 4-nitrobenzaldehyde (**41b**) (75.56 mg, 0.5 mmol) and barbituric acid (**9**) (51 mg, 0.4 mmol) according to general procedure 3.5.3.1. Yellow solid, Yield = 43% (55 mg); Quantitative NMR Purity = 97.11%; ¹H NMR (400 MHz, DMSO) δ 11.40 (s, 1H), 11.26 (d, *J* = 4.2 Hz, 1H), 8.26 (s, 1H), 7.84 (s, 1H), 7.61 (d, *J* = 7.7 Hz, 1H), 7.41 (dt, *J* = 16.0, 5.5 Hz, 1H), 7.13 (dd, *J* = 8.0, 2.3 Hz, 1H). HRMS (ESI) for C₁₁H₇N₃O₅ ([M+H]⁺): calculated 261.0386, found 261.0375.

5-(4-bromobenzylidene)pyrimidine-2,4,6(1H,3H,5H)-trione (43c). Synthesized from 4-bromobenzaldehyde (**41c**) (50 mg, 0.27 mmol) and barbituric acid (**9**) (28 mg, 0.22 mmol) according to general procedure 3.5.3.1. Yellow solid, Yield = 54% (82 mg); Quantitative NMR Purity = 99%; ¹H NMR (400 MHz, DMSO) δ 11.42 (s, 1H), 11.27 (s, 1H), 8.23 (s, 1H), 7.99 (d, *J* = 8.5 Hz, 2H), 7.68 (d, *J* = 8.6 Hz, 2H).

3.5.3.2 General synthesis procedure of compound (44a-f):

A mixture of various hydroxy-substituted benzaldehydes (**42a-c**) (1 eq.) and various methyl bromoesters (1 eq.) was suspended in DMF. Sodium hydride (2 eq.) was added to suspension, and the reaction mixture was stirred at room temperature for 24 h. After completion of the reaction, water was added to the reaction mixture, and the mixture was extracted in ethyl acetate (50 mL×3). The combined organic layers were dried over

anhydrous sodium sulfate, filtered, and concentrated *in vacuo*. The crude products were purified by column chromatography. to yield the desired products (**44a-f**).

methyl 2-(4-formylphenoxy)acetate (44a). Synthesized from 4-Hydroxybenzaldehyde (**42a**) (1.098g, 9 mmol) and methyl 2-bromoacetate (864 μ L, 9 mmol) in DMF. Reagents were suspended, and sodium hydride (216 mg, 10.8 mmol) was added according to the general procedure 3.5.3.2. Yellow oily compound, Yield = 72% (298 mg); $^1\text{H NMR}$ (400 MHz, CDCl_3) δ 9.89 (d, $J = 2.1$ Hz, 1H), 7.87 – 7.80 (m, 2H), 7.01 (dd, $J = 8.6, 1.6$ Hz, 2H), 4.73 (d, $J = 1.4$ Hz, 2H), 3.81 (d, $J = 1.9$ Hz, 3H).

methyl 2-(2-formylphenoxy)acetate (44b). Synthesized from 2-Hydroxybenzaldehyde (**42b**) (183 mg, 1.5 mmol) and methyl 2-bromoacetate (230 mg, 1.5 mmol) in DMF. Reagents were suspended, and sodium hydride (60 mg, 1.5 mmol) was added according to the general procedure 3.5.3.2. Yellow oily compound, Yield = 68% (130 mg); $^1\text{H NMR}$ (400 MHz, CDCl_3) δ 10.47 (dd, $J = 2.3, 1.2$ Hz, 1H), 7.82 – 7.70 (m, 1H), 7.49 – 7.38 (m, 1H), 7.07 – 6.92 (m, 1H), 6.87 – 6.74 (m, 1H), 4.70 (d, $J = 2.4$ Hz, 2H), 3.84 – 3.63 (m, 3H).

methyl 2-(3-formylphenoxy)acetate (44c). Synthesized from 3-Hydroxybenzaldehyde (**42c**) (183 mg, 1.5 mmol) and methyl 2-bromoacetate (230 mg, 1.5 mmol) in DMF was suspended, and sodium hydride (60 mg, 1.5 mmol) added according to the general procedure 3.5.3.2. Yellow oily compound, Yield = 65% (198 mg); $^1\text{H NMR}$ (400 MHz, CDCl_3) δ 10.00 (d, $J = 3.6$ Hz, 1H), 7.58 – 7.46 (m, 2H), 7.39 (dd, $J = 2.6, 1.1$ Hz, 1H), 7.25 (ddd, $J = 7.9, 2.7, 1.3$ Hz, 1H), 4.74 (d, $J = 3.5$ Hz, 2H), 3.84 (s, 3H).

methyl 4-(4-formylphenoxy)butanoate (44d). Synthesized from 4-Hydroxybenzaldehyde (**42a**) (122.12 mg, 1.5 mmol) and methyl 4-bromobutanoate (181 mg, 1 mmol) in DMF was suspended and sodium hydride (48 mg, 1 mmol) added according to the general procedure 3.5.3.2. Creamy crystalline solid, Yield = 69% (154 mg); $^1\text{H NMR}$ (400 MHz, CDCl_3) δ 9.89 (s, 1H), 7.91 – 7.76 (m, 2H), 7.07 – 6.94 (m, 2H), 4.11 (t, $J = 6.1$ Hz, 2H), 3.71 (s, 3H), 2.55 (t, $J = 7.2$ Hz, 2H), 2.24 – 2.08 (m, 2H).

methyl 4-(2-formylphenoxy)butanoate (44e). Synthesized from 2-Hydroxybenzaldehyde (**42b**) (122.12 mg, 1.5 mmol) and methyl 4-bromobutanoate (181 mg, 1 mmol) in DMF was suspended and sodium hydride (48 mg, 1 mmol) added according to the general procedure 3.5.3.2. Yellow oily compound, Yield = 53% (162 mg); $^1\text{H NMR}$ (400 MHz, CDCl_3) δ 10.50 (d, $J = 0.7$ Hz, 1H), 7.85 (dd, $J = 7.7, 1.8$ Hz,

1H), 7.55 (ddd, J = 8.5, 7.4, 1.8 Hz, 1H), 7.04 (t, J = 7.5 Hz, 1H), 6.99 (d, J = 8.4 Hz, 1H), 4.16 (t, J = 6.1 Hz, 2H), 3.71 (s, 3H), 2.58 (t, J = 7.2 Hz, 2H), 2.25 – 2.18 (m, 2H).

methyl 4-(3-formylphenoxy)butanoate (44f). Synthesized from 3-Hydroxybenzaldehyde (**42c**) (122.12 mg, 1.5 mmol) and methyl 4-bromobutanoate (181 mg, 1 mmol) in DMF was suspended and sodium hydride (48 mg, 1 mmol) added according to the general procedure 3.5.3.2. Yellow oily compound, Yield = 37% (112 mg); ¹H NMR (400 MHz, CDCl₃) δ 9.96 (dd, J = 6.4, 5.3 Hz, 1H), 7.47 – 7.41 (m, 2H), 7.37 (s, 1H), 7.18 – 7.13 (m, 1H), 4.06 (ddd, J = 6.1, 4.1, 1.5 Hz, 2H), 3.71 – 3.68 (m, 3H), 2.54 (td, J = 7.2, 1.7 Hz, 2H), 2.19 – 2.09 (m, 2H).

3.5.3.3 Synthesis procedure of compound (45 a-f):

A mixture of derived aldehydes (**44a-f**) (1 eq.) and barbituric acid (**9**) (0.8 eq.) was suspended in ethanol and stirred the reaction mixture for 40 min at room temperature. After completion of the reaction, the obtained precipitate was filtered and washed with dichloromethane 3-4 times to remove unreacted aldehydes. The obtained solids were dried and collected as a compound (**45a-f**).

methyl 2-(4-((2,4,6-trioxotetrahydropyrimidin-5(2H)-ylidene)methyl)phenoxy)acetate (45a). Synthesized from methyl 2-(4-formylphenoxy)acetate (**44a**) (260 mg, 1.25 mmol) and barbituric acid (**9**) (128 mg, 1 mmol) according to the general procedure 3.5.3.3. Bright yellow solid, Yield = 67% (256 mg); Quantitative NMR Purity = 97%; ¹H NMR (400 MHz, DMSO): δ = 3.73 Hz (s, 1H), 4.97 Hz (s, 2H), 7.06 Hz (t, 1H), 7.08 Hz (t, 1H), 8.25 Hz (s, 1H), 8.33 Hz (t, 1H), 8.35 Hz (t, 1H), 11.22 Hz (s, 1H, N-H), 11.34 Hz (s, 1H, N-H). HRMS (ESI) for C₁₄H₁₂N₂O₆ ([M+H]⁺): calculated 304.0695, found 304.0675.

methyl 2-(2-((2,4,6-trioxotetrahydropyrimidin-5(2H)-ylidene)methyl)phenoxy)acetate (45b). Synthesized from methyl 2-(2-formylphenoxy)acetate (**44b**) (195 mg, 1 mmol) and barbituric acid (**9**) (1102.4 mg, 0.8 mmol) according to the general procedure 3.5.3.3. Yellow solid, Yield= 56% (170 mg); Quantitative NMR Purity = 94.52%; ¹H NMR (400 MHz, DMSO) δ 8.55 (s, 1H), 7.97 – 7.90 (m, 1H), 7.48 (dt, J = 15.8, 4.3 Hz, 1H), 7.01 (t, J = 7.5 Hz, 2H), 4.93 (s, 2H), 3.69 (s, 3H). HRMS (ESI) for C₁₄H₁₂N₂O₆ ([M+H]⁺): calculated 304.0695, found 304.0683.

methyl 2-(3-((2,4,6-trioxotetrahydropyrimidin-5(2H)-ylidene)methyl)phenoxy)acetate (45c). Synthesized from methyl 2-(3-

formylphenoxy)acetate (**44c**) (195 mg, 1 mmol) and barbituric acid (**9**) (102.4 mg, 0.8 mmol) according to the general procedure 3.5.3.3. Yellow solid, Yield= 54% (166 mg); Quantitative NMR Purity = 99%; ¹H NMR (400 MHz, DMSO) δ 8.23 (s, 1H), 7.80 (s, 1H), 7.55 (dd, J = 15.1, 5.2 Hz, 1H), 7.39 (t, J = 6.8 Hz, 1H), 7.11 (dd, J = 8.2, 2.4 Hz, 1H), 4.79 (s, 2H), 3.75 (s, 3H). HRMS (ESI) for C₁₄H₁₂N₂O₆ ([M+H]⁺): calculated 304.0695, found 304.069.

methyl **4-(4-((2,4,6-trioxotetrahydropyrimidin-5(2H)-ylidene)methyl)phenoxy)butanoate (45d)**. Synthesized from methyl 4-(4-formylphenoxy)butanoate (**44d**) (100 mg, 0.45 mmol) and barbituric acid (**9**) (46 mg, 0.36 mmol) according to the general procedure 3.5.3.3. Yellow solid, Yield = 80% (120 mg); Quantitative NMR Purity = 98%; ¹H NMR (400 MHz, DMSO) δ 8.30 (d, J = 8.9 Hz, 1H), 8.22 (s, 1H), 7.05 (dd, J = 25.7, 8.8 Hz, 1H), 4.10 (t, J = 6.3 Hz, 1H), 3.59 (s, 1H), 2.46 (t, J = 7.3 Hz, 1H), 1.99 (p, J = 6.7 Hz, 1H). HRMS (ESI) for C₁₆H₁₈N₂O₆ ([M+H]⁺): calculated 332.1008, found 332.1001.

methyl **4-(2-((2,4,6-trioxotetrahydropyrimidin-5(2H)-ylidene)methyl)phenoxy)butanoate (45e)**. Synthesized from methyl 4-(2-formylphenoxy)butanoate (**44e**) (104 mg, 0.47 mmol) and barbituric acid (**9**) (48 mg, 0.376 mmol) according to the general procedure 3.5.3.3. Bright yellow solid, Yield = 76% (114 mg); Quantitative NMR Purity = 94%; ¹H NMR (400 MHz, DMSO) δ 8.49 (s, 1H), 7.95 (dd, J = 7.8, 1.3 Hz, 1H), 7.52 – 7.46 (m, 1H), 7.08 (d, J = 8.3 Hz, 1H), 6.97 (t, J = 7.6 Hz, 1H), 4.09 (t, J = 6.2 Hz, 2H), 3.57 (d, J = 3.9 Hz, 3H), 2.04 – 1.94 (m, 2H). HRMS (ESI) for C₁₆H₁₈N₂O₆ ([M+H]⁺): calculated 332.1008, found 332.0998.

methyl **4-(3-((2,4,6-trioxotetrahydropyrimidin-5(2H)-ylidene)methyl)phenoxy)butanoate (45f)**. Synthesized from methyl 4-(3-formylphenoxy)butanoate (**44f**) (100 mg, 0.45 mmol) and barbituric acid (**9**) (46 mg, 0.36 mmol) according to the general procedure 3.5.3.3. Yellowish white powder, Yield = 69% (103.1 mg); Quantitative NMR Purity = 97%; ¹H NMR (400 MHz, DMSO) δ 8.23 (s, 1H), 7.78 (s, 1H), 7.51 (t, J = 8.1 Hz, 1H), 7.37 (t, J = 8.0 Hz, 1H), 7.09 (dd, J = 8.1, 2.3 Hz, 1H), 4.00 (t, J = 6.3 Hz, 2H), 3.58 (s, 3H), 2.46 (t, J = 7.2 Hz, 2H), 1.98 (p, J = 6.8 Hz, 2H). HRMS (ESI) for C₁₆H₁₆N₂O₆ ([M+H]⁺): calculated 332.1008, found: 332.1008.

3.5.3.4 General Synthesis procedure of compound (47a-c):

A mixture of hydroxy-substituted aldehyde (**42a-c**) (1 eq.) and dibromoalkane (**46**) (3 eq.) was suspended in DMF, and potassium carbonate (2 eq.) was added. The reaction was stirred at room temperature for 24 hrs. After completion of the reaction, water was added to the reaction mixture, and the mixture was extracted in ethyl acetate (50 mL × 3). The combined organic layers were dried over anhydrous sodium sulfate, filtered, and concentrated *in vacuo*. The crude products were purified by column chromatography to yield the desired product (**47a-c**).

4-(2-bromoethoxy)benzaldehyde (47a). Synthesized from 4-hydroxybenzaldehyde (**42d**) (1.098 g, 9 mmol) and dibromoethane (**46a**) (2.340 mL, 27 mmol) according to the general procedure 3.5.3.4. Yellowish compound, Yield = 43% (885 mg); ¹H NMR (400 MHz, CDCl₃): δ = 0.9 Hz (m, 2H), 1.29 Hz (m, 3H), 3.69 Hz (t, 2H), 4.39 Hz (t, 2H), 7.04 Hz (m, 2H), 7.87 Hz (m, 2H) and 9.91 Hz (s, 1 H)

4-(3-bromopropoxy)benzaldehyde (47b). Synthesized from 4-hydroxybenzaldehyde (**42d**) (1.098 g, 9 mmol) and dibromopropane (**46b**) (2.742 mL, 27 mmol) according to the general procedure 3.5.3.4. White crystalline compound, Yield= 70% (1522 mg); ¹H NMR (400 MHz, CDCl₃): δ = 2.36 Hz (td, 2H), 3.63 Hz (t, 2H), 4.21 (t, 2H), 7.02 Hz (m, 2H), 7.85 Hz (m, 2H) and 9.90 Hz (s, 1H)

2-(2-bromoethoxy)benzaldehyde (47c). Synthesized from 2-hydroxybenzaldehyde (**42a**) (3.0 g, 24.566 mmol) and dibromoethane (**46a**) (13.844 mL, 27.698 mmol) according to the general procedure 3.5.3.4. White crystalline compound, Yield= 52% (2914 mg); ¹H NMR (400 MHz, CDCl₃) δ 10.57 (d, J = 0.7 Hz, 1H), 7.89 (dd, J = 7.7, 1.8 Hz, 1H), 7.57 (tt, J = 11.8, 3.1 Hz, 1H), 7.28 (s, 1H), 7.10 (t, J = 7.5 Hz, 1H), 6.99 (d, J = 8.4 Hz, 1H), 4.45 (t, J = 6.0 Hz, 2H), 3.74 (t, J = 6.0 Hz, 2H).

3.5.3.5 General Synthesis procedure of compound (48a-f):

To a suspension of compound (**46a-c**) (1 eq.) in DMF, various hydroxy methyl benzoate (1 eq.) was added. Potassium carbonate (3 eq.) and potassium iodide (2.5 eq.) was added to the suspension, and the reaction mixture was stirred at room temperature for 12 h. After the completion of the reaction, water was added to the reaction mixture, and it was extracted with ethyl acetate (50 mL×3). The combined organic layers were dried over anhydrous sodium sulphate, filtered, and concentrated *in vacuo*. The crude products were purified by column chromatography to obtain the desired products (**48a-f**).

methyl 2-(2-(4-formylphenoxy)ethoxy)benzoate (48a). Synthesized from 4-(2-bromoethoxy)benzaldehyde (**46a**) (229 mg, 1 mmol) and methyl-2-hydroxybenzoate (760.7 mg, 1 mmol) according to the general procedure 3.5.3.5. White powder, Yield = 87% (262 mg); ¹H NMR (400 MHz, CDCl₃): δ = 3.83 Hz (s, 3H), 4.45 Hz (m, 4H), 7.06 Hz (m, 4H), 7.48 Hz (m, 1H), 7.80 Hz (m, 1H) and 7.85 Hz (m, 2H).

methyl 2-(3-(4-formylphenoxy)propoxy)benzoate (48b). Synthesized from 4-(3-bromopropoxy)benzaldehyde (**46b**) (243 mg, 1 mmol) and methyl-2-hydroxybenzoate (152.14 mg, 1 mmol) according to the general procedure 3.5.3.5. Pale yellow crystalline solid, Yield = 85% (267 mg); ¹H NMR (400 MHz, CDCl₃): δ = 2.33 Hz (p, 2H), 3.88 Hz (s, 3H), 4.27 Hz (dt, 4H), 7.00 Hz (m, 4H), 7.44 Hz (m, 1H) and 7.80 Hz (m, 3H)

methyl 4-(2-(4-formylphenoxy)ethoxy)benzoate (48c). Synthesized from 4-(2-bromoethoxy)benzaldehyde (**46a**) (1.5 g, 6.55 mmol) and methyl-4-hydroxybenzoate (997 mg, 6.55 mmol) according to the general procedure 3.5.3.5. Off-white crystalline solid, Yield = 85% (1670 mg); ¹H NMR (400 MHz, DMSO) δ 9.85 (s, 1H), 7.95 – 7.90 (m, 2H), 7.88 (dd, J = 9.1, 2.2 Hz, 2H), 7.17 (d, J = 8.7 Hz, 2H), 7.10 (d, J = 8.9 Hz, 2H), 4.44 (dd, J = 10.6, 5.4 Hz, 4H), 3.80 (s, 3H).

methyl 3-(2-(4-formylphenoxy)ethoxy)benzoate (48d). Synthesized from 4-(2-bromoethoxy)benzaldehyde (**46a**) (458 mg, 2 mmol) and methyl-3-hydroxybenzoate (304 mg, 2 mmol) according to the general procedure 3.5.3.5. Yellowish oil, Yield = 47% (280 mg); ¹H NMR (400 MHz, CDCl₃) δ 9.94 (d, J = 11.6 Hz, 1H), 8.02 – 7.80 (m, 2H), 7.73 – 7.68 (m, 1H), 7.64 (dd, J = 2.5, 1.5 Hz, 1H), 7.39 (t, J = 8.0 Hz, 1H), 7.18 (ddd, J = 8.2, 2.7, 0.9 Hz, 1H), 7.12 – 7.07 (m, 2H), 4.49 – 4.37 (m, 4H), 3.94 (s, 2H).

methyl 2-(2-(2-formylphenoxy)ethoxy)benzoate (48e). Synthesized from 2-(2-bromoethoxy)benzaldehyde (**46c**) (344 mg, 1.5 mmol) and methyl-2-hydroxybenzoate (288 mg, 1.5 mmol) according to the general procedure 3.5.3.5. Yield = 89% (400 mg); Yellowish oil. ¹H NMR (400 MHz, CDCl₃) δ 10.45 (d, J = 0.6 Hz, 1H), 7.86 (dd, J = 7.7, 1.8 Hz, 1H), 7.81 (dd, J = 7.7, 1.7 Hz, 1H), 7.58 (ddd, J = 8.5, 7.4, 1.8 Hz, 1H), 7.53 – 7.47 (m, 1H), 7.07 (ddd, J = 9.6, 8.4, 4.7 Hz, 4H), 4.57 – 4.46 (m, 4H), 3.83 (s, 3H).

methyl 4-(2-(2-formylphenoxy)ethoxy)benzoate (48f). Synthesized from 2-(2-bromoethoxy)benzaldehyde (**46c**) (344 mg, 1.5 mmol) and methyl-4-hydroxybenzoate (288 mg, 1.5 mmol) according to the general procedure 3.5.3.5. Yellowish oil, Yield =

73% (329 mg); ¹H NMR (400 MHz, DMSO) δ 10.49 (s, 0H), 8.01 (d, J = 8.9 Hz, 0H), 7.86 (dd, J = 7.7, 1.8 Hz, 0H), 7.62 – 7.51 (m, 0H), 7.06 (s, 0H), 6.96 (d, J = 8.8 Hz, 0H), 4.55 – 4.35 (m, 1H), 3.89 (s, 1H).

3.5.3.6 General Synthesis procedure of compound (49a-f):

A mixture of derived aldehyde (**48a-f**) (1 eq.) and barbituric acid (**9**) (0.8 eq.) was added to ethanol, and the reaction mixture was stirred for 40 min at room temperature. After completion of the reaction, the yellow colored precipitate was formed. The precipitate was filtered and washed with dichloromethane 3-4 times to remove unreacted aldehyde (**48a-f**). The solid was dried and collected as compounds (**49a-f**).

methyl 2-(2-(4-((2,4,6-trioxotetrahydropyrimidin-5(2H)-ylidene)methyl)phenoxy)ethoxy)benzoate (49a). Synthesized from methyl 2-(2-(4-formylphenoxy)ethoxy)benzoate (**48a**) (60 mg, 0.2 mmol) and barbituric acid (**9**) (21 mg, 0.16 mmol) according to the general procedure 3.5.3.6. Bright yellow solid, Yield = 49% (40 mg); Quantitative NMR Purity = 99%; ¹H NMR (400 MHz, DMSO): δ = 3.75 Hz (s, 3H), 4.45 Hz (t, 4H), 7.05 Hz (t, 1H), 7.14 Hz (d, 2H), 7.25 Hz (d, 1H), 7.55 Hz (t, 1H), 7.65 Hz (d, 1H), 8.27 Hz (s, 1H), 8.39 Hz (t, 2H), 11.21 Hz (s, 1H N-H), 11.33 Hz (s, 1H N-H). HRMS (ESI) for C₂₁H₁₈N₂O₇ ([M+H]⁺): calculated 424.1271, found 424.1306

methyl 2-(3-(4-((2,4,6-trioxotetrahydropyrimidin-5(2H)-ylidene)methyl)phenoxy)propoxy)benzoate (49b). Synthesized from methyl 2-(3-(4-formylphenoxy)propoxy)benzoate (**48b**) (63 mg, 0.2 mmol) and barbituric acid (**9**) (21 mg, 0.16 mmol) according to the general procedure 3.5.3.6. Bright yellow solid, Yield = 64% (55 mg); Quantitative NMR Purity = 96.41%; ¹H NMR (400 MHz, DMSO): δ = 2.22 Hz (m, 2H), 3.78 Hz (s, 3H), 4.44 Hz (t, 2H), 4.34 Hz (t, 2H), 7.03 Hz (t, 1H), 7.10 Hz (dd, 2H), 7.20 Hz (d, 1H), 7.54 Hz (t, 1H), 7.66 Hz (dd, 1H), 8.25 Hz (s, 1H), 8.38 Hz (dd, 2H) 11.2 Hz (s, 1H), 11.32 Hz (s, 1H) HRMS (ESI) for C₂₂H₂₀N₂O₇ ([M+H]⁺): calculated 410.1114, found 410.1127.

methyl 4-(2-(4-((2,4,6-trioxotetrahydropyrimidin-5(2H)-ylidene)methyl)phenoxy)ethoxy)benzoate (49d). Synthesized from methyl 4-(2-(4-formylphenoxy)ethoxy)benzoate (**48c**) (300 mg, 1 mmol) and barbituric acid (**9**) (102 mg, 0.8 mmol) according to the general procedure 3.5.3.6. Yellow solid. Yield= 96% (392 mg); Quantitative NMR Purity = 98.57%; ¹H NMR (400 MHz, DMSO) δ 8.31 (d, J = 9.0 Hz, 2H), 8.23 (s, 1H), 7.97 – 7.85 (m, 2H), 7.08 (dd, J = 8.8, 3.7 Hz, 4H), 4.48

– 4.36 (m, 4H), 3.79 (s, 3H). HRMS (ESI) for $C_{21}H_{18}N_2O_7$ ($[M+H]^+$): calculated 410.1114, found 410.1129.

methyl **3-(2-(4-((2,4,6-trioxotetrahydropyrimidin-5(2H)-ylidene)methyl)phenoxy)ethoxy)benzoate (49d)**. Synthesized from methyl 3-(2-(4-formylphenoxy)ethoxy)benzoate (**48d**) (150 mg, 0.5 mmol) and barbituric acid (**9**) (51.2 mg, 0.4 mmol) according to the general procedure 3.5.3.6. Yellow solid, Yield = 64% (130 mg); Quantitative NMR Purity = 99.48%; 1H NMR (400 MHz, DMSO) δ 8.33 (d, J = 9.1 Hz, 1H), 8.25 (s, 1H), 7.57 (d, J = 7.7 Hz, 1H), 7.50 – 7.48 (m, 1H), 7.45 (d, J = 7.8 Hz, 1H), 7.30 – 7.24 (m, 1H), 7.11 (d, J = 9.0 Hz, 1H), 4.54 – 4.30 (m, 1H), 3.83 (s, 1H). HRMS (ESI) for $C_{21}H_{18}N_2O_7$ ($[M+H]^+$): calculated 410.1114, found 410.1089.

methyl **2-(2-(2-((2,4,6-trioxotetrahydropyrimidin-5(2H)-ylidene)methyl)phenoxy)ethoxy)benzoate (49e)**. Synthesized from methyl 2-(2-(2-formylphenoxy)ethoxy)benzoate (**48e**) (388 mg, 1.292 mmol) and barbituric acid (**9**) (132 mg, 0.8 mmol) according to the general procedure 3.5.3.6. Yellow solid, Yield = 70% (372 mg); Quantitative NMR Purity = 98.8%; 1H NMR (400 MHz, DMSO) δ 8.49 (s, 1H), 7.90 (d, J = 7.8 Hz, 2H), 7.63 (t, J = 9.6 Hz, 1H), 7.51 (t, J = 7.8 Hz, 2H), 7.18 (t, J = 7.9 Hz, 2H), 7.06 – 6.91 (m, 2H), 4.41 (dd, J = 12.5, 4.6 Hz, 4H), 3.66 (s, 3H). HRMS (ESI) for $C_{21}H_{18}N_2O_7$ ($[M+H]^+$): calculated 410.1114, found 410.11.

methyl **4-(2-(2-((2,4,6-trioxotetrahydropyrimidin-5(2H)-ylidene)methyl)phenoxy)ethoxy)benzoate (49f)**. Synthesized from methyl 4-(2-(2-formylphenoxy)ethoxy)benzoate (**48f**) (50 mg, 0.167 mmol) and barbituric acid (**9**) (17 mg, 0.134 mmol) according to the general procedure 3.5.3.6. Yellow solid, Yield = 42% (29 mg); Quantitative NMR Purity = 93.6%; 1H NMR (400 MHz, DMSO) δ 8.48 (d, J = 7.8 Hz, 1H), 7.89 (dd, J = 11.3, 4.3 Hz, 3H), 7.55 – 7.49 (m, 1H), 7.18 (d, J = 8.3 Hz, 1H), 7.08 (d, J = 8.9 Hz, 2H), 7.00 (t, J = 7.6 Hz, 1H), 4.40 (dt, J = 41.7, 20.9 Hz, 4H), 3.79 (s, 3H). HRMS (ESI) for $C_{21}H_{18}N_2O_7$ ($[M+H]^+$): calculated 410.1114, found 410.1091.

3.5.3.7 General Synthesis procedure of compound (50a-b):

The solution of sodium hydroxide (5 eq.) in 10 mL methanol/water (1:1) was prepared. The NaOH solution (10 mL) was added to the compounds **22a-b** (1 eq.) and stirred at room temperature for 4-5 h. After completion of the reaction, the reaction mixture was concentrated *in vacuo*. Water was added to the reaction mixture, and pH was adjusted

between 2-3 by adding dilute acid till yellow colored precipitate formed. The precipitate was filtered and washed with dichloromethane 2-3 times to get the pure product (**50a-b**).

2-(2-(4-((2,4,6-trioxotetrahydropyrimidin-5(2H)-ylidene)methyl)phenoxy)ethoxy)benzoic acid (50a). Synthesized from methyl 2-(2-(4-((2,4,6-trioxotetrahydropyrimidin-5(2H)-ylidene)methyl)phenoxy)ethoxy)benzoate (**49a**) according to the general procedure 3.5.3.7. Bright yellow solid, Yield = 52% (29 mg); ^1H NMR (400 MHz, DMSO): δ = 4.11 Hz (dd, 4H), 6.74 Hz (t, 1H), 6.82 Hz (d, 1H), 6.88 Hz (t, 2H), 7.25 Hz (td, 1H), 7.33 Hz (dd, 1H), 7.58 Hz (t, 1H), 7.6 Hz (t, 1H) 7.96 Hz (d, 1H N-H), 9.55 Hz (s, 1H). HRMS (ESI) for $\text{C}_{20}\text{H}_{16}\text{N}_2\text{O}_7$ ($[\text{M}+\text{H}]^+$): calculated 396.0958, found 396.0952.

2-(3-(4-((2,4,6-trioxotetrahydropyrimidin-5(2H)-ylidene)methyl)phenoxy)propoxy)benzoic acid (50b). Synthesized from methyl 2-(3-(4-((2,4,6-trioxotetrahydropyrimidin-5(2H)-ylidene)methyl)phenoxy)propoxy)benzoate (**49b**) according to the general procedure 3.5.3.7. Bright yellow solid, Yield = 56% (136 mg); Quantitative NMR Purity = 93.75%; ^1H NMR (400 MHz, DMSO): δ = 1.90 Hz (m, 2H), 3.9 Hz (t, 2H), 4.04 Hz (t, 2H), 6.70 Hz (t, 1H), 6.76 Hz (d, 1H), 6.79 Hz (d, 1H), 6.85 Hz (d, 1H), 7.19 Hz (td, 1H), 7.33 Hz (dd, 1H), 7.94 Hz (s, 1H), 8.04 Hz (d, 1H), 8.06 Hz (d, 1H), 10.89 Hz (s, 1H), 11.01 Hz (s, 1H). HRMS (ESI) for $\text{C}_{21}\text{H}_{18}\text{N}_2\text{O}_7$ ($[\text{M}+\text{H}]^+$): calculated 410.1114, found 410.1097.

3.5.4 *In vitro* screening for *MtUng* activity inhibition assays

3.5.4.1 Fluorescence-based assay

To perform the *MtUng* activity inhibition assays, a hairpin DNA oligomer containing five uracils in a row (5'-CUUUUUGAGCTTTTGCTCAAAAAG-3') was used. The oligomer was modified with a fluorophore (5-Carboxyfluorescein or 5-FAM) at the 5' end and a quencher (Black Hole Quencher-1 or BHQ-1) at the 3' end. The excitation and emission maxima of 5-FAM are 496 nm and 520 nm, respectively, and the absorbance maxima of BHQ-1 is 534 nm. The oligomer was dissolved in MilliQ water, while all the inhibitor compounds were dissolved in 100 mM DMSO. The reactions were carried out in 96-well clear-bottom black-colored Corning plates using a buffer containing 50 mM Tris-Cl (pH 8.0), 1 mM Na₂EDTA, and 37.6 nM BSA. The protein and oligomer concentrations used were 0.3 nM and 30 nM, respectively. To test for

melting oligo (fluorescence increase), 80 mM NaOH was used as a positive control in place of *MtUng*. The reaction mixtures were shaken orbitally (1.5 mm amplitude) for 10 seconds before each reading, and fluorescence was monitored every 2 minutes for 40 minutes at 37 °C. The excitation and emission wavelengths used were similar to the excitation and emission maxima of 5-FAM, and the experiments were performed in a bottom reading mode using Tecan Infinite 200Pro. The excitation and emission bandwidths were set at 9 and 20 nm, respectively.

3.5.4.2 Radioactivity based assay

For the inhibition assay, 5 ng of *MtUng* was incubated with different concentrations of inhibitors in 10 µl of reaction buffer [50 mM Tris-HCl (pH8.0), 1 mM Na₂EDTA, 1 mM DTT, and 25 µg/ml BSA] for 15 min at room temperature. Reaction mixtures were then placed on ice for 5 min, followed by incubation at room temperature for 5 min. Approximately 0.1 pmol of a 5' P³² end-labeled uracil containing DNA oligomer (5'- ctcaagtgUaggcatgcttttgcacgcctgcactga -3') was then added to the reaction mixture and incubated for 15 min at 37 °C. The oligomer has a G:U pair in the stem at the 9th position of the stem-loop structure. Reactions were then stopped by the addition of 8 µl of 0.2 N NaOH and heating at 90 °C for 10 min, mixed with 12 µl formamide dye (80% formamide, 0.05% of bromophenol blue, and xylene cyanol FF each, 10 mM NaOH and 2 mM Na₂EDTA) and heated for another 10 min at 90 °C. 15 µl of each was analyzed on 15% polyacrylamide 8 M urea gels, exposed, and images were taken using a phosphorimager (Fujifilm analyzer). Product formation was analyzed, and IC₅₀ values were calculated using the GraphPad Prism 8 software.

REFERENCES

- (1) Lindahl, T. Instability and Decay of the Primary Structure of DNA. *Nature* **1993**, 362 (6422), 709–715. <https://doi.org/10.1038/362709a0>.
- (2) David, S. S.; O’Shea, V. L.; Kundu, S. Base-Excision Repair of Oxidative DNA Damage. *Nature* **2007**, 447 (7147), 941–950. <https://doi.org/10.1038/nature05978>.
- (3) Krokan, H. E.; Standal, R.; Slupphaug, G. DNA Glycosylases in the Base Excision Repair of DNA. *Biochem. J.* **1997**, 325 (1), 1–16. <https://doi.org/10.1042/bj3250001>.
- (4) Wallace, S. S. Base Excision Repair: A Critical Player in Many Games. *DNA Repair (Amst)*. **2014**, 19, 14–26. <https://doi.org/10.1016/j.dnarep.2014.03.030>.
- (5) Hans E. Krokan and Magnar Bjørås. Base Excision Repair. *Cold Spring Harb Perspect Biol* 2013;5a012583 **2013**, 5, a012583. https://doi.org/10.1142/9789812706782_0002.
- (6) Lindahl, T. An N Glycosidase from Escherichia Coli That Releases Free Uracil from DNA Containing Deaminated Cytosine Residues. *Proc. Natl. Acad. Sci. U. S. A.* **1974**, 71 (9), 3649–3653. <https://doi.org/10.1073/PNAS.71.9.3649>.
- (7) Drohat, A. C.; Coey, C. T. Role of Base Excision “Repair” Enzymes in Erasing Epigenetic Marks from DNA. *Chem. Rev.* **2016**, 116 (20), 12711–12729. <https://doi.org/10.1021/acs.chemrev.6b00191>.
- (8) Wilson, D. M.; Bohr, V. A. The Mechanics of Base Excision Repair, and Its Relationship to Aging and Disease. *DNA Repair (Amst)*. **2007**, 6 (4), 544–559. <https://doi.org/10.1016/j.dnarep.2006.10.017>.
- (9) Mechetin, G. V; Endutkin, A. V; Diatlova, E. A.; Zharkov, D. O. Inhibitors of DNA Glycosylases as Prospective Drugs. *Int. J. Mol. Sci.* **2020**, 21 (9), 3118. <https://doi.org/10.3390/IJMS21093118>.
- (10) Svilar, D.; Goellner, E. M.; Almeida, K. H.; Sobol, R. W. Base Excision Repair and Lesion-Dependent Subpathways. *Antioxid. Redox Signal.* **2011**, 14 (12), 2491–2507.
- (11) Jacobs, A. L.; Schär, P. DNA Glycosylases: In DNA Repair and Beyond. *Chromosoma* **2012**, 121 (1), 1–20. <https://doi.org/10.1007/s00412-011-0347-4>.
- (12) Drohat, A. C.; Maiti, A. Mechanisms for Enzymatic Cleavage of the N-Glycosidic Bond in DNA. *Org. Biomol. Chem.* **2014**, 12 (42), 8367–8378.

<https://doi.org/10.1039/c4ob01063a>.

- (13) Prakash, A.; Doublie, S.; Wallace, S. S. The Fpg/Nei Family of DNA Glycosylases: Substrates, Structures, and Search for Damage. *Prog. Mol. Biol. Transl. Sci.* **2012**, *110*, 71–91. <https://doi.org/10.1016/B978-0-12-387665-2.00004-3>.
- (14) Schormann, N.; Ricciardi, R.; Chattopadhyay, D. Uracil-DNA Glycosylases - Structural and Functional Perspectives on an Essential Family of DNA Repair Enzymes. *Protein Sci.* **2014**, *23* (12), 1667–1685. <https://doi.org/10.1002/pro.2554>.
- (15) Zharkov, D. O.; Mechetin, G. V.; Nevinsky, G. A. Uracil-DNA Glycosylase: Structural, Thermodynamic and Kinetic Aspects of Lesion Search and Recognition. *Mutat. Res. - Fundam. Mol. Mech. Mutagen.* **2010**, *685* (1–2), 11–20. <https://doi.org/10.1016/j.mrfmmm.2009.10.017>.
- (16) Kosaka, H.; Hoseki, J.; Nakagawa, N.; Kuramitsu, S.; Masui, R. Crystal Structure of Family 5 Uracil-DNA Glycosylase Bound to DNA. *J. Mol. Biol.* **2007**, *373* (4), 839–850. <https://doi.org/10.1016/j.jmb.2007.08.022>.
- (17) Sang, P. B.; Srinath, T.; Patil, A. G.; Woo, E. J.; Varshney, U. A Unique Uracil-DNA Binding Protein of the Uracil DNA Glycosylase Superfamily. *Nucleic Acids Res.* **2015**, *43* (17), 8452–8463. <https://doi.org/10.1093/nar/gkv854>.
- (18) Chung, J. H.; Im, E. K.; Park, H. Y.; Kwon, J. H.; Lee, S.; Oh, J.; Hwang, K. C.; Lee, J. H.; Jang, Y. A Novel Uracil-DNA Glycosylase Family Related to the Helix-Hairpin-Helix DNA Glycosylase Superfamily. *Nucleic Acids Res.* **2003**, *31* (8), 2045–2055. <https://doi.org/10.1093/nar/gkg319>.
- (19) Liu, P.; Burdzy, A.; Sowers, L. C. Substrate Recognition by a Family of Uracil-DNA Glycosylases: UNG, MUG, and TDG. *Chem. Res. Toxicol.* **2002**, *15* (8), 1001–1009. <https://doi.org/10.1021/tx020030a>.
- (20) Slupphaug, G.; Eftedal, I.; Kavli, B.; Bharati, S.; Hellet, N. M.; Haug, T.; Krokan, H. E.; Levine, D. W. Properties of a Recombinant Human Uracil-DNA Glycosylase from the UNG Gene and Evidence That UNG Encodes the Major Uracil-DNA Glycosylase. *Biochemistry* **1995**, *34* (1), 128–138. <https://doi.org/10.1021/bi00001a016>.
- (21) Saikrishnan, K.; Bidya Sagar, M.; Ravishankar, R.; Roy, S.; Purnapatre, K.; Handa, P.; Varshney, U.; Vijayan, M. Domain Closure and Action of Uracil

- DNA Glycosylase (UDG): Structures of New Crystal Forms Containing the Escherichia Coli Enzyme and a Comparative Study of the Known Structures Involving UDG. *Acta Crystallogr. Sect. D Biol. Crystallogr.* **2002**, *58* (8), 1269–1276. <https://doi.org/10.1107/S0907444902009599>.
- (22) Arif, S. M.; Geethanandan, K.; Mishra, P.; Surolia, A.; Varshney, U.; Vijayan, M. Structural Plasticity in Mycobacterium Tuberculosis Uracil-DNA Glycosylase (MtUng) and Its Functional Implications. *Acta Crystallogr. Sect. D Biol. Crystallogr.* **2015**, *71*, 1514–1527. <https://doi.org/10.1107/S1399004715009311>.
- (23) Slupphaug, G.; Mol, C. D.; Kavli, B.; Arvai, A. S.; Krokan, H. E.; Tainer, J. A. A Nucleotide-Flipping Mechanism from the Structure of Human Uracil-DNA Glycosylase Bound to DNA. *Nature* **1996**, *384* (6604), 87–92. <https://doi.org/10.1038/384087a0>.
- (24) Kara, H.; Ponchon, L.; Bouaziz, S. Backbone Resonance Assignment of the Human Uracil DNA Glycosylase-2. *Biomol. NMR Assign.* **2018**, *12* (1), 37–42. <https://doi.org/10.1007/s12104-017-9776-1>.
- (25) Buchinger, E.; Wiik, S.; Kusnierczyk, A.; Rabe, R.; Aas, P. A.; Kavli, B.; Slupphaug, G.; Aachmann, F. L. Backbone ¹H, ¹³C and ¹⁵N Chemical Shift Assignment of Full-Length Human Uracil DNA Glycosylase UNG2. *Biomol. NMR Assign.* **2018**, *12* (1), 15–22. <https://doi.org/10.1007/s12104-017-9772-5>.
- (26) Kaushal, P. S.; Talawar, R. K.; Varshney, U.; Vijayan, M. Structure of Uracil-DNA Glycosylase from Mycobacterium Tuberculosis: Insights into Interactions with Ligands. *Acta Crystallogr. Sect. F Struct. Biol. Cryst. Commun.* **2010**, *66* (8), 887–892. <https://doi.org/10.1107/S1744309110023043>.
- (27) Krokan, H. E.; Otterlei, M.; Nilsen, H.; Kavli, B.; Skorpen, F.; Andersen, S.; Skjelbred, C.; Akbari, M.; Aas, P. A.; Slupphaug, G. Properties and Functions of Human Uracil-DNA Glycosylase from the UNG Gene. *Prog. Nucleic Acid Res. Mol. Biol.* **2001**, *68*, 365–386. [https://doi.org/10.1016/s0079-6603\(01\)68112-1](https://doi.org/10.1016/s0079-6603(01)68112-1).
- (28) Leiros, I.; Moe, E.; Smalås, A. O.; McSweeney, S. Structure of the Uracil-DNA-Glycosylase (UNG) from *Deinococcus Radiodurans*. *Acta Crystallogr. Sect. D* **2005**, *61* (8), 1049–1056. <https://doi.org/10.1107/S090744490501382X>.
- (29) Mol, C. D.; Arvai, A. S.; Slupphaug, G.; Kavli, B.; Alseth, I.; Krokan, H. E.;

- Tainer, J. A. Crystal Structure and Mutational Analysis of Human Uracil-DNA Glycosylase: Structural Basis for Specificity and Catalysis. *Cell* **1995**, *80* (6), 869–878. [https://doi.org/10.1016/0092-8674\(95\)90290-2](https://doi.org/10.1016/0092-8674(95)90290-2).
- (30) Schonhofs, J. D.; Stivers, J. T. DNA Translocation by Human Uracil DNA Glycosylase: The Case of Single-Stranded DNA and Clustered Uracils. *Biochemistry* **2013**, *52* (15), 2526–2544. <https://doi.org/10.1021/bi301562n>.
- (31) Pearl, L. H. Structure and Function in the Uracil-DNA Glycosylase Superfamily. *Mutat. Res. - DNA Repair* **2000**, *460* (3–4), 165–181. [https://doi.org/10.1016/S0921-8777\(00\)00025-2](https://doi.org/10.1016/S0921-8777(00)00025-2).
- (32) Oyakhrome, S.; Issifou, S.; Pongratz, P.; Barondi, F.; Ramharter, M.; Kun, J. F.; Missinou, M. A.; Lell, B.; Kremsner, P. G. Randomized Controlled Trial of Fosmidomycin-Clindamycin versus Sulfadoxine-Pyrimethamine in the Treatment of Plasmodium Falciparum Malaria. *Antimicrob. Agents Chemother.* **2007**, *51* (5), 1869–1871. <https://doi.org/10.1128/AAC.01448-06>.
- (33) Kara, H.; Chazal, N.; Bouaziz, S. Is Uracil-DNA Glycosylase UNG2 a New Cellular Weapon Against HIV-1? *Curr. HIV Res.* **2019**, *17* (3), 148–160. <https://doi.org/10.2174/1570162X17666190821154331>.
- (34) Cone, R.; Bonura, T.; Friedberg, E. C. Inhibitor of Uracil-DNA Glycosylase Induced by Bacteriophage PBS2. Purification and Preliminary Characterization. *J. Biol. Chem.* **1980**, *255* (21), 10354–10358. [https://doi.org/10.1016/s0021-9258\(19\)70472-4](https://doi.org/10.1016/s0021-9258(19)70472-4).
- (35) Warner, H. R.; Johnson, L. K.; Snustad, D. P. Early Events after Infection of Escherichia Coli by Bacteriophage T5. III. Inhibition of Uracil-DNA Glycosylase Activity. *J. Virol.* **1980**, *33* (1), 535–538. <https://doi.org/10.1128/jvi.33.1.535-538.1980>.
- (36) Wang, Z.; Mosbaugh, D. W. Uracil-DNA Glycosylase Inhibitor of Bacteriophage PBS2: Cloning and Effects of Expression of the Inhibitor Gene in Escherichia Coli. *J. Bacteriol.* **1988**, *170* (3), 1082–1091. <https://doi.org/10.1128/jb.170.3.1082-1091.1988>.
- (37) Wang, Z.; Mosbaugh, D. W. Uracil-DNA Glycosylase Inhibitor Gene of Bacteriophage PBS2 Encodes a Binding Protein Specific for Uracil-DNA Glycosylase. *J. Biol. Chem.* **1989**, *264* (2), 1163–1171. [https://doi.org/10.1016/s0021-9258\(19\)85067-6](https://doi.org/10.1016/s0021-9258(19)85067-6).

- (38) Assefa, N. G.; Niiranen, L.; Johnson, K. A.; Leiros, H. K. S.; Smalås, A. O.; Willassen, N. P.; Moe, E. Structural and Biophysical Analysis of Interactions between Cod and Human Uracil-DNA N-Glycosylase (UNG) and UNG Inhibitor (Ugi). *Acta Crystallogr. Sect. D Biol. Crystallogr.* **2014**, *70* (8), 2093–2100. <https://doi.org/10.1107/S1399004714011699>.
- (39) Putnam, C. D.; Shroyer, M. J. N.; Lundquist, A. J.; Mol, C. D.; Arvai, A. S.; Mosbaugh, D. W.; Tainer, J. A. Protein Mimicry of DNA from Crystal Structures of the Uracil-DNA Glycosylase Inhibitor Protein and Its Complex with Escherichia Coli Uracil-DNA Glycosylase. *J. Mol. Biol.* **1999**, *287* (2), 331–346. <https://doi.org/10.1006/jmbi.1999.2605>.
- (40) Krokan, H.; Wittwer, C. U. Uracil DNA-Glycosylase from HeLa Cells: General Properties, Substrate Specificity and Effect of Uracil Analogs. *Nucleic Acids Res.* **1981**, *9* (11), 2599–2614. <https://doi.org/10.1093/nar/9.11.2599>.
- (41) Blaisdell, P.; Warner, H. Partial Purification and Characterization of a Uracil-DNA Glycosylase from Wheat Germ. *J. Biol. Chem.* **1983**, *258* (3), 1603–1609. [https://doi.org/10.1016/S0021-9258\(18\)33027-8](https://doi.org/10.1016/S0021-9258(18)33027-8).
- (42) Jiang, Y. L.; Krosky, D. J.; Seiple, L.; Stivers, J. T. Uracil-Directed Ligand Tethering: An Efficient Strategy for Uracil DNA Glycosylase (UNG) Inhibitor Development. *J. Am. Chem. Soc.* **2005**, *127* (49), 17412–17420. <https://doi.org/10.1021/ja055846n>.
- (43) Chung, S.; Parker, J. B.; Bianchet, M.; Amzel, L. M.; Stivers, J. T. Impact of Linker Strain and Flexibility in the Design of a Fragment-Based Inhibitor. *Nat. Chem. Biol.* **2009**, *5* (6), 407–413. <https://doi.org/10.1038/nchembio.163>.
- (44) Krosky, D. J.; Bianchet, M. A.; Seiple, L.; Chung, S.; Amzel, L. M.; Stivers, J. T. Mimicking Damaged DNA with a Small Molecule Inhibitor of Human UNG2. *Nucleic Acids Res.* **2006**, *34* (20), 5872–5879. <https://doi.org/10.1093/nar/gkl747>.
- (45) Focher, F.; Verri, A.; Spadari, S.; Manservigi, R.; Gambino, J.; Wright, G. E. Herpes Simplex Virus Type 1 Uracil-DNA Glycosylase: Isolation and Selective Inhibition by Novel Uracil Derivatives. *Biochem. J.* **1993**, *292* (Pt 3), 883–889. <https://doi.org/10.1042/BJ2920883>.
- (46) Bianchet, M. A.; Seiple, L. A.; Jiang, Y. L.; Ichikawa, Y.; Amzel, L. M.; Stivers, J. T. Electrostatic Guidance of Glycosyl Cation Migration along the Reaction

- Coordinate of Uracil DNA Glycosylase. *Biochemistry* **2003**, *42* (43), 12455–12460. <https://doi.org/10.1021/bi035372+>.
- (47) Schormann, N.; Banerjee, S.; Ricciardi, R.; Chattopadhyay, D. Structure of the Uracil Complex of Vaccinia Virus Uracil DNA Glycosylase. *Acta Crystallogr. Sect. F Struct. Biol. Cryst. Commun.* **2013**, *69* (12), 1328–1334. <https://doi.org/10.1107/S1744309113030613>.
- (48) Werner, R. M.; Jiang, Y. L.; Gordley, R. G.; Jagadeesh, G. J.; Ladner, J. E.; Xiao, G.; Tordova, M.; Gilliland, G. L.; Stivers, J. T. Stressing-out DNA? The Contribution of Serine-Phosphodiester Interactions in Catalysis by Uracil DNA Glycosylase. *Biochemistry* **2000**, *39* (41), 12585–12594. <https://doi.org/10.1021/bi001532v>.
- (49) Serrano-Heras, G.; Ruiz-Masó, J. A.; Del Solar, G.; Espinosa, M.; Bravo, A.; Salas, M. Protein P56 from the Bacillus Subtilis Phage Φ 29 Inhibits DNA-Binding Ability of Uracil-DNA Glycosylase. *Nucleic Acids Res.* **2007**, *35* (16), 5393–5401. <https://doi.org/10.1093/nar/gkm584>.
- (50) Asensio, J. L.; Pérez-Lago, L.; Lázaro, J. M.; González, C.; Serrano-Heras, G.; Salas, M. Novel Dimeric Structure of Phage Φ 29-Encoded Protein P56: Insights into Uracil-DNA Glycosylase Inhibition. *Nucleic Acids Res.* **2011**, *39* (22), 9779–9788. <https://doi.org/10.1093/nar/gkr667>.
- (51) Baños-Sanz, J. I.; Mojardín, L.; Sanz-Aparicio, J.; Lázaro, J. M.; Villar, L.; Serrano-Heras, G.; González, B.; Salas, M. Crystal Structure and Functional Insights into Uracil-DNA Glycosylase Inhibition by Phage Φ 29 DNA Mimic Protein P56. *Nucleic Acids Res.* **2013**, *41* (13), 6761–6773. <https://doi.org/10.1093/nar/gkt395>.
- (52) Wang, H. C.; Hsu, K. C.; Yang, J. M.; Wu, M. L.; Ko, T. P.; Lin, S. R.; Wang, A. H. J. Staphylococcus Aureus Protein SAUGI Acts as a Uracil-DNA Glycosylase Inhibitor. *Nucleic Acids Res.* **2014**, *42* (2), 1354–1364. <https://doi.org/10.1093/nar/gkt964>.
- (53) Mehta, A.; Raj, P.; Sundriyal, S.; Gopal, B.; Varshney, U. Use of a Molecular Beacon Based Fluorescent Method for Assaying Uracil DNA Glycosylase (Ung) Activity and Inhibitor Screening. *Biochem. Biophys. Reports* **2021**, *26*, 100954. <https://doi.org/10.1016/j.bbrep.2021.100954>.
- (54) Jiang, Y. L.; Chung, S.; Krosky, D. J.; Stivers, J. T. Synthesis and High-

- Throughput Evaluation of Triskelion Uracil Libraries for Inhibition of Human DUTPase and UNG2. *Bioorg. Med. Chem.* **2006**, *14* (16), 5666–5672. <https://doi.org/10.1016/J.BMC.2006.04.022>.
- (55) Suksangpleng, T.; Leartsakulpanich, U.; Moonsom, S.; Siribal, S.; Boonyuen, U.; Wright, G. E.; Chavalitshewinkoon-Petmitr, P. Molecular Characterization of Plasmodium Falciparum Uracil-DNA Glycosylase and Its Potential as a New Anti-Malarial Drug Target. *Malar. J.* **2014**, *13* (1), 149. <https://doi.org/10.1186/1475-2875-13-149>.
- (56) Chung, S.; Parker, J. B.; Bianchet, M.; Amzel, L. M.; Stivers, J. T. Impact of Linker Strain and Flexibility in the Design of a Fragment-Based Inhibitor. *Nat. Chem. Biol.* **2009**, *5* (6), 407–413. <https://doi.org/10.1038/nchembio.163>.
- (57) Nuth, M.; Huang, L.; Saw, Y. L.; Schormann, N.; Chattopadhyay, D.; Ricciardi, R. P. Identification of Inhibitors That Block Vaccinia Virus Infection by Targeting the DNA Synthesis Processivity Factor D4. *J. Med. Chem.* **2011**, *54* (9), 3260–3267. <https://doi.org/10.1021/jm101554k>.
- (58) Zhang, H.; Zhang, L.; Jiang, J.; Yu, R. A Highly Sensitive Electrochemical Platform for the Assay of Uracil-DNA Glycosylase Activity Combined with Enzymatic Amplification. *Anal. Sci.* **2013**, *29* (2), 193–198. <https://doi.org/10.2116/analsci.29.193>.
- (59) Tao, J.; Song, P.; Sato, Y.; Nishizawa, S.; Teramae, N.; Tong, A.; Xiang, Y. A Label-Free and Sensitive Fluorescent Method for the Detection of Uracil-DNA Glycosylase Activity. *Chem. Commun.* **2015**, *51* (5), 929–932. <https://doi.org/10.1039/c4cc06170e>.
- (60) Venkatesh, J.; Kumar, P.; Krishna, P. S. M.; Manjunath, R.; Varshney, U. Importance of Uracil DNA Glycosylase in Pseudomonas Aeruginosa and Mycobacterium Smegmatis, G+C-Rich Bacteria, in Mutation Prevention, Tolerance to Acidified Nitrite, and Endurance in Mouse Macrophages. *J. Biol. Chem.* **2003**, *278* (27), 24350–24358. <https://doi.org/10.1074/jbc.M302121200>.
- (61) Malshetty, V. S.; Jain, R.; Srinath, T.; Kurthkoti, K.; Varshney, U. Synergistic Effects of UdgB and Ung in Mutation Prevention and Protection against Commonly Encountered DNA Damaging Agents in Mycobacterium Smegmatis. *Microbiology* **2010**, *156* (Pt 3), 940–949. <https://doi.org/10.1099/MIC.0.034363-0>.

- (62) Sasseti, C. M.; Rubin, E. J. Genetic Requirements for Mycobacterial Survival during Infection. *Proc. Natl. Acad. Sci. U. S. A.* **2003**, *100* (22), 12989–12994. <https://doi.org/10.1073/pnas.2134250100>.
- (63) Kurthkoti, K.; Varshney, U. Detrimental Effects of Hypoxia-Specific Expression of Uracil DNA Glycosylase (Ung) in Mycobacterium Smegmatis. *J. Bacteriol.* **2010**, *192* (24), 6439–6446. <https://doi.org/10.1128/JB.00679-10>.
- (64) Arif, S. M.; Geethanandan, K.; Mishra, P.; Surolia, A.; Varshney, U.; Vijayan, M. Structural Plasticity in Mycobacterium Tuberculosis Uracil-DNA Glycosylase (MtUng) and Its Functional Implications. *Acta Crystallogr. Sect. D Biol. Crystallogr.* **2015**, *71*, 1514–1527. <https://doi.org/10.1107/S1399004715009311>.
- (65) Kaushal, P. S.; Talawar, R. K.; Krishna, P. D. V.; Varshney, U.; Vijayan, M. Unique Features of the Structure and Interactions of Mycobacterial Uracil-DNA Glycosylase: Structure of a Complex of the Mycobacterium Tuberculosis Enzyme in Comparison with Those from Other Sources. *Acta Crystallogr. Sect. D Biol. Crystallogr.* **2008**, *64* (5), 551–560. <https://doi.org/10.1107/S090744490800512X>.
- (66) Lindahl, T.; Ljungquist, S.; Siebert, W.; Nyberg, B.; Sperens, B. DNA N Glycosidases. Properties of Uracil DNA Glycosidase from Escherichia Coli. *J. Biol. Chem.* **1977**, *252* (10), 3286–3294. [https://doi.org/10.1016/s0021-9258\(17\)40386-3](https://doi.org/10.1016/s0021-9258(17)40386-3).
- (67) Bennett, S. E.; Schimerlik, M. I.; Mosbaugh, D. W. Kinetics of the Uracil-DNA Glycosylase/Inhibitor Protein Association. Ung Interaction with Ugi, Nucleic Acids, and Uracil Compounds. *J. Biol. Chem.* **1993**, *268* (36), 26879–26885. [https://doi.org/10.1016/S0021-9258\(19\)74193-3](https://doi.org/10.1016/S0021-9258(19)74193-3).
- (68) Kaushal, P. S.; Talawar, R. K.; Krishna, P. D. V.; Varshney, U.; Vijayan, M. Unique Features of the Structure and Interactions of Mycobacterial Uracil-DNA Glycosylase: Structure of a Complex of the Mycobacterium Tuberculosis Enzyme in Comparison with Those from Other Sources. *Acta Crystallogr. Sect. D Biol. Crystallogr.* **2008**, *64* (5), 551–560. <https://doi.org/10.1107/S090744490800512X>.
- (69) Raj, P.; Selvam, K.; Roy, K.; Mani Tripathi, S.; Kesharwani, S.; Gopal, B.; Varshney, U.; Sundriyal, S. Identification of a New and Diverse Set of

- Mycobacterium Tuberculosis Uracil-DNA Glycosylase (MtUng) Inhibitors Using Structure-Based Virtual Screening: Experimental Validation and Molecular Dynamics Studies. *Bioorg. Med. Chem. Lett.* **2022**, *76*, 129008. <https://doi.org/10.1016/j.bmcl.2022.129008>.
- (70) Mehta, A.; Raj, P.; Sundriyal, S.; Gopal, B.; Varshney, U. Use of a Molecular Beacon Based Fluorescent Method for Assaying Uracil DNA Glycosylase (Ung) Activity and Inhibitor Screening. *Biochem. Biophys. Reports* **2021**, *26*, 100954. <https://doi.org/10.1016/j.bbrep.2021.100954>.
- (71) Liu, Y.; Li, P.; Mu, W.; Sun, Y.; Liu, R.; Yang, J.; Liu, G. Design, Synthesis, and Anticancer Activity of Cinnamoylated Barbituric Acid Derivatives. *Chem. Biodivers.* **2022**, *19* (2). <https://doi.org/10.1002/cbdv.202100809>.
- (72) Singh, P.; Kaur, J.; Bhardwaj, A. Synthesis of Highly Functionalized Barbituric Acids and Study of Their Interactions with P-Glycoprotein and Mg²⁺ - Potential Candidates for Multi Drug Resistance Modulation. *Eur. J. Med. Chem.* **2010**, *45* (3), 1256–1262. <https://doi.org/10.1016/j.ejmech.2009.12.033>.
- (73) Sundriyal, S.; Viswanad, B.; Ramarao, P.; Chakraborti, A. K.; Bharatam, P. V. New PPAR γ Ligands Based on Barbituric Acid: Virtual Screening, Synthesis and Receptor Binding Studies. *Bioorganic Med. Chem. Lett.* **2008**, *18* (18), 4959–4962. <https://doi.org/10.1016/j.bmcl.2008.08.028>.
- (74) Dixit, V. A.; Rathi, P. C.; Bhagat, S.; Gohlke, H.; Petersen, R. K.; Kristiansen, K.; Chakraborti, A. K.; Bharatam, P. V. Design and Synthesis of Novel Y-Shaped Barbituric Acid Derivatives as PPAR γ Activators. *Eur. J. Med. Chem.* **2016**, *108*, 423–435. <https://doi.org/10.1016/j.ejmech.2015.11.030>.
- (75) Grosdidier, A.; Zoete, V.; Michielin, O. Fast Docking Using the CHARMM Force Field with EADock DSS. *J. Comput. Chem.* **2011**, *32* (10), 2149–2159. <https://doi.org/10.1002/jcc.21797>.
- (76) Grosdidier, A.; Zoete, V.; Michielin, O. SwissDock, a Protein-Small Molecule Docking Web Service Based on EADock DSS. *Nucleic Acids Res.* **2011**, *39* (suppl), W270–W277. <https://doi.org/10.1093/nar/gkr366>.
- (77) Goddard, T. D.; Huang, C. C.; Meng, E. C.; Pettersen, E. F.; Couch, G. S.; Morris, J. H.; Ferrin, T. E. UCSF ChimeraX: Meeting Modern Challenges in Visualization and Analysis. *Protein Sci.* **2018**, *27* (1), 14–25. <https://doi.org/10.1002/pro.3235>.

- (78) BIOVIA, Dassault Systèmes, Discovery Studio Visualizer, 20.1.0, San Diego: Dassault Systèmes, 2020.

CHAPTER 4

Summary and Future Prospects

4.1 CONCLUSION AND FUTURE PERSPECTIVE

AMR poses a serious threat to the globe by rapidly developing resistance to the current therapies, thus leading to ineffective treatment. Several deadly pathogens like *M. tuberculosis* and *P. falciparum* have achieved resistance to the available antibiotics leading to treatment failure, cost hikes in the healthcare sector, compromised lifestyle, and socioeconomic burden, thus pushing the healthcare system to a pre-antibiotic era. Millions of people are continuously affected due to AMR, and thousands die yearly. Developing and under-developed countries are especially facing the AMR issue due to poor healthcare facilities and the economic burden on the healthcare sector. Moreover, very few molecules have received FDA approval in the past three decades. Thus, novel antimicrobial agents are urgently required to combat the challenge of AMR. To achieve this aim, new antimicrobial targets, and novel chemical space need to be explored.

In this thesis, we explored two enzyme targets, DXR and MtUng, for inhibitor design. We have used the SBDD approach to design inhibitors, given the availability of crystal structures for both targets. In both cases, we started with the small fragment-like molecules, which were further grown rationally to achieve higher potency. The synthetic tractability of the designed molecules was kept in mind to achieve experimental validation.

4.1.1 DXR Inhibitors development

Since DXR is a metalloenzyme, it utilizes a divalent metal cation accompanied by β -NADPH to convert the DXP into MEP for isoprenoid biosynthesis in bacteria and certain parasites. Since DXR homologue is not present in humans, it is a viable antimicrobial target. Fosmidomycin is a potent and natural DXR inhibitor, discovered in the early 1980s; since then, several modifications around fosmidomycin have been made to overcome the challenges related to FSM. Being highly polar, FSM poses challenges related to cell permeability and poor bioavailability. Also, the hydroxamate group, the MBG in FSM, is known to have metabolic instability and toxicity issues. The medicinal chemistry efforts to overcome these challenges mostly revolve around increasing FSM lipophilicity by modifying the linker chain and prodrug approach. Very few attempts have been made to replace the hydroxamate group with other lipophilic MBGs that have been successfully employed for other targets.

Thus, this work mainly focused on replacing the hydroxamate group with various lipophilic fragments with a metal-chelating ability similar to hydroxamate. For designing the reported series of molecules, structure-based molecular modeling was used extensively while keeping in mind the synthetic tractability of the molecules.

After extensive literature, we identified nearly 103 metal chelating fragments from the literature capable of coordinating DXR metal ions. Out of these, ~13 fragments showed promising results in modeling studies and were available for commercial procurement. Indeed, these fragments (F2, F5, F7, F8, F9, and F12) displayed excellent DXR inhibition when tested at 100 μ M. The selected fragments were further grown to attach the essential pharmacophoric unit, a phosphonate moiety, guided by the docking results. Overall, 60 molecules were designed using this protocol, and the desired interactions with the active site metal ion and other residues were confirmed using a docking study. The predicted poses of these molecules were found to occupy hydrophobic pockets A and B as expected. Finally, chemical synthesis was optimized for synthesizing the designed molecules resulting in the synthesis of ~30 novel new chemical entities (NCEs).

Finally, the molecules were screened against the commercially available recombinant *E. coli* DXR enzyme. Unfortunately, all synthesized molecules could not be screened against DXR due to several practical problems faced during the COVID pandemic, such as significant import delays and increased costs. Nonetheless, in addition to the fragments, a total of 17 final molecules were screened *in vitro*, with eight molecules displaying good to moderate inhibition shown in Fig. 4.1, using the enzyme inhibition assay with eight molecules (**62a**, **62e**, **68a-b**, **68e**, **73a**, and **76a-b**) with good to moderate IC₅₀ values (Chapter 2 Table 2.5).

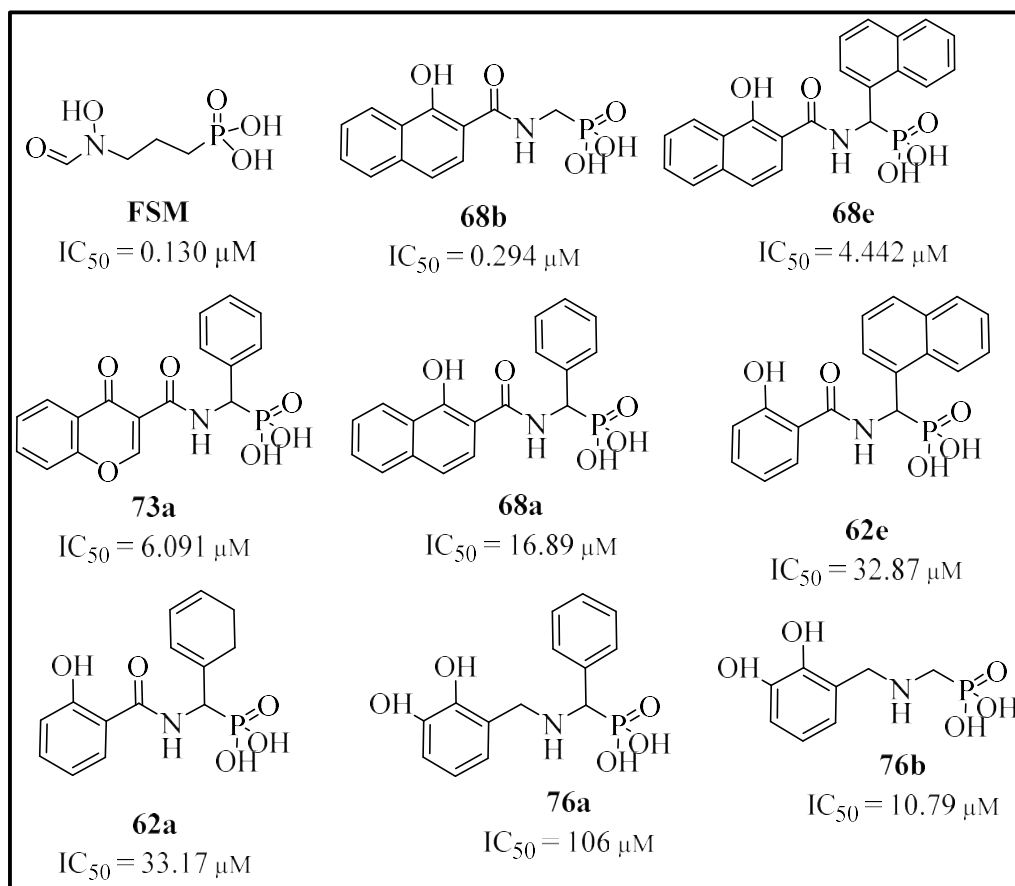


Fig. 4.1 Structure and IC_{50} values of non-hydroxamate DXR inhibitors reported in this work.

Compound **68b**, with 1-hydroxy-2-naphthoic acid as MBG and without any lipophilic attachment found to be the most potent compound in the series with $IC_{50} = 0.294 \mu\text{M}$, which is comparable to FSM with $IC_{50} = 0.130 \mu\text{M}$ analyzed using same assay protocol. Compounds **68e** and **73a** also showed fair inhibition with IC_{50} values of $4.44 \mu\text{M}$ and $6.091 \mu\text{M}$, respectively. Compounds **68b** and **68e** have the same MBG 1-hydroxy-2-naphthoic acid, whereas compound **73a** has chromone-3-carboxylic acid as MBG. Compound **68a** with 1-hydroxy-2-naphthoic acid as MBG showed $IC_{50} = 16.89 \mu\text{M}$. **62a** and **62e** with salicylic acid as MBG showed IC_{50} values in a 30-35 μM range. These results indicate that the lipophilic aromatic rings are well tolerated as MBG replaces hydroxamate functionality. 1-hydroxy-2-naphthoic acid-derived compounds exhibited more potency than salicylic acid and 2,3-dihydroxybenzoic acid derivatives. 1-hydroxy-2-naphthoic acid is more hydrophobic and can accommodate well in hydrophobic pocket B, thus showing better enzyme inhibition than other MBGs. However, lipophilic substituents vary in each case, and further optimization is required.

Earlier reported hydroxamate-based DXR inhibitors have demonstrated the importance of three carbon spacers between the hydroxamate group and phosphonic acid. In the case of non-hydroxamate DXR inhibitors, two carbon spacer lengths between the metal chelating group and phosphonic acid were well tolerated compared to hydroxamate derivatives. High enzyme inhibition by compound **68b** shows that replacing the hydroxamate functional group with non-hydroxamate functionality may alter the structural requirements to become a potent DXR inhibitor. However, the effect of varying the linker length is yet to explore. This study demonstrates that the replacement of the hydroxamate group is possible to design non-hydroxamate lipophilic DXR inhibitors using SBDD.

In whole-cell activity, out of 17 compounds tested, compound **76b** successfully inhibited the cell growth in *A. baumannii*, *E. coli*, *S. typhimurium*, and *V. cholerae*. at higher concentrations at 500 μM . IC_{50} for this compound could not be determined due to the high concentration of **76b**. These compounds were also tested against *M. tuberculosis*, where four compounds (**62c**, **62e**, **68b**, and **68e**) inhibited cell growth in *Mtb*. Compound **68e** showed the lowest cell growth inhibition with $\text{MIC} = 125 \mu\text{M}$, and the rest three compounds (**62c**, **62e**, and **68b**) showed $\text{MIC} = > 125 \mu\text{M}$. Compound **68e** showed $\text{IC}_{50} = 4.442 \mu\text{M}$ in an enzyme inhibition assay. The most potent inhibitor in the series, **68b** with $\text{IC}_{50} = 0.294 \mu\text{M}$, showed $\text{MIC} = >125 \mu\text{M}$. Both compounds have NA as MBG. Rest other compounds were found inactive in *M. tuberculosis* even at high concentrations (200 μM and 500 μM). Thus, NA showed comparatively better tolerance to the replacement of the hydroxamate group in the design of non-hydroxamate lipophilic DXR inhibitors.

In overall conclusion, non-hydroxamate lipophilic DXR inhibitors were designed, synthesized, and evaluated against the DXR enzyme inhibition. We started this process from fragments that showed enzyme inhibition at 100 μM . Finally, we obtained the inhibitors showing the enzyme inhibition at the 0.2-30 μM range, with potent lead molecule showing activity in nanomolar concentration (Fig. 4.2).

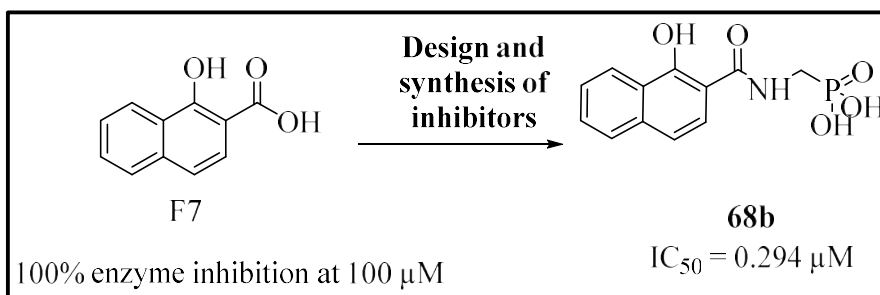


Fig. 4.2 From fragment to potent inhibitor

Thus, in summary, we designed, synthesized, and performed the *in-vitro* evaluation of the non-hydroxamate lipophilic small molecule inhibitors as per the proposed objectives.

- i. We collected 106 fragments from the literature and identified ~20 metal chelating fragments.
- ii. Based on novelty and synthetic tractability, we performed *in-vitro* screening of 13 fragments at 100 μ M.
- iii. We designed ~60 molecules with MBG-containing fragments and phosphonic acid containing α -aminophosphonates by fragment merging strategy, driven by target-based inhibitor design.
- iv. We synthesized 27 designed inhibitors and four molecules without phosphonate attachment. We performed *in-vitro* screening of the 17 synthesized molecules at 50 μ M and IC_{50} determination for eight molecules against the *E. coli* DXR enzyme using enzyme inhibitor assay.
- v. For 17 molecules, *in-vitro* screening against a panel of gram-negative and gram-positive bacteria was performed.

4.1.1.1 Scope for future work:

This thesis work was intended to design novel DXR inhibitors with increased lipophilicity and non-hydroxamate MBG. This preliminary work is a baby step toward adding much-needed structural diversity to the arsenal against DXR enzyme. However, following future studies can be taken for further development of these NCEs molecules.

1. Few molecules display enzyme inhibition at the micromolar range of the enzyme based *in vitro* assay. Since this is preliminary work, further improvement in potency against the enzyme is needed to obtain meaningful

results in the whole cell-based assays. Thus, a detailed SAR study is needed for each MBG explored in this study.

2. These molecules can be tested against DXR from other species.
3. The detailed binding mechanism and the enzyme activity of the remaining molecules should be evaluated in the future.
4. The permeability across the cell membrane needs to be studied.

4.1.2 *MtUng* Inhibitors

Another target selected for this work is UNG, which is essential for the survival of *Mtb* pathogen and other species important to maintain the genomic integrity of pathogens. Very few UNG inhibitors have been reported in the literature to date. All these inhibitors are uracil-derived with micromolar ranges of activity. Instead of well-defined UBP, only uracil-based compounds are reported in the literature. We selected the uracil-mimicking ring from the literature to explore structural diversity. For the development of *MtUng* inhibitors, based on their similarity with the uracil ring, we screened several ring fragments against *MtUng*. Among these rings, the Barbituric acid ring showed the promising inhibition of the *MtUng* enzyme comparable to uracil. Thus, the BA ring was selected for further derivatization and SAR studies. With the help of molecular docking-derived poses, we designed and synthesized several benzylidene derivatives of BA and evaluated these *in vitro* against the enzyme. The inhibition potential of these molecules was evaluated using two distinct enzymatic assays. In the radioactivity-based assay, molecules **45a** and **49a** were obtained as the lead molecules with IC₅₀ of 500 μM and 100 μM, respectively. Compound **45a** also displayed the most potent activity in the fluorescence-based assay with IC₅₀ 300 μM, thus, further validating the results obtained with the radioactivity-based assay. The structures of synthesized inhibitors are given in Fig. 4.3.

The SAR study and molecular docking suggest that the ester-bearing lipophilic chain/aromatic ring at the para position of the benzylidene ring is favorable for the *MtUng* inhibition. Conversely, the presence of polar carboxylate function was found to be relatively unfavorable.

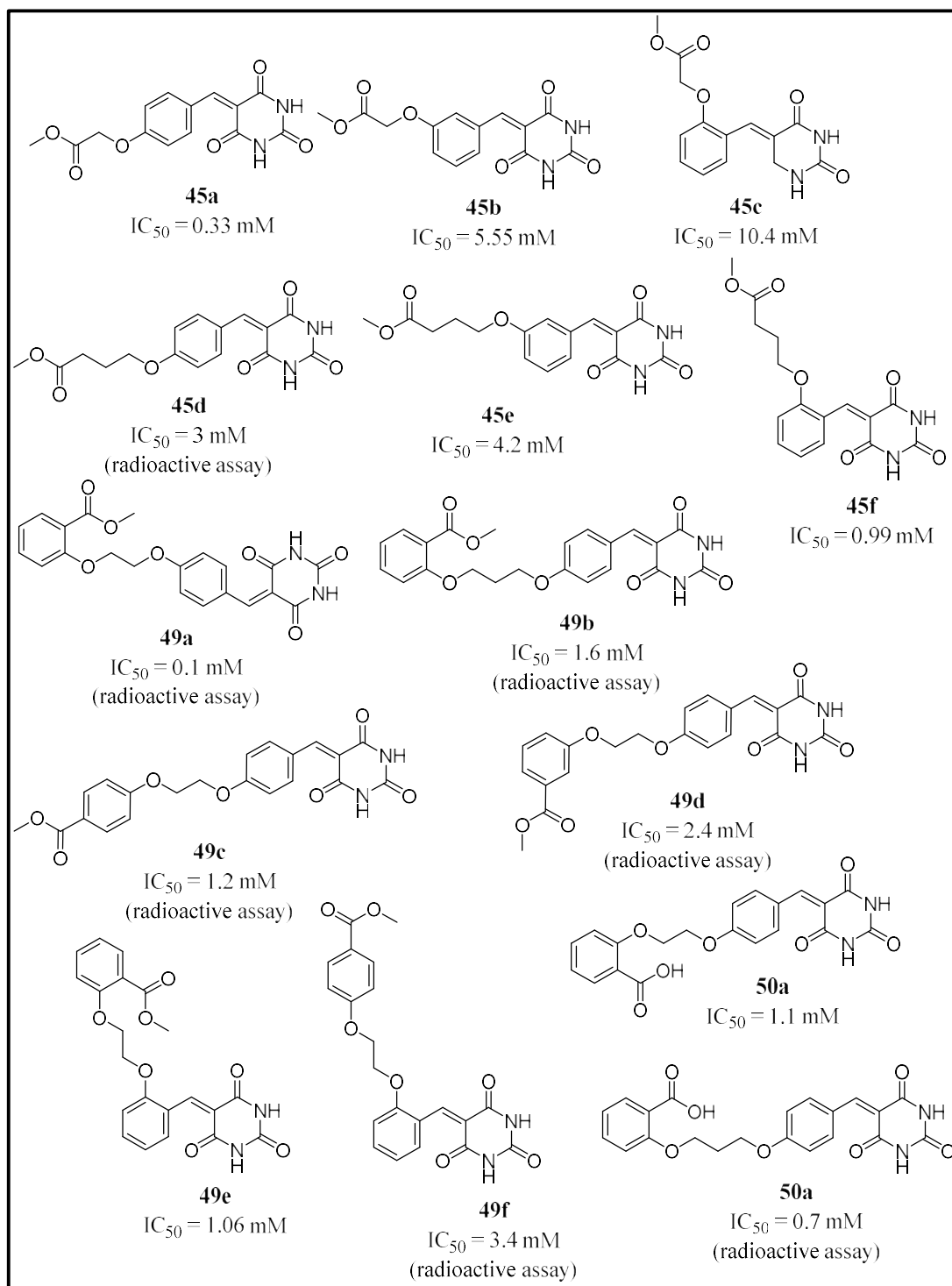


Fig. 4.3 Structures and IC_{50} values of *MtUng* inhibitors reported in this work.

In summary, we designed and synthesized benzylidene derivatives of BA and evaluated them against the *MtUng* enzyme in the radioactive-based assay as well as fluorescence-based assay as per the proposed objectives.

- i. We identified 12 different uracil-mimicking ring fragments from literature based on the 2D structural similarity to uracil.
- ii. We performed molecular docking studies for these ring fragments to determine the binding energies and *in-vitro* enzyme inhibition assay for IC₅₀ calculations of the selected fragments.
- iii. Further, we designed and synthesized 17 benzylidene derivatives of BA acid guided by SBDD and performed an *in-vitro* enzyme inhibition assay for IC₅₀ calculations to identify the potent *MtUng* inhibitor. These molecules, like other reported UNG inhibitors, displayed IC₅₀ values in lower mM to μM ranges. However, some of these synthesized molecules showed intrinsic fluorescence properties, making it difficult to evaluate these compounds in the fluorescent-based assay.

4.1.2.1 Scope for future work:

MtUng inhibitors have to compete with DNA-protein interaction which occurs over a large surface area. Thus, modulating such interaction with small molecules is challenging

1. Although, this work has established BA as a potential non-uracil ring for the design of *MtUng* inhibitor, the *in vitro* potency needs further improvement for this series. After potency optimization the potent analogues can be screened for the antimycobacterial activity.
2. At higher concentrations, some analogs showed poor aqueous solubility, thus creating hurdles during IC₅₀ measurement. Thus, to improve the solubility of the inhibitors further optimization is required.
3. The SAR can be expanded in future around linker and the tail aromatic ring.
4. The reported *MtUng* structures co-crystallized with other ring fragments could also be employed in the future to design other non-uracil *MtUng* inhibitors.
5. The selectivity (over human counterparts) of BA derivatives reported in this work should be studied to ensure their safety.

Annexure I

List of Publications

1. **Kesharwani, Sharyu**, and Sandeep Sundriyal. "Non-hydroxamate inhibitors of 1-deoxy-d-xylulose 5-phosphate reductoisomerase (DXR): A critical review and future perspective." *European Journal of Medicinal Chemistry* 213 (2021): 113055. <https://doi.org/10.1016/j.ejmech.2020.113055>
2. Raj, Prateek, Karthik Selvam, Koyel Roy, Shailesh Mani Tripathi, **Sharyu Kesharwani**, Balasubramanian Gopal, Umesh Varshney, and Sandeep Sundriyal. "Identification of a new and diverse set of Mycobacterium tuberculosis uracil-DNA glycosylase (MtUng) inhibitors using structure-based virtual screening: Experimental validation and molecular dynamics studies." *Bioorganic & Medicinal Chemistry Letters* 76 (2022): 129008. <https://doi.org/10.1016/j.bmcl.2022.129008>
3. **Sharyu Kesharwani**, Prateek Raj, Anju Paul, Koyel Roy, Amritansh Bhanot, Avani Mehta, Aiswarya Gopal, Umesh Varshney, Balasubramanian Gopal, and Sandeep Sundriyal. "Crystal structures of non-uracil ring fragments in complex with Mycobacterium tuberculosis uracil DNA glycosylase (MtUng) as a starting point for novel inhibitor design: A case study with the barbituric acid fragment." *European Journal of Medicinal Chemistry* (2023): 115604. <https://doi.org/10.1016/j.ejmech.2023.115604>
4. **Sharyu Kesharwani**, Eeba, Nisheeth Agarwal, Sandeep Sundriyal. "Design and synthesis of non-hydroxamate lipophilic inhibitors of 1-deoxy-D-xylulose 5-phosphate reductoisomerase (DXR): in silico, in vitro and antibacterial studies" Manuscript Number: EJMECH-D-23-02574

List of conferences

1. **Kesharwani S**, Sundriyal S.*, Poster presentation titled "Towards the design of non-hydroxamate lipophilic DXR inhibitors as potential antimicrobials" at international conference American Chemical Society, Fall Annual Meeting Chicago, IL, August 2022
2. **Kesharwani S**, Sundriyal S.*, Poster presentation titled "Design and Synthesis of lipophilic non-hydroxamate DXR inhibitors" at national conference Recent Trends and Challenges in Drug Discovery (RTCDD-2023) held on March 2023 (BITS Pilani, Pilani campus)
3. **Kesharwani S**, Sundriyal S.*, Poster presentation titled "A comprehensive review of various targets for anti-tubercular drug discovery" at national conference Towards End TB: Achievements, Challenges and Future Direction held on March 2023 (Translational Health Science and Technology Institute, THSTI, Faridabad)

Awards

1. Recipient of DST SERB Government of India International Travel Award (SERB-ITS), July 2022

2. Recipient of Council of Scientific and Industrial Research CSIR Travel Award, August 2022

Annexure II

Biography of Supervisor

Sandeep Sundriyal is an Assistant Professor in the Department of Pharmacy, Birla Institute of Technology and Science - Pilani (BITS-Pilani), Rajasthan, India. He received his doctoral degree in Medicinal Chemistry in 2008, for which he was awarded *Eli-Lilly Asia Outstanding Thesis Award*. Dr. Sundriyal gained ~ 8 years of postdoctoral experience at different USA and UK institutes, including one as a Marie Curie International Incoming Fellow at Imperial College London. He is also a ‘Fellow of the Higher Education Academy (FHEA)’ of UK. During his postdoctoral stints, he designed and synthesized ligands for various therapeutic targets, including histone lysine methyltransferases (HKMTs) inhibitors as antimalarial and anticancer agents. His current research interest includes antimicrobial and antiparasitic drug design. Dr. Sundriyal’s lab employs computational and synthetic chemistry to further the goals of the ongoing projects. He has over 30 research publications in international peer reviewed journals and has presented his work in several conferences. His current research is funded by several Indian Government agencies, such as DST-SERB, ICMR, and DBT. He is currently supervising and co-supervising 9 Ph.D. students.



Biography of candidate

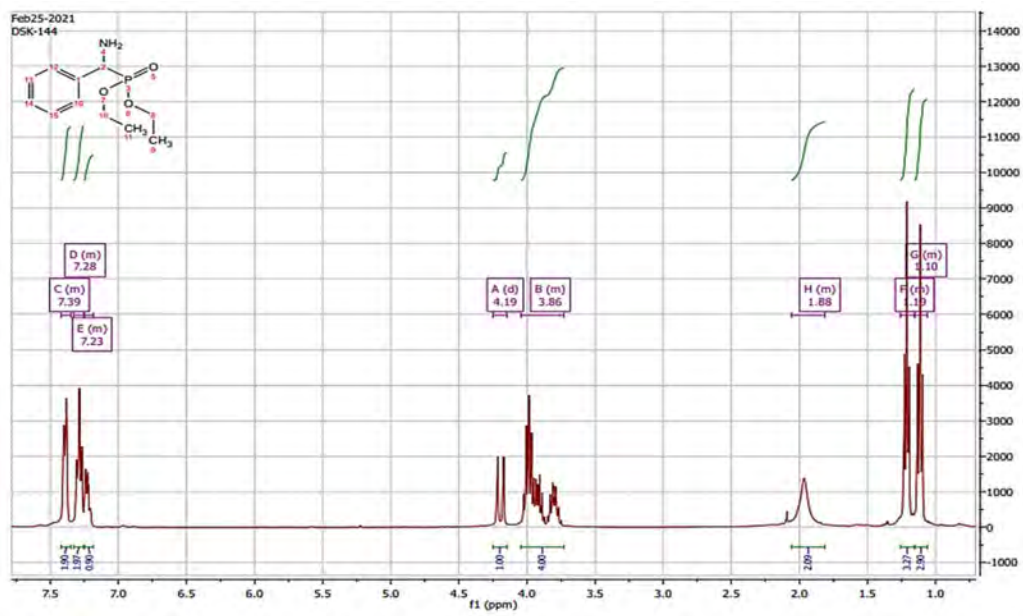
Sharyu Kesharwani graduated with a bachelor in Pharmacy from the department of Pharmaceutical Sciences, Nagpur University in 2016. She received her M. S. (Pharm) degree in Medicinal Chemistry from the National Institute of Pharmaceutical Education and Research, Kolkata in 2018. In 2019, she joined in the Department of Pharmacy of BITS Pilani, Pilani campus Rajasthan and she is working on her



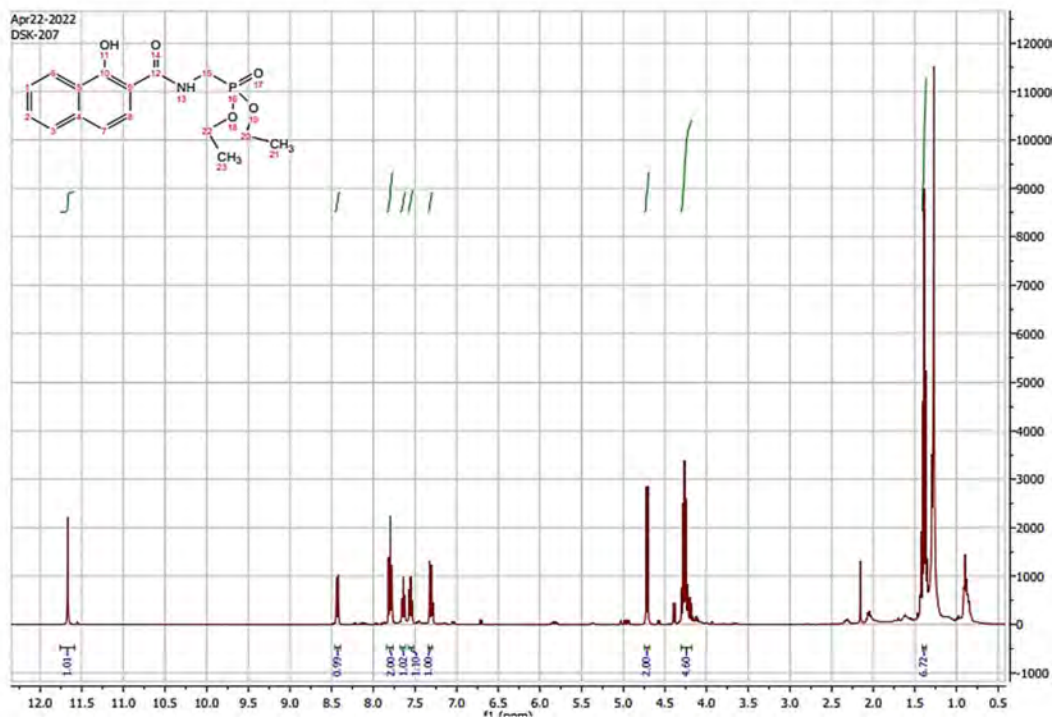
Ph.D. in Pharmaceutical Medicinal Chemistry under the Guidance of Dr. Sandeep Sundriyal, Assistant Professor at BITS Pilani Rajasthan. Her research work focuses on design and synthesis of novel lipophilic small molecules as Non-hydroxamate DXR inhibitors and *MtUng* inhibitors as potential antimicrobial agents.

Annexure III

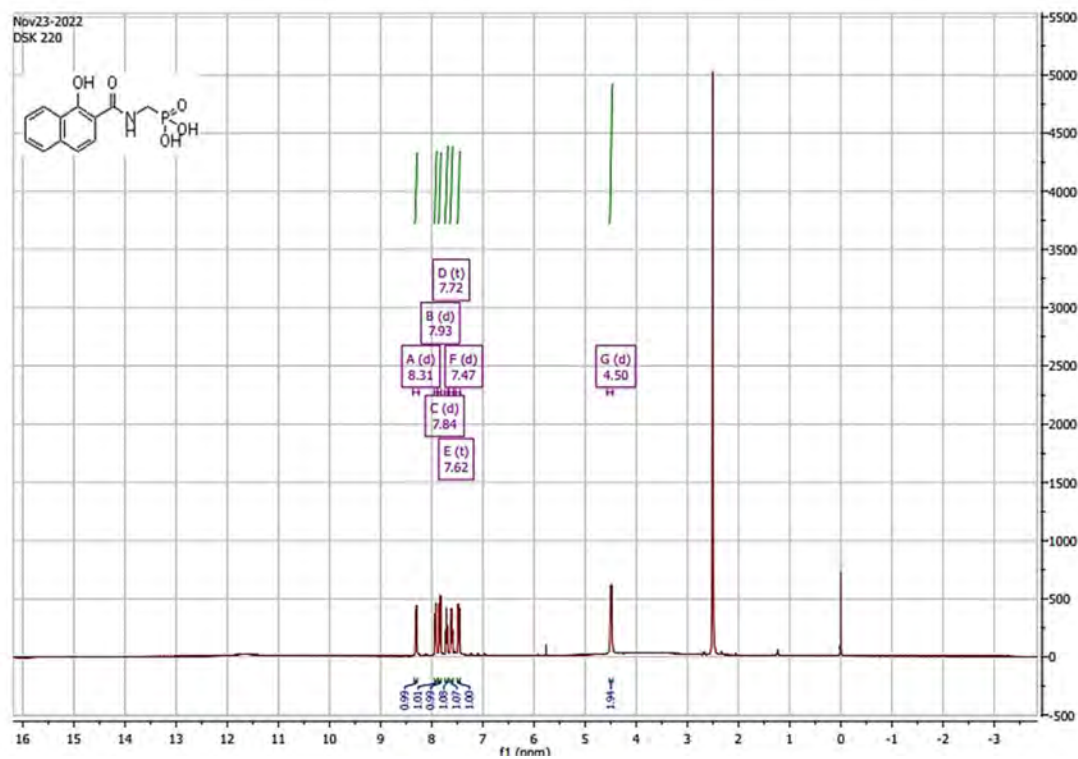
^1H NMR of alpha aminophosphonate



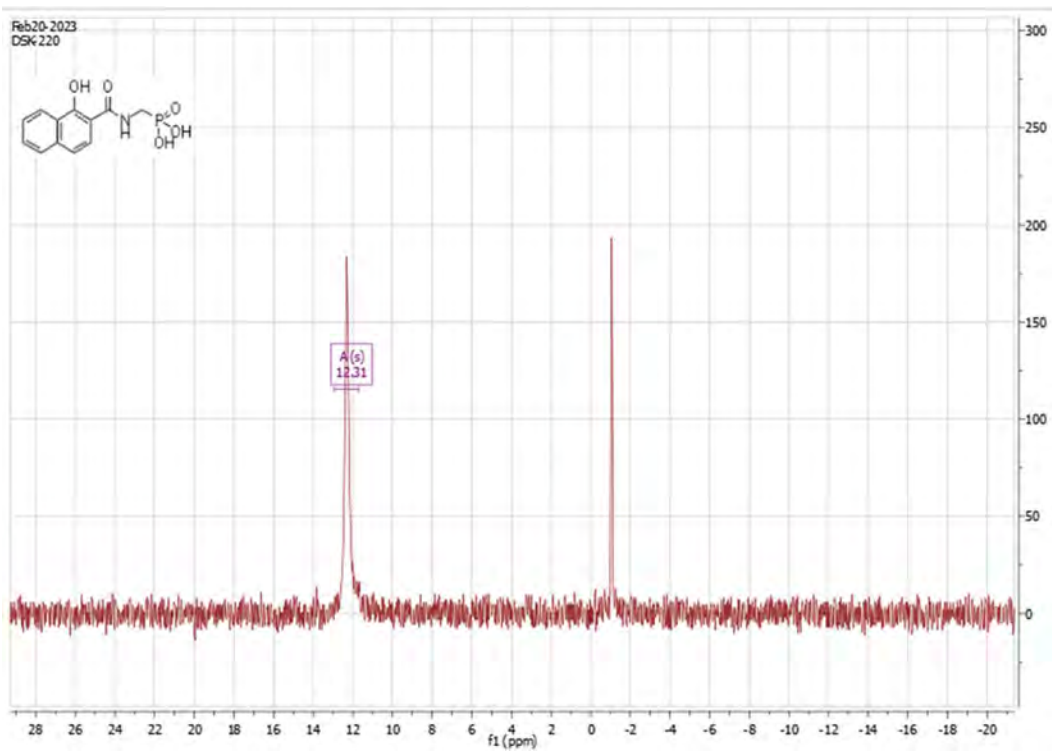
^1H NMR of the non-hydroxamate ester derivative



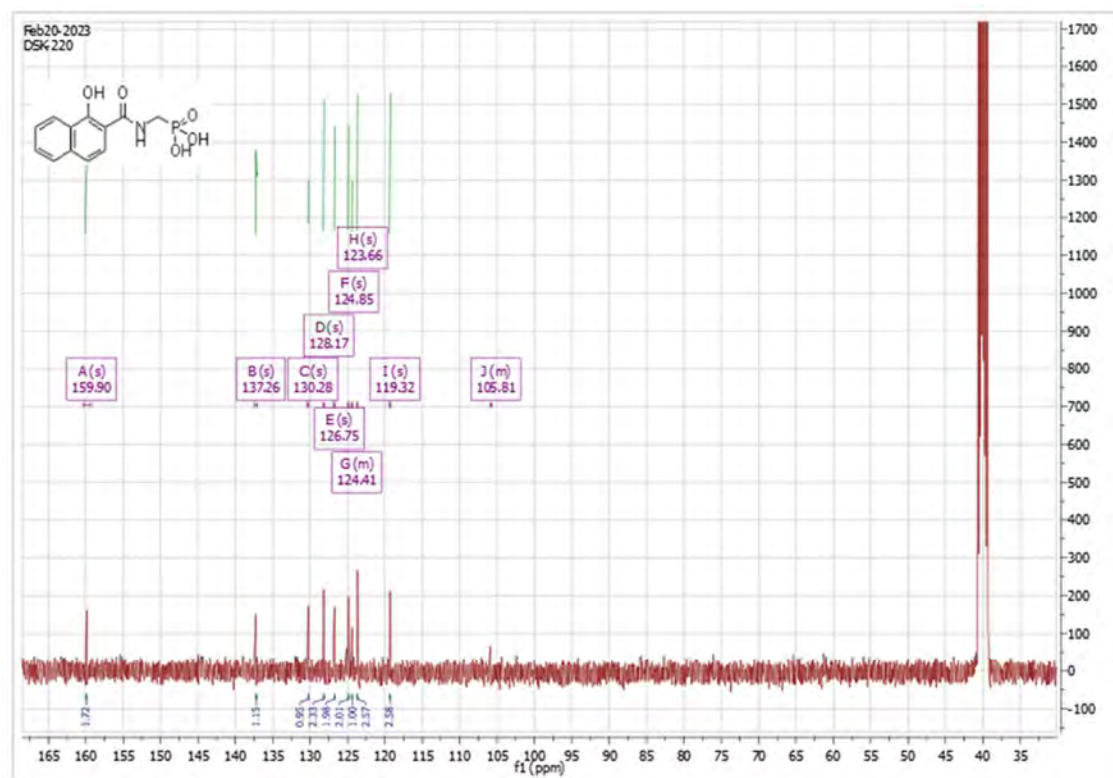
^1H NMR of non-hydroxamate lipophilic DXR inhibitor (**68b**)



³¹P NMR non-hydroxamate lipophilic DXR inhibitor (**68b**)



¹³C NMR non-hydroxamate lipophilic DXR inhibitor (**68b**)

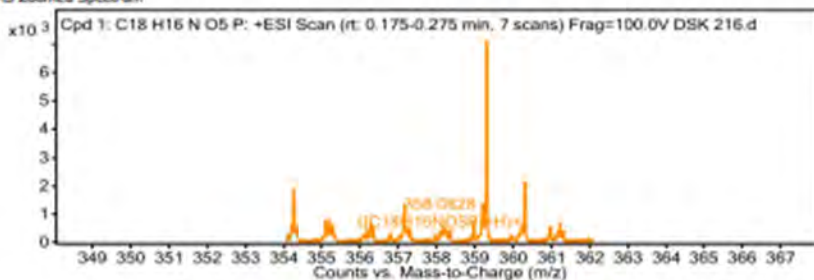


Mass spectrum of non-hydroxamate lipophilic DXR inhibitor (**68a**)

Compound Table

Compound Label	RT	Mass	Abund	Formula	Tgt Mass	Diff (ppm)
Cpd 1: C18 H16 N O5 P	0.192	357.0756	366	C18 H16 N O5 P	357.0766	-2.96

MS Zoomed Spectrum



MS Spectrum Peak List

m/z	Calc m/z	Diff(ppm)	z	Abund	Formula	Ion
358.0828	358.0839	2.95	1	365.56	C18H16NO5P	(M+H)+

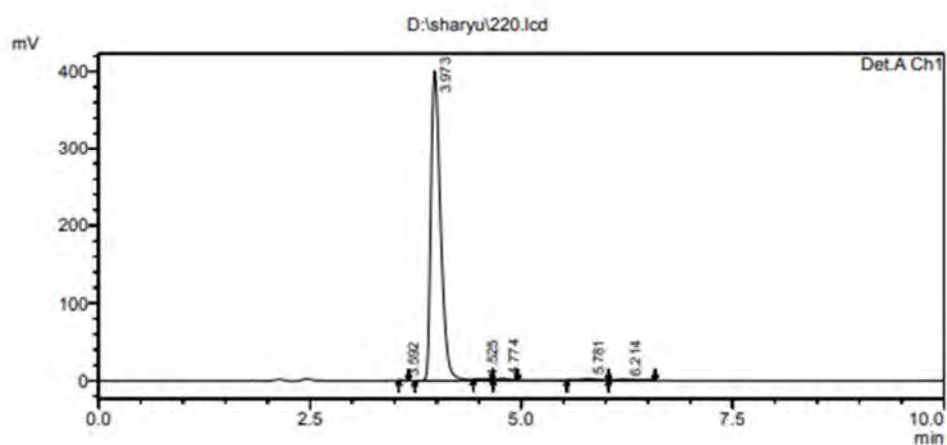
HPLC analysis of non-hydroxamate lipophilic DXR inhibitor (**68b**)

==== Shimadzu LCsolution Analysis Report ====

D:\sharyu\220.lcd

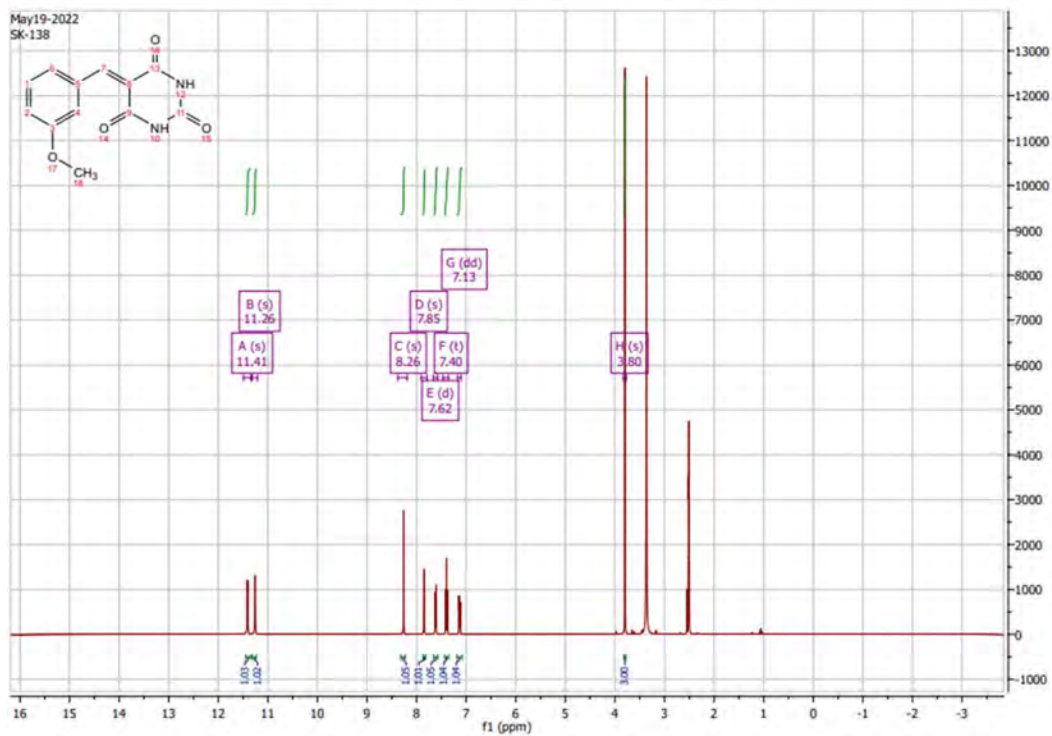
Acquired by : Admin
 Sample Name : 220
 Sample ID : 220
 Tray# : 1
 Vail # : 5
 Injection Volume : 20 uL
 Data File Name : 220.lcd
 Method File Name : sharyu.lcm
 Batch File Name : hhh.lcb
 Report File Name : Default.lcr
 Data Acquired : 28-Oct-09 12:30:08 AM
 Data Processed : 28-Oct-09 12:40:12 AM

<Chromatogram>

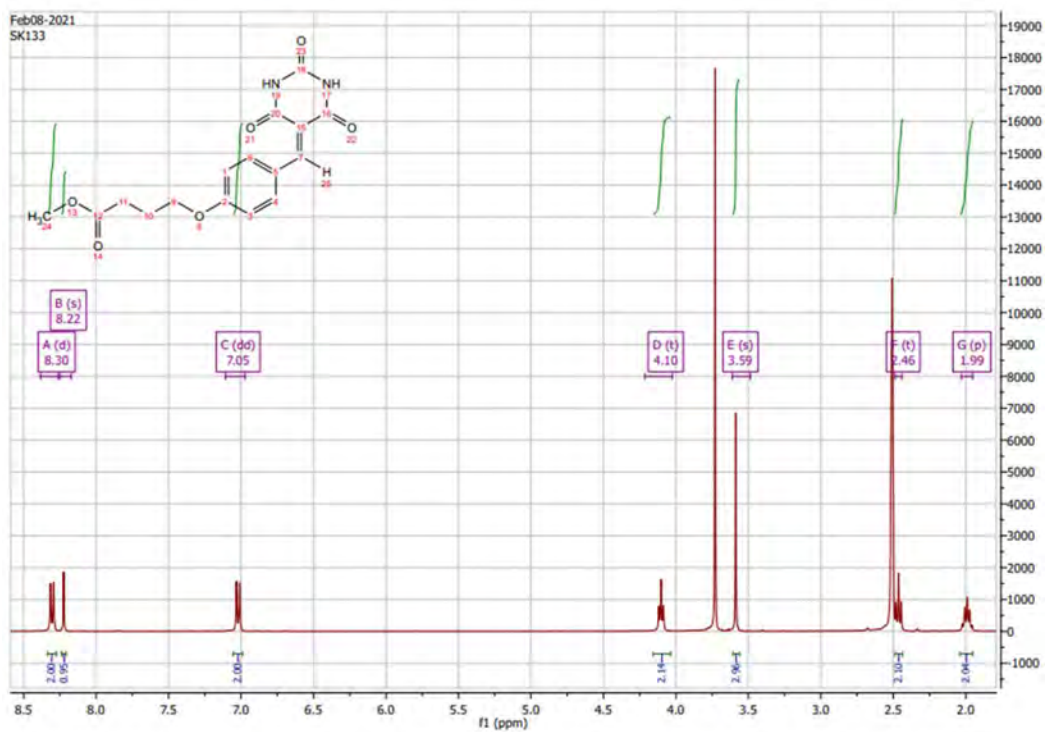


Peak#	Ret. Time	Area%	Area	k'	T.Plate#	Tailing F.
1	3.592	0.0042	137	0	17668.29	1.336
2	3.973	98.1674	3202908	0.106	5395.706	1.558
3	4.525	0.1344	4384	0.26	9053.94	1.238
4	4.774	0.5112	16679	0.329	9612.992	1.254
5	5.781	0.8321	27150	0.61	6859.316	1.25
6	6.214	0.3507	11441	0.73	7989.099	1.129

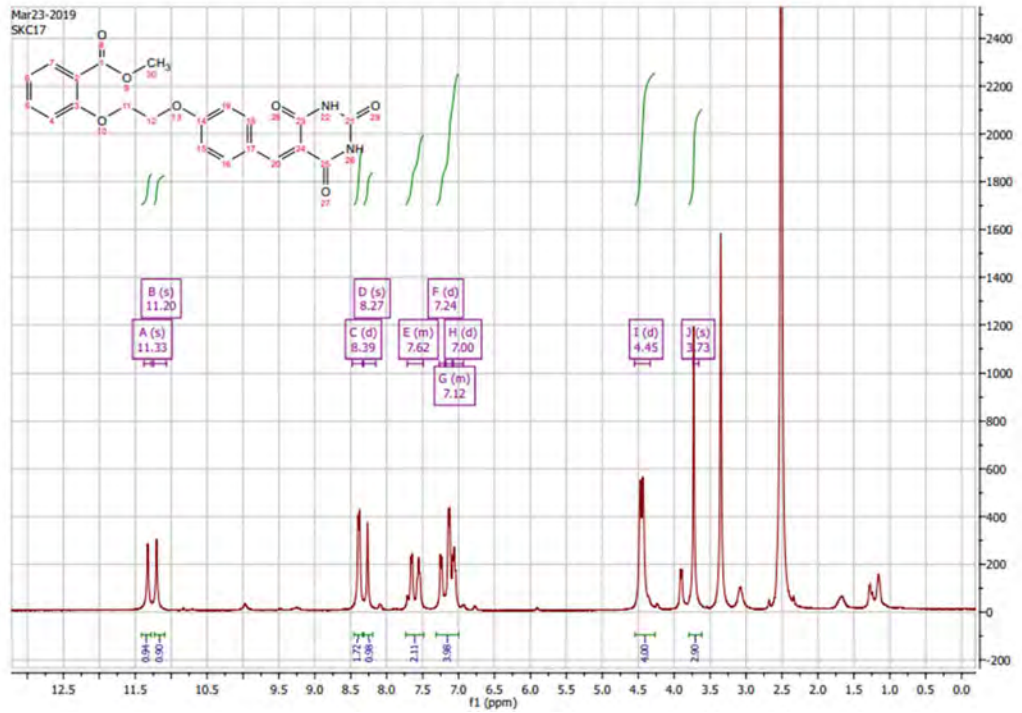
¹H NMR of *MtUng* inhibitor (**43a**)



^1H NMR of *MtUng* inhibitor (**45d**)



^1H NMR of *MtUng* inhibitor (**49a**)



¹H NMR of *Mt*Ung inhibitor (**50b**)

